



Saliveros, Efstratios (1988) *The aerodynamic performance of the NACA-4415 aerofoil section at low Reynolds numbers.*  
MSc(R) thesis.

<http://theses.gla.ac.uk/3050/>

Copyright and moral rights for this thesis are retained by the author

A copy can be downloaded for personal non-commercial research or study, without prior permission or charge

This thesis cannot be reproduced or quoted extensively from without first obtaining permission in writing from the Author

The content must not be changed in any way or sold commercially in any format or medium without the formal permission of the Author

When referring to this work, full bibliographic details including the author, title, awarding institution and date of the thesis must be given

**"THE AERODYNAMIC PERFORMANCE OF  
THE NACA-4415 AEROFOIL SECTION AT LOW  
REYNOLDS NUMBERS"**

A Thesis

Submitted to the Faculty of  
Engineering for the Fulfilment of  
the Requirements for the Degree  
of

Master of Science, (M.Sc.)

by

***Efstratios Saliveros, B.Sc.***

Department of Aerospace Engineering

University of Glasgow

Glasgow G12 8QQ

November 1988

"© 1988, E. Saliveros"

## PREFACE

The work described in this Dissertation was carried out by the author at the Department of Aerospace Engineering, University of Glasgow, between October 1986, and September 1987, and is original in content except where otherwise stated.

Department of Aerospace Engineering  
University of Glasgow  
Glasgow G12 8QQ

A handwritten signature in blue ink, appearing to read "E. Saliveros". The signature is written diagonally across the page, with the letters "E." and "Saliveros" clearly legible.

E. Saliveros

November, 1988

## ABSTRACT

In this experimental investigation, the performance and the boundary layer characteristics of the NACA-4415 aerofoil section were examined for an incidence range of  $-5.10^\circ \leq \alpha \leq 22.90^\circ$  and for the Reynolds number range of  $50,000 \leq Re \leq 600,000$ . Chordwise static pressure distributions were obtained, from which aerodynamic force and moment coefficients, namely  $C_N$ ,  $C_T$ , and  $C_{M_C}/4$ , were calculated using a simple Trapezoidal Rule method. These pressure distributions proved to be useful for the identification and location of the various boundary layer phenomena which occurred around the aerofoil. The "surface oil" flow visualisation technique was also used and photographs were obtained to record the various flow states over the upper surface of the aerofoil. The nominal two-dimensional data obtained in this study were compared with those from other facilities and previously tested aerofoils at the University of Glasgow. These latter comparisons were for the GU25-5(11)8, GA(W)-1 and NACA-0015 aerofoil sections.

### ACKNOWLEDGEMENTS

I would like to express my sincere gratitude to my supervisor Dr. R. A. McD. Galbraith for his recommendation of this project and his valuable advice, assistance and guidance throughout this work.

I would also like to express my profound gratitude to the Head of the Department of Aerospace Engineering, Professor B. E. Richards, without whose support and encouragement I would not have had the opportunity to work on this research project.

I owe many special thanks to Mr. G. Kokkodis for his advice and help during the early experimental stages of this work, and to Drs. F. N. Coton, A. Kokkalis and to Mr. R. D. Gordon for their useful suggestions and comments.

I am also thankful to the technicians, Messrs David J. Perrins, James C. Carr and John A. Kitching, for their efforts, and the goodwill that they have shown to me, assisting in any way they possibly could and for providing me with all the necessary equipment and tools when I really needed them. Special praises go to Mr. Kitching for his excellent job of constructing and polishing the model, to Mr. David M. Whitelaw and to the staff of the Photographic Department for their efforts of developing the pictures that appear in this work.

Finally, I would like to thank my parents for their tremendous support and encouragement that they have given me throughout my life and to my wife Catherine for the patience and understanding that she has shown during my studies at university.

## LIST OF CONTENTS

	Page
PREFACE.....	i
ABSTRACT.....	ii
ACKNOWLEDGEMENTS.....	iii
LIST OF CONTENTS.....	iv
LIST OF TABLES.....	vi
LIST OF FIGURES.....	vii
NOMENCLATURE.....	xvii
CHAPTER	
I. INTRODUCTION.....	1
1.1 Background Information.....	1
1.2 Boundary-Layer Characteristics/Separation Bubble....	4
1.3 Scope of the Present Study.....	8
II. EXPERIMENTAL APPARATUS.....	10
2.1 Wind Tunnel Facilities.....	10
2.2 Wind Tunnel Model.....	11
2.3 Computer Facilities.....	12
2.4 Static Pressure Measurements.....	13
2.5 Flow Visualisation and Photographic Equipment....	15
III. EXPERIMENTAL PROCEDURE.....	17
3.1 Static Pressure Distribution Measurements.....	17
3.2 Experimental Limitations.....	26
3.3 Flow Visualisation.....	28
IV. PRESENTATION AND DISCUSSION OF RESULTS.....	31
4.1 Performance as a Function of Angle of Attack.....	32

4.1.1	Introductory Comments.....	32
4.1.2	$Re = 50,000$ .....	34
4.1.3	$Re = 75,000$ .....	37
4.1.4	$Re = 100,000$ .....	40
4.1.5	$Re \geq 125,000$ .....	44
4.2	Pressure Coefficient Variation with Reynolds numbers at Constant Angles of Attack.....	49
4.3	Flow Visualisation Over the Upper Surface of the NACA-4415 Aerofoil.....	51
4.4	$C_N$ , $C_{Mc}/4$ and $C_T$ with Variation of Angles of Attack.....	57
4.5	$C_{Nmax}$ Variation with Reynolds Numbers.....	61
4.6	Comparison of the NACA-4415 Aerofoil Section Characteristics with Existing Data.....	63
4.7	Comparison of the NACA-4415 Aerofoil Section Characteristics with GU25-5(11)8, NASA GA(W)1 and NACA-0015 Sections.....	65
V.	CONCLUSIONS AND RECOMMENDATIONS FOR FURTHER STUDIES.....	71
5.1	Summary of Conclusions.....	72
5.2	Recommendations for Further Studies.....	76
5.3	Concluding Remarks.....	79
APPENDIX: Manufacture and Assembly of NACA-4415 Aerofoil Model.....		81
REFERENCES.....		84
TABLES.....		90
FIGURES.....		95

LIST OF TABLES

TABLE	Page
1. Coordinates of NACA-4415 Aerofoil Section.....	90
2. Locations of Pressure Tappings on NACA-4415 Aerofoil Section.....	91
3. Two-Dimensional Angle of Attack Summary.....	92
4. Estimated Locations of Laminar Separation Points on the Lower Surface of a NACA-4415 Aerofoil Section Using a Viscid-Inviscid Analysis Method.....	93
5. Useful Information About Past and Present Wind Tunnels Used to Test NACA-4415 Aerofoil Sections..	94

## LIST OF FIGURES

Figure	Page
1.1 Chord Reynolds Number versus Flight Velocity for a Variety of Natural and Man-Made Flying Objects.....	95
1.2 A Typical Laminar Separation Bubble Formed over the Upper Surface Of an Aerofoil.....	95
1.3 Turbulence Effects on Stall Hysteresis (a) and Pressure Distribution (b) for the Wortmann FX-63-137 Aerofoil Section. ( $Re=100,000$ ).....	96
1.4 Turbulence Effects on Stall Hysteresis (a) and Pressure Distribution (b) for the Wortmann FX-63-137 Aerofoil Section. ( $Re=200,000$ ).....	96
1.5 Acoustic Effects on Stall Hysteresis (a) and Pressure Distribution (b) for the Wortmann FX-63-137 Aerofoil Section. ( $Re=200,000$ ).....	96
1.6 Sketch of a Laminar Separation Bubble.....	97
1.7 Four Different Types of Static Stall.....	98
1.8 Typical Aerofoil Pressure Distribution with Laminar Separation Bubbles.....	98
1.9 Experimental Static Pressure Distribution over the NACA-4415 Aerofoil at an Incidence of $-5.10^\circ$ and at a Reynolds Number of 298,051.....	99
2.1 A Plan View of the Glasgow University's Low Speed Wind Tunnel.....	100
2.2 Cross-Sectional View of the Working Section of the Glasgow University's Low Speed Wind Tunnel..	101
2.3 Positions of the Pressure Tappings Around the NACA-4415 Aerofoil Model.....	102
2.4 Pressure Distribution Comparison Between Two Wortmann Aerofoils of Having Different Pressure Tap Configurations at $16^\circ$ Angle of Attack and $Re=200,000$ .....	103

2.5	Pressure Distribution Comparison Between Two Wortmann Aerofoils of Having Different Pressure Tap Configurations at $8^\circ$ Angle of Attack and $Re=80,000$ .....	104
3.1	Sequence of Events During Pressure Distribution Measurements.....	105
3.2	Schematic of Instrumentation used for the Data Acquisition.....	106
3.3	Section Lift and Profile Drag Coefficients Versus Angle of Attack for $R_C=150,000$ for the Smooth Lissaman Airfoil.....	107
3.4	Section Lift and Profile Drag Coefficients Versus Angle of Attack for $R_C=150,000$ for the Smooth Miley Airfoil.....	107
3.5	The NACA-4415 Aerofoil Installed in the Glasgow University's Low Speed Wind Tunnel.....	108
4.1.1	3-D Plots of $C_p$ vs $x/c$ vs $\alpha$ for the Lower (a) and Upper (b) Surface of a NACA-4415 Aerofoil Section and $Re=50,000$ .....	109
4.1.2	3-D Plots of $C_p$ vs $x/c$ vs $\alpha$ for the Lower (a) and Upper (b) Surface of a NACA-4415 Aerofoil Section and $Re=75,000$ .....	110
4.1.3	3-D Plots of $C_p$ vs $x/c$ vs $\alpha$ for the Lower (a) and Upper (b) Surface of a NACA-4415 Aerofoil Section and $Re=100,000$ .....	111
4.1.4	3-D Plots of $C_p$ vs $x/c$ vs $\alpha$ for the Lower (a) and Upper (b) Surface of a NACA-4415 Aerofoil Section and $Re=125,000$ .....	112
4.1.5	3-D Plots of $C_p$ vs $x/c$ vs $\alpha$ for the Lower (a) and Upper (b) Surface of a NACA-4415 Aerofoil Section and $Re=150,000$ .....	113
4.1.6	3-D Plots of $C_p$ vs $x/c$ vs $\alpha$ for the Lower (a) and Upper (b) Surface of a NACA-4415 Aerofoil Section and $Re=175,000$ .....	114

4.1.7	3-D Plots of $C_p$ vs $x/c$ vs $\alpha$ for the Lower (a) and Upper (b) Surface of a NACA-4415 Aerofoil Section and $Re=200,000$ .....	115
4.1.8	3-D Plots of $C_p$ vs $x/c$ vs $\alpha$ for the Lower (a) and Upper (b) Surface of a NACA-4415 Aerofoil Section and $Re=250,000$ .....	116
4.1.9	3-D Plots of $C_p$ vs $x/c$ vs $\alpha$ for the Lower (a) and Upper (b) Surface of a NACA-4415 Aerofoil Section and $Re=300,000$ .....	117
4.1.10	3-D Plots of $C_p$ vs $x/c$ vs $\alpha$ for the Lower (a) and Upper (b) Surface of a NACA-4415 Aerofoil Section and $Re=350,000$ .....	118
4.1.11	3-D Plots of $C_p$ vs $x/c$ vs $\alpha$ for the Lower (a) and Upper (b) Surface of a NACA-4415 Aerofoil Section and $Re=400,000$ .....	119
4.1.12	3-D Plots of $C_p$ vs $x/c$ vs $\alpha$ for the Lower (a) and Upper (b) Surface of a NACA-4415 Aerofoil Section and $Re=450,000$ .....	120
4.1.13	3-D Plots of $C_p$ vs $x/c$ vs $\alpha$ for the Lower (a) and Upper (b) Surface of a NACA-4415 Aerofoil Section and $Re=500,000$ .....	121
4.1.14	3-D Plots of $C_p$ vs $x/c$ vs $\alpha$ for the Lower (a) and Upper (b) Surface of a NACA-4415 Aerofoil Section and $Re=550,000$ .....	122
4.1.15	3-D Plots of $C_p$ vs $x/c$ vs $\alpha$ for the Lower (a) and Upper (b) Surface of a NACA-4415 Aerofoil Section and $Re=600,000$ .....	123
4.1.16	Pressure Distribution Around the NACA-4415 Aerofoil Section at Incidences Close to Complete Stall ( $Re=175,000$ ) .....	124
4.1.17	Pressure Distribution Around the NACA-4415 Aerofoil Section at Incidences Close to Complete Stall ( $Re=300,000$ ) .....	125

4.1.18	Pressure Distribution Around the NACA-4415 Aerofoil Section at Incidences Close to Complete Stall ( $Re=400,000$ ) .....	126
4.1.19	Locations of the Various Boundary Layer Phenomena on the Upper Surface of the NACA-4415 Aerofoil Section at $Re=75,000$ .....	127
4.1.20	Locations of the Various Boundary Layer Phenomena on the Upper Surface of the NACA-4415 Aerofoil Section at $Re=100,000$ .....	128
4.2.1	3-D Plot of $C_p$ vs $x/c$ vs $Re$ for the Upper Surface of the NACA-4415 Aerofoil Section at $\alpha=-5.10^\circ$ ...	129
4.2.2	3-D Plot of $C_p$ vs $x/c$ vs $Re$ for the Upper Surface of the NACA-4415 Aerofoil Section at $\alpha=-3.10^\circ$ ...	129
4.2.3	3-D Plot of $C_p$ vs $x/c$ vs $Re$ for the Upper Surface of the NACA-4415 Aerofoil Section at $\alpha=-1.10^\circ$ ...	130
4.2.4	3-D Plot of $C_p$ vs $x/c$ vs $Re$ for the Upper Surface of the NACA-4415 Aerofoil Section at $\alpha=-0.10^\circ$ ...	130
4.2.5	3-D Plot of $C_p$ vs $x/c$ vs $Re$ for the Upper Surface of the NACA-4415 Aerofoil Section at $\alpha= 0.90^\circ$ ...	131
4.2.6	3-D Plot of $C_p$ vs $x/c$ vs $Re$ for the Upper Surface of the NACA-4415 Aerofoil Section at $\alpha= 2.90^\circ$ ...	131
4.2.7	3-D Plot of $C_p$ vs $x/c$ vs $Re$ for the Upper Surface of the NACA-4415 Aerofoil Section at $\alpha= 4.90^\circ$ ...	132
4.2.8	3-D Plot of $C_p$ vs $x/c$ vs $Re$ for the Upper Surface of the NACA-4415 Aerofoil Section at $\alpha= 6.90^\circ$ ...	132
4.2.9	3-D Plot of $C_p$ vs $x/c$ vs $Re$ for the Upper Surface of the NACA-4415 Aerofoil Section at $\alpha= 9.90^\circ$ ...	133
4.2.10	3-D Plot of $C_p$ vs $x/c$ vs $Re$ for the Upper Surface of the NACA-4415 Aerofoil Section at $\alpha=10.90^\circ$ ...	133

4.2.11	3-D Plot of $C_p$ vs $x/c$ vs $Re$ for the Upper Surface of the NACA-4415 Aerofoil Section at $\alpha=11.90^\circ$ .....	134
4.2.12	3-D Plot of $C_p$ vs $x/c$ vs $Re$ for the Upper Surface of the NACA-4415 Aerofoil Section at $\alpha=12.90^\circ$ .....	134
4.2.13	3-D Plot of $C_p$ vs $x/c$ vs $Re$ for the Upper Surface of the NACA-4415 Aerofoil Section at $\alpha=13.90^\circ$ .....	135
4.2.14	3-D Plot of $C_p$ vs $x/c$ vs $Re$ for the Upper Surface of the NACA-4415 Aerofoil Section at $\alpha=14.90^\circ$ .....	135
4.2.15	3-D Plot of $C_p$ vs $x/c$ vs $Re$ for the Upper Surface of the NACA-4415 Aerofoil Section at $\alpha=15.90^\circ$ .....	136
4.2.16	3-D Plot of $C_p$ vs $x/c$ vs $Re$ for the Upper Surface of the NACA-4415 Aerofoil Section at $\alpha=16.90^\circ$ .....	136
4.2.17	3-D Plot of $C_p$ vs $x/c$ vs $Re$ for the Upper Surface of the NACA-4415 Aerofoil Section at $\alpha=17.90^\circ$ .....	137
4.2.18	3-D Plot of $C_p$ vs $x/c$ vs $Re$ for the Upper Surface of the NACA-4415 Aerofoil Section at $\alpha=18.90^\circ$ .....	137
4.2.19	3-D Plot of $C_p$ vs $x/c$ vs $Re$ for the Upper Surface of the NACA-4415 Aerofoil Section at $\alpha=19.90^\circ$ .....	138
4.2.20	3-D Plot of $C_p$ vs $x/c$ vs $Re$ for the Upper Surface of the NACA-4415 Aerofoil Section at $\alpha=20.90^\circ$ .....	138
4.2.21	Typical Surface Pressure Distributions With and Without Separation Bubble.....	139
4.3.1	Flow Visualisation Photographs of the Upper Surface of the NACA-4415 Aerofoil Section at Various Reynolds Numbers and at $\alpha=-5.10^\circ$ .....	140
4.3.2	Flow Visualisation Photographs of the Upper Surface of the NACA-4415 Aerofoil Section at Various Reynolds Numbers and at $\alpha=-1.10^\circ$ .....	141

4.3.3	Flow Visualisation Photographs of the Upper Surface of the NACA-4415 Aerofoil Section at Various Reynolds Numbers and at $\alpha = 2.90^\circ$	142
4.3.4	Flow Visualisation Photographs of the Upper Surface of the NACA-4415 Aerofoil Section at Various Reynolds Numbers and at $\alpha = 6.90^\circ$	143
4.3.5	Flow Visualisation Photographs of the Upper Surface of the NACA-4415 Aerofoil Section at Various Reynolds Numbers and at $\alpha = 9.90^\circ$	144
4.3.6	A sequence of Flow Visualisation Photographs of the Upper Surface of the NACA-4415 Aerofoil at $Re=600,000$ and $\alpha=9.90^\circ$	145
4.3.7	Flow Visualisation Photographs of the Upper Surface of the NACA-4415 Aerofoil Section at Various Reynolds Numbers and at $\alpha=11.90^\circ$	146
4.3.8	A sequence of Flow Visualisation Photographs of the Upper Surface of the NACA-4415 Aerofoil at $Re=600,000$ and at $\alpha=11.90^\circ$	147
4.3.9	Flow Visualisation Photographs of the Upper Surface of the NACA-4415 Aerofoil Section at Various Reynolds Numbers and at $\alpha=13.90^\circ$	148
4.3.10	Flow Visualisation Photographs of the Upper Surface of the NACA-4415 Aerofoil Section at Various Reynolds Numbers and at $\alpha=15.90^\circ$	149
4.3.11	Flow Visualisation Photographs of the Upper Surface of the NACA-4415 Aerofoil Section at Various Reynolds Numbers and at $\alpha=17.90^\circ$	150
4.3.12	Flow Visualisation Photographs of the Upper Surface of the NACA-4415 Aerofoil Section at Various Reynolds Numbers and at $\alpha=18.90^\circ$	151
4.3.13	Flow Visualisation Photographs of the Upper Surface of the NACA-4415 Aerofoil Section at Various Reynolds Numbers and at $\alpha=19.90^\circ$	152

4.3.14 A sequence of Flow Visualisation Photographs of the Upper Surface of the NACA-4415 Aerofoil at Re=450,000 and at $\alpha=19.90^\circ$ .....	153
4.3.15 Comparison between $C_p$ and Flow Visualisation Data Regarding the Locations of the Various Boundary Layer Phenomena occurring on the Upper Surface of the NACA-4415 Model at Re=150,000.....	154
4.3.16 Comparison between $C_p$ and Flow Visualisation Data Regarding the Locations of the Various Boundary Layer Phenomena occurring on the Upper Surface of the NACA-4415 Model at Re=200,000.....	155
4.3.17 Comparison between $C_p$ and Flow Visualisation Data Regarding the Locations of the Various Boundary Layer Phenomena occurring on the Upper Surface of the NACA-4415 Model at Re=250,000.....	156
4.3.18 Comparison between $C_p$ and Flow Visualisation Data Regarding the Locations of the Various Boundary Layer Phenomena occurring on the Upper Surface of the NACA-4415 Model at Re=300,000.....	157
4.3.19 Comparison between $C_p$ and Flow Visualisation Data Regarding the Locations of the Various Boundary Layer Phenomena occurring on the Upper Surface of the NACA-4415 Model at Re=350,000.....	158
4.3.20 Comparison between $C_p$ and Flow Visualisation Data Regarding the Locations of the Various Boundary Layer Phenomena occurring on the Upper Surface of the NACA-4415 Model at Re=400,000.....	159
4.3.21 Comparison between $C_p$ and Flow Visualisation Data Regarding the Locations of the Various Boundary Layer Phenomena occurring on the Upper Surface of the NACA-4415 Model at Re=500,000.....	160
4.3.22 Comparison between $C_p$ and Flow Visualisation Data Regarding the Locations of the Various Boundary Layer Phenomena occurring on the Upper Surface of the NACA-4415 Model at Re=600,000.....	161

4.4.1	Normal Force, Quarter Chord Pitching Moment and Tangential Force Coefficient Variation With Angle of Attack at Re=50,000.....	162
4.4.2	Normal Force, Quarter Chord Pitching Moment and Tangential Force Coefficient Variation With Angle of Attack at Re=75,000.....	163
4.4.3	Normal Force, Quarter Chord Pitching Moment and Tangential Force Coefficient Variation With Angle of Attack at Re=100,000.....	164
4.4.4	Normal Force, Quarter Chord Pitching Moment and Tangential Force Coefficient Variation With Angle of Attack at Re=125,000.....	165
4.4.5	Normal Force, Quarter Chord Pitching Moment and Tangential Force Coefficient Variation With Angle of Attack at Re=150,000.....	166
4.4.6	Normal Force, Quarter Chord Pitching Moment and Tangential Force Coefficient Variation With Angle of Attack at Re=175,000.....	167
4.4.7	Normal Force, Quarter Chord Pitching Moment and Tangential Force Coefficient Variation With Angle of Attack at Re=200,000.....	168
4.4.8	Normal Force, Quarter Chord Pitching Moment and Tangential Force Coefficient Variation With Angle of Attack at Re=250,000.....	169
4.4.9	Normal Force, Quarter Chord Pitching Moment and Tangential Force Coefficient Variation With Angle of Attack at Re=300,000.....	170
4.4.10	Normal Force, Quarter Chord Pitching Moment and Tangential Force Coefficient Variation With Angle of Attack at Re=350,000.....	171
4.4.11	Normal Force, Quarter Chord Pitching Moment and Tangential Force Coefficient Variation With Angle of Attack at Re=400,000.....	172
4.4.12	Normal Force, Quarter Chord Pitching Moment and Tangential Force Coefficient Variation With Angle of Attack at Re=450,000.....	173

4.4.13	Normal Force, Quarter Chord Pitching Moment and Tangential Force Coefficient Variation With Angle of Attack at Re=500,000.....	174
4.4.14	Normal Force, Quarter Chord Pitching Moment and Tangential Force Coefficient Variation With Angle of Attack at Re=550,000.....	175
4.4.15	Normal Force, Quarter Chord Pitching Moment and Tangential Force Coefficient Variation With Angle of Attack at Re=600,000.....	176
4.4.16	Quarter Chord Pitching Moment Coefficient versus Angle of Attack for the Wortmann FX-63-137 Aerofoil ( $R_C=100,000$ ) .....	177
4.4.17	NACA-23012 Aerofoil Data for AR=4.0 .....	177
4.4.18	Lift Coefficient versus Uncorrected Incidence of a NACA-23012 Aerofoil at a Reynolds Number of 350,000.....	178
4.4.19	Measured Aerodynamic Characteristics of a NACA-23012 Airfoil.....	178
4.4.20	Comparison of Results for the Occurrence of the 'kink' on $C_N$ and $C_{Mc}/4$ Curves with those Defining Fully Laminar Flow Using Coton's Method.....	179
4.4.21	Two Dimensional Lift and Drag Coefficients versus Angle of Attack, Re=80,000.....	179a
4.5.1	Maximum Normal Force Coefficient Variation with Reynolds number.....	179
4.5.2	Lift Coefficient Variation with Incidence and Reynolds Number of a NACA-4415 Aerofoil Tested at Stuttgart (1962-72) .....	180
4.5.3	Lift Coefficient Variation with Incidence and Reynolds Number of a NACA-4415 Aerofoil Tested at NACA VDT (1934) .....	181
4.5.4	Lift Coefficient Variation with Incidence and Reynolds Number of a NACA-4415 Aerofoil Tested at NACA LTT (1945) .....	182
4.5.5	Normal Force Coefficient Variation with Incidence and Reynolds Number of a NACA-4415 Aerofoil Tested at University of Glasgow (1987) .....	183

4.5.6	Lift Coefficient Variation With Incidence of a Wortmann FX-63-137 Aerofoil Tested at a Reynolds Number of 200,000.....	185
4.6	Comparison of Lift and Quarter Chord Pitching Moment Coefficients of the NACA-4415 Aerofoil Obtained at Different Test Environments and Wind Tunnels.....	186
4.7.1	Normal Force Coefficient Contours for the NACA-4415 Aerofoil with Incidence and Reynolds Number.....	187
4.7.2	Normal Force Coefficient Contours for the GU25-5(11)8 Aerofoil with Incidence and Reynolds Number.....	188
4.7.3	Normal Force Coefficient Contours for the NASA GA(W)-1 Aerofoil with Incidence and Reynolds Number.....	189
4.7.4	Normal Force Coefficient Contours for the NACA-0015 Aerofoil with Incidence and Reynolds Number.....	190
A1.	Construction of the NACA-4415 Model.....	191

## NOMENCLATURE

$c$	Aerofoil chord length, mm
$C_L$	Lift coefficient
$C_{Mc/4}$	Quarter chord pitching moment
$C_N$	Normal force coefficient
$C_{Nmax}$	Maximum normal force coefficient
$C_p$	Pressure coefficient
$C_T$	Tangential force coefficient
$dC_{Mc/4}/d\alpha$	Quarter chord pitching moment curve slope
$dC_N/d\alpha$	Normal force curve slope
$g$	Gravitational acceleration, m/s <sup>2</sup>
$H$	Atmospheric pressure height, mm Hg
$h_{21}$	Differential pressure height between atmospheric and static pressure, mm H <sub>2</sub> O
$h_{sw}$	Differential pressure height between settling chamber and working section, mm H <sub>2</sub> O
$k$	Wind tunnel calibration constant
$P_1$	Static pressure based at surface of aerofoil, Nm <sup>2</sup>
$P_2$	Atmospheric pressure, Nm <sup>2</sup>
$P_s$	Pressure at wind tunnel settling chamber, Nm <sup>2</sup>
$P_w$	Pressure at wind tunnel working section, Nm <sup>2</sup>
$q$	Free stream dynamic pressure, Nm <sup>2</sup>
$R$	Specific gas constant, kJ/KgK
$Re_C$	Reynolds number based on aerofoil chord
$T_a$	Tunnel air speed, °C
$V$	Free stream velocity, m/s
$x$	Chordwise co-ordinate

### Greek Symbols

$\alpha$	Angle of attack, deg.
$\alpha_g$	Geometric angle of attack, deg.
$\epsilon_B$	Total blockage factor
$\rho$	Density of air, Kg/m <sup>3</sup>
$\rho_m$	Density of mercury relative to water
$\rho_w$	Density of water, Kg/m <sup>3</sup>

### Subscripts

$a$	air
$c$	chord
$g$	geometric
$m$	mercury
$s$	settling chamber
$w$	working section, water

## **CHAPTER I**

### **INTRODUCTION**

#### **1.1 BACKGROUND INFORMATION**

In aerodynamic applications, the low Reynolds number regime is usually taken as that for which the chord Reynolds number falls below 1,000,000. In the past, study of this flow regime has not been actively investigated since most aerodynamic vehicles operate at much higher Reynolds numbers. The last twenty years, however, have seen a growing interest in low Reynolds number flows since a number of applications have evolved requiring aerofoil sections that operate at low Reynolds numbers. A working knowledge of the associated flow phenomena is therefore necessary.

Low Reynolds number applications occur when any combination of the following conditions is present:

- a) low free stream velocity
- b) low air density
- c) small aerofoil chord.

These conditions are found to exist on remotely piloted vehicles (RPV's) used for surveillance, sampling and

monitoring in both military and scientific roles, operating at high altitudes, mini-RPV's flying at low altitudes, high altitudes jet-engine fan blades, etc. Additional applications are found in the inboard sections of helicopter, propeller, and in wind turbine rotors. Figure 1.1 succinctly illustrates the various Reynolds number regimes. Efforts in designing low Reynolds number aerofoil sections which possess high aerodynamic efficiencies have been effective together with much experimental work to determine the performance of existing aerofoils at those Reynolds numbers (Ref.1).

Flow behaviour at chord Reynolds number less than 1,000,000 is widely known to involve some significantly different characteristics when compared to higher Reynolds number flows. These flow characteristics create difficulties relating to the management of the aerofoil boundary layer as well as difficulties associated with accurate wind tunnel measurements (Refs 2,3). Lissaman states, that as a general criterion there exists a critical Reynolds number of about 70,000 below which aerofoil performance is very poor and above which impressive improvements are observed (Ref.4). Very important areas of concern are the occurrence and behaviour of the leading edge laminar separation bubbles and the associated phenomenon of transition from laminar to turbulent flow (Figure 1.2). It is well known that separation is highly sensitive at low Reynolds numbers and plays a very

important role in determining the development of the boundary layer which, in turn, affects the overall performance of the aerofoil.

On close examination of the wind tunnel test data below the 1,000,000 range of Reynolds numbers using models with the same aerofoil sections, it is possible to observe that there is a number of inconsistencies among the test results. This can be attributed to a variety of causes including inaccurate measurement techniques, or due to solid and wake blockage effects, and differences between test environments. These blockage effects are discussed in detail in References 5 and 6. In the past, researchers have often been puzzled by other researchers questioning test data accuracy, data acquisition techniques, data measurement reliability, model accuracy or even tunnel corrections. Mueller et al (Ref.7) describes some of the methods used to identify the level of free stream disturbances and their influence on the performance of low Reynolds number aerofoils.

The problems associated with obtaining accurate wind tunnel data for aerofoil sections at low Reynolds numbers are compounded by the extreme sensitivity of the boundary layers to the free stream disturbance environment. The disturbance environment present in the test section of a low speed wind tunnel is usually determined by the free stream turbulence levels, acoustic phenomena and mechanical

vibrations. Although these disturbances may be reduced and, to some extent, controlled, they cannot be eliminated. If proper care is taken to reduce or account for such phenomena, then more meaningful results may be obtained. By taking account of turbulence intensity levels and acoustic disturbances Sumantran et al (Ref.8) obtained considerable differences in the test data and in particular the stall hysteresis loop and pressure distributions (Figures 1.3, 1.4 and 1.5). These Figures illustrate that the range of turbulence levels between 0.02% and 0.2% is quite important whilst above a value of 0.2% may have negligible effects. At these increased values maximum lift coefficients appear to remain unaffected. Similar results were also obtained by Mueller (Ref.9), during an investigation on the performance of two aerofoils influenced by free stream disturbances at low Reynolds numbers.

## 1.2 BOUNDARY LAYER CHARACTERISTICS / SEPARATION BUBBLE

The phenomena of boundary layer separation and transition at low Reynolds numbers have been known to be very important for a long time because of their effect on the aerofoils performance. With the existence of turbulent flow over an aerofoil, drag is increased and so a desirable design for an aerofoil, therefore, would be to maintain laminar flow over a large proportion of its length. Such a design would lead to higher lift and lower drag values. At low Reynolds numbers, however, where the flow tends to

remain laminar it may have been expected to produce flows tending towards this aim. Unfortunately, the inability of the laminar boundary layer to sustain large adverse pressure gradients leads to the separation of the flow from the aerofoil surface within the pressure recovery region. This results in large losses of lift and increased drag.

If the laminar shear layer separates from the surface and undergoes transition to turbulent flow, and the turbulent shear layer has sufficient entrainment to reattach, then the well known "separation bubble" will be formed. The separation bubble is defined as that region in which slowly recirculating air is trapped between the separation and re-attachment points. A simple diagram of the separation bubble is shown in Figure 1.6. The length of the separation bubble is defined as the distance between the separation and re-attachment points and is usually expressed in non-dimensional form as a percentage of the chord length.

Laminar separation bubbles have been studied for many years (Refs 10-15). Generally their behaviour is used to describe the performance and stalling characteristics of aerofoils. These stalling characteristics can be classified into four different categories:

- a) Trailing edge stall
- b) Leading edge or short-bubble stall
- c) Long bubble or thin aerofoil stall

- d) Combination of both trailing edge and leading edge stall.

The characteristics of these categories are illustrated in Figure 1.7.

"Trailing edge stall" generally occurs on moderately thick aerofoils ( $\geq 10\% \text{ x/c}$ ). It is identified by forward movement of the turbulent separation point as incidence is increased causing a decrease in the lift curve slope, and a gradual loss of lift beyond the maximum without causing a sharp drop in the lift coefficient. "Leading edge" or "short bubble stall" occurs when a short bubble situated just downstream of the leading edge suction peak "bursts", causing gross flow separation. This occurs when the leading edge adverse pressure gradient is too severe for the flow to re-attach. The third type, the "long bubble" or "thin aerofoil stall", is described as the movement of the bubble's re-attachment point towards the trailing edge of the aerofoil with increasing angle of attack. The long bubble increases in length gradually until it covers the entire aerofoil. The maximum lift is relatively small compared with other types of stall and if the angle of attack is increased further this will lead to lift reduction. The final type of stall occurs when the aerofoil experiences a combination of trailing edge separation and leading edge short bubble bursting. At angles of attack just prior to the leading edge bubble bursting, the lift curve slope dips as the lift decreases

only gradually due to significant trailing edge separation. With increases in angle of attack the leading edge bubble bursts resulting in a sudden decrease in lift and a large increase in drag. In Reference 11, Chappell calls such behaviour a "combined stall" due to the occurrence of both forward movement of the turbulent separation point and the leading edge bubble bursting.

Separation bubbles are typically described as "long" or "short" depending on their relative lengths. A "long" bubble covers a separated region of about 20%-40% of the chord, while the length of a "short" bubble covers only a few percent. A short bubble generally makes little impact on the pressure distribution around an aerofoil (Figure 1.8). Lissaman (Ref.4) also uses the above criterion in defining long bubbles, but states that the short bubble could not form unless the chord Reynolds number is greater than 100,000.

Many of the separation bubbles identified in this study occurred as far downstream as 65% or even 75% of the chord with turbulent re-attachment very close to the trailing edge. These bubbles were "long" according to their length criterion (20%-40% of the chord), but became shorter in length and moved towards the leading edge at increased incidence. When the aerofoil was set at negative angles of attack (e.g.  $\alpha=-5.1^\circ$ ,  $Re=300,000$ ) two separation bubbles were formed, a "long" and a "short" one. Figure 1.9,

illustrates a pressure distribution with the two separation bubbles formed on the upper and lower surfaces clearly shown. The long bubble formed near the trailing edge on the upper surface and the short one close to the leading edge on the lower surface of the aerofoil.

During the stalling process, on the NACA-4415 aerofoil, a combination of both trailing edge separation and leading edge short bubble bursting was observed, indicating that the aerofoil's stalling characteristic fell into the fourth category as mentioned earlier. The two-dimensional behaviour of the NACA-4415 aerofoil with increasing angle of attack and Reynolds number is described in Chapter IV.

### 1.3 SCOPE OF THE PRESENT STUDY

The investigation carried out in this study was to identify possible advantageous characteristics of the NACA-4415 aerofoil section at Reynolds numbers below or equal to 600,000. This work is also part of the continuing research programme at the University of Glasgow dedicated to revealing the performance and boundary layer characteristics of aerofoils which are currently being used on the rotor blades of various wind turbines and helicopters. In addition to this investigation, comparison was made with three other aerofoils previously tested using the same wind tunnel facilities. It is hoped that what was observed will

be valuable to future researchers and may give an indication of the phenomena which other aerofoil sections operating in the same low Reynolds number regime, would experience.

Static pressure measurements were taken to obtain values of normal force and pressure drag coefficients as well as pitching moment coefficients. An assessment of the first order boundary layer characteristics was made and it revealed that the most important feature was the separation bubbles developed on the upper and lower surfaces of the model. Flow visualisation was also carried out to examine the flow phenomena over the aerofoil's upper surface and useful information was recorded in the form of photographs which were subsequently used in the analysis of the test data.

## **CHAPTER II**

### **EXPERIMENTAL APPARATUS**

All experimental data presented in this report were obtained using the facilities of the Aerospace Engineering Department's Laboratory at the University of Glasgow. The test model, a NACA-4415 aerofoil section was used and its performance determined over a wide range of low chord Reynolds numbers. Static pressure distributions were obtained using pressure tappings which were connected via three electronic selector boxes, to a micromanometer and thence to a DEC MINC (PDP 11/23) mini-computer system. Aerodynamic force and moments coefficients were obtained by integrating the static pressure distribution of the aerofoil. The "surface oil" flow visualisation technique was also used and photographs were obtained to record the various flow states that occurred around the aerofoil. The technique provided useful information for a better understanding of the aerofoil's performance and boundary layer characteristics.

#### **2.1    WIND TUNNEL FACILITIES**

All tests were conducted in the Aerospace Engineering

Department's medium sized low speed wind tunnel which is an atmospheric-pressure closed-return type and has a rectangular cross section of 1.143m width and 0.838m height (Figures 2.1 and 2.2). Its upper and lower walls contain graduated turntables for mounting the model vertically. This was done in such a way as to provide rotation about the quarter chord axis.

Since the tunnel operated at atmospheric pressures only, the Reynolds number was varied by means of changing the tunnel airspeed. The minimum and maximum air flow velocities obtained in the test section were approximately 2.5 and 30.0 m/s respectively. Kokkalis, (Ref.16), investigated the turbulence intensity level and found that in the longitudinal direction it was 0.4% while in the lateral direction it was 0.6%. Both of these components were measured at the centre of the working section and under a free stream velocity of 10.0 m/s.

## 2.2 WIND TUNNEL MODEL

The model used in these experiments had a NACA-4415 aerofoil section. The construction of this model was carried out at the Aerospace Engineering Department's manufacturing and assembly facilities during the period December 1986 to February 1987. Full details of the construction of this model are given in the Appendix. The chord length was 300.0 mm, and the span 838.0 mm giving an

aspect ratio of 2.8. The dimensions were chosen so they would match those of GU25-5(11)8, NASA GA(W)-1 and NACA-0015 models previously tested under the same conditions in the same wind tunnel facility (Refs 17 and 18). The aerofoil's co-ordinates are listed in Table 1.

The NACA-4415 aerofoil section was chosen because it belongs to the NACA-44XX family of aerofoil sections which are widely used for the rotor blades of horizontal axes wind turbines. Galbraith et al (Ref.19), provides a tabulated list not only of the NACA-44XX aerofoil series but also of the NASA GA(W)-1 and NACA-0015 aerofoil sections showing their wide applicability to various types of wind turbines.

### 2.3 COMPUTER FACILITIES

In the present study, data acquisition and data reduction for all pressure measurements was accomplished with the aid of a DEC MINC (PDP 11/23) mini-computer. The data acquisition system consisted of PDP 11/23 processor interfaced with two RX02M diskette drives. Each diskette has a capacity of 512 kB. One of the diskettes was used as the system's device (DY0:) containing the necessary operating system software while the other (DY1:) was used for data and programs storage. The console used with this system, while the computer operated in the data acquisition mode, was a DEC VT105. An IBM computer system and an EPSON

MX-80 printer were also connected with the computer system for the production of draft pressure distribution plots.

Analog to digital conversion was accomplished by a 12-bit A/D converter (MNCAD). In conjunction with the A/D converter a programmable clock (MNCKW) was also used. Both the A/D converter and the clock were plugged into the MINC's chassis in a configured mode.

All the collected and reduced data files were transferred from the diskettes to a VAX 11/750 computer main-frame via a lengthy process. The VAX 11/750 coupled with a VERSATEC plotter and using GINO graphics routines, produced high quality plots. The VAX 11/750 computer system used to produce the required plots and permanent storage of the data for Data Base Management (D.B.M).

#### 2.4 STATIC PRESSURE MEASUREMENTS

Aerofoil pressure distributions were obtained using a specially constructed model with pressure tappings mounted on its mid-span position on the upper and lower surfaces along the chord length. Pressure data were obtained for ranges of 50,000 to 600,000 chord Reynolds numbers and  $-5.10^\circ$  to  $22.90^\circ$  of angles of attack.

A total of sixty pressure tappings were placed around the aerofoil so a good assessment of the chordwise

pressure distribution could be achieved. Thirty nine of those were placed on the upper surface with the remaining twenty one on the lower surface of the model. The locations of these tappings were measured using a vernier height gauge and are listed in Table 2. Figure 2.3 illustrates the shape of the aerofoil's cross section together with the positions of the pressure tappings on both the upper and lower surfaces. The pressure tappings were staggered over the first 11.4% and 8% of the chord from the leading edge on the upper and lower surfaces respectively, and at 22% from the trailing edge on the upper surface. Staggering the pressure tappings was deliberate to avoid any interference which might exist between a downstream pressure tapping and an upstream one (Ref.1). Figures 2.4 and 2.5 show clearly wide differences in pressure distribution measurements between an "in-line" and "staggered" pressure tapping model tested under the same wind tunnel conditions. As seen in Figure 2.4, the "in-line" pressure tap model has a lower suction peak and fails to indicate the existing leading edge separation bubble. Figure 2.5 also demonstrates that the pressure tappings, placed "in-line", cause earlier transition.

The use of two electronic micromanometers was required to measure free stream dynamic pressures and differential pressures at each pressure tapping. Both micromanometers are of MDC-FC002 and FC012 types and have ranges of  $+/-19.99$  and  $+/-199.9$  mm of  $H_2O$ .

The accuracy of the MDC-FC002 micromanometer, calibrated by the manufacturers using precision water column manometers, is +/-1%, whilst for the FC012 type it is 0.2% or 0.3% depending on range of pressure. Their linearity is +/-0.5% or +/-1.0%, and their output voltage signal is 0-2 VDC or 0-5 VDC respectively (see Reference 22).

Alongside the micromanometers, three selector boxes were provided to accommodate all pressure tubes. Each selector box has a maximum of twenty pressure fittings attached at its rear panel together with an output pressure port connected to the input of the FC012 micromanometer. These selector boxes enabled an automatic selection of each pressure tapping so that the corresponding pressure measurement could be carried out. This automatic selection of the tappings was achieved by using an IEEE Standard 488-1975 Bus Controller mounted in the PDP 11/23 computer. The communication path between the PDP 11/23 and the selector boxes was provided by the IEEE Bus interface cable.

## 2.5 FLOW VISUALISATION AND PHOTOGRAPHIC EQUIPMENT

In addition to the pressure coefficient and force measurements on the NACA-4415 model tested much useful information about the boundary layer was obtained by

visually observing the nature of the fluid flow past the surface of the model. For this purpose, the surface oil flow visualisation technique was considered. This technique was chosen because of its successful application on different aerofoil models tested in the same wind tunnel by previous researchers (Refs 17, 18, 20 and 21).

This flow visualisation technique was performed using Odina-oil, Saturn Yellow "Dayglo" fluorescent powder and liquid paraffin for a thinner. The viscosity of the mixture was adjusted by trial and error until a suitable ratio was obtained. This mixture was then applied on the upper surface of the model by careful stippling using an ordinary sponge. Extra care was taken so the oil mixture was uniformly distributed on the whole area of the upper surface of the model. Once the solution was applied to the model it was illuminated using two ultra-violet light sources. They made the visualisation solution appear bright yellow, and therefore enabled the user to observe and study the flow patterns as they developed.

A NIKON FE-2 50mm camera was used to obtain still photographs of the fluorescing powder once the pattern had developed. The camera was equipped with ultra-violet and polarising filters so that only the visible light from the powder impinges on the photographic emulsion. Photographs were obtained using ILFORD XP1-400 ASA film.

## CHAPTER III

### EXPERIMENTAL PROCEDURE

#### 3.1 STATIC PRESSURE DISTRIBUTION MEASUREMENTS

The chordwise pressure distributions were obtained at the mid-span of the specially constructed pressure model using the PDP 11/23 data acquisition system, two electronic micromanometers and three selector boxes. An ordinary thermometer and a barometer were also used to measure the wind tunnel air temperature and atmospheric pressure respectively during each test. Two programs were used extensively in this study for the collection and reduction of the data, namely AEROFL.BAS and CNTM41.FOR. The data collection program (AEROFL.BAS) written in BASIC computer language and the data reduction program (CNTM41.FOR) written in FORTRAN language. The main reason of writing AEROFL.BAS in BASIC was that the three selector boxes could only operate under BASIC language commands. These programs are a modification of the programs GEOR.BAS and CNDM.FOR used by Kokkodis (Ref.18). The modification was necessary to improve time consumption and accuracy of the reduced data. A set of programs was also written to present the reduced data files in a graphical form. All the plotting

programs were written in FORTRAN and, together with GINO graphics routines, a presentation of chordwise pressure distributions in two and three dimensional form, as well as force and moments coefficients versus angles of attack, was available.

The main assumption made for this part of the study was that the airflow remained uniform, steady and incompressible in its entire journey through the tunnel. Using the above assumption the pressure coefficient is defined as

$$C_p = (P_1 - P_2) / [(1/2) \cdot \rho_a \cdot V^2] = (P_1 - P_2) / q \quad (3.1)$$

where  $P_1$  refers to static pressure on the surface of the aerofoil

$P_2$  refers to atmospheric pressure and

$q$  refers to free stream dynamic pressure.

The pressure difference  $(P_1 - P_2)$  can also be written as  
(Ref.23)

$$(P_2 - P_1) = \rho_w \cdot g \cdot h_{21} \quad (3.2)$$

and the free stream dynamic pressure as

$$(1/2) \cdot \rho_a \cdot v^2 = k \cdot (P_s - P_w) = k \cdot (\rho_w \cdot g \cdot h_{sw}) \quad (3.3)$$

where  $k$  is referred to as the wind tunnel calibration factor. For the wind tunnel concerned,  $k$  equals to 1.18. Thus, equation (3.1) can be re-written as

$$C_p = - h_{21} / k \cdot h_{sw} \quad (3.4)$$

Therefore to determine the pressure coefficient it was only necessary to measure two pressure differences, both measured in mm H<sub>2</sub>O.

The flow chart illustrating the sequence of events during the chordwise pressure distribution measurements is shown in Figure 3.1. A schematic representation of the various electronic instruments used and their interconnections is also shown in Figure 3.2. The free stream dynamic pressure was measured in terms of the difference between a total head and a static pressure reading using the MDC-FC002 electronic micromanometer. The static pressure was measured by means of an orifice in the wall of the working section, well upstream of the model. The total head pressure was measured through another orifice placed in the tunnel's settling chamber wall upstream of the contraction. The two orifices were connected to the measuring head of the micromanometer via rubber tubes and

the pressure difference was then recorded. In addition, a second micromanometer (FCO12) measured the pressure difference between static pressures from each tapping on the model and the atmospheric pressure.

Before each set of tests, a warm up time of twenty to thirty minutes was allowed so that the electronics of the two micromanometers as well as the selector boxes and the A/D converter were brought up to desired operational temperatures. At the beginning and end of each test, the wind tunnel air temperature and the atmospheric pressure were recorded. The air temperature was measured using an ordinary thermometer inserted through an orifice in the side wall of the tunnel upstream of the test section. The atmospheric pressure was obtained using a mercury barometer. The barometer height ((H) in mm Hg) and air temperature ((T<sub>a</sub>) in °C) were substituted into expression (3.5) which determined the wind tunnel air density (Ref.24).

$$\rho_{air} = (\rho_m \cdot \rho_w \cdot g \cdot H) / (R \cdot T_a) \quad (3.5)$$

The determination of wind tunnel air density was necessary in order to reduce to the minimum any experimental errors concerning the air velocity and hence the free stream dynamic pressure and Reynolds number.

As mentioned earlier in Chapter II, three selector

boxes were used to accommodate all pressure tubes. Each selector box had twenty pressure ports at its rear panel. The connection of the pressure tubes was made in such a way that tube labelled as number one in selector box I corresponded to the pressure tapping nearest to the trailing edge on the upper surface of the model. The pressure tapping nearest to the trailing edge on the lower surface corresponded to tube number sixty connected to selector box III. An IEEE Bus cable provided the communication link between the PDP 11/23 computer and the selector boxes. The boxes were connected to the Bus by multiple conductor cables. With the help of the IEEE Bus cable the selection of a particular pressure port, and therefore of a pressure tapping on the model, could be carried out automatically by the acquisition program.

Each selector box also has a main output pressure port which allows the pressure of a selected pressure tapping to be transmitted into the FC012 micromanometer. The manometer could then measure the pressure difference between the atmospheric pressure and the static pressure of the selected pressure tapping. The reading was then fed into the A/D converter of the PDP 11/23 computer as an analog voltage signal. The selector boxes were entirely governed by the computer which allowed complete computer control of the experiment for the duration of each test.

A "test" consisted of the chordwise static pressure

distribution data taken at mid-span of the model for one Reynolds number condition and for one angle of attack. During each test, the data acquisition program stepped through the model once, sampling each pressure tapping forty times in a period of one second. The sampling process for each test began at the trailing edge and proceeded along the upper surface to the leading edge then on to the lower surface pressure tappings starting from the leading edge and progressing to the trailing edge. The cycle of the selection of the forty samples for each pressure tapping was carried out twice and two average values were obtained. If the difference between the two averages was between  $\pm 2\%$  of the first average then this value was stored on the system's diskette before progressing to the next tapping. However, in case the above convergence criterion was not satisfied, then the whole process of taking new values would be repeated up to a maximum of twenty times. If still no convergence was obtained after the twenty cycles then the last average value was recorded together with a warning that this particular pressure tapping did not converge. Therefore, it was easy to observe that the time taken for each test varied in the present investigation. During some tests the time used was considerable. This occurred due to the large flow fluctuations for very low Reynolds numbers (see Figures 4.1.1 and 4.1.2).

The selected pressure measurements from each tapping

were stored on diskettes so that the reduction process of the data could be carried out after the completion of the tests. Before any experiments were begun, several runs were carried out to check for possible pressure tube leaks at various wind tunnel speeds and angles of attack as well as the data acquisition process. After the completion of each test the corresponding pressure distribution was displayed on the screen of the DEC VT105 monitor. This allowed a checking of any pressure abnormalities that might have occurred during the experiment and therefore a re-run, for that particular angle of attack and Reynolds number, was carried out.

During each set of tests, the wind tunnel operated at the desired speed until the completion of the tests. This had an effect on the dynamic pressure which with increasing angle of attack was reduced due to wind tunnel blockage effects. The dynamic pressure was originally set with zero angle of attack for each set of tests. Generally, the dynamic pressure decreased for each set of tests up to a maximum of 3% of its initial value, prior to complete stall.

In general, a complete set of tests for the NACA-4415 aerofoil at one Reynolds number condition included angles of attack prior to the commencement of positive lift to angles beyond full stall. Measurements were taken for at least every degree of incidence. The

Reynolds number range varied from 50,000 to 600,000 with a step increment of 25,000 for the first 200,000. After 200,000 Reynolds number, the step increment increased to 50,000 until it reached 600,000. A grand total of 597 tests were performed for 15 different Reynolds number conditions.

The CNTM41.FOR computer program was used for the integration of pressure distributions to obtain normal force and pressure drag coefficients, together with leading edge and quarter chord pitching moment coefficients. The integration of pressure distributions was based on a trapezoidal rule approximation method. When using chordwise pressure distributions this method is relatively accurate provided there is close spacing of pressure tappings around the aerofoil. The program also stored pressure coefficients data in files formatted for plotting using the available software in the Aerospace Engineering Department's VAX 11/750 computer library.

Throughout this investigation, the generated force and moment coefficients remained uncorrected for two-dimensional blockage effects and streamline curvature. There were two main reasons for leaving these coefficients uncorrected. Firstly, because no attempt was made to measure the wake behind the aerofoil by using a wake traverse method, and secondly, because of the limited validity of the derived two-dimensional equations, applied for such corrections. These equations are only valid for

flows over aerofoils which are wholly subsonic and fully attached (Refs 5 and 6).

Such wake measurements would have been essential for obtaining a value of the total blockage factor,  $\epsilon_B$ , at different geometric angles of attack. Although the flow over the present aerofoil matched the subsonic criterion, it did not match the fully attached flow. This was because of the presence of a separation bubble on either the upper or lower surfaces and trailing edge separation at incidences greater than  $8^\circ - 9^\circ$ . Full details of the expressions involved for correcting wind tunnel aerodynamic force and moment coefficients data are given in References 5 and 6.

The only correction made in this study, however, was of the angle of attack. Kelling (Ref.21) discovered in his investigation that the flow approaching the test section is yawed by approximately  $+/-0.6$  degrees depending on the direction in which the test incidence is measured. Here, the positioning of the model in the working section contributed to a negative flow yawing angle. Therefore, the actual angle of attack was obtained by subtracting 0.6 degrees from the measured geometric incidence, i.e.

$$\alpha = \alpha_g - 0.6^\circ \quad (3.6)$$

### 3.2 EXPERIMENTAL LIMITATIONS

The main experimental limitation experienced in this study was the inability to obtain data for the NACA-4415 aerofoil at angles of attack greater than  $19.40^\circ$  and for 550,000 Reynolds number. This problem was encountered due to the fact that the FC012 electronic micromanometer went out of range. Pressure values exceeding the micromanometer's operational limit were usually observed on the upper surface and very close to the leading edge. When this occurred no further collection of data was allowed and the test was terminated.

Exactly the same problem occurred for the 600,000 Reynolds number and for angles of attack greater than  $13.40^\circ$ . For a matter of interest however the micromanometer was set to manual with a maximum off-set value of -40.7 mm H<sub>2</sub>O as the zero setting. This allowed the micromanometer to extend its operational limit to +240.6 and -159.2 mm H<sub>2</sub>O. Once again, however, it proved impossible to reach full stalling angles. By pure coincidence, the maximum angle of attack obtained for both the 550,000 and 600,000 Reynolds number cases was  $19.40^\circ$ . One might speculate that the data collected for Reynolds number equal to 600,000 and for angle of attack greater than  $13.40^\circ$  is not accurate enough and should be considered with skepticism. Figure 4.4.15 however, illustrates that there are no major discrepancies

of the aerodynamic force coefficients against angle of attack plots for angles of attack greater than  $\alpha=13.40^\circ$  and therefore the data could be treated as such of lower Reynolds numbers.

Generally, in an experimental investigation of the aerodynamic performance of an aerofoil, a consideration must be made for every possible aspect which might affect its overall performance. Such an aspect is the hysteresis effect occurring near the stalling angles of attack. The aerodynamic forces are strongly dependent on this hysteresis phenomenon and on the direction at which the stalling angle is approached. Hysteresis is of practical importance because it could strongly affect the recovery from stall and/or flight conditions.

Two possible hysteresis loops exist, the "high-lift" or "clockwise" and "low-lift" or "counterclockwise" hysteresis. By increasing the angle of attack the lift and drag forces are increased. When stall is finally reached the lift experiences a large drop while drag experiences a great increase. Reducing the angle of attack slightly the former values of the aerodynamic forces are not restored. Instead, the angle of attack may have to be reduced by several degrees before lift and drag revert to values obtained under conditions of increasing angle of attack. This is known as the "high-lift" or "clockwise" hysteresis

loop and mainly happens to aerofoils experiencing early transition caused by a separation bubble.

For the "low-lift" or "counterclockwise" hysteresis loop, the lift and drag experience sudden increases at a certain angle of attack. In this case, reducing the angle of attack, lift and drag keep increasing until maximum values are obtained. Reducing it even further causes lift and drag forces to revert to values obtained with increasing angles of attack. This type of hysteresis loop is mainly caused by the increase of the long bubble and its abrupt collapse to a short bubble. Figures 3.3 and 3.4 show that the Lissaman aerofoil exhibits the "high-lift" hysteresis loop while the Miley produces the "low-lift" hysteresis loop.

In this study, however, considering that there is a very high turbulence intensity level (0.5%) in the wind tunnel used and following the observations of Sumantran et al and Mueller (Refs 8 and 9), it is thought that hysteresis effects may be considered to be negligible. Therefore, no attempt was made to show any hysteresis effects which might occur on the lift curve slopes.

### 3.3 FLOW VISUALISATION

Flow visualisation was accomplished using the surface oil-film technique. This technique was carried out on the

NACA-4415 aerofoil model with all the pressure orifices sealed. No quantitative pressure measurements were made at this stage, since the objective was to observe any flow phenomena which may occur. Photographs were taken of the model's upper surface at different angles of attack and Reynolds numbers. This method had been used very successfully in the past (References 18 and 20) at tunnel speeds over 10m/s but with very limited success at lower velocities. The interpretation of flow visualisation photographs taken in the study, as well as in previous studies for speeds lower than 10m/s, indicate that the surface oil-film flow visualisation technique as used, was performing at its limit and the oil-film probably altered the boundary layer characteristics of the aerofoil giving inaccurate results.

It was found from initial photographic studies that good results could be obtained for all ranges of flow conditions if the camera shutter speed was 1/15 second and the aperture was set at f:2.0. All photographs in this study were obtained using these camera settings. Film developing and printing was accomplished using the Aeronautics Department photographic facilities as well as those of the Photographic Department.

The model was mounted vertically in the test section (Figure 3.5) and the NIKON FE-2 camera mounted on a tripod positioned approximately 60cm from the test section side

wall. Typically, it was necessary to shut down the tunnel between tests in order to apply the correct oil film. Extra care was taken to ensure that this oil film was uniformly distributed over the aerofoil. Without delay the angle of attack was set and the tunnel speed was brought up from zero to its desired value. The oil started to move along the chord in streaks. Since the model was mounted vertically in the test section, gravitational effects gave a downward bias to the flow pattern. The flow pattern was allowed to develop until no further flow changes were observed. The surface flow patterns were then photographed.

Leading edge separation bubbles were clearly visible and noted as narrow vertical bands of trapped recirculating oil covering a small area of the model surface along the span (Figure 4.3.11). Long bubbles were characterised by a separation line followed by a region where the oil remained stationary. The location of the re-attachment point was identified as the line immediately behind the bubble, indicated by the beginning of a wider dark band representing fully attached flow (Figure 4.3.2). Following the dark band, and for angles of attack greater than  $11.90^\circ$ , an uneven line developed which represented the turbulent separation front.

The main advantage of this flow visualisation method is that the different flow fields formed on the surface of the aerofoil could easily be distinguished.

## CHAPTER IV

### PRESNTATION AND DISCUSSION OF RESULTS

This chapter presents a selection and detailed discussion of the most pertinent results obtained from both the chordwise static pressure distribution and flow visualisation measurements on a NACA-4415 aerofoil. From these measurements, the two-dimensional performance of the aerofoil with respect to angle of attack,  $\alpha$ , and chord Reynolds number,  $Re_C$ , was determined.

Due to the large amount of data collected during the present investigation, pseudo-three-dimensional representations were developed to illustrate the static pressure distributions over the aerofoil. They are plotted against the full range of angles of attack considered at constant Reynolds numbers and vice versa. Aerodynamic force and moment coefficients, used for studying the performance of an aerofoil, were obtained by integrating the chordwise pressure distribution using a simple trapezoidal rule method. These coefficients are presented as a function of angle of attack for each Reynolds number tested. No corrections, to the results throughout this study for the

effects of two-dimensional wake, solid blockage, and of streamline curvature (refer to Section 3.1), were applied to the data.

Further, a surface flow visualisation technique was used to assist understanding of the flow mechanisms which might have affected the behaviour of the boundary layer over the upper surface of the aerofoil.

The analysis of the results obtained from the pressure and flow visualisation measurements helped to clarify the two dimensional performance of this aerofoil in the Reynolds number range considered.

#### 4.1 PERFORMANCE AS A FUNCTION OF ANGLE OF ATTACK AND REYNOLDS NUMBER

##### 4.1.1 Introductory Comments

The chordwise static pressure distribution plots for the NACA-4415 aerofoil at a Reynolds number range of 50,000 to 600,000 and for angles of attack ranging from  $-5.10^\circ$  to  $22.90^\circ$  are illustrated in figures 4.1.1 to 4.1.15 and 4.2.1 to 4.2.20. The first set shows the pressure variations over the upper and lower surfaces at various incidences while the Reynolds number is kept constant. The second set is a presentation of the pressure differences that occur on the upper surface of the aerofoil for the Reynolds number range

examined, at constant angles of attack. Both sets of figures offer a good indication of the presence of laminar separation bubbles, as well as, the locations of turbulent boundary layer separations, on the upper or lower surface of the model. The locations of laminar separation and turbulent re-attachment points, however, could not be always ascertained from these figures. It was found that the performance of the aerofoil at these low Reynolds numbers was dictated by the positions of laminar separation, transition and turbulent re-attachment. Turbulent boundary layer separation, however, had an effect upon the generation of the aerodynamic forces and pitching moments. Due to the observed repeatability of the boundary layer phenomena over the test range, only the first three Reynolds number cases (i.e. 50,000, 75,000 and 100,000) are examined in detail.

For Reynolds numbers as low as 50,000 and 75,000, the static pressure distribution plots show that the pressure along the chord length fluctuates quite strongly for all angles of attack tested. These pressure fluctuations are possibly due to environmental disturbances in the wind tunnel. Previous studies (Refs 7,8) have shown that for low Reynolds number regimes, environmental disturbances have played a significant part in the behaviour of the boundary layer and, consequently, the performance of an aerofoil. Such fluctuations in pressure make the study of the boundary layer itself a very formidable task. The amount of

data collected from the present tests, however, allows a detailed discussion of the flow phenomena around the aerofoil to be carried out with some confidence.

Identification of the various boundary layer phenomena from the pressure distribution plots was carried out using the following criteria. Areas of relatively constant pressure indicated the position of laminar or turbulent flow separation. The location of flow transition and that of turbulent re-attachment were assessed from the classical interpretation of the pressure profiles exhibiting bubble characteristics. Arena et al (Ref.12) describes turbulence re-attachment as that point where the pressure, when it is fully recovered, is nearly equal to the value measured for a turbulent boundary layer over an aerofoil with no presence of a separation bubble (Figure 4.2.21).

#### 4.1.2 $Re_C = 50,000$

The pressure distributions over the upper and lower surface of the aerofoil for a Reynolds number of 50,000 are shown in Figures 4.1.1(a) and (b) respectively. Examining these figures it may be observed, that on the lower surface, a laminar separation bubble is formed close to the leading edge. At  $-5.10^\circ$ , the length of the bubble appears to be between 23% and 33% of the chord, which according to the length criteria, described in Section 1.2, the bubble

is considered to be "long". With increasing incidence, however, the separation bubble persists, increases in length slightly and moves aft towards the trailing edge. As indicated by the pressure distribution plots, the bubble seems to disappear at a higher incidence, but due to pressure fluctuations, it is very difficult to assess the incidence at which this occurs.

In contrast to the lower surface, the behaviour of the boundary layer over the upper surface (Fig.4.1.1(b)) appears to be more simple. Due to the pressure fluctuations little can be said about the behaviour of the boundary layer, except that the suction peak moves closer to the leading edge with increasing incidence and that stalling of the aerofoil is believed to occur at an incidence of  $6.90^\circ$ . The location of stall is taken from the pressure distribution plots which show that aft of  $x/c=0.15$  the pressure coefficient is nearly constant, indicating that leading edge flow separation has occurred. With increasing incidence the aerofoil remained stalled and laminar separation progresses forward from  $x/c=0.15$  at  $\alpha=6.90^\circ$  to approximately  $x/c=0.03$  at  $\alpha=22.90^\circ$ .

From the aerodynamic force and moment coefficient plots, shown in Figure 4.4.1, the normal force coefficient,  $C_N$ , appears to vary in a linear manner over the range from  $-5.10^\circ$  to  $0.90^\circ$  of angles of attack. Over the same range,

however, the quarter chord pitching moment coefficient,  $C_{Mc}/4$ , decreases in magnitude with increasing incidence. Zero normal force is obtained at an angle of attack of about  $-1.50^\circ$ . As the angle of attack is increased the  $C_N$  curve slope gradually decreases. From the incidence where stall occurs ( $6.90^\circ$ ),  $C_N$  rises very slowly. Due to fluctuations of the  $C_N$  curve between  $6.90^\circ$  and  $22.90^\circ$ , however, only an average value of  $dC_N/d\alpha=1.71$  has been estimated.

Between angles of attack of  $0.90^\circ$  and  $13.40^\circ$ ,  $C_{Mc}/4$  coefficient maintains an approximately constant value of  $-0.09$ . As incidence increases to  $22.90^\circ$  the magnitude of  $C_{Mc}/4$  decreases; exceeding  $-0.13$  at high angles of attack. Minimum tangential force coefficient of  $0.037$  occurs at  $\alpha=-0.10^\circ$ . From  $\alpha=4.90^\circ$  to  $22.90^\circ$ , however, it remains relatively constant, having an average value of  $0.015$  (Fig.4.4.1).

The aerofoil's performance at this Reynolds number can be characterised as very poor, especially for angles of attack greater than  $6.90^\circ$  where it approximates that of a flat plate.

#### 4.1.3 $Re_C = 75,000$

At this Reynolds number the performance is dominated by the formation of separation bubbles on both the upper and lower surfaces. Pressure fluctuations persist over the test range, but are much less than those observed at  $Re=50,000$ . Upper and lower surface static pressure distributions and aerodynamic coefficients are presented in Figures 4.1.2 and 4.4.2 respectively.

For  $\alpha=-5.10^\circ$ , a leading edge separation bubble is formed on the lower surface (Fig. 4.1.2(a)). It appears to be shorter than that observed for  $Re=50,000$  and occupies about 18% of the chord. Additionally, laminar separation occurs at  $x/c=0.08$  while transition and turbulent flow re-attachment are approximately at  $x/c=0.23$  and  $x/c=0.28$  respectively. Also, turbulent flow separation appears to be present at the  $x/c=0.88$ . For increased incidences, the bubble continued to exist but with slight increase in length until around  $\alpha=-0.10^\circ$  where it has disappeared.

The behaviour of the flow over the upper surface (Fig.4.1.2(b)) is dominated by the formation of a persistent separation bubble over almost the whole range of angles of attack tested up to the stall. For small angles of attack as low as  $-5.10^\circ$ , laminar separation is at about  $x/c=0.56$  with transition possibly occurring close to the

trailing edge. At increased incidence, the laminar separation point moves forward and the flow does not re-attach until  $\alpha=-2.10^\circ$ . There is then an abrupt re-attachment close to the trailing edge forming an upper surface long separation bubble. This bubble occupies approximately 50% of the chord with laminar separation occurring at about  $x/c=0.50$  and transition at  $x/c=0.84$ . With further increases in incidence, the separation bubble migrates forward and shortens to 40% at  $\alpha=3.90^\circ$  and 35% at  $\alpha=9.90^\circ$ . Just before stall, however, its overall length is around 13% chord. Turbulent flow separation first appears around the  $12.40^\circ$  incidence and moves upstream towards the leading edge with increasing angle of attack. At  $\alpha=16.40^\circ$  turbulent flow separation has moved to  $x/c=0.62$  causing a 38% chord trailing edge separation. Leading edge separation, caused by the "burst" of the bubble occurred at  $\alpha=16.90^\circ$ . The bubble's progression, discussed above, is illustrated in figure 4.1.19 where the location of laminar separation, transition, turbulent re-attachment and turbulent separation are shown.

The formation of the upper and lower surface bubbles as well as their disappearance played a significantly important part into the performance of the aerofoil. Prior to the upper surface bubble formation, the  $dC_N/d\alpha$  curve

slope increased gradually to a large value of approximately 9.50 (Fig.4.4.2). When the bubble formed, at  $\alpha=-2.10^\circ$  (Fig.4.1.2(b)), the magnitude of the slope reduced to 6.7 (a decrease of nearly 30%) and remained so until there was no lower surface bubble at  $\alpha=-0.10^\circ$ . The disappearance of the lower surface bubble probably caused the  $dC_N/d\alpha$  value to decrease even further by nearly 13% to an approximate value of 5.85. Over the same variation of incidence, the quarter chord pitching moment coefficient decreased in magnitude reaching a minimum of -0.106 at  $\alpha=0.90^\circ$ . In the range  $-1.10^\circ < \alpha < 4.90^\circ$ , however,  $dC_{Mc}/d\alpha$  fluctuates between -0.105 and -0.097. The tangential force coefficient, however, is different and increases in magnitude to a maximum of 0.03 at  $\alpha=-3.10^\circ$  and then decreases gradually with increasing incidence. From  $\alpha=4.90^\circ$  the magnitude of the  $dC_N/d\alpha$  slope decreases reaching a minimum at  $12.40^\circ$ , at which  $C_N$  attains its maximum value of approximately 1.41.

Over the same incidence range ( $8.90^\circ$  to  $16.40^\circ$ ) the quarter chord pitching moment coefficient increases in a somehow unsteady manner with a sharp rise of about 22% between  $11.90^\circ$  and  $12.90^\circ$ . This increase is thought to have occurred due to the initiation of trailing edge flow

separation. Similarly,  $C_T$  continues to decrease further with increasing incidence, reaching a minimum value of -0.274 at  $\alpha=15.90^\circ$ .

Leading edge flow separation (see figure 4.1.2(b)) causes the aerofoil to stall at an angle of attack of  $\alpha=16.90^\circ$ . This is manifested by a large decrease in both the normal force and pitching moment coefficients, together with a sharp rise in the tangential force coefficient (Fig. 4.4.2). At this incidence,  $C_N$  and  $C_{M_C}/4$  have dropped to 0.84 and -0.114, while  $C_T$  reached a value of 0.013.

At this chord Reynolds number, the performance of the aerofoil has improved considerably compared to the 50,000 case.

#### 4.1.4 $Re_C = 100,000$

Figure 4.1.3 illustrates the static pressure distributions around the aerofoil at various angles of attack. For this Reynolds number and the remaining cases the pressure fluctuations which dominated the first two Reynolds numbers cases, are greatly reduced and the identification of boundary layer phenomena was made easier. From the pressure distributions it may be observed that separation bubbles are formed on both the upper and lower

surfaces. From an incidence of  $-5.10^\circ$  to  $-0.10^\circ$ , the aerofoil has a lower surface separation bubble close to the leading edge. This then extends downstream with increasing incidence (Fig. 4.1.3(a)). At  $\alpha=-0.10^\circ$  the bubble has moved to mid-chord occupying approximately 30% of the chord length and laminar separation has moved to  $x/c=0.48$ , with transition and turbulent re-attachment at about  $x/c=0.68$  and  $x/c=0.78$  respectively. For  $\alpha=0.90^\circ$ , however, the corresponding pressure distribution shows that the bubble has disappeared and this had a significant effect on the aerofoil's performance which exhibited a noticeable "kink" in the normal force and pitching moment curves. Detail discussion of the "kink" is given in Section 4.4.

The behaviour of the upper surface boundary layer is again influenced by the existence of a separation bubble Fig.4.1.3(b). Static pressure distribution plots, however, show that at  $\alpha=-5.10^\circ$  laminar separation and transition of the flow appear to occur at approximately  $x/c=0.62$  and  $0.92$  respectively, with no indication of turbulent re-attachment. As the incidence is increased, the flow tends to re-attach and at an angle of  $-3.10^\circ$  is located at  $x/c=0.94$ . This forms a long separation bubble covering about 40% of the chord. At this incidence, laminar separation and transition have moved to their new positions of  $x/c=0.56$  and  $0.86$  respectively. The bubble then exhibits similar trends, with increasing incidence, to that of the

$Re=75,000$  case.

It is observed that it forms at a lower incidence and monotonically migrates towards the leading edge, whilst decreasing in length as incidence is increased. Trailing edge separation also takes place at  $\alpha=12.90^\circ$  and moves rapidly upstream with increasing incidence. However, just prior to stall ( $\alpha=16.40^\circ$ ), the bubble develops close to the leading edge covering 10% of the chord, while the trailing edge separation point has progressed to  $x/c=0.56$ . The migration of the bubble along the chord together with that of the trailing edge separation location is illustrated in figure 4.1.20.

By examining the aerodynamic coefficients (Fig. 4.4.3), it is noticeable that the  $dC_N/d\alpha$  value changed in magnitude at four different incidences before stall was eventually reached. In the first stage, from  $-5.10^\circ$  to  $-2.10^\circ$ , its value was found to be about 7.3. At  $\alpha=-2.10^\circ$  the flow on the upper surface re-attached forming a long bubble. It could be argued that the change of flow behaviour on that surface caused the reduction of the curve slope to a magnitude of 5.9, a decrease of nearly 20%. The curve slope remained constant in magnitude until the leading edge bubble on the lower surface disappeared at  $-0.10^\circ$ .

The re-attachment of the flow also produced distinct effects on  $dC_{Mc}/4/d\alpha$  curve slope. Prior to flow re-attachment ( $-2.10^\circ$ ) the  $C_{Mc}/4$  curve has a negative slope, whilst for greater incidence values the slope became positive. It remained positive until  $C_{Mc}/4$  reached a maximum value of  $-0.030$  at  $14.40^\circ$  except, when the lower surface bubble disappeared, a slight "kink" is obvious on both the  $C_N$  and  $C_{Mc}/4$  curves. This "kink" is more distinct in greater Reynolds numbers (Figs 4.4.4 to 4.4.15) and is discussed in Section 4.4.

For angles of attack between  $0.90^\circ$  and  $3.90^\circ$ ,  $dC_N/d\alpha$  (Fig.4.4.3) obtained a value of 5.44. The flow in this incidence range is probably fully attached, apart, of course, for the bubble formation. A further incidence increase to  $7.90^\circ$  increased the rate of movement of transition and re-attachment points over their predecessors (Fig.4.1.3(b)). This caused the boundary layer to become turbulent prematurely, which probably affected the  $C_N$  curve slope by reducing it to 4.6. Further increases in incidence lead to additional losses in  $dC_N/d\alpha$ . A maximum normal force coefficient of 1.375 was achieved at an angle of attack of  $12.40^\circ$ . For greater incidences the  $C_N$  was reduced as the trailing edge separation increased until when leading edge

separation (bubble burst) occurred at  $16.65^\circ$ ,  $C_N$  and  $C_{Mc}/4$  dropped from 1.294 to 0.829 and -0.034 to -0.110 respectively, while  $C_T$  increased from -0.260 to 0.005.

#### 4.1.5 $Re_C \geq 125,000$

Static pressure distributions over the aerofoil for Reynolds numbers between 125,000 and 600,000 are shown in Figures 4.1.4 to 4.1.15. Examining these figures, it may be observed that the trends are similar to those discussed in the last two Reynolds number cases. An attempt to discuss each figure individually would have provided no extra information about the behaviour of the boundary layer, than has already been discussed. Therefore, only a brief discussion of the most obvious changes in pressure will be described here. As far as the aerodynamic parameters are concerned they appear to undergo some noticeable changes, particularly in moderate angles of attack (less than  $4^\circ$ ) and beyond  $C_{Nmax}$ . A discussion of their behaviour will be presented in Section 4.4.

Although the most unusual discontinuities in pressure distribution occurred on the upper surface of the aerofoil, some slight changes were also observed on the lower surface. There the pressure distributions (Figs 4.1.4(a) to 4.1.15(a)) indicate that, at incidences below zero degrees, a separation bubble forms close to the

leading edge. With increasing Reynolds number, however, it shortens by approximately 8-12% per 50,000 of Reynolds number. When the angle of attack is gradually increased the bubble travels rapidly downstream until it disappears at a small incidence. The disappearance of this bubble is observed to take place at an incidence not higher than  $1.90^\circ$  for the lower Reynolds number range (i.e.,  $125,000 \leq Re_C \leq 200,000$ ) and not later than  $0.90^\circ$  for the higher regimes. Further increases in angle of attack, did not feature any unusual discontinuities in  $C_p$  until the incidence at which stall occurred. It is understood, that when this happened, the suction peak on the upper surface collapsed and the centre of pressure shifted aft towards the trailing edge. This is clearly noticeable by the sudden forward movement of the stagnation point towards the leading edge.

As was described above, a laminar separation bubble was also formed on the upper surface (Figs 4.1.4(b) to 4.1.15(b)). It was observed that its formation was near the trailing edge and, as the angle of attack increased, it migrated upstream. When formed, it is described as a "long" bubble, according to bubble length criteria. With increasing incidence, however, it travels upstream and becomes a "short" bubble covering only a small percentage of the chord. This is clearly illustrated in figure 4.1.10(b) where, for example, at a Reynolds number of 350,000 the bubble is about 25% of the chord at an

incidence of  $-5.10^\circ$  and is reduced to approximately 4% at  $17.90^\circ$ . Apart from these changes in location and size of the laminar separation bubble, turbulent flow separation also takes place near the trailing edge at a certain angle of attack; depending on the Reynolds number.

This separation moves towards the leading edge with increasing incidence at a faster rate than that of the laminar separation, transition and re-attachment points. It is apparent, that when the separation bubble establishes itself within the first 15% of the chord, its rate of displacement slows substantially from about 10% to less than 4% of the chord per degree of increasing incidence, depending on the Reynolds number (Figs 4.1.4(b) to 4.1.15(b)). From these figures it is also noticed that the higher the Reynolds number, the earlier trailing edge separation occurs.

In the present investigation, it became apparent that the boundary layer around the aerofoil proved to be very sensitive at these low Reynolds number regimes and particularly for incidences close to stall. Occasionally, during a single static pressure measurement test, the aerofoil experienced two different flow conditions, i.e. a fully attached and a fully separated. The occurrence of these flow phenomena is clearly shown in figure 4.1.16(b). This Figure illustrates that at a Reynolds number of approximately 300,000 and at an angle of attack of  $18.90^\circ$ ,

(8-20)

a short bubble is situated close to the leading edge on the upper surface of the aerofoil. Laminar separation and transition occur at the locations of  $x/c=0.035$  and  $0.055$  respectively, while re-attachment, indicated by the end of the sharp pressure recovery region, occurs at approximately  $x/c=0.075$ . As the pressure continues to increase, past the re-attachment point, turbulent flow separation takes place at about  $x/c=0.44$ . After this the pressure coefficient experiences a sudden decrease in value at approximately  $x/c=0.56$  and remains relatively constant for the rest of the chord length.

In contrast with the upper surface, the lower surface pressure distribution shows that as the pressure decreases aft of the stagnation point at  $x/c=0.025$ , it experiences again a sudden increase. This occurs around  $x/c=0.06$  and the pressure decreases steadily from that point to the trailing edge.

Since the pressure distribution around the aerofoil was displayed on the computer's visual display terminal (VT105), immediately after the completion of each test run, it was possible to check those pressure abnormalities that had occurred during the experiment before any data analysis was made. By retesting the NACA-4415 aerofoil for the same incidence ( $18.90^\circ$ ) and Reynolds number (300,000), it was observed that the aerofoil was fully stalled (Fig. 4.1.16(c)).

Comparing the data of figure 4.1.16(b) with that of the stalled case (Fig.4.1.16(c)), it may be noticed that the upper surface pressure coefficient values from 0.62 x/c to the trailing edge, together with those from the leading edge to 0.05 x/c on the lower surface, are almost identical. Bearing in mind that the order in which the static pressure measurements were made (refer to Section 3.1), the most obvious explanation is that the aerofoil was originally stalled and a flow perturbation triggered the boundary layer to re-attach. A short time later, the flow re-separated and subsequently re-attached. From these figures it is clear that the boundary layer is so sensitive that it is possible to change its state from fully separated to fully attached and vice-versa (Figs 4.1.17 and 4.1.18). Such boundary layer behaviour was only observed at incidences close to stall and can be attributed to the wind tunnel's environmental disturbances, such as mechanical vibrations, noise and high turbulence intensity level.

Similar observations were also made by Kokkodis (Ref.18) for a NASA GA(W)-1 and a NACA-0015 aerofoil sections tested under the same conditions, emphasising the extreme sensitivity of the boundary layer in these low Reynolds numbers ( $0.5 \times 10^5 \leq Re_C \leq 6.0 \times 10^5$ ) regardless of the aerofoil section.

## 4.2 PRESSURE COEFFICIENT VARIATION WITH REYNOLDS NUMBERS AT CONSTANT ANGLES OF ATTACK

The pressure distribution over the upper surface of the NACA-4415 aerofoil for constant incidences and a variation of Reynolds numbers is illustrated in figures 4.2.1 to 4.2.20. From these figures it may be observed that the laminar separation point over the upper surface appears to occur further aft as the angle of attack and Reynolds numbers increase up to  $-0.10^\circ$  and 200,000 respectively (Figs 4.2.1 to 4.2.4). For the same range of angles of attack and for higher Reynolds numbers, its location moves upstream, in the way that a conventional laminar separation point should have behaved.

Further increases in incidence up to  $9.90^\circ$  (Figs 4.2.5 to 4.2.9) showed that its position was approximately within 5% of the chord for all Reynolds numbers considered. Meanwhile, since transition of the flow occurs earlier with increasing Reynolds number, turbulent flow re-attachment also occurs earlier, resulting in a reduced bubble length. For example at an incidence of  $-0.10^\circ$  (Fig.4.2.4), the bubble occupies approximately 30% of the chord at a Reynolds number of 125,000. In contrast to this and at a Reynolds number of 600,000, the bubble covers less than 15% of the chord. Similar reductions, of more than half of its original size, were also noticed for the remaining cases considered. The transition and re-attachment locations,

which, as described above, occur earlier with increasing Reynolds number, have similar locations for incidences between  $0.90^\circ$  and  $10.90^\circ$  and Reynolds numbers higher than 450,000 (Figs 4.2.5 to 4.2.10). This clearly indicates that, for these incidences and Reynolds number regimes, the gross behaviour of the boundary layer is similar. It is also in this test range that incipient trailing edge separation occurs (Fig.4.2.9).

For angles of attack of  $11.90^\circ$  and  $12.90^\circ$  (Figs 4.2.11 and 4.2.12), however, there is anomalous pressure data, in that the bubble is difficult to distinguish and, indeed, could be reasonably argued, not to exist. Test cases on either side of these data and the evidence of flow visualisation clearly indicate bubble existence (Figs 4.2.10 and 4.2.13, 4.3.7 and 4.3.9).

For higher angles of attack ( $\alpha > 13.9^\circ$ ), the separation bubble continues to decrease in length and moves closer to the leading edge until full stall occurs. At which the bubble "bursts" resulting in a mixed type of stall since significant trailing edge separation develops from lower incidences. Stall of the aerofoil starts initially from the lower Reynolds number regimes (Fig.4.2.16) and progresses towards the higher ones until the aerofoil is fully stalled for all the Reynolds numbers test range (Fig.4.2.20).

Bastedo (Ref.33) also found, during his experimental

investigation of a Wortmann FX-63-137 aerofoil, similar difficulties of locating the upper surface separation bubble from pressure data within a particular incidence range. Using a direct injection smoke-flow-visualisation technique illuminated by a laser sheet, however, he was able to observe that the bubble not only existed but was also very thin (less than 1mm in thickness) as it moved forward with increasing incidence. He explains, that as the bubble becomes thinner it allows transmission of the free stream pressure, of the external potential flow field, to the aerofoil surface. Therefore, the pressure plateau normally characteristic of a separation bubble is masked by this effect. Such an explanation might also be accepted for the pressure peculiarities observed in the present investigation mentioned above.

#### 4.3 FLOW VISUALISATION OVER THE UPPER SURFACE OF THE NACA-4415 AEROFOIL

The particular method used to visualise the upper surface flow fields, was the oil flow method. This technique has been described in detail previously in Section 2.5. It has limited applicability, however, (refer to Section 3.3), and no attempt to use it below a Reynolds number of 150,000 was made. Therefore, tests were only carried out at Reynolds numbers between 150,000 and 600,000, for discrete angles of attack. During these tests, a large number of photographs were collected, from which

only a representative few are presented here (Figs 4.3.1 to 4.3.14). Full presentation of these pictures is given in Reference 25. From these photographs, the main features of the boundary layer, such as laminar or turbulent flow separation and flow re-attachment, are easily obtained.

It should be noted that for these flow visualisation tests, the tunnel speed was increased from zero to its desired value after setting the angle of attack. Therefore, the flow pattern does not necessarily represent the situation which might be obtained when stall is approached at constant Reynolds number, by increasing the angle of attack, as it was done for the pressure measurement tests.

Figure 4.3.1 shows the flow developments that occur over the upper surface of the aerofoil at various Reynolds numbers but with a fixed incidence of  $-5.10^\circ$ . Here the flow may be termed nominally two-dimensional, except near the upper model/tunnel interface. There minor three-dimensionality is observed to occur at almost all the Reynolds numbers considered. The laminar separation bubble can easily be distinguished, forming just prior to the mid-chord position and re-attaching near the trailing edge. Its position across the span is more clearly seen at the Reynolds numbers of 300,000 and 600,000, with laminar separation occurring at a much later location compared to the other Reynolds numbers cases (Figs 4.3.1(b) and (e)).

At the lower half of the model for the 600,000 case, as well as, the mid-span position for the 500,000 Reynolds number (Fig.4.3.1(d)), turbulent oil streaks are observed. These cut through the separation bubbles and are mainly caused by lumps of "Dayglo" powder pigments located just ahead of the bubble which induce transition. Uniform trailing edge separation is also noticed to have taken place at approximately  $x/c=0.98$  for a Reynolds number of 300,000 (Fig.4.3.1(b)). As the Reynolds number increases the length of the bubble is reduced. Such reductions are caused by the occurrence of earlier re-attachment.

As the angle of attack is increased to  $-1.10^\circ$  (Fig.4.3.2), the bubble appears to be positioned close to the mid-chord for all the Reynolds numbers tested. Comparing the separation bubbles in this figure with those obtained in the previous angle of attack case, it may be noticed that they not only become shorter with increasing Reynolds numbers, but also move upstream with increasing incidence. The length of the bubble reduces by almost 30% between 250,000 and 600,000 Reynolds numbers. Trailing edge separation is also observed to have occurred at about  $x/c=0.94$  at the Reynolds numbers of 250,000 and 350,000 (Fig.4.3.2(a) and (b)).

Further increases in incidence up to  $9.90^\circ$  (Figs 4.3.3 to 4.3.5), indicate that although the nature of the flow over the model remains two-dimensional, there is

little flow separation at the upper model/tunnel wall junction. The centre of the bubble is located at approximately 20-30% of the chord, depending on Reynolds number. Trailing edge separation is present at all Reynolds numbers tested, and increases with increasing angle of attack.

At an incidence of  $6.90^\circ$  and a Reynolds number of 500,000 (Fig.4.3.4(d)), the bubble in the lower part of the model is broken due to the presence of a powder particle, located at  $x/c=0.03$ , which trip the boundary layer from laminar to turbulent. It is also noticed that as the Reynolds number becomes higher than 400,000 and 300,000 for angles of attack of  $6.90^\circ$  and  $9.90^\circ$  respectively, oil starts to escape from the bubble into the turbulent region of the flow. This is probably caused by the thinning of the separation bubble, as described in the previous section. It is assumed that as the bubble gets thinner with increasing incidence, the thickness of the oil, which is trapped inside the bubble, becomes thicker than the bubble itself and therefore, the shear stresses just above the bubble drive the oil into the turbulent flow region. This phenomenon can be seen quite clearly in Figure 4.3.6 where a sequence of photographs was taken at intervals of approximately fifteen seconds.

The flow behaviour over the aerofoil at an incidence of  $11.90^\circ$  and for various Reynolds numbers, is shown in

Figure 4.3.7. At this incidence, the laminar separation bubble is close to the leading edge and its length is reduced considerably by about 50% when compared to the corresponding value at  $9.90^\circ$ . Turbulent flow separation is now in the mid-span region around 70-80% of the chord. The separation line, however, indicates three-dimensional flow behaviour. Finally, as in the previous case, oil accumulation in the laminar separation bubble is significant and some escapes into the general flow (Fig.4.3.8).

At angles of attack of  $13.90^\circ$  and  $15.90^\circ$  (see figures 4.3.9 and 4.3.10), the separation bubble is clearly in the leading edge region and covers only 4-5% of the chord. Trailing edge separation is greater than 50% of the chord and strong vortical flows are evident of the wall/model interfaces. It may also be observed that, between 400,000 and 500,000 Reynolds numbers, flow behaviour differs between  $13.90^\circ$  and  $15.90^\circ$  incidence. This difference is that, at  $13.90^\circ$  incidence, obvious three-dimensional flow exists over the lower half of the model. At  $15.90^\circ$ , however, the flow is closer to its original nominally two-dimensional status, and the two vortices end appear to be of similar extent.

For angles of attack  $17.90^\circ$  and  $18.90^\circ$  (Figs 4.3.11 and 4.3.12), the flow pattern is similar to that observed at  $15.90^\circ$ , but the separation bubble is almost at the

leading edge, and the flow reversals covers almost 70% of the chord. Nominal two-dimensionality persists; even at lower Reynolds numbers than before (Fig.4.3.11(b)).

The flow development for an incidence of  $19.90^\circ$  is shown in Figure 4.3.13. For Reynolds numbers up to 400,000 (Figs 4.3.13(a), (b) and (c)) the aerofoil is stalled and the flow separates from the 1% chord location. At higher Reynolds numbers, however, the flow remains attached for 25% of the chord with the separation bubble still present. Assymetry of the junction vortices is noticeable; the lower vortex forming away from the model/tunnel wall junction.

For a Reynolds number of 400,000 (Fig.4.3.14), the flow, although separated from the aerofoil's surface (Figs 4.3.14(a) and (b)), suddenly changed its status from fully separated to fully attached (Figs 4.3.14(c) and (d)). A similar behaviour was also observed during the pressure measurements. This again illustrates the sensitivity of the boundary layer at incidences near full stall.

Surface oil flow visualisation technique provided an interesting correlation with the pressure measurements. That is, it confirmed, for Reynolds numbers higher than 200,000 the indications given by the pressure distributions for the existence and behaviour of the laminar separation bubbles. It may be noticed, however, that laminar separation, as well as, turbulent re-attachment and

trailing edge separation, occur earlier with the oil flow measurements than those deduced from the pressure profiles (Figs. 4.3.15 to 22).

The origins of this mismatch are at present unknown and it is anticipated that in order to resolve the conflicting data, especially at low Reynolds numbers, further detailed investigations will be requested.

Such an investigation should include a more sophisticated analysis of the pressure coefficient data and a less intrusive method of flow visualisation (perhaps liquid crystals). Oil flow visualisation is normally highly informative but at the very low Reynolds numbers considered, where the boundary layer is very sensitive, the accumulated oil droplets may have had a severe effect. With this in mind, the results presented here for Reynolds numbers less than 600,000 must therefore be viewed with reservations until the matter is resolved.

#### 4.4 $C_N$ , $C_{Mc}/4$ AND $C_T$ WITH VARIATION OF ANGLES OF ATTACK

The normal force, tangential force and quarter chord pitching moment coefficients plotted against angle of attack, are shown in Figures 4.4.1 to 4.4.15. In general, the trend of the curves is that  $C_N$  and  $C_{Mc}/4$  increase with

increasing incidence, while  $C_T$  decreases. This behaviour continues until the magnitude of the curve slopes reaches a minimum. For angles of attack prior to the obvious "kink" at low incidences, however, the  $dC_N/d\alpha$  curve slope is at its greatest. As the maximum value of  $C_N$  is approached, the slope decreases gradually until maximum  $C_N$  is achieved. This decrease in slope was caused by both the thickening of the boundary layer and, primarily, the occurrence of trailing edge separation (see figures 4.2.1 to 4.2.20). Increases in incidence above  $C_{N\max}$  lead to substantial decreases in  $C_N$ . As above, this may be attributed to the large regions of trailing edge separation on the upper surface of the aerofoil. Continued increases of incidence result in sudden loss of  $C_N$  due to the laminar separation bubble bursting. Therefore, due to the occurrence of trailing edge separation and the bursting of the leading edge bubble, the stall behaviour of the NACA-4415 aerofoil shows that it is of the combined category; discussed in Section 1.2.

At Reynolds numbers greater than 200,000 and incidence values greater than  $\alpha_{C_{N\max}}$  (Figs 4.4.5-4.4.13), the  $C_N$  curve levels off as the effects of turbulent separation become manifest. Also, from the force and moment curves, it may be noticed that the zero normal force

incidence shifts towards the design value of  $-4^\circ$  with increased Reynolds number; this shift is clearly noticeable between 50,000 and 125,000 Reynolds numbers (Figs 4.4.1 to 4.4.5). The stalling angle may also be observed to increase (Table 3).

Similar behaviour of the curve slopes is observed at higher Reynolds numbers, except between 400,000 and 500,000. In this Reynolds number range, normal force coefficients exhibit an increase just before leading edge flow separation occurs. This increase in  $C_N$  may be attributed to various flow phenomena such as flow reversal, three-dimensionality of the flow, or to blockage effects which may be quite significant at such high angles of attack. The three-dimensionality of the flow alters the pressure distribution along the span, and is normally initiated at the corners between the model and the tunnel walls. These flow phenomena become most evident at high incidence, as shown in figures 4.3.7 to 4.3.13.

Throughout all the figures of  $C_N$  and  $C_{MC}/4$  discussed above, there is an obvious "kink", mentioned earlier. Close examination of figures 4.4.1 to 4.4.15, may reveal that the "kink" occurs at angles of attack between  $-0.10^\circ$  and  $3.90^\circ$ , depending on Reynolds numbers. Examination of the relative pressure distributions (Figs 4.1.1 to 4.1.15) did not indicate any obvious cause of the effect. Previous investigations, on aerofoil sections at low Reynolds

numbers, have also shown the existence of "kinks" similar to those observed here (Refs 26, 36, 37 and 38). Some of the results obtained from these investigations are presented in figures 4.4.16, 17, 18 and 19.

In the present investigation, it was originally assumed that the "kink" was initiated by the disappearance of the lower surface separation bubble. However, from a later analysis of the pressure distribution plots, it was apparent that this was not the case. The reason for this is, that, for flow conditions at which the separation bubble on the lower surface should have disappeared were not coincident with that of the "kink". Flow visualisation of the lower surface may have provided information about the behaviour of the leading edge bubble to support the above argument.

Further investigation was therefore carried out using the two-dimensional viscid-inviscid aerofoil analysis method of Coton and Galbraith (Refs 27 and 39). The outcome of this work revealed that, for Reynolds numbers greater than 100,000, the lower surface boundary layer experienced laminar flow separation well after the incidence at which the lower surface bubble should have collapsed. This separation moved slowly towards the trailing edge with increasing incidence. However, when a certain angle of attack was reached, the separation point suddenly advanced to the trailing edge. This implied that the lower surface

boundary layer, prior to that incidence, was experiencing a significant region of turbulent flow, whereas, above this angle of attack, the boundary layer was laminar and fully attached. A comparison between this angle of attack and the one at which the "kink" was observed to occur, showed good agreement (Fig.4.4.20 and Table 4).

Similar flow phenomena over the lower surface of a Wortman FX-63-147 aerofoil were also observed by Bastedo (Ref.33). He claims, however, that the non-linearity of the  $C_L$  and  $C_D$  curve slopes (Fig. 4.4.21) at moderate incidences was caused by the formation of a separation bubble on the upper surface. Similar statement was also given by Poll et al (Ref.37) who states, that the occurrence of the "kink" on the aerodynamic curves is not only dependent on the Reynolds number but also to the establishment of the short separation bubble on the upper surface.

#### 4.5 $C_{Nmax}$ VARIATION WITH REYNOLDS NUMBERS

This investigation showed a variation in the magnitude of  $C_{Nmax}$  at three different ranges, over the considered Reynolds number range ( $1.0 \times 10^5 \leq Re_C \leq 6.0 \times 10^5$ ), see figure 4.5.1. This variation of  $C_{Nmax}$  is different from that of the existing data for the same aerofoil tested at higher or similar Reynolds number ranges (Refs 29 and 34). From these data, it may be noticed that  $C_{Nmax}$  rises with increasing

Reynolds numbers (Figs 4.5.2 and 4.5.3). Further comparison with data from Reference 28, however, indicates similarities between results (Fig.4.5.4).

Between 100,000 and 200,000 Reynolds numbers,  $C_{N\max}$  occurs at  $12.40^\circ$  for the lower Reynolds number regime, but at  $12.90^\circ$  for the higher; as shown in Table 4. The value of  $C_{N\max}$  remains relatively constant at 1.38, with a small increase to 1.39 at 200,000 Reynolds number.

In the Reynolds number range  $2.5 \times 10^5 \leq Re_C \leq 6.0 \times 10^5$  (Figure 4.5.1), it may be observed that  $C_{N\max}$  reduces steadily from 1.39 to 1.32, with its sharpest reduction occurring between 400,000 and 450,000. After 450,000, however,  $C_{N\max}$  stabilises at a value of 1.32 whilst the  $C_{N\max}$  incidence reduces to  $11.90^\circ$ , where it remained (Table 3). This downward shift is a consequence of an early initiation of trailing edge separation but subsequent slower penetration towards the leading edge and the bursting of the laminar separation bubble (i.e., abrupt stall) was delayed until several degrees after  $C_{N\max}$  had occurred (Figures 4.5.5(a) and (b)).

From a Reynolds number of 150,000 onwards and with increased incidence, the movement of the turbulent separation point appears to reduce its contribution to the

normal force of the upper surface, while the same increase in incidence expands the lower surface normal force contribution. The balancing of these two effects produced a "flat" region on the  $C_N$  curve slope prior to complete stall. Data from References 29 and 26 relating to the NACA-4415 and Wortmann FX-63-137 aerofoil sections respectively, shows the same tendency (Figs 4.5.2 and 4.5.6).

#### 4.6 COMPARISON OF NACA-4415 AEROFOIL SECTION CHARACTERISTICS WITH EXISTING DATA

Two-dimensional data for the NACA-4415 aerofoil section have been obtained in the past through experimental investigations performed in the United States (1937-47) and West Germany (1962-72), (Refs 28, and 29). The wind tunnels used for these tests were the NACA LTT (Low Turbulence Tunnel) and the IAG Stuttgart wind tunnel. Two-dimensional tests were performed using smooth NACA-4415 aerofoil models at Reynolds numbers ranging from  $0.7 \times 10^6$  to  $3.0 \times 10^6$  (Figs 4.5.2 and 4.5.3) These results were corrected of blockage and streamline curvature effects.

For the comparative analysis between the present and existing data, extra information was essential about the type and size of the cross-sectional area of the working section of the above wind tunnels; the turbulence intensity together with the model sizes. This information became

available from References 28, 29, 30 and 31 and is presented in Table 5.

Since the Reynolds number range at which the NACA LTT and the Stuttgart wind tunnels were operating was between  $0.7 \times 10^6$  and  $3.0 \times 10^6$ , higher than that of the present investigation ( $0.5 \times 10^4 \leq Re_C \leq 0.6 \times 10^5$ ), a direct comparison of these results was not possible. Therefore, a brief correlation of the aerodynamic characteristics of these data was made here, as discussed below.

Variations of normal force and pitching moment coefficients obtained in this study at a Reynolds number of 600,000, are plotted in figure 4.6(a) against the corresponding coefficients from the other investigations at a Reynolds number of 700,000 (Refs 28, and 29). It is clear from the figure, that all the data are in reasonable agreement up to an incidence of  $11^\circ$ . For angles of attack greater than this, however, the curves diverge and, in particular, when maximum lifts are attained at  $12^\circ$ ,  $14^\circ$  and  $16^\circ$  they are well separated from each other. The maximum values of lift coefficients at these incidences were 1.27, 1.28 and 1.38.

From the pitching moment coefficient data (Fig. 4.6(b)) it may be observed that the trends of the curves are quite similar. Comparing the present data with the Stuttgart data, the present data exhibit considerably

higher pitching moments for the entire incidence range. This difference varies from approximately 0.010 to 0.027 with increasing incidence. In comparison with the NACA LTT data, however, it may be noticed that the values agree reasonably well between  $-2^\circ$  and  $6^\circ$  of angles of attack. For greater incidences the present data is substantially higher, especially near the stall.

These variations, observed in the lift and pitching moment curves, are possibly due to the differences in turbulence intensity levels as well as the effects of noise and mechanical vibrations, which in this study are believed to have been quite considerable. Also, bearing in mind that the considerable differences between wind tunnels and model sizes, shown in Table 4, the above variations in the curves were expected. It was very difficult to predict, however, exactly how these differences would influence the results.

#### 4.7 COMPARISON OF NACA-4415 AEROFOIL SECTION

##### CHARACTERISTICS WITH GU25-5(11)8, NASA-GA(W)-1 AND NACA-0015 SECTIONS

In order to obtain a better overall picture of how the NACA-4415 aerofoil performs with increasing Reynolds numbers ( $Re$ ) and increasing incidence ( $\alpha$ ),  $C_N$  contours were plotted, against the above parameters and are illustrated

in Figure 4.7.1. The main advantage of the development of  $C_L$  or  $C_N$  contours against a base of incidence and Reynolds number, is that it shows clearly the overall behaviour of an aerofoil at various untested Reynolds numbers. Regions in which the contour lines lie very close to one another, at a small range of Reynolds numbers, are regarded as "critical", since the slightest increase or decrease in Reynolds number or incidence will result in considerable changes in lift or normal force coefficients.

From Figure 4.7.1, it is evident that the performance of the aerofoil improves considerably between 50,000 and 75,000 Reynolds numbers. At the lower value, the aerofoil appears to be in the subcritical range in which it suffers badly from laminar separation without subsequent re-attachment. This is demonstrated by the corresponding pressure distribution behaviour given in Figure 4.1.1, and by the normal force curve which approximates that of a flat plate (Fig. 4.4.1). At the higher Reynolds number, however, it is indicated that the aerofoil operates above the critical Reynolds number, since its performance is considerably improved (Fig. 4.4.2).

Figure 4.7.1 also shows that for further increases in Reynolds numbers up to 450,000, the  $C_N$  varies very little for angles of attack less than  $10^\circ$ , and is almost constant for greater incidences and Reynolds numbers. The maximum normal force coefficient decreases with increasing Reynolds

number by approximately 5% between 75,000 and 600,000. It may also be observed from the  $C_N$  contours that, decreasing the Reynolds numbers results in reduction of the zero normal force coefficient angle of attack, from its designed value of  $-4^\circ$  to  $-1.5^\circ$ . This is mainly due to the thickening of the boundary layer which reduces the effective camber of the aerofoil at lower speeds.

It could be said, that the overall performance of this aerofoil is satisfactory, especially for angles of attack less than  $10^\circ$  and for Reynolds numbers greater than 75,000, indicating that the aerofoil could be safely operated between these Reynolds number and incidence ranges.

The comparison of the NACA-4415 with the GU25-5(11)8 (Ref.17) and GA(W)-1, NACA-0015 sections (Ref.18) is presented in figures 4.7.2, 3 and 4. For this purpose, the present model was constructed in such a way as to match the dimensions of the other three aerofoil sections (i.e. thickness/chord ratio and aspect ratio). The main assumption of carrying out the above comparison was that if two or more aerofoil sections having similar dimensions, being tested under the same wind tunnel environmental conditions (i.e. turbulence intensity, noise and mechanical vibrations levels) and using the same wind tunnel facilities, the results of those tests could be directly comparable.

It may be noticed, from the above figures, that the performance of the GU25-5(11)8 section is strongly affected by laminar separation without re-attachment, particularly at Reynolds numbers lower than 350,000. For greater Reynolds numbers, however, where flow re-attachment occurs, the performance of this aerofoil increases considerably to quite impressive standards. This can be seen clearly in Figure 4.7.2, where, for example, at an incidence of  $6^\circ$  and in a short Reynolds number range between  $2.5 \times 10^5$  and  $4.0 \times 10^5$ , the  $C_L$  magnitude changes dramatically from about 0.35 to 1.17, an increase of more than 240%.

From Figures 4.7.1, 3 and 4, it may also be observed, that the performance of the GA(W)-1 improves at a slower rate than the NACA-4415 and NACA-0015, between the range of  $0.5 \times 10^5 \leq Re_C \leq 1.5 \times 10^5$  and  $\alpha < 5^\circ$ . For these aerofoils, further increases in incidence showed little variation in  $C_N$  until  $C_{N\max}$  was obtained. As incidence and Reynolds number increased even further, a reduction in  $C_N$  occurred. This decrease is more abrupt for the GA(W)-1 and NACA-0015 aerofoils, indicating a leading edge type of stall, regardless of Reynolds number. For the NACA-4415 section, however, the loss of lift was more gradual due to trailing edge flow separation, with the abrupt loss occurring at a higher incidence.

As a concluding remark, it may be said that all aerofoils examined in this investigation appear to have their own operational limits. The NACA-4415 together with the GU25-5(11)8 aerofoil could be safely operated at Reynolds numbers greater than 100,000 and 400,000 respectively. The operational limits of the GA(W)-1 and NACA-0015 aerofoils are similar to the NACA-4415 but due to their early leading edge stall characteristic, they have been shortened. The contours also indicate that the GU25-5(11)8 aerofoil stalls at an earlier incidence, while for the other three aerofoils stall is delayed as Reynolds number increases. The occurrence of earlier stalling, as stated by Laing and Kokkodis (Refs 35 and 18), is due to earlier trailing edge separation caused by the formation of the separation bubble at mid-chord of the aerofoil. It should also be mentioned, that maximum normal force coefficient for the GA(W)-1 and NACA-0015 sections increases slightly with increasing Reynolds numbers, while for the NACA-4415 and GU25-5(11)8, it decreases.

The NACA-4415 appears to be, generally, superior to GA(W)-1 and NACA-0015 since it produces higher  $C_N$  values for the same increase in incidence and it has more favourable stalling characteristics. It is also more favourable to the GU25-5(11)8, but only at Reynolds numbers lower than 350,000. For higher Reynolds numbers, however, the GU25-5(11)8 aerofoil section shows its great

superiority by producing the highest  $C_N$  values of all those sections considered.

## CHAPTER V

### CONCLUSIONS AND RECOMMENDATIONS FOR FURTHER STUDIES

The present study could be described as a preliminary investigation into the performance of a NACA-4415 aerofoil section tested at Reynolds numbers ranging from 50,000 to 600,000. The main objectives were to accumulate sufficient chordwise static pressure data to attain the aerodynamic forces and moments, namely  $C_N$ ,  $C_T$ , and  $C_{M_C}/4$ , and to assess how these forces and moments have been affected by the behaviour of the boundary layer around the aerofoil. The boundary layer behaviour was examined by studying the static pressure distributions that occurred over the aerofoil in conjunction with a selection of flow visualisation photographs which were taken to record the flow phenomena that occurred over the upper surface of the aerofoil only.

Furthermore, the aerodynamic characteristics of the present aerofoil section were compared with those obtained for the GU25-5(11)8, NASA GA(W)-1 and NACA-0015 previously tested using the same facilities.

### 5.1 SUMMARY OF CONCLUSIONS

The analysis of the results from the chordwise pressure distribution measurements showed that the upper and lower surfaces of the aerofoil were dominated by the development of two laminar separation bubbles. The lower surface bubble, defined as "short", initially forms close to the leading edge at negative angles of attack. As incidence is gradually increased it progresses towards the trailing edge, while its length slowly increases. At a certain incidence, however, depending on the Reynolds number, the bubble disappears. In contrast with the lower surface bubble, that on the upper surface, originally described as "long", travels rapidly upstream becoming shorter in length with increasing incidence and Reynolds number. As it moves to within 15% of the chord from the leading edge its rate of movement was shown to slow down considerably. Flow separation was also observed to occur, sometimes covering an area as high as 65% of the chord from the trailing edge. When a certain angle of attack was reached the bubble "burst" causing massive flow separation over the aerofoil.

The sensitivity of the boundary layer was also highlighted during both the pressure and flow visualisation measurements. It was observed, that at incidences just prior to complete flow separation the boundary layer behaved rather erratically. In that it would alternate from

being fully attached to fully separated, in a non-periodic fashion within a few seconds. This was thought to be caused by the large environmental disturbances, at such incidences, present during the experiments, causing the boundary layer to flick-on and off from one state to another.

From a series of oil-film flow visualisation experiments, conducted to study the nature and behaviour of the flow over the upper surface of the model, a number of flow visualisation photographs were taken. In the analysis that followed, vital information was obtained about the behaviour of the boundary layer. It was revealed that at low incidences a "long" laminar separation bubble was formed close to the trailing edge, moving upstream and becoming shorter in length as the incidence and Reynolds number were increased. This gave confirmation of the existence and behaviour of such a bubble, indicated by the earlier pressure distribution measurements. Three-dimensionality of the flow was also observed, especially for incidences higher than  $11.90^\circ$  and prior to complete stall.

The oil-film flow visualisation technique became very useful, especially in cases where the laminar separation bubble, although present, was unable to be detected by the pressure measurement method. However, when detection of the separation bubble and trailing edge flow separation was obtained, there was generally a close agreement between the

results obtained by the two methods; in particular, at a Reynolds number equal to 600,000. For the lower Reynolds number ranges, there was some slight disagreement between the laminar and turbulent flow separation points, while turbulent re-attachment points matched each other exceptionally well for all incidences and Reynolds numbers.

The aerodynamic forces and moments generated to study the performance of the aerofoil in these low Reynolds number regimes, were found also to be affected by the behaviour of the boundary layer. In cases where the development and disappearance of the separation bubbles had occurred, on either the upper or lower surface of the aerofoil,  $dC_N/d\alpha$  and  $dC_{Mc}/4/d\alpha$  were affected. This manifested itself in an obvious magnitudes change. This was most evident when the lower surface turbulent boundary layer changed to fully laminar state over a narrow range of incidences. As a result of this, a slight "kink" developed on the aerodynamic coefficient curves and was present over the majority of the Reynolds numbers tested.

The most dominant feature in the normal force and pitching moment curves, apart from the "kink", was the gentle decrease in  $C_N$  and an increase in  $C_{Mc}/4$  and  $C_T$  with increased incidence. This was due to the obvious penetration of the trailing edge separation towards the leading edge. When complete stall occurred an abrupt

reduction in aerodynamic coefficient magnitudes was observed. From an examination of the pressure profiles, this was caused by the "bursting" of the upper surface separation bubble in the region close to the leading edge. Therefore, the behaviour of the normal force and the quarter chord pitching moment coefficients, suggested that the stalling characteristic of the NACA-4415 aerofoil section was that of a "combined stall", i.e. a combination of trailing and leading edge stall. As Reynolds number was increased, stalling of the aerofoil was found to occur at a higher incidence. The maximum normal force coefficient also varied for Reynolds numbers below 400,000. For higher Reynolds numbers, however, it remained relatively constant having a value of approximately 1.32.

The critical Reynolds number for the NACA-4415 aerofoil was found to lie between 50,000 and 75,000. It was demonstrated that, when the aerofoil operated below the critical Reynolds number, its performance was similar to that of a flat plate, while when operated above it, it behaved like a conventional aerofoil. Although the aerofoil was well behaved for Reynolds numbers between 450,000 and 600,000, its performance below this regime was more dependent on Reynolds numbers, especially at incidences greater than 8°.

Present and existing data were also examined and showed that the differences in test environments, wind

tunnels, model sizes, etc., can have considerable effects. With this in mind, however, it is difficult to predict the way they will affect the results of this particular series of tests.

Lastly, comparing the characteristics of the present aerofoil with those of the GU25-5(11)8, NASA GA(W)-1 and NACA-0015, revealed that the GU25-5(11)8 showed superiority over the other three aerofoils for Reynolds numbers above 350,000, by producing the highest  $C_N$  values. For lower Reynolds numbers, however, it behaved in a very unstable manner, with all the other aerofoils greatly superior to it, especially at moderate to low incidences. The NACA-4415 aerofoil is pre-eminent over GA(W)-1 and NACA-0015 for all Reynolds numbers tested, as it generates higher  $C_N$  values, has better stalling characteristics and a higher operational range.

## 5.2 RECOMMENDATIONS FOR FURTHER STUDY

The NACA-4415 aerofoil section is known to be widely used on the rotor blades of various Horizontal Axis Wind Turbines (HAWT). These turbines operate in an open atmospheric environment and therefore are exposed to the elements. Because of their operational environment some roughness to the blades in the form of rain droplets, dust or even in the form of bird droppings and dead insects, may exist. These can affect the performance of the blades and consequently that of the turbine. Bearing in mind such

conditions, it is therefore suggested that further experiments should be carried out with the application of some roughness on either the upper or lower surface of the present NACA-4415 aerofoil model. The applied roughness could be in the form of a trip wire covering the whole length of the span, having different diameter sizes, located at various positions along the chord length, etc.

As mentioned in Section 4.4, the existence of the slight "kink" on the  $C_N$  and  $C_{Mc}/4$  curve slopes was thought to have been caused by the occurrence of full laminar flow on the lower surface of the aerofoil. It is therefore advisable, that in future, a surface oil-film flow visualisation technique should be employed to study the boundary layer behaviour on the lower surface. Its use might prove most useful to confirm or refute the sudden downstream movement of the laminar separation point inferred by using the method of Coton and Galbraith (Refs 27 and 39). Additionally, since the surface oil flow visualisation technique, utilised for studying the behaviour of the boundary layer over the upper surface of the model, gave apparently misleading results for Reynolds numbers below 200,000, an alternative technique, such as the direct smoke injection, could be recommended.

For a limited number of experiments, however, it was noticed that the upper surface separation bubble, although present, as indicated by the flow visualisation pictures,

could not be identified from the pressure distribution plots. In such cases, further experiments are required to examine the nature and behaviour of the flow. This could be accomplished by using a large number of hot film anemometry gauges over the upper surface of the model.

Finally, due to the large amount of time consumed in the present investigation for the data acquisition procedure, an alternative method should be employed and a possible alternative is described below.

The pressure tappings used for recording the pressure variation around the present aerofoil at various incidences and Reynolds numbers, should be substituted by a number of miniature pressure transducers. By employing such pressure transducers an automatic and simultaneous pressure recording can be obtained with the help of a Transient Recording System linked to a highly compatible computer. The computer could be programmed to display the pressure distribution around the aerofoil in a graphical form on its visual display terminal or onto a printer after each test run. Such a procedure will allow the user to check for any faults in the collected data immediately after each test and if necessary to repeat the test. When all test runs are completed, the computer can perform the necessary integrations of each pressure distribution, producing plots of the aerodynamic forces and moments. This will enable the user to start an immediate analysis of the aerodynamic char-

cteristics of that particular aerofoil.

Such a data acquisition and data reduction procedure could not only save a considerable amount of the researcher's time, but would allow him also to test more aerofoils inside the permitted time given. The shortcomings and difficulties for the employment of such a method, however, are recognised.

### 5.3 CONCLUDING REMARKS

The results of this study provided valuable information about the aerodynamic characteristics of the NACA-4415 aerofoil and the behaviour of the boundary layer, when tested two-dimensionally for Reynolds numbers below 600,000. From the acquired data, speculations may arise about the validity of the results, mainly because of the high levels of free stream turbulence, noise and mechanical vibrations in the working section of the test facility. However, because the above aerofoil is used extensively in HAWT applications, which in turn are operating in an environment possessing similar perturbations, the present data could be considered as valid.

A search of the available literature did not bring to light any two-dimensional data about the NACA-4415 aerofoil tested at Reynolds numbers below 700,000. Therefore, since the blades of HAWT machines, designed and constructed for

wind tunnel experimental purposes, operate usually in regimes lower than 1,000,000, the present data could prove very valuable.

Finally, due to the uncertainty of the performance of aerofoil sections tested below Reynolds numbers of 500,000, as shown in the present investigation, it is hoped that this will encourage future researchers to examine the behaviour of other aerofoils currently operating in these low Reynolds number regimes.

## APPENDIX

### MANUFACTURE AND ASSEMBLY OF NACA-4415 AEROFOIL MODEL

The construction of the NACA-4415 aerofoil model was carried out in the manufacturing facilities located in the Aerospace Engineering Department of the University of Glasgow. The facilities consist of two blocks of wax together with a fixed head cutting machine, fitted with router and follower which was used to cut the wax into the required aerofoil shape. Figure A1 shows the model under construction, divided into two halves, as well as the locations of the structural materials used.

Before the cutting of the wax, the x and y coordinates of the NACA-4415 aerofoil were plotted onto a 1/4 inch thick mild steel plate using a vernier height gauge to ensure accuracy of the profile. The steel plate was cut to provide the required upper and lower surfaces of the aerofoil and mounted on the wax cutting machine with the router follower resting on it. After machining, Slipwax was applied to ease mould release and the wax surface polished to give a good finish. Epoxy resin gel-coat was then spread and left to harden. This gel-coat covered both surfaces for the required span length of the model.

Holes representing the pressure orifices were drilled through the hardened surface of the gel-coat into the wax at the chosen surface locations. At this stage, pins having the same diameter were inserted into the pressure orifices preventing them from getting blocked when glass fibre and epoxy resin were added to model. Four layers of 280 gm/m<sup>2</sup> glass fibre woven roving together with epoxy resin applied between each layer were laid on the gel-coat surface at an angle of +/- 45° to give a strong torsional stiffness.

Balsa wood blocks were then cut to fill the aerofoil shape and positioned at each end of the model, allowing room for 1/4 inch aluminium plates to finish off the ends. The relevant balsa wood was then drilled to allow for the extension of the brass pressure tubes out past the length of the model. When these blocks were in place the brass pressure tubes were allocated on the model. Epoxy resin foam mixture was then poured into the model and left to harden. When this was complete the model was ready to be machined flat. After machining, either the upper or lower surface model was removed from the wax block and placed on top of the other so that the leading edges and balsa wood blocks were parallel with each other. While in position, four holes were drilled through the balsa woods to take 3/8 inch dia. dowel pins. The pins prevented either half of the model from slipping. Epoxy resin mixture was then applied to both flat surfaces. The top half of the model was then pressed carefully to squeeze out any excess foam. Extra

care was taken by checking constantly that no slipping movement had occurred since the slightest movement could misalign the whole model.

When the resin had set, the whole model was removed from the wax mould. The aluminium end plates were filled to the ends of the model and fixed by woodscrewing them on the balsa wood blocks in conjunction with an epoxy bond. The accuracy of the model's profile was carefully checked using the templates and bumps or indentations on the surface were rectified by filling in with gel-coat and rubbing down with wet and dry emery paper. The brass pressure tubes were checked for any blockages and cleaned out by blowing through with compressed air. Finally, when accuracy of the aerofoil profile was achieved and the pressure tubes cleaned, the model was ready to be installed into the tunnel. The connection of the brass pressure tubes with the pressure ports at the rear of the selector boxes was achieved using plastic tubes.

## REFERENCES

1. Mueller, T.J.

"Low Reynolds number Vehicles" AGARDograph No.288, February 1985.

2. Mueller, T.J., Jansen, B.J.Jr.

"Aerodynamic Measurements at Low Reynolds Numbers", AIAA paper No. 82-0598, 1982.

3. Marchman, J.F.

"Aerodynamic Testing at Low Reynolds Numbers", Journal of Aircraft, Vol.24, No.2, February 1987.

4. Lissaman, P.B.S.

"Low Reynolds Number Airfoils", Annual Review of Fluid Mechanics, Palo Alto, California: Annual Reviews, Inc., Vol. 15, pp. 223-239, 1983.

5. Pope, A., Rae, W.H., Jr.

"Low Speed Wind Tunnel Testing", John Wiley & Sons, New York, 1984.

6. E.S.D.U.

"Wind Tunnel Corrections", 'Aerodynamics', Volume 13, Item Number 76028, November 1976.

7. Mueller, T.J., Pohlen, L.J., Conigliaro, P.E., Jansen, B.J.Jr.

"The Influence of Free Stream Disturbances on Low Reynolds Number Airfoil Experiments", Experiments in Fluids, Vol.1, pp. 3-14, 1983.

8. Sumantran, V., Sun, Z., Marchman, J.F.III.

"Acoustic and Turbulence Influence on Low Reynolds Number Wing Pressure Distributions", Conference on Low Reynolds Number Airfoil Aerodynamics, Notre Dame, June 16-18, 1985.

9. Mueller, T.J.  
*"The Influence of Laminar Separation and Transition on Low Reynolds Number Airfoil Hysteresis"*, AIAA 17th Conference on Fluid Dynamics, Plasma Dynamics and Lasers, Colorado, June 25-27, 1984.
10. Horton, H.P.  
*"Laminar Separation Bubbles in Two and Three Dimensional Incompressible Flow"*, Ph.D. Thesis, Queen Mary College, University of London, London, 1968.
11. Chappell, P.D.  
*"Flow Separation and Stall Characteristics of Plane, Constant-Sections Wings in Subcritical Flow"*, The Aeronautical Journal of the Royal Aeronautical Society, Vol. 72, pp. 82-90, January 1968.
12. Arena, A.V., Mueller, T.J.  
*"Laminar Separation, Transition, and Turbulent Re-attachment near the Leading Edge of Airfoils"*, AIAA Journal, Vol.18, No.17, pp.747-753, July 1980.
13. Gaster, M.  
*"The Structure and Behaviour of Laminar Separation Bubbles"*, ARC R & M, No. 3595, March 1969.
14. van den Berg, B.  
*"Role of Laminar Separation Bubbles in Airfoil Leading-Edge Stalls"*, AIAA Journal, Vol.19, No.5, pp. 553-556, May 1981.
15. Ward, J.W.  
*"The Behaviour and Effects of Laminar Separation Bubbles on Aerofoils in Incompressible Flow"*, Journal of the Royal Aeronautical Society, Vol.67, pp. 783-789, December 1963.

16. Kokkalis, A.  
*"An Investigation into the Wake Flow Behind Circular Cylinders Fitted with Slat Devices"*, M.Sc. Thesis, Department of Aeronautics and Fluid Mechanics, University of Glasgow, March 1983.
17. Lunde, K.  
*"Wind Tunnel Testing of Aerofoil Sections"*, Final Year Project, Department of Aeronautics and Fluid Mechanics, University of Glasgow, April 1983.
18. Kokkodis, G.  
*"Low Reynolds Number Performance of a NACA-0015 and a GA(W)-1 Aerofoil"*, M.Sc. Thesis, Department of Aeronautics and Fluid Mechanics, University of Glasgow, February 1987.
19. Galbraith, R.A.McD, Coton,F.N., Saliveros,E., Kokkodis,G.  
*"Aerofoil Scale Effects and the Relevance to Wind Turbines"*, Ninth Annual Wind Energy Conference, Edinburgh, Scotland, 1-3 April, 1987.
20. Spalding, D.J.  
*"Wind Tunnel Testing of Aerofoil Sections"*, Final Year Project, Department of Aeronautics and Fluid Mechanics, University of Glasgow, March 1985.
21. Kelling, F.H.  
*"Experimental Investigation of a High Lift Low Drag Aerofoil"*, G.U. Report No. 6802, Department of Aeronautics and Fluid Mechanics, University of Glasgow, 1968.
22. Furness Controls Limited.  
*"Instruction Manuals of FC002 and FC012 Micromanometers"*.
23. Duncan, W.J., Thom, A.S., Young, A.D.  
*"Mechanics of Fluids"*, Published by Edward Arnold Ltd., Second Edition, London, 1970.

24. Houghton, E.L., Carruthers, N.B.  
*"Aerodynamics for Engineering Students"*, Published by Edward Arnold Ltd., Third Edition, London, 1982.
25. Saliveros, E.  
*"Collection of Flow Visualisation Photographs over the Upper Surface of a NACA-4415 Aerofoil"*, Report in Progress, Department of Aerospace Engineering, University of Glasgow, February 1988.
26. Huber, A.F.II.  
*"The Effects on Roughness on an Airfoil at Low Reynolds Numbers"*, M.Sc. Thesis, University of Notre Dame, Notre Dame, Indiana, May 1985.
27. Coton, F.N.  
*"Contribution to the Prediction of Low Reynolds Number Aerofoil Performance"*, Ph.D. Thesis, Department of Aeronautics and Fluid Mechanics, University of Glasgow, December 1987.
28. Loftin, L.K., Jr., Smith, H.A.  
*"Aerodynamic Characteristics of 15 NACA Airfoil Sections at Seven Reynolds Numbers From  $0.7 \times 10^6$  to  $9.0 \times 10^6$ "*, NACA Technical Note 1945, October, 1949.
29. Althaus, D.  
*"Stuttgarter Profilkatalog I"*, Institut fur Aerodynamik und Gasdynamik der Universitat Stuttgart, 1972.
30. Miley, S.J.  
*"A Catalog of Low Reynolds Number Airfoil Data for Wind Turbine Applications"*, Department of Aerospace Engineering, Texas A&M University, Texas 77843, February 1982.
31. Riegels, F.N.  
*"Aerofoil Sections"*, Published by Butterworths and Co. (Publishers) Ltd., London, 1961.

32. Galbraith, R.A.MCD.  
*"The Aerodynamic Characteristics of a GU25-5(11)8 Aerofoil for Low Reynolds Numbers"*, Experiments in Fluids, Vol.3, pp. 253-256, 1985.
33. Bastedo, W.G.Jr.  
*"Performance of an Aerofoil and Three Rectangular Planform Wings at Low Reynolds Numbers"*, M.Sc. Thesis, Department of Aerospace and Mechanical Engineering, Notre Dame, Indiana, December 1984.
34. Jacobs, E.N., Sherman, A.  
*"Airfoil Section Characteristics as Affected by Variations of the Reynolds Numbers"*, NACA Technical Report No. 586, 23rd Annual Report, 1937.
35. Laing, S.  
*"Wind Tunnel Testing of Aerofoil Sections"*, Final Year Project, Department of Aeronautics and Fluid Mechanics, University of Glasgow, April 1984.
36. Clayton, B.R.  
*"BWEA Initiative of Wind Assisted Ship Propulsion"*, Journal of Wind Engineering and Industrial Aerodynamics, Vol. 19, pp. 251-276, 1985.
37. Poll, D.I.A., Mansoor, A.  
*"On the Determination of the Two-Dimensional Characteristics of Aerofoils at Low Reynolds Numbers"*, International Conference on Aerodynamics at Low Reynolds Numbers ( $10^4 < Re < 10^6$ ), London, 15-18 October, 1986.
38. van Ingen, J.L., Boermans, L.M.M.  
*"Aerodynamics at Low Reynolds Numbers: A Review of Theoretical and Experimental Research at Delft University of Technology"*, International Conference on Aerodynamics at Low Reynolds Numbers ( $10^4 < Re < 10^6$ ), London, 15-18 October, 1986.

39. Coton, F.N., Galbraith, R.A.McD.  
*"A Simple Method for the Prediction of Separation Bubble formation on Aerofoils at Low Reynolds Numbers"*, International Conference on Aerodynamics at Low Reynolds Numbers ( $10^4 < Re < 10^6$ ), London, 15-18 October, 1986.

**TABLE 1.**  
Coordinates of NACA-4415 Aerofoil Section

UPPER SURFACE		LOWER SURFACE	
x/c	y/c	x/c	y/c
1.00000	0.00156	0.99979	-0.00156
0.96946	0.01100	0.96771	-0.00284
0.93865	0.02002	0.93576	-0.00415
0.90781	0.02863	0.90397	-0.00505
0.87697	0.03682	0.87236	-0.00689
0.84617	0.04460	0.84095	-0.00833
0.81545	0.05198	0.80978	-0.00981
0.78483	0.05814	0.77887	-0.01134
0.75437	0.06550	0.74824	-0.01292
0.72408	0.07164	0.71793	-0.01454
0.69400	0.07738	0.68795	-0.01619
0.66418	0.08270	0.65834	-0.01787
0.63463	0.08762	0.62911	-0.01956
0.60540	0.09211	0.60029	-0.02126
0.57652	0.09620	0.57191	-0.02294
0.54802	0.09986	0.54399	-0.02460
0.51994	0.10311	0.51654	-0.02622
0.49231	0.10594	0.48960	-0.02778
0.46515	0.10835	0.46319	-0.02926
0.43851	0.11034	0.43732	-0.03066
0.41241	0.11192	0.41201	-0.03195
0.38662	0.11306	0.38756	-0.03314
0.36119	0.11363	0.36396	-0.03433
0.33640	0.11364	0.34097	-0.03552
0.31228	0.11310	0.31861	-0.03667
0.28888	0.11203	0.29690	-0.03776
0.26621	0.11046	0.27584	-0.03878
0.24433	0.10842	0.25544	-0.03968
0.22324	0.10592	0.23572	-0.04046
0.20299	0.10302	0.21669	-0.04109
0.18360	0.09972	0.19836	-0.04156
0.16508	0.09607	0.18074	-0.04185
0.14748	0.09209	0.16385	-0.04194
0.13080	0.08782	0.14770	-0.04181
0.11507	0.08329	0.13231	-0.04147
0.10030	0.07854	0.11768	-0.04088
0.08651	0.07360	0.10383	-0.04006
0.07370	0.06850	0.09078	-0.03898
0.06190	0.06327	0.07854	-0.03765
0.05110	0.05794	0.06712	-0.03604
0.04133	0.05255	0.05655	-0.03417
0.03257	0.04712	0.04683	-0.03203
0.02484	0.04168	0.03798	-0.02960
0.01814	0.03624	0.03001	-0.02690
0.01247	0.03084	0.02294	-0.02392
0.00738	0.02549	0.01154	-0.01709
0.00164	0.01501	0.00386	-0.00912
0.00000	0.00000	0.00000	0.00000

**TABLE 2.**  
 Locations of Pressure Tappings on NACA-4415  
 Aerofoil Section

UPPER SURFACE			
x/c	y/c	x/c	y/c
0.979666	0.007933	0.234400	0.108833
0.959866	0.013533	0.193267	0.103267
0.940166	0.018966	0.153267	0.095133
0.919166	0.024833	0.133600	0.090067
0.899200	0.030200	0.114600	0.084633
0.878966	0.035600	0.104533	0.081200
0.860866	0.040066	0.095866	0.078200
0.840266	0.045466	0.085334	0.074466
0.820334	0.050400	0.076000	0.070733
0.799466	0.055200	0.065800	0.066533
0.780000	0.059466	0.055266	0.061267
0.739466	0.068072	0.045733	0.056266
0.679266	0.079626	0.035200	0.051300
0.619266	0.089691	0.027133	0.042666
0.558733	0.098301	0.015800	0.035800
0.500266	0.105039	0.008733	0.028733
0.437200	0.110399	0.004334	0.025000
0.375533	0.113334	0.000667	0.012466
0.315667	0.113066	0.000025	0.003667
0.275466	0.110977		

LOWER SURFACE			
x/c	y/c	x/c	y/c
0.001533	-0.009866	0.181033	-0.042166
0.010166	-0.015466	0.234733	-0.040531
0.016766	-0.020533	0.281466	-0.038440
0.028466	-0.026334	0.382000	-0.033394
0.039667	-0.030485	0.480733	-0.028366
0.049600	-0.033766	0.581266	-0.022600
0.059466	-0.036165	0.681266	-0.016833
0.069933	-0.038031	0.779334	-0.011600
0.079466	-0.039370	0.879866	-0.006777
0.100600	-0.041061	0.979800	-0.002425
0.139433	-0.042366		

**TABLE 3.**

## 2-D ANGLE OF ATTACK SUMMARY

Reynolds Number	$C_N = 0$	$C_{N\max}$	$[C_{Mc/4}]_{\max}$	Stall
50,000	-1.50	4.90	7.90	-----
75,000	-2.90	12.40	14.90	16.90
100,000	-3.80	12.40	14.40	16.65
125,000	-4.10	12.90	14.90	17.40
150,000	-4.20	12.90	14.90	17.40
175,000	-4.20	12.90	14.90	17.40
200,000	-4.10	12.90	14.90	17.90
250,000	-4.10	11.90	13.90	18.40
300,000	-4.10	11.90	13.90	18.90
350,000	-4.10	11.90	13.90	18.90
400,000	-4.10	11.90	13.40	19.40
450,000	-4.10	11.90	13.90	19.40
500,000	-4.10	11.90	13.90	20.40
550,000	-4.10	11.90	14.90	-----
600,000	-4.10	11.90	14.90	-----

TABLE 4.

Estimated locations of laminar separation points on the lower surface of a NACA-4415 aerofoil section using a viscid-inviscid analysis method.

**TABLE 5.**

Useful Information About Past and Present Wind Tunnels Used  
to Test NACA-4415 Aerofoil Sections.

Tunnel	Type	Test Section	Velocity (m/s)	Turbulence Intensity	Chord (m)	Test	Aspect Ratio
<b>NACA LTT</b> Low Turbulence Tunnel	Closed Return	0.90mx2.29m (Closed)	70	0.03%	0.6	2-D	3.81
<b>IAG STUTTGART=1</b> Stuttgart Laminar Wind Tunnel	Closed Return	0.73mx2.73m (Closed)	91	0.02%	0.5 <sup>1</sup> & 1.0 <sup>2</sup>	2-D	5.46 & 2.73
<b>GLASGOW UNIVERSITY</b> Low Speed Wind Tunnel	Closed Return	0.84mx1.14m (Closed)	30	≈0.50%	0.3	2-D	2.80

1: for Reynolds numbers up to  $1.5 \times 10^6$

2: for Reynolds numbers  $> 1.5 \times 10^6$

(Adapted from References 28, 29, 30 and 31)

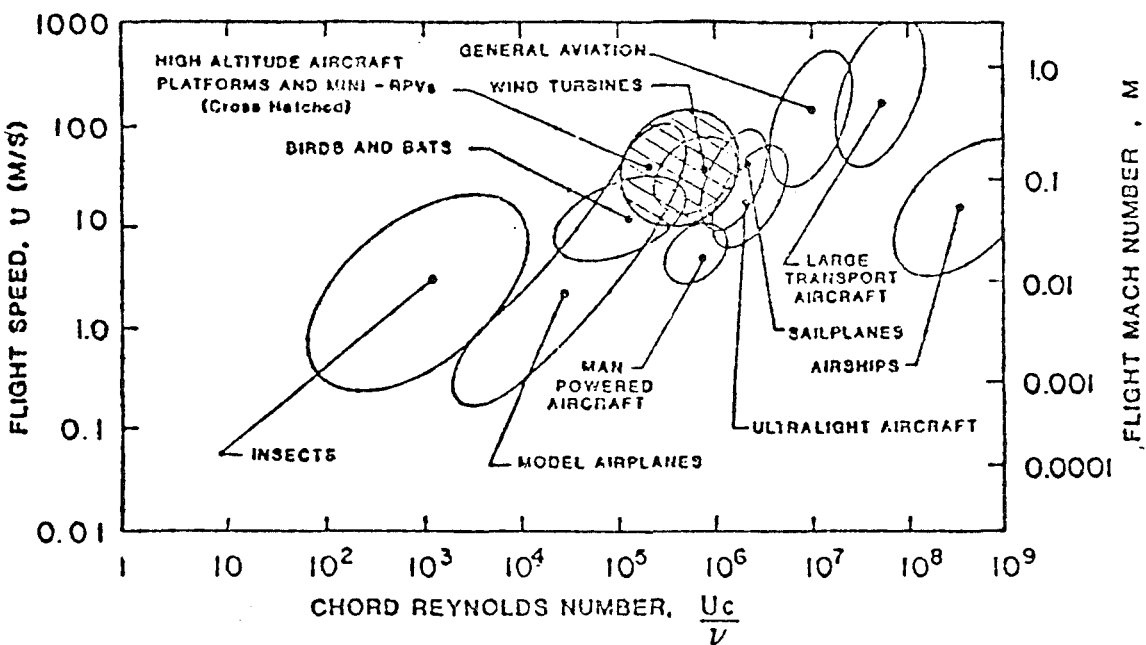


Figure 1.1. Chord Reynolds Number versus Flight Velocity for a Variety of Natural and Man-Made Flying Objects. (Adapted from Reference 1)

### Sep. Bubble with turbulent reattachment

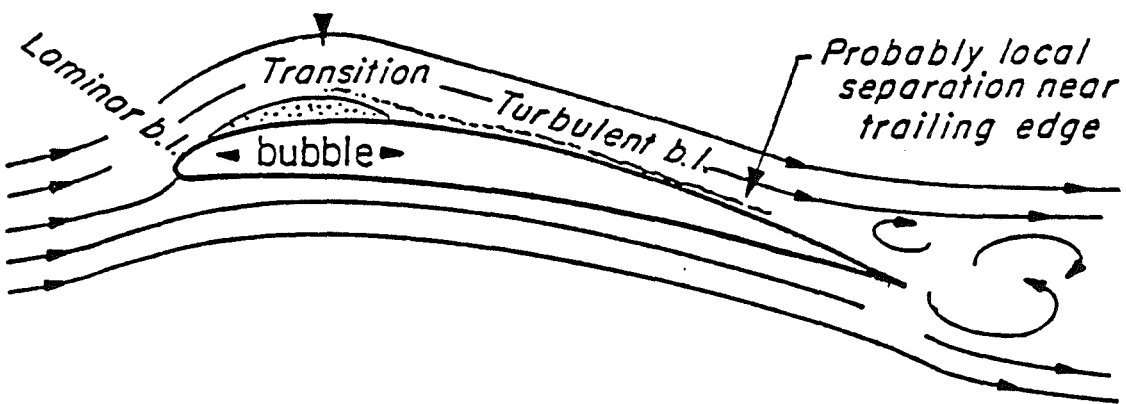


Figure 1.2. A Typical Laminar Separation Bubble Formed over the Upper Surface of an Aerofoil.  
(Adapted from Reference 1)

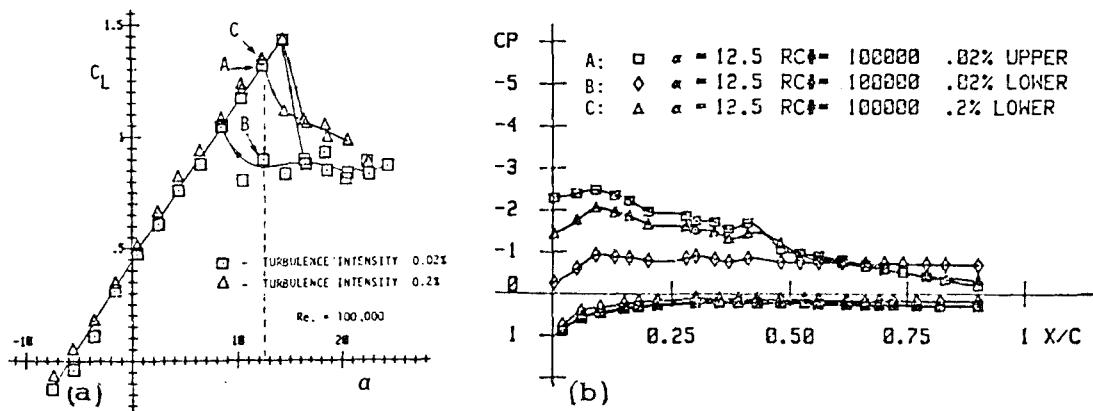


Figure 1.3. Turbulence Effects on Stall Hysteresis (a) and Pressure Distribution (b) for the Wortmann FX-63-137 Aerofoil Section. ( $Re=100,000$ )  
(Adapted from Reference 7)

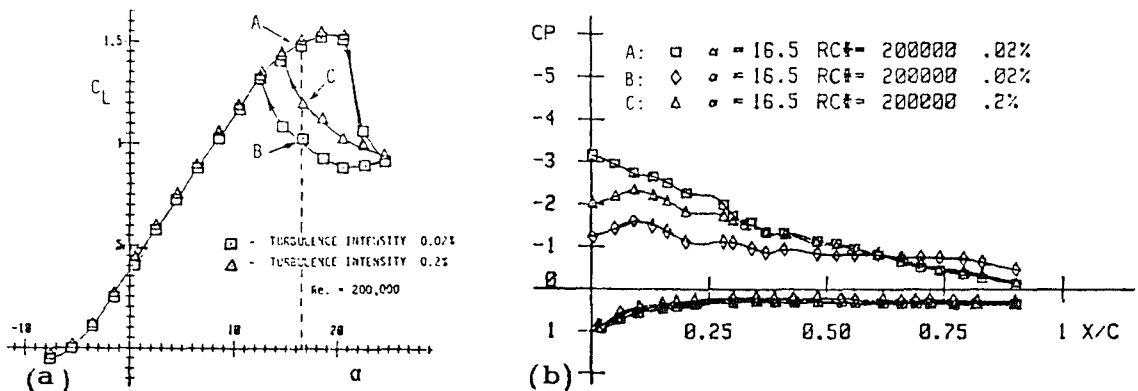


Figure 1.4. Turbulence Effects on Stall Hysteresis (a) and Pressure Distribution (b) for the Wortmann FX-63-137 Aerofoil Section. ( $Re=200,000$ )  
(Adapted from Reference 7)

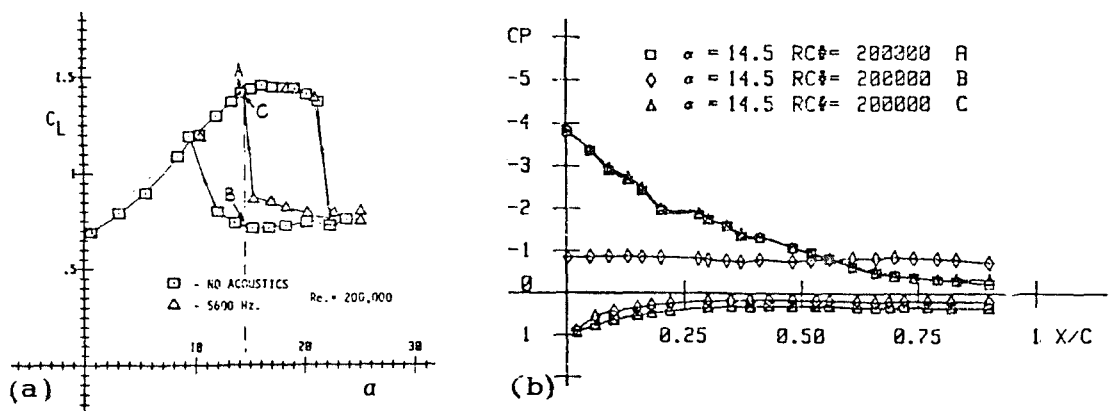


Figure 1.5. Acoustic Effects on Stall Hysteresis (a) and Pressure Distribution (b) for the Wortmann FX-63-137 Aerofoil Section. ( $Re=200,000$ )  
(Adapted from Reference 7)

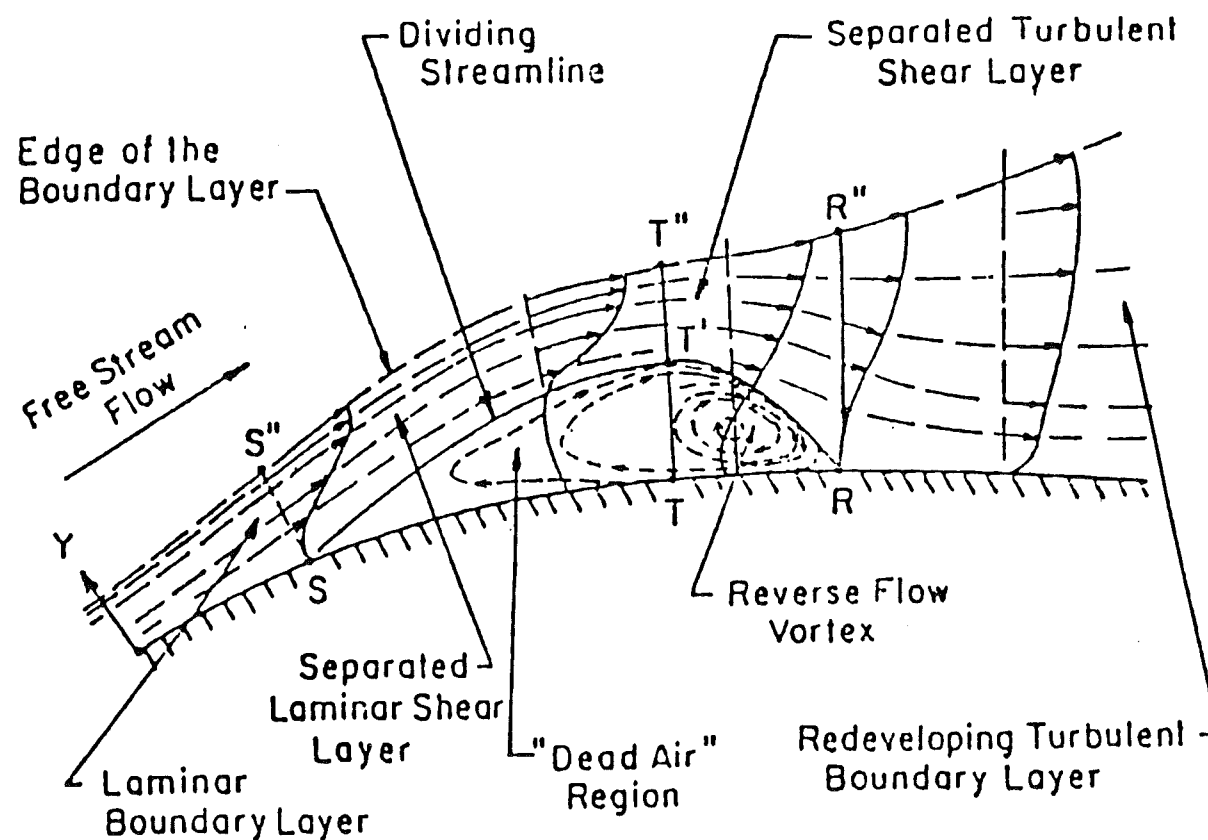


Figure 1.6. Sketch of a Laminar Separation Bubble.

(Adapted from Reference 10)

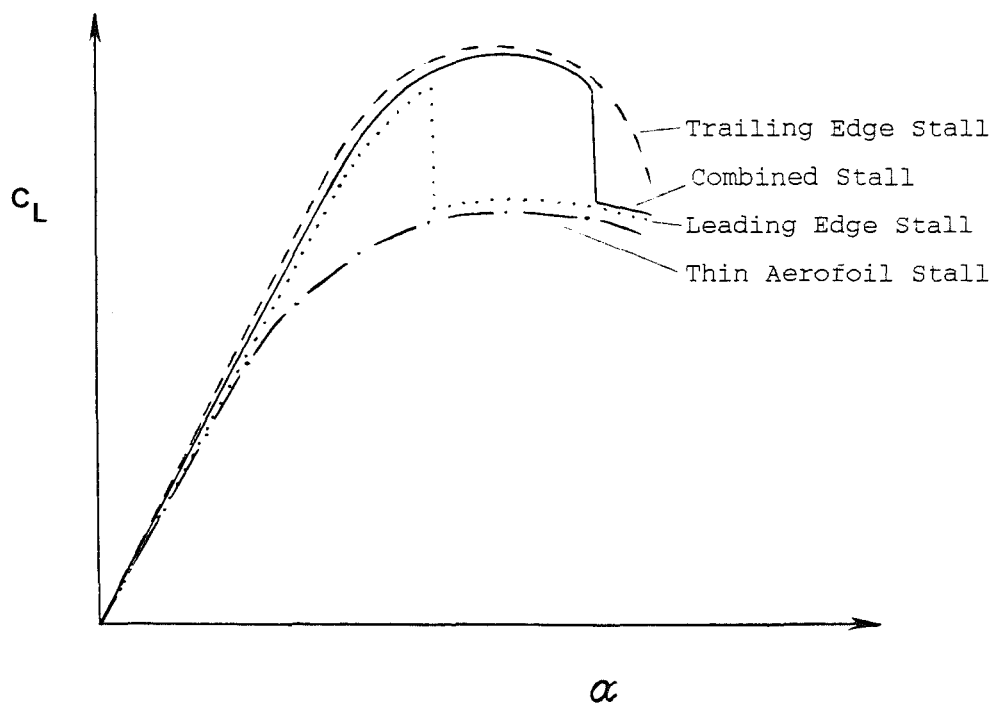


Figure 1.7. Four Different Types of Static Stall

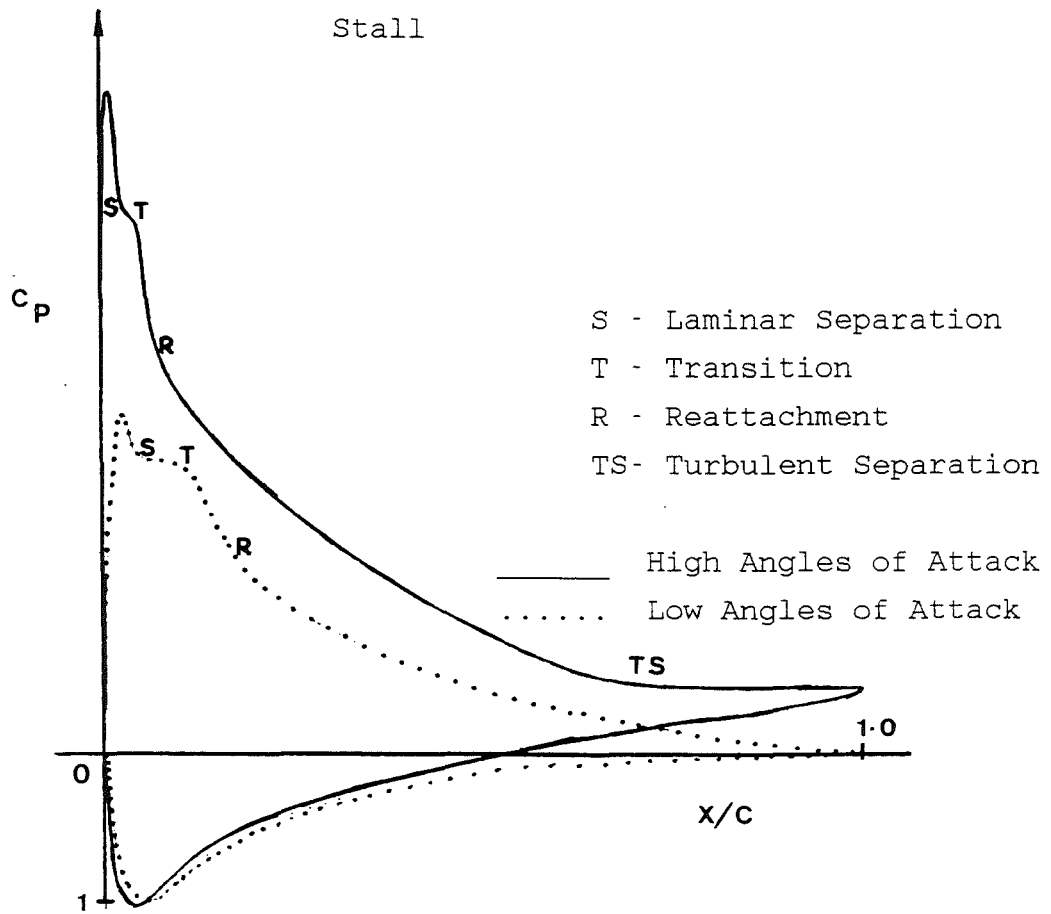


Figure 1.8. Typical Aerofoil Pressure Distribution with Laminar Separation Bubbles.

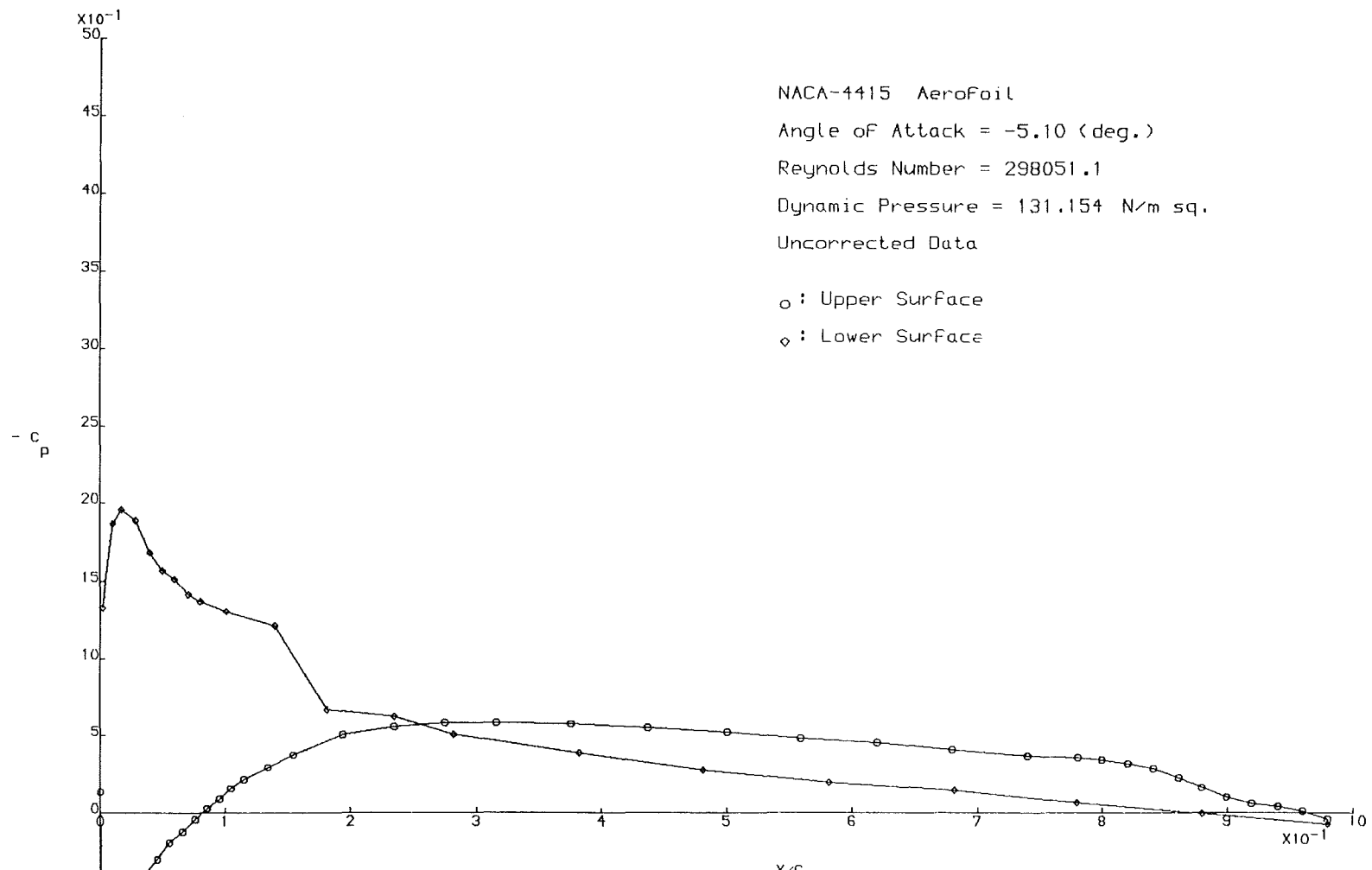
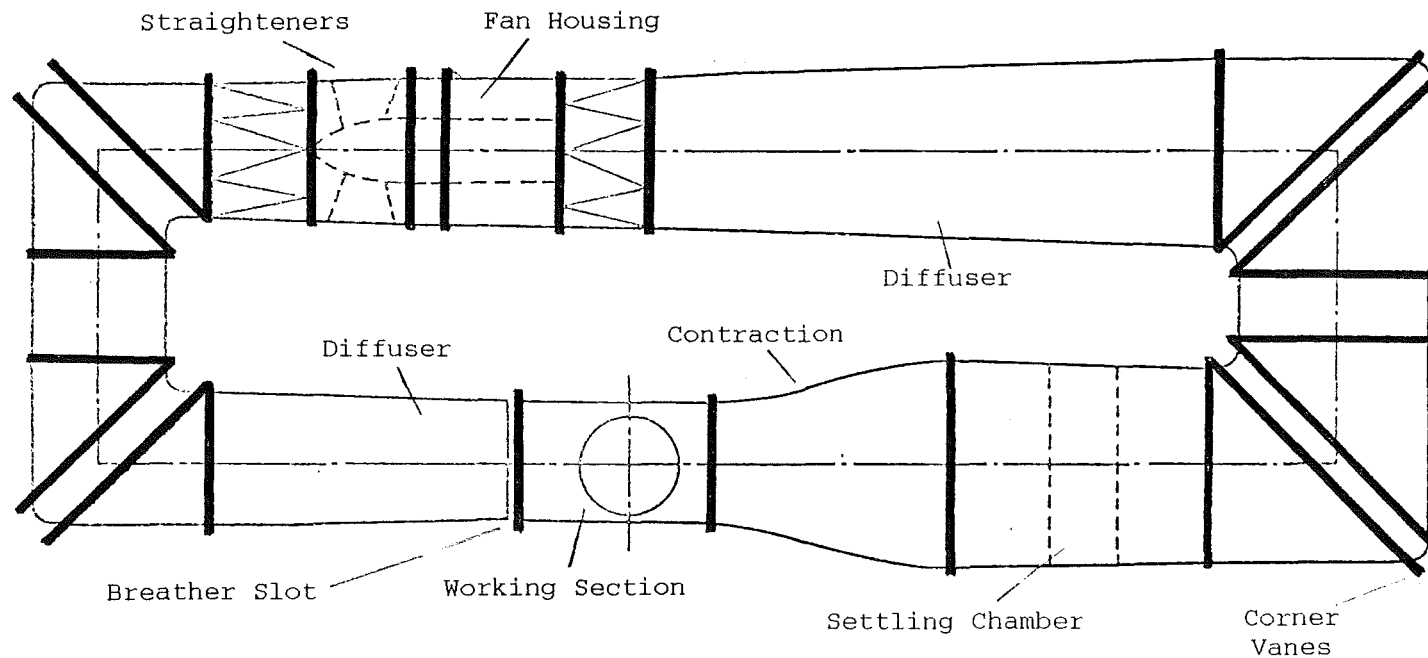


Figure 1.9. Experimental Static Pressure Distribution over the NACA-4415 Aerofoil at an Incidence of  $-5.10^\circ$  and at a Reynolds Number of 298,051.



0.383m x 1.143m WIND TUNNEL

Figure 2.1. A Plan View of the Glasgow University's Low Speed Wind Tunnel.

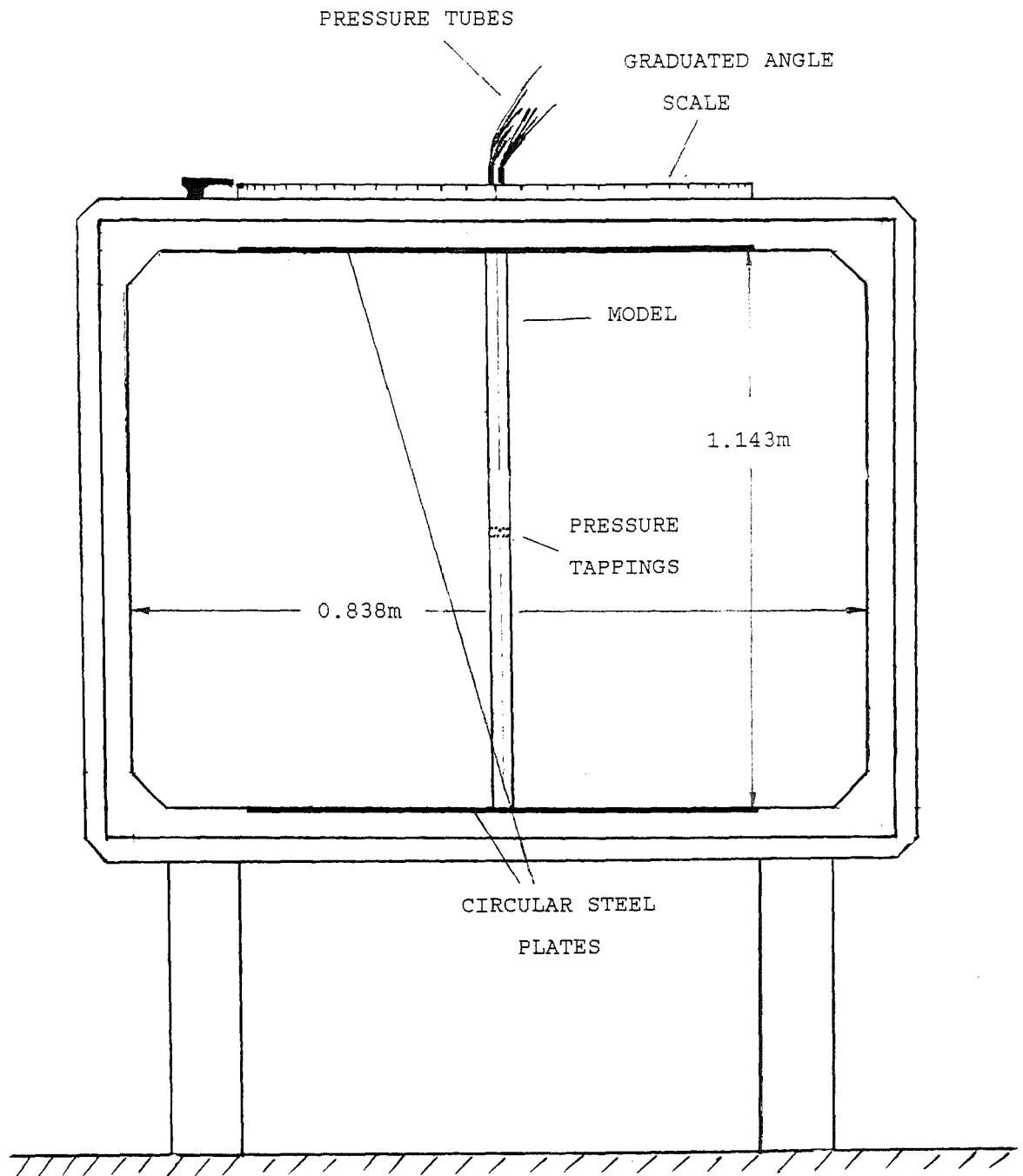


Figure 2.2. Cross-Sectional View of the Working Section of the Glasgow University's Low Speed Wind Tunnel.

NACA - 4415 AEROFOIL SECTION

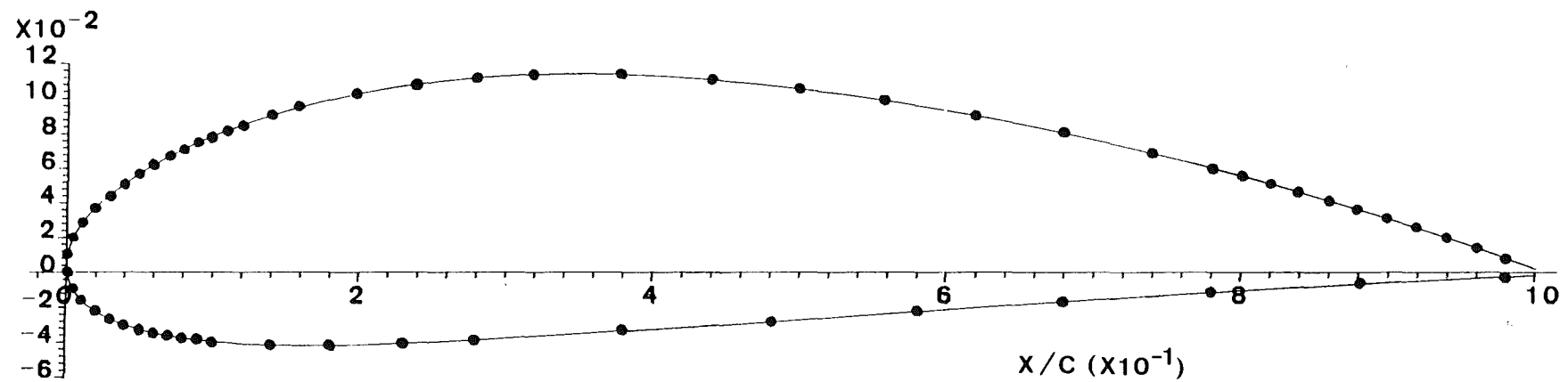


Figure 2.3. Positions of the Pressure Tappings Around the  
NACA-4415 Aerofoil Model.

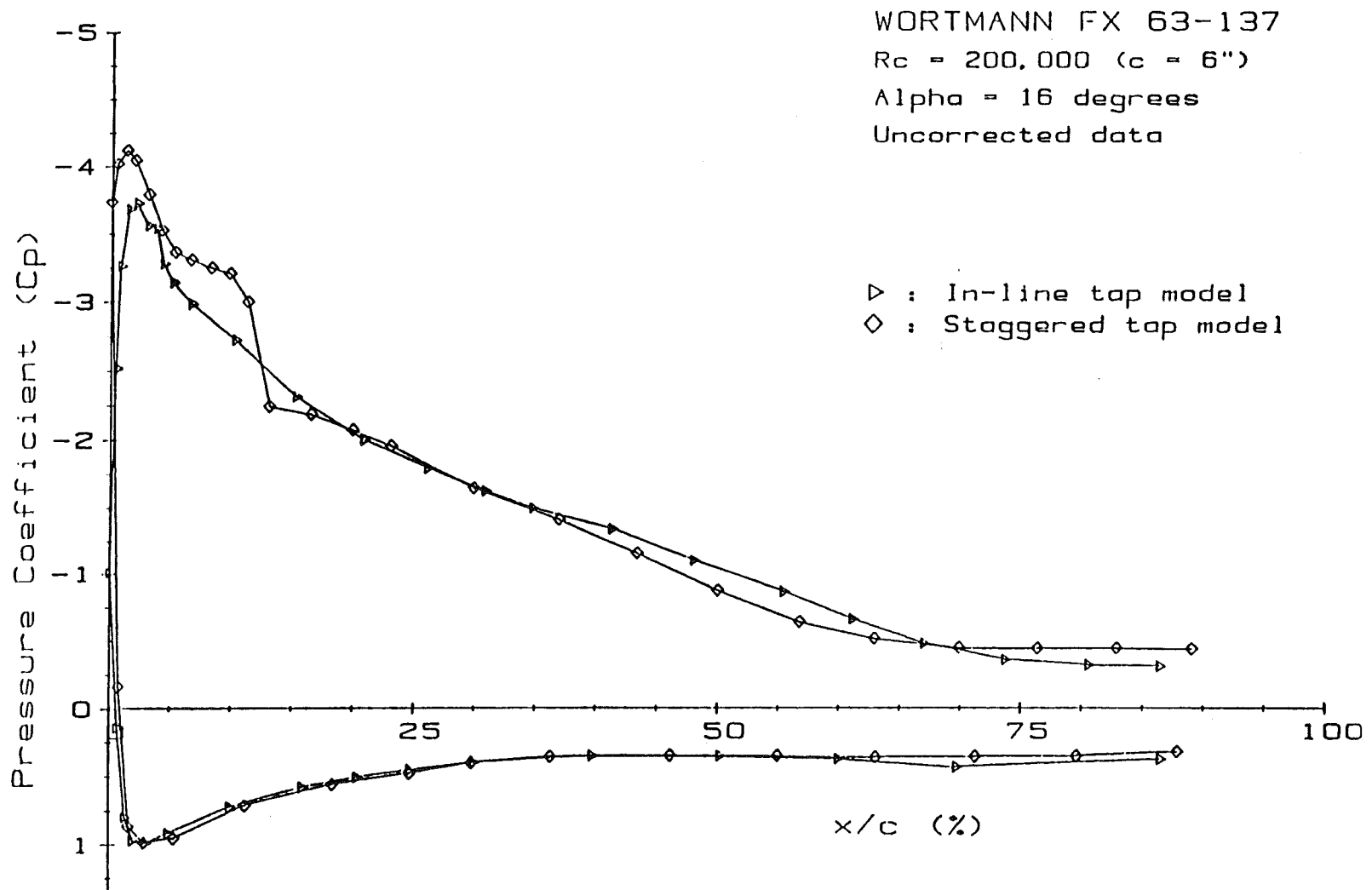


Figure 2.4. Pressure Distribution Comparison Between two Wortmann Aerofoils Having Different Pressure Tap Configurations at  $16^\circ$  Angle of Attack and  $Re=200,000$ . (Adapted from Reference 1 )

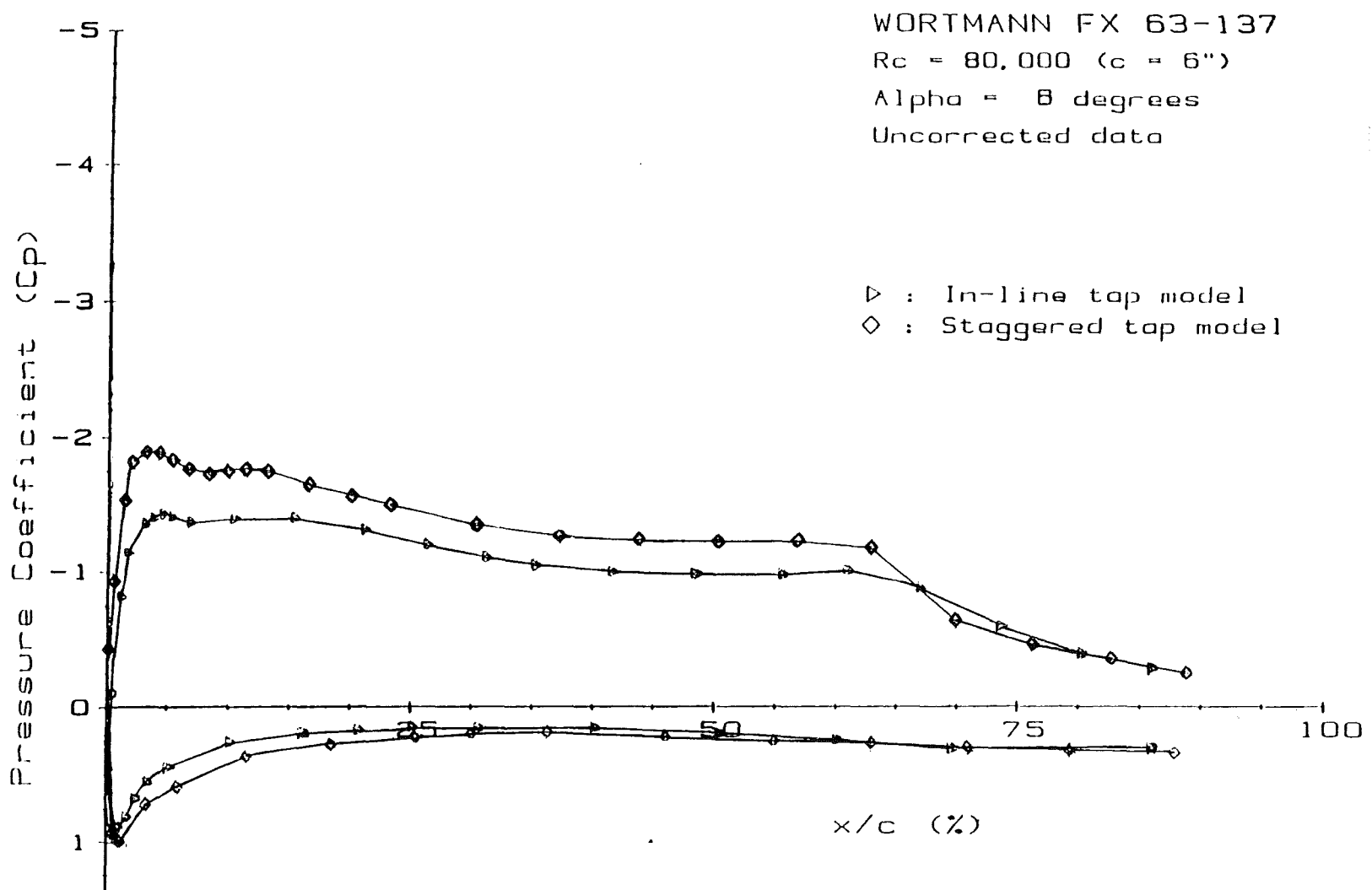


Figure 2.5. Pressure Distribution Comparison Between two Wortmann Aerofoils Having Different Pressure Tap Configurations at  $8^\circ$  Angle of Attack and  $Re=80,000$ . (Adapted from Reference 1)

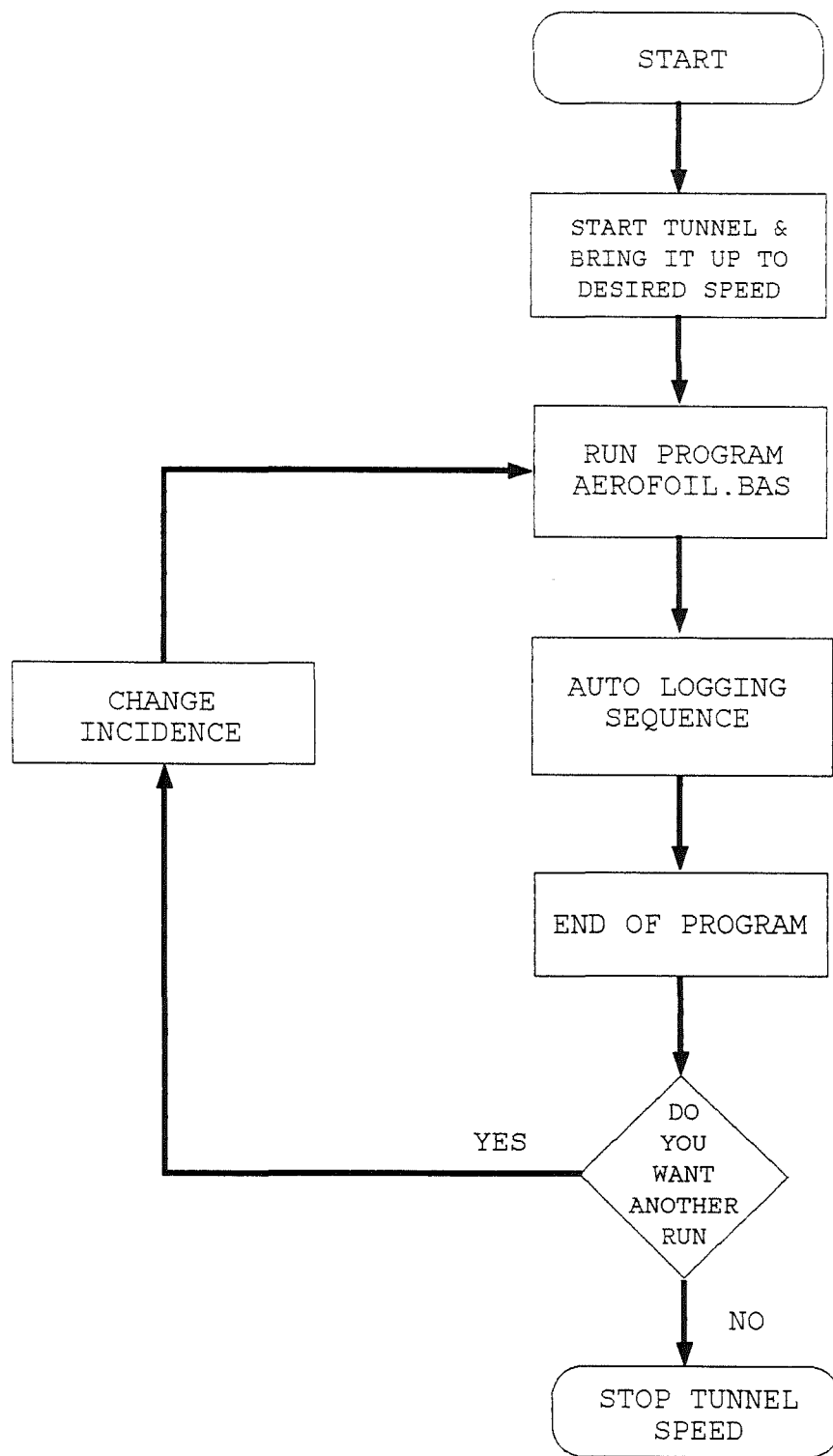


Figure 3.1. Sequence of events during pressure distribution measurements

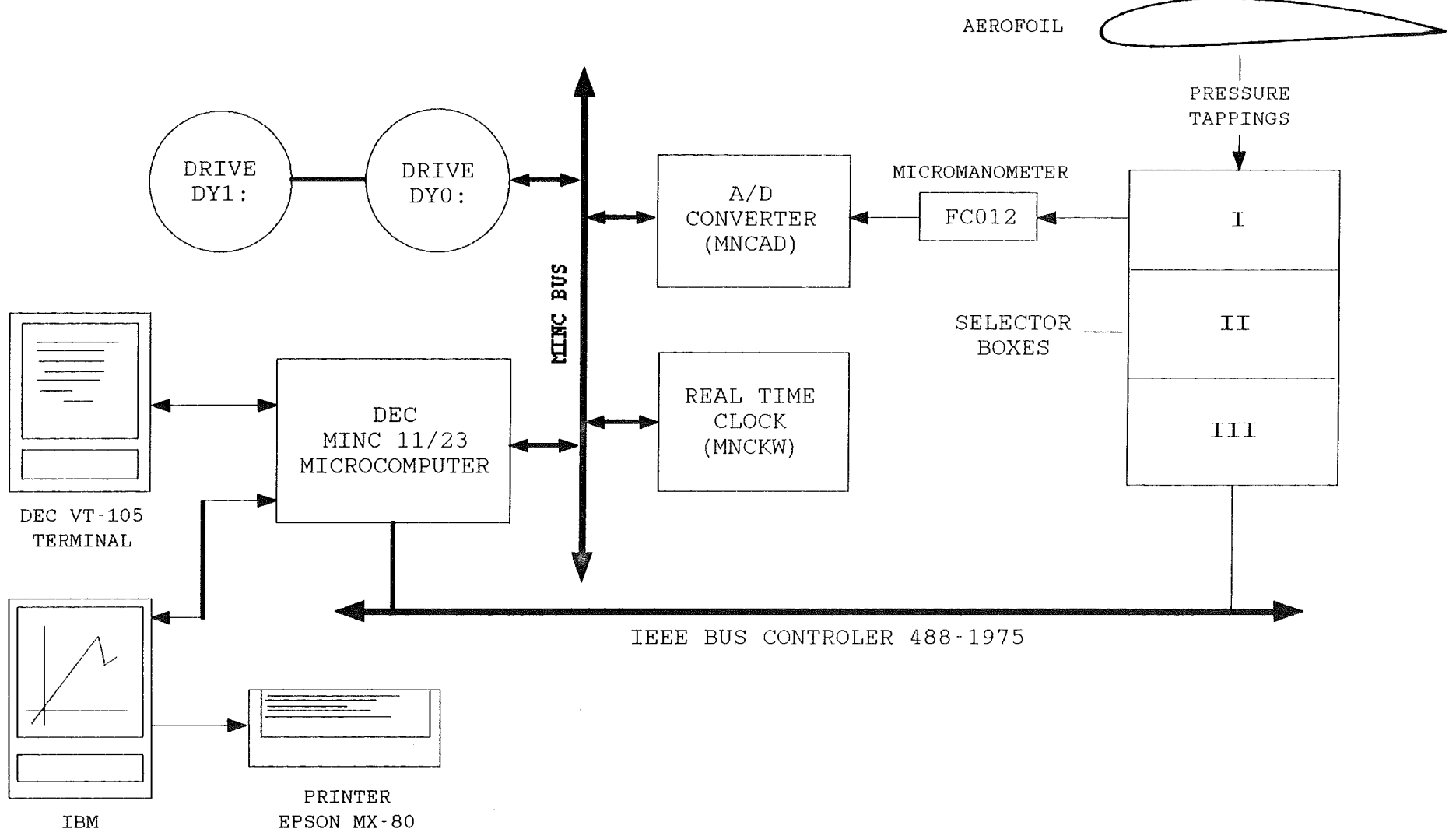


Figure 3.2. Schematic of Instrumentation used for the data acquisition.

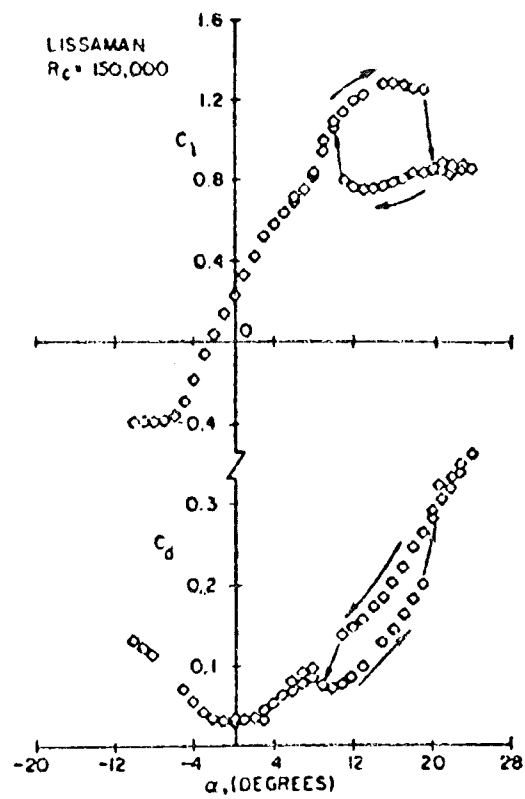


Figure 3.3. Section Lift and Profile Drag Coefficients Versus Angle of Attack for  $R_c=150,000$  for the Smooth Lissaman Airfoil.

(Adapted from Reference 9)

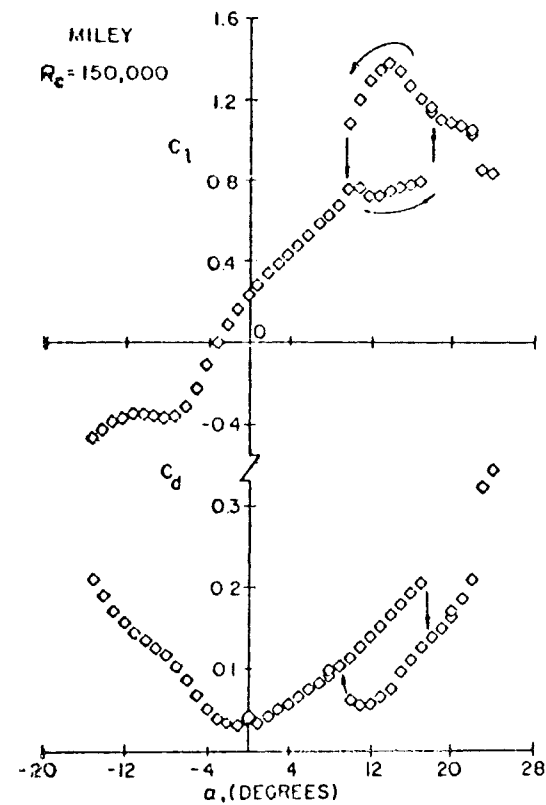


Figure 3.4. Section Lift and Profile Drag Coefficients Versus Angle of Attack for  $R_c=150,000$  for the Smooth Miley Airfoil.

(Adapted from Reference 9)

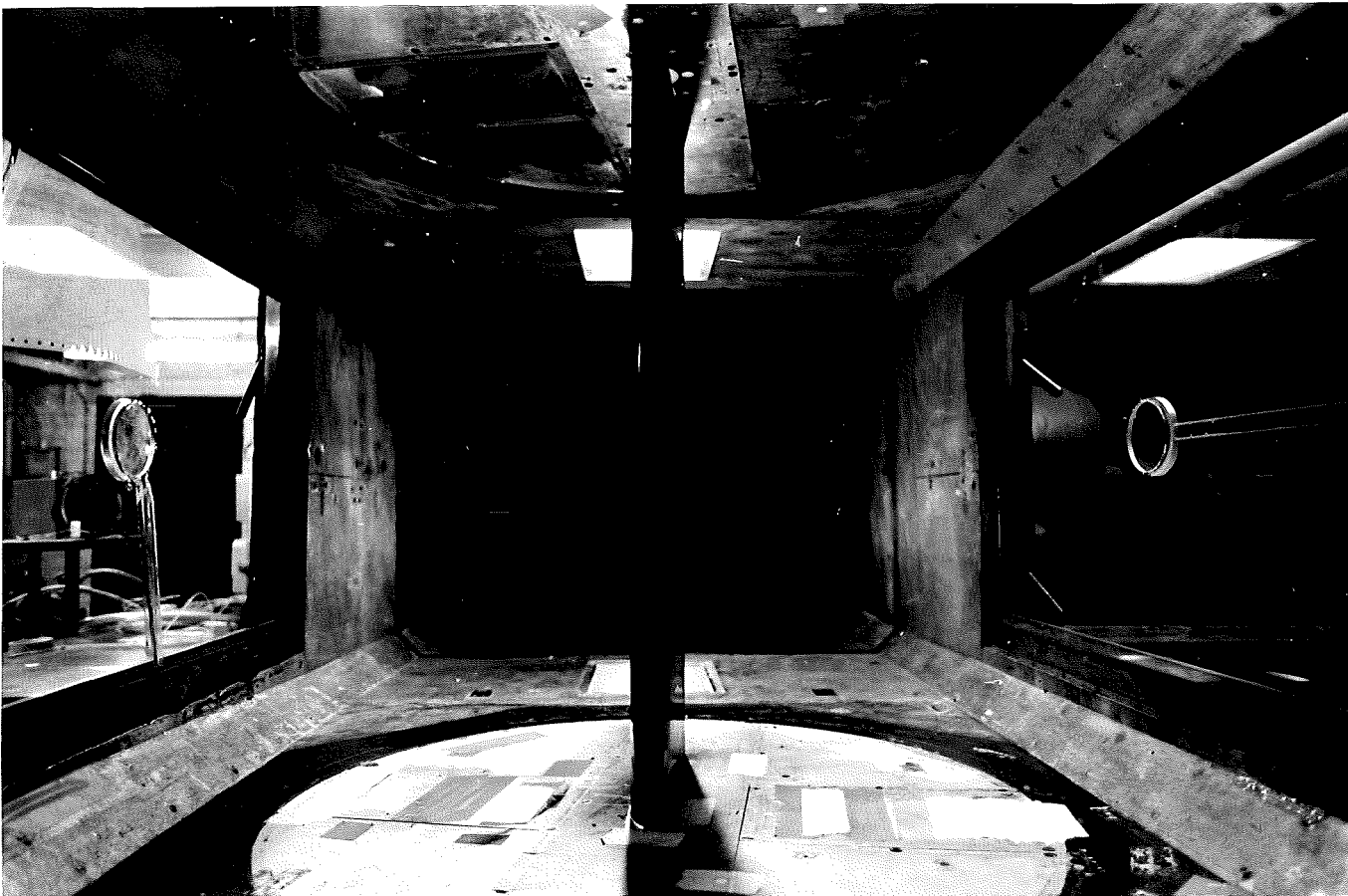


Figure 3.5. The NACA-4415 Aerofoil Installed in the Glasgow University's Low Speed Wind Tunnel

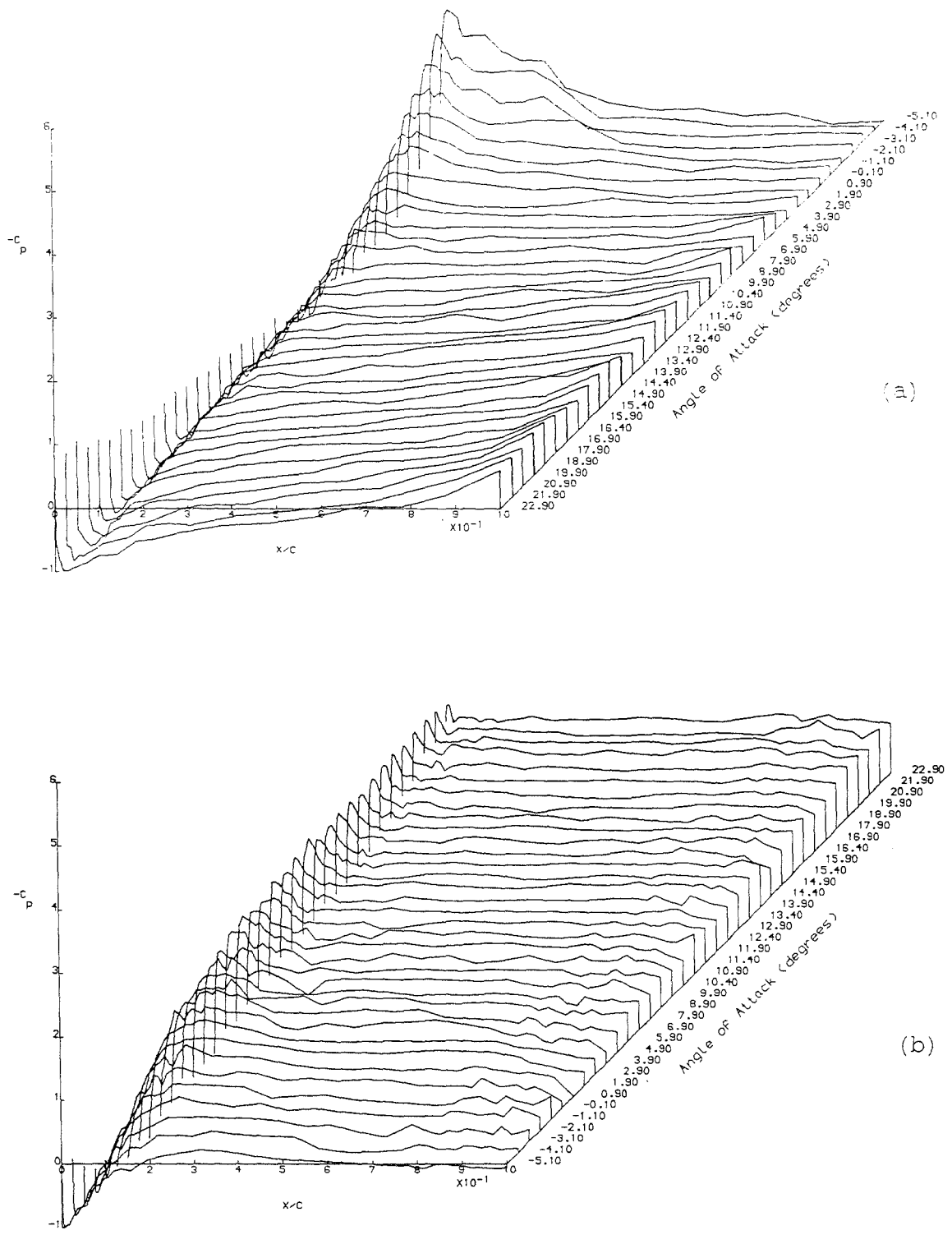


Figure 4.1.1. 3-D Plots of  $C_p$  vs  $x/c$  vs  $\alpha$  for the Lower (a) and Upper (b) Surface of a NACA-4415 Aerofoil Section and  $Re=50,000$ .

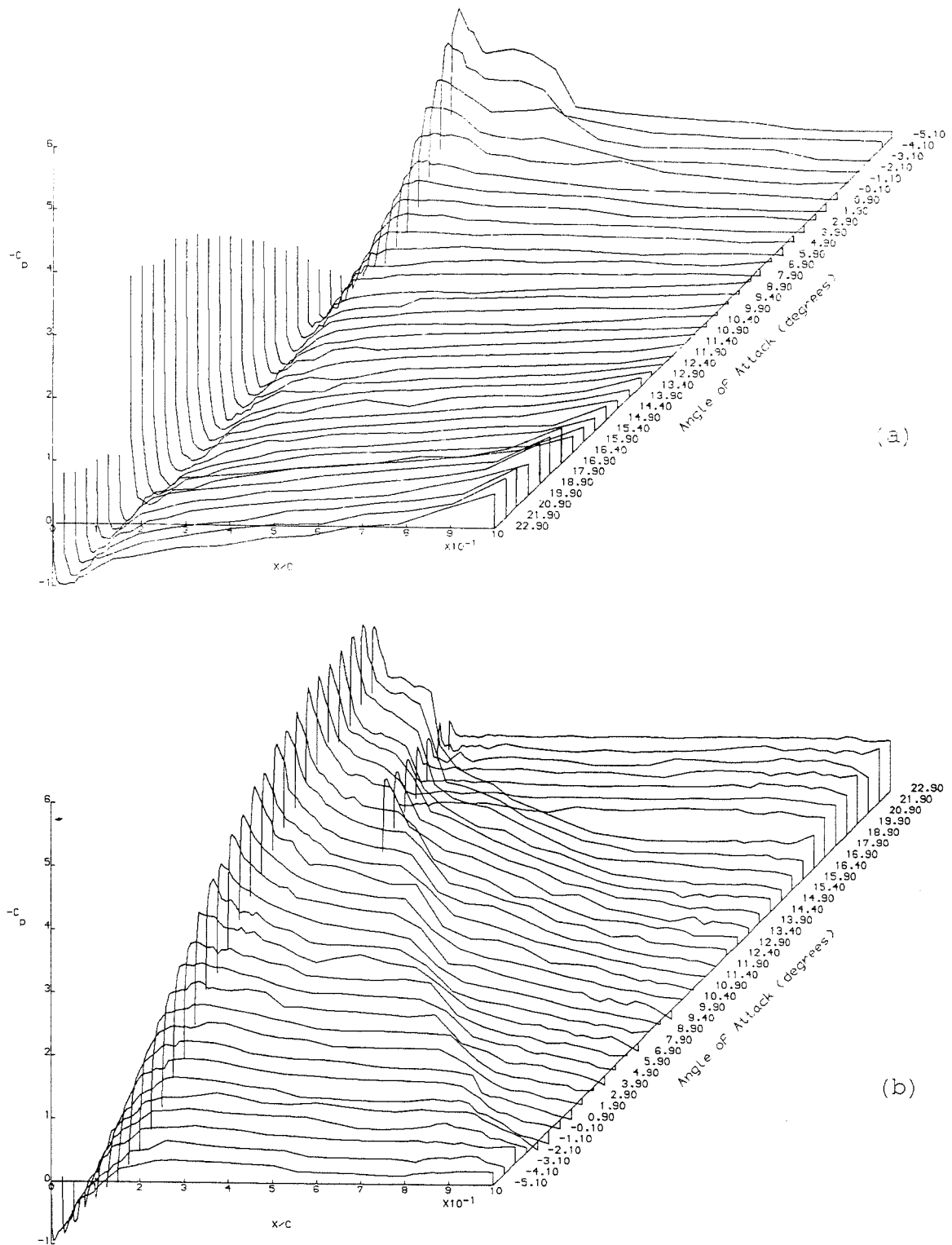


Figure 4.1.2. 3-D Plots of  $C_p$  vs  $x/c$  vs  $\alpha$  for the Lower (a) and Upper (b) Surface of a NACA-4415 Aerofoil Section and  $Re=75,000$ .

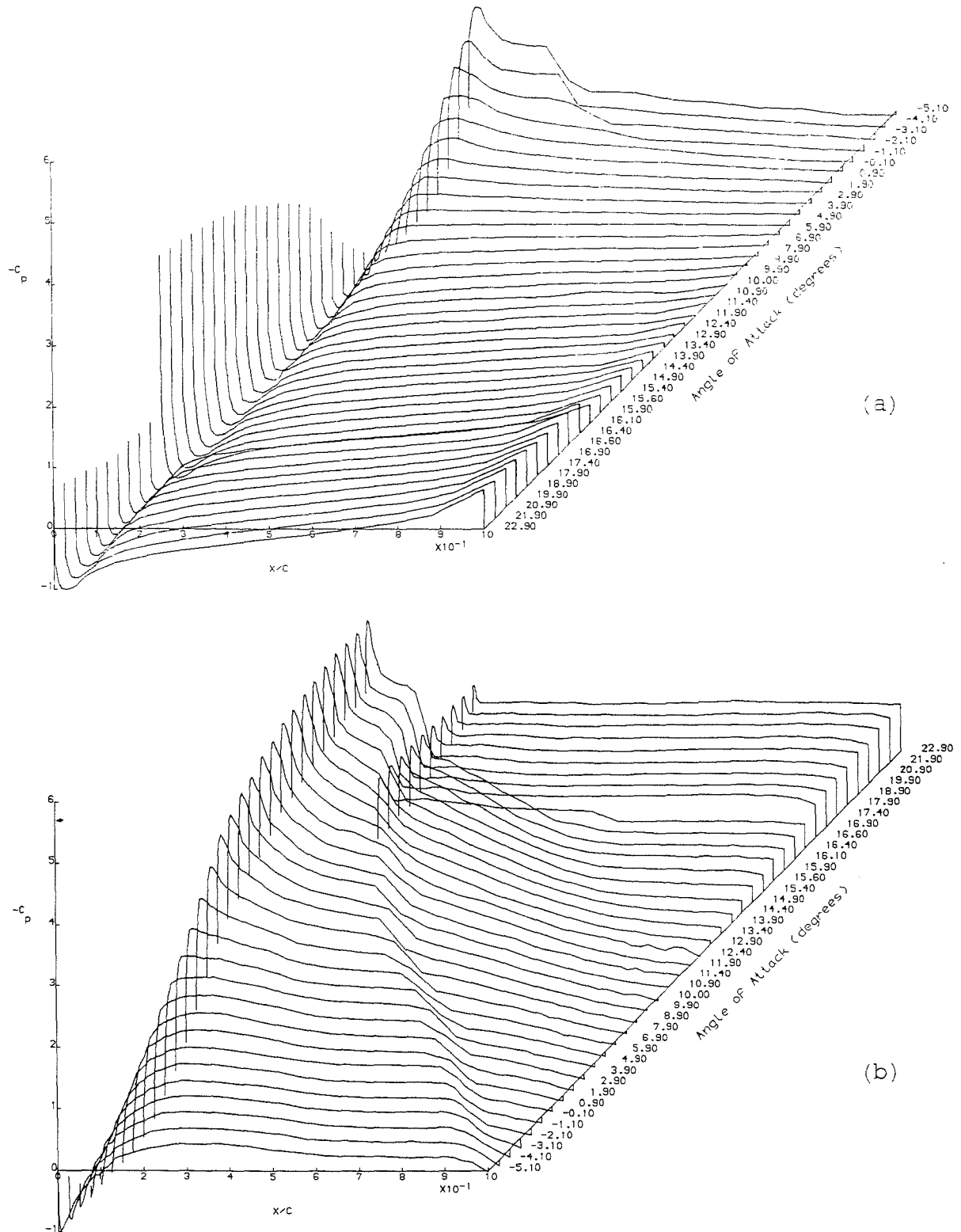


Figure 4.1.3. 3-D Plots of  $C_p$  vs  $x/c$  vs  $\alpha$  for the Lower (a) and Upper (b) Surface of a NACA-4415 Aerofoil Section and  $Re=100,000$ .

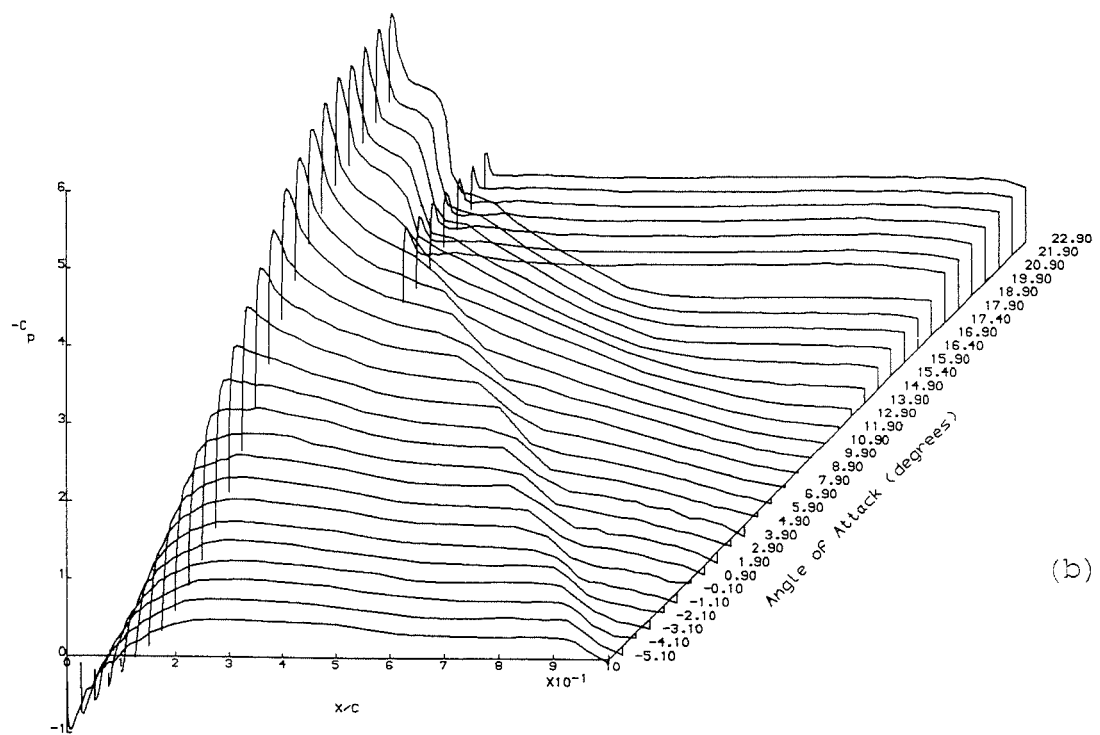
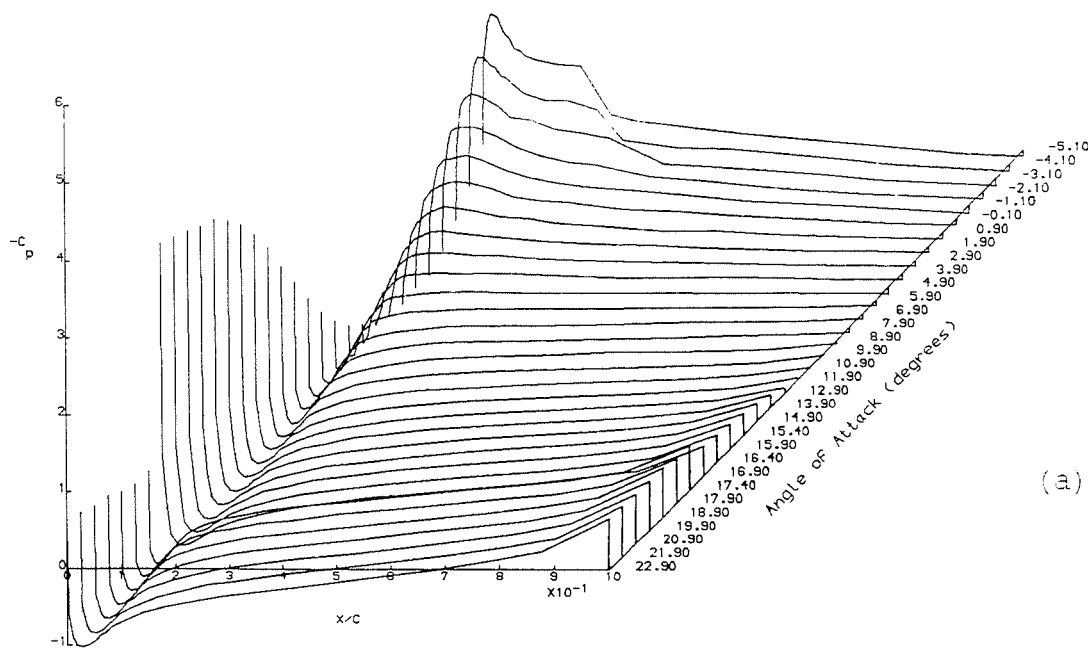


Figure 4.1.4. 3-D Plots of  $C_p$  vs  $x/c$  vs  $\alpha$  for the Lower (a) and Upper (b) Surface of a NACA-4415 Aerofoil Section and  $Re=125,000$ .

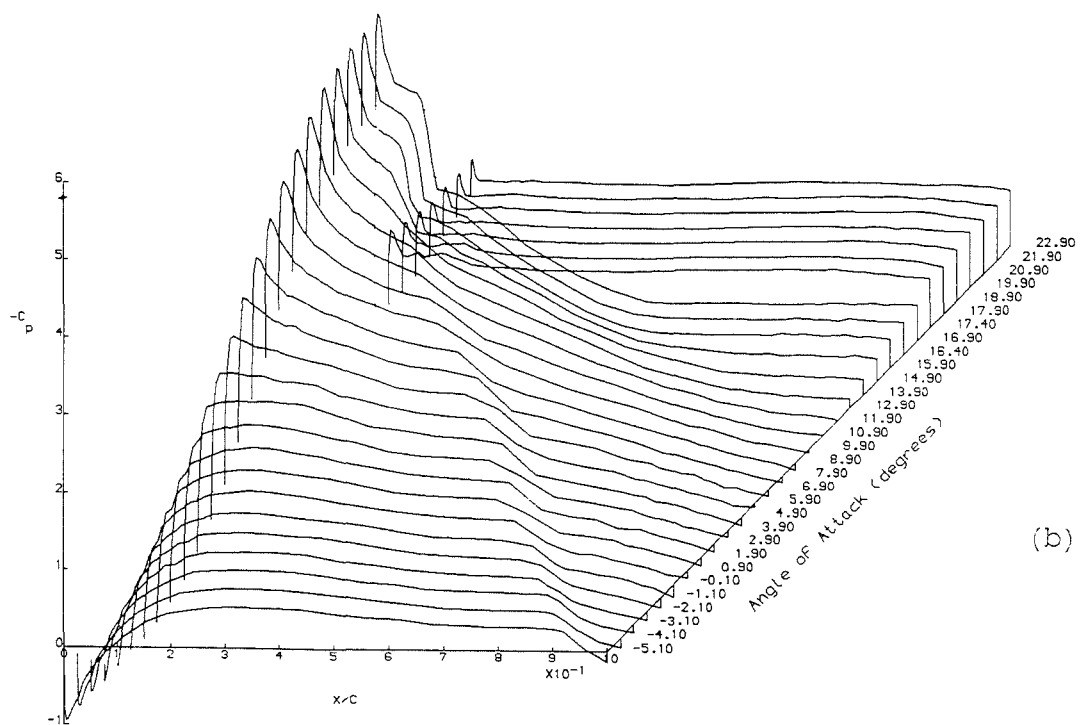
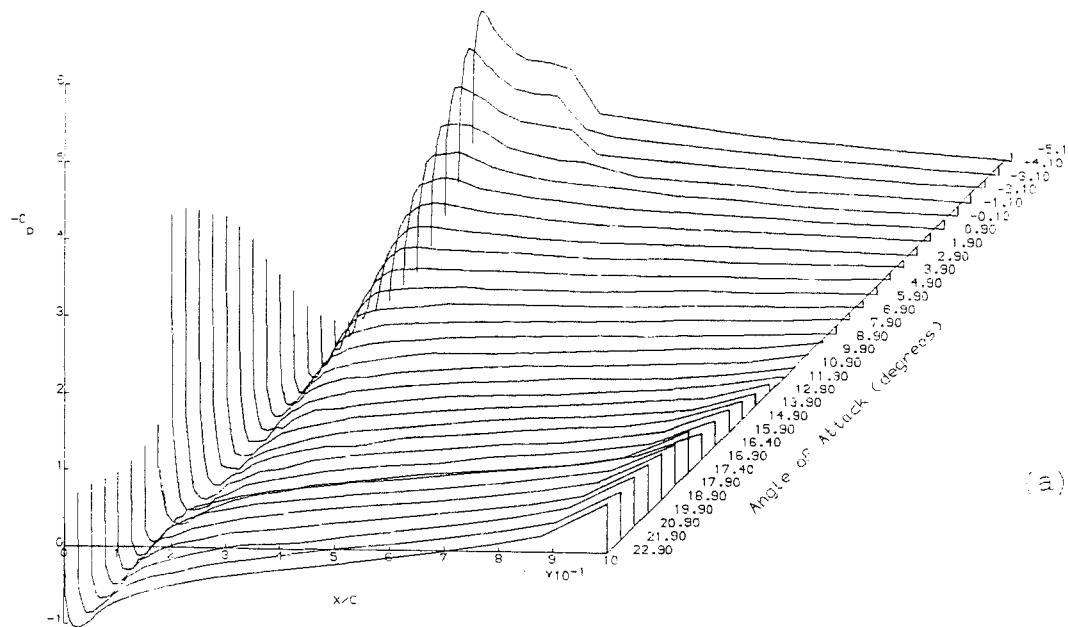


Figure 4.1.5. 3-D Plots of  $C_p$  vs  $x/c$  vs  $\alpha$  for the Lower (a) and Upper (b) Surface of a NACA-4415 Aerofoil Section and  $Re=150,000$

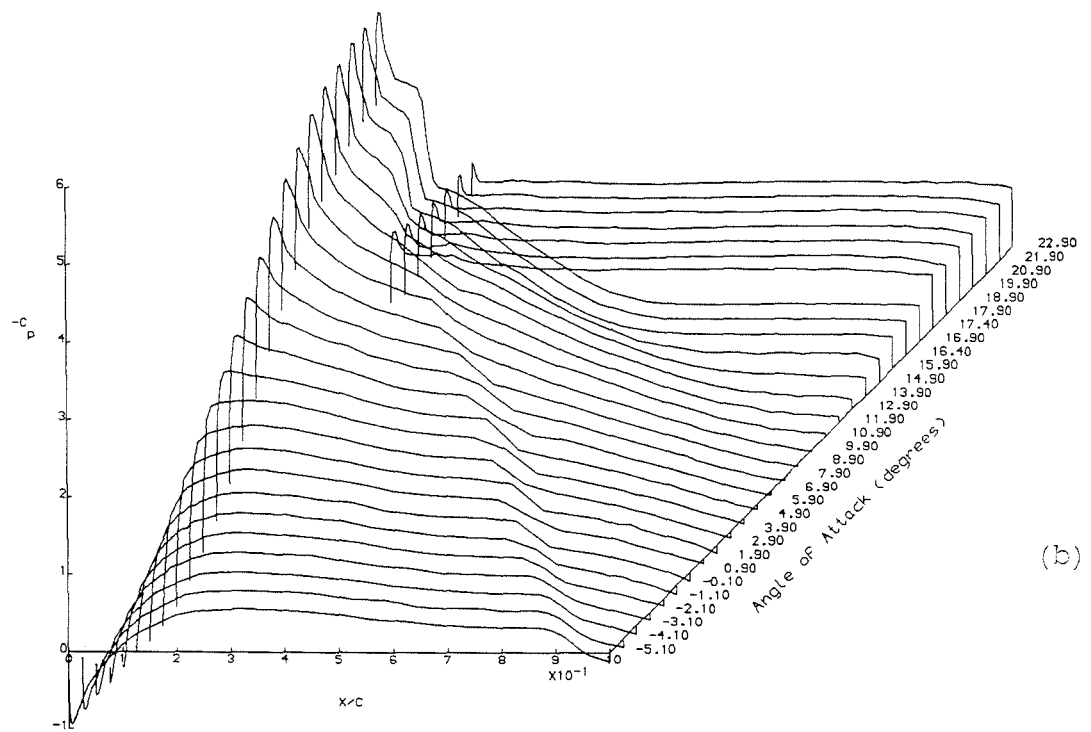
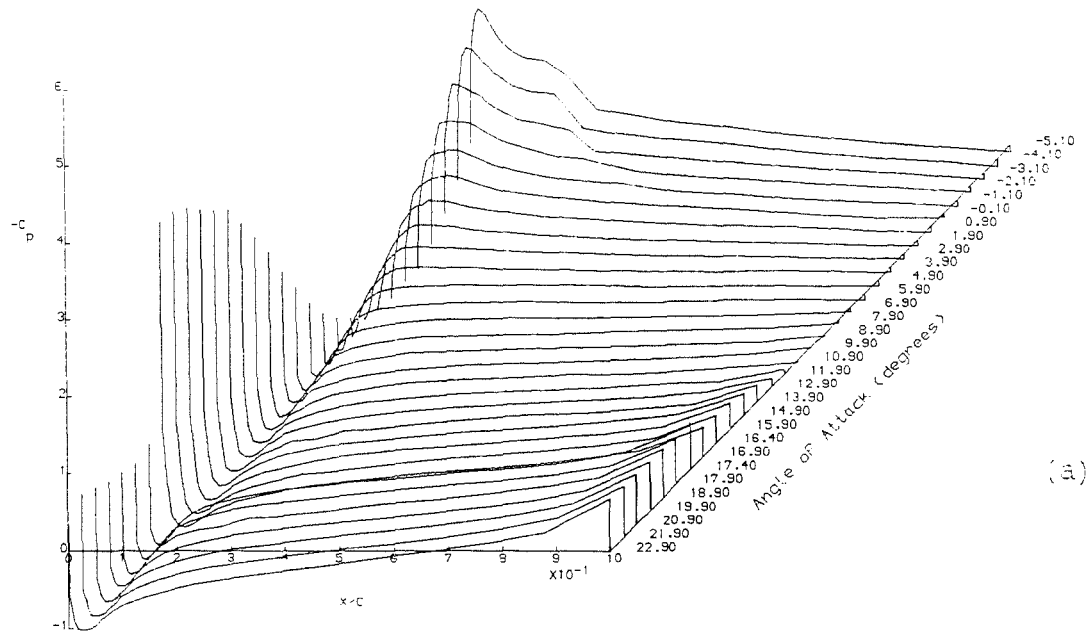


Figure 4.1.6. 3-D Plots of  $C_p$  vs  $x/c$  vs  $\alpha$  for the Lower (a) and Upper (b) Surface of a NACA-4415 Aerofoil Section and  $Re=175,000$ .

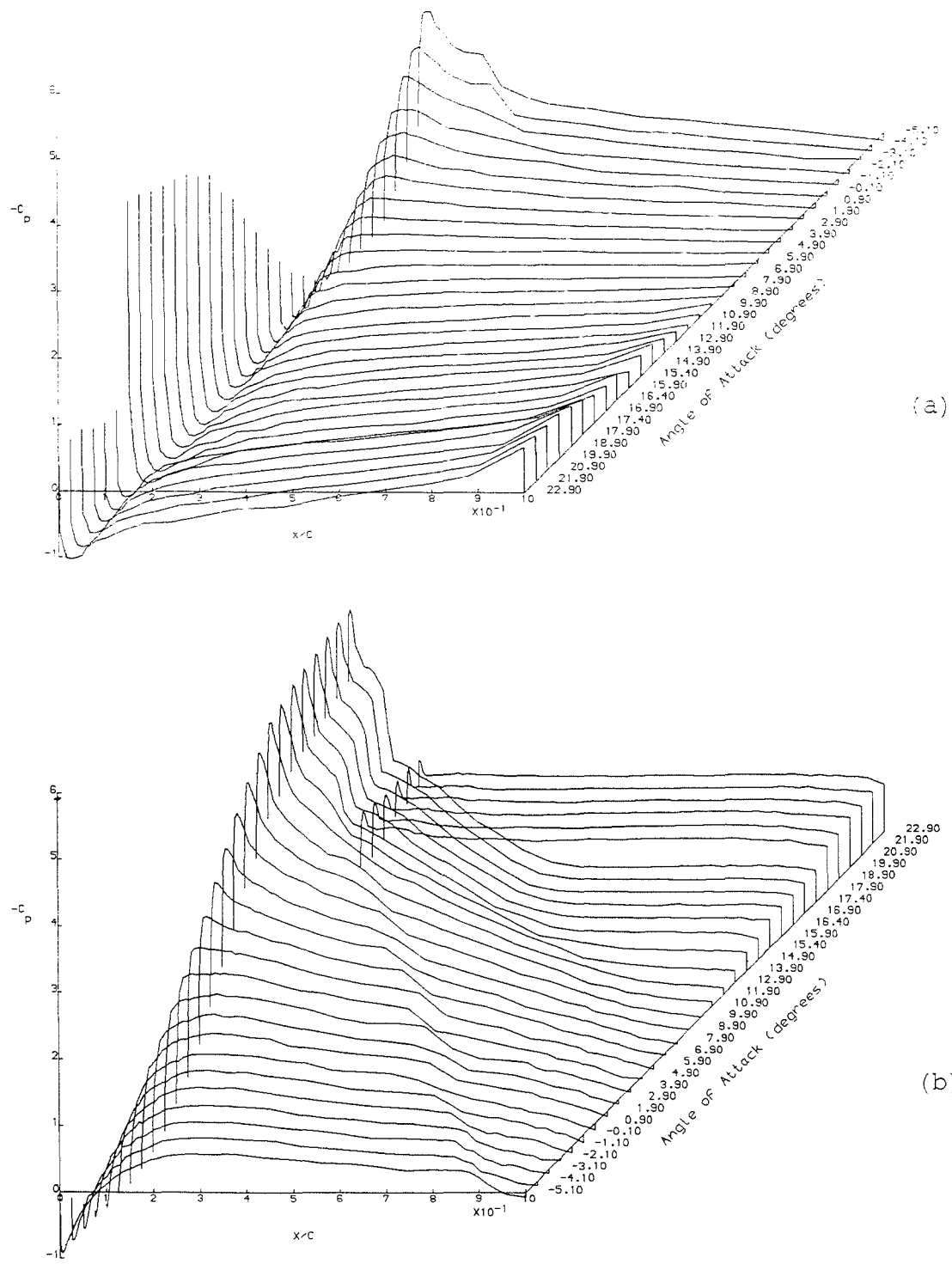


Figure 4.1.7. 3-D Plots of  $C_p$  vs  $x/c$  vs  $\alpha$  for the Lower (a) and Upper (b) Surface of a NACA-4415 Aerofoil Section and  $Re=200,000$ .

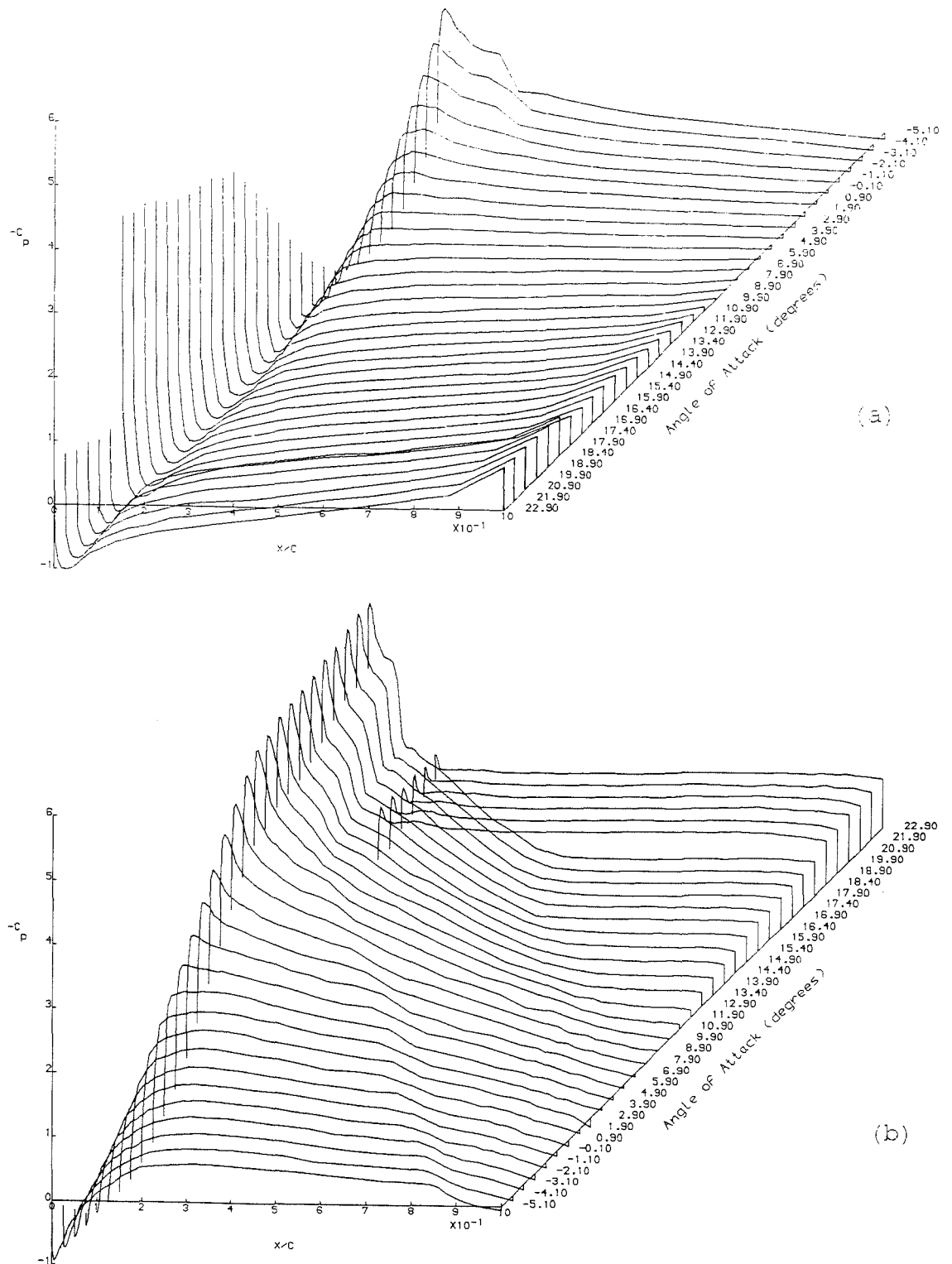


Figure 4.1.8. 3-D Plots of  $C_p$  vs  $x/c$  vs  $\alpha$  for the Lower (a) and Upper (b) Surface of a NACA-4415 Aerofoil Section and  $Re=250,000$ .

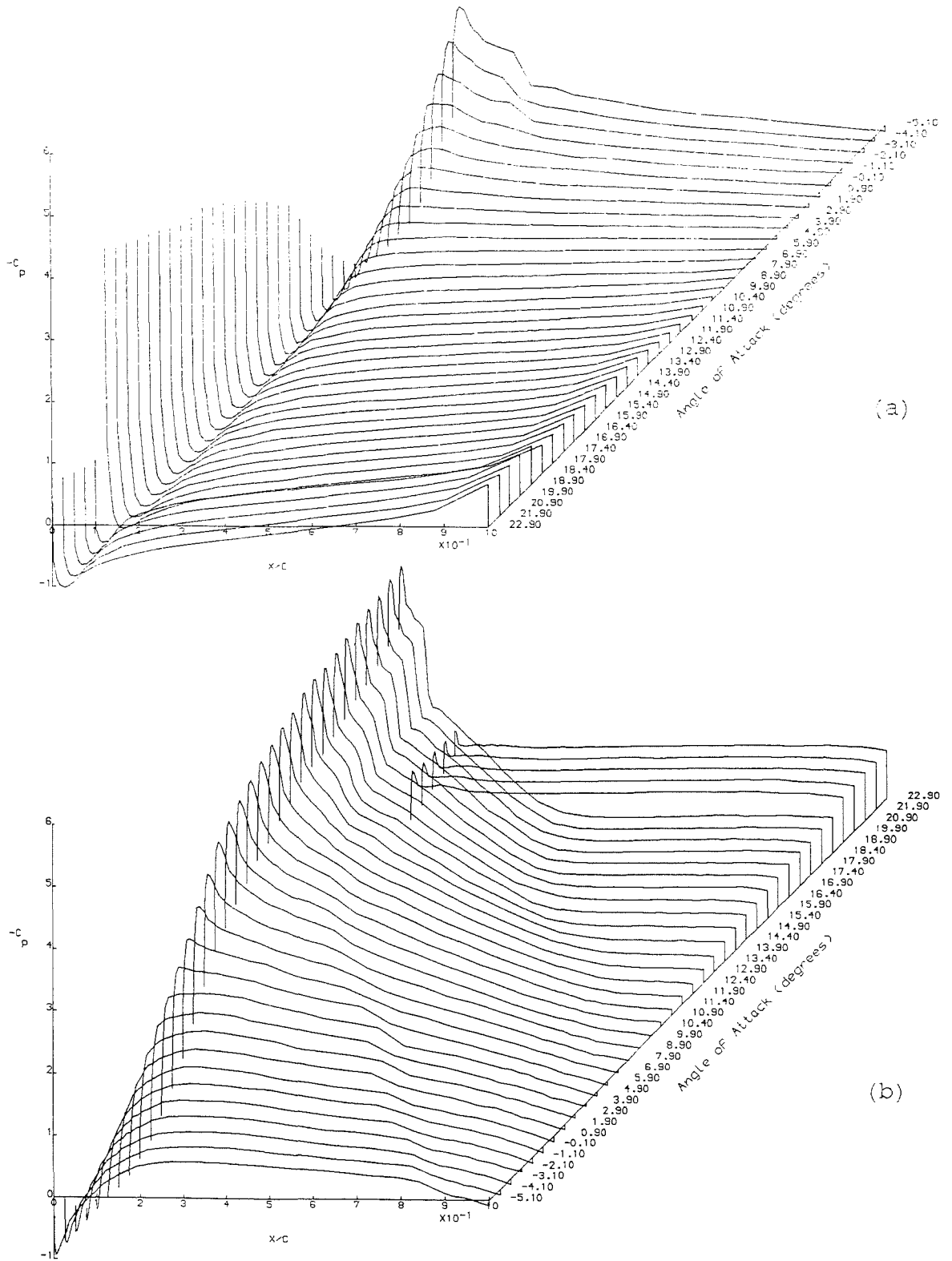


Figure 4.1.9. 3-D Plots of  $C_p$  vs  $x/c$  vs  $\alpha$  for the Lower (a) and Upper (b) Surface of a NACA-4415 Aerofoil Section and  $Re=300,000$ .

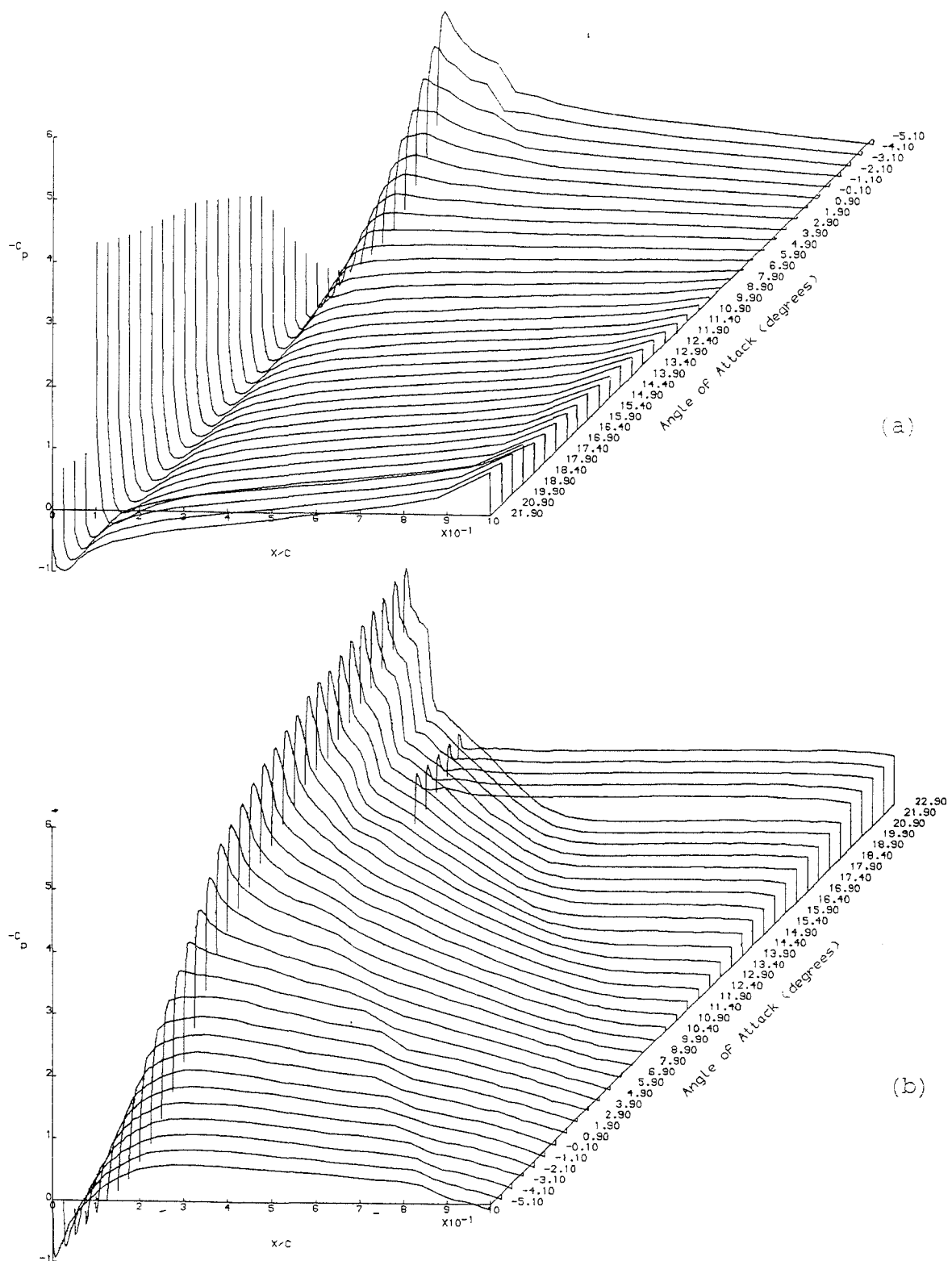


Figure 4.1.10. 3-D Plots of  $C_p$  vs  $x/c$  vs  $\alpha$  for the Lower (a) and Upper (b) Surface of a NACA-4415 Aerofoil Section and  $Re=350,000$ .

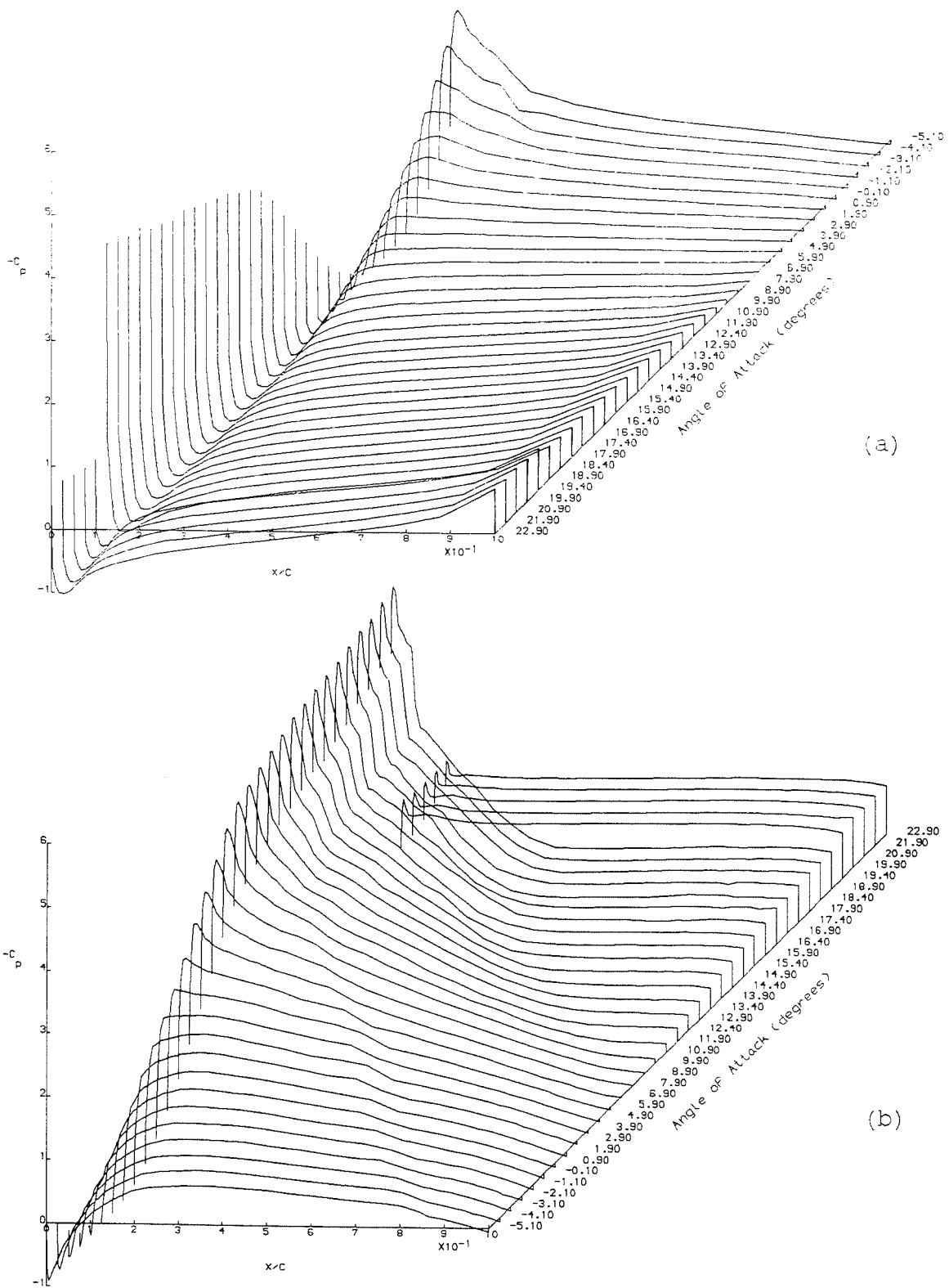


Figure 4.1.11. 3-D Plots of  $C_p$  vs  $x/c$  vs  $\alpha$  for the Lower (a) and Upper (b) Surface of a NACA-4415 Aerofoil Section and  $Re=400,000$ .

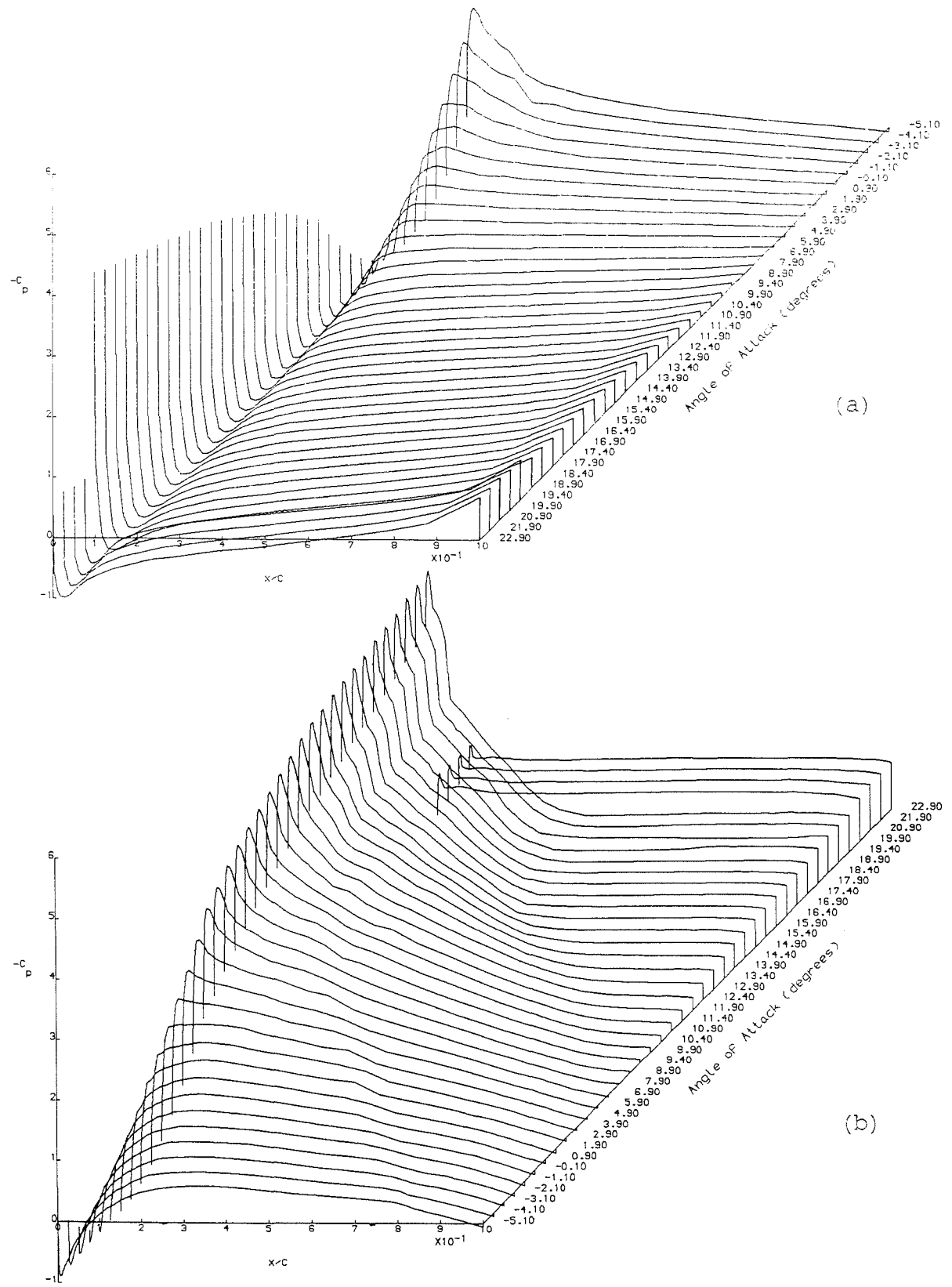


Figure 4.1.12. 3-D Plots of  $C_p$  vs  $x/c$  vs  $\alpha$  for the Lower (a) and Upper (b) Surface of a NACA-4415 Aerofoil Section and  $Re=450,000$ .

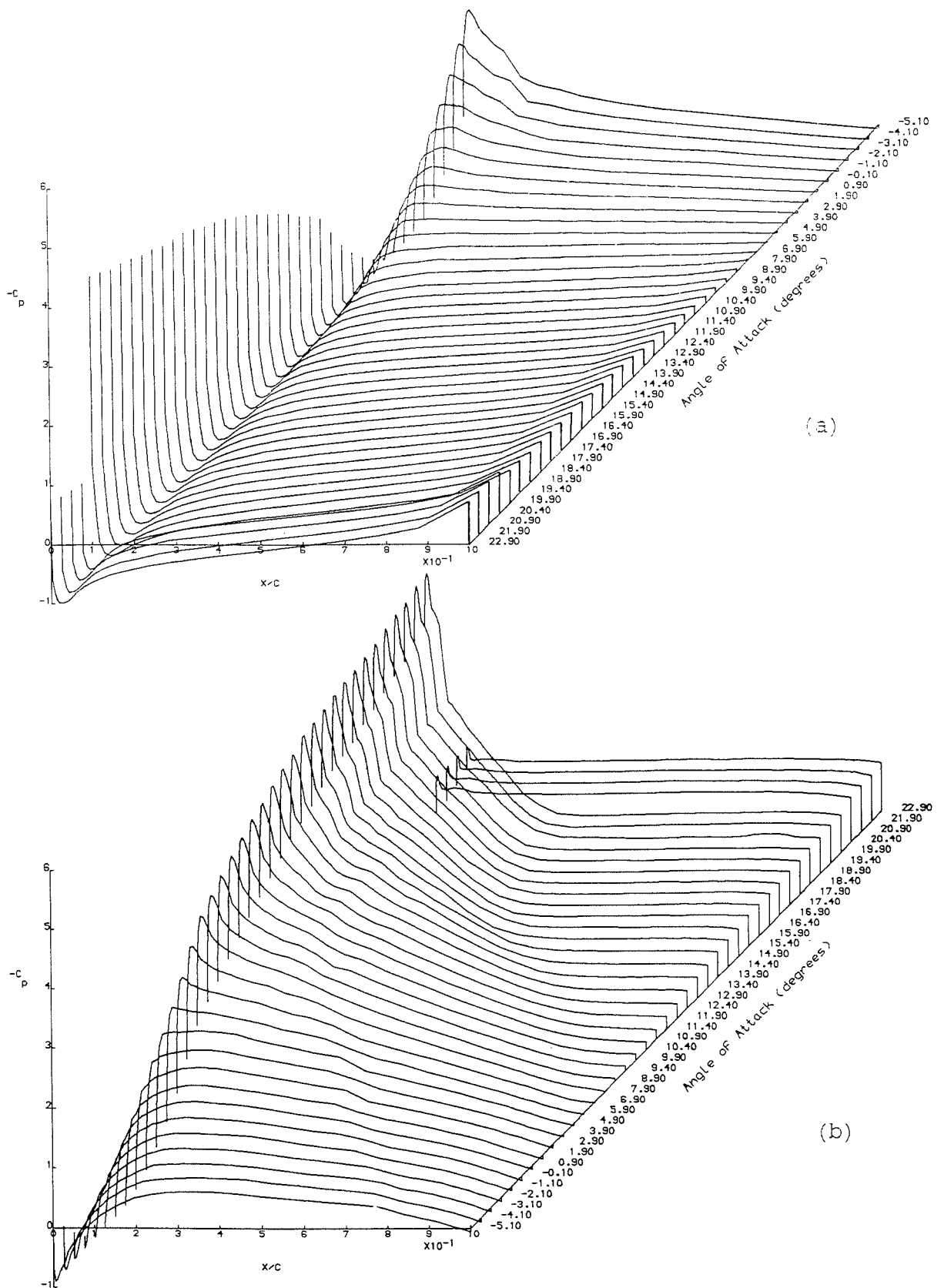


Figure 4.1.13. 3-D Plots of  $C_p$  vs  $x/c$  vs  $\alpha$  for the Lower (a) and Upper (b) Surface of a NACA-4415 Aerofoil Section and  $Re=500,000$ .

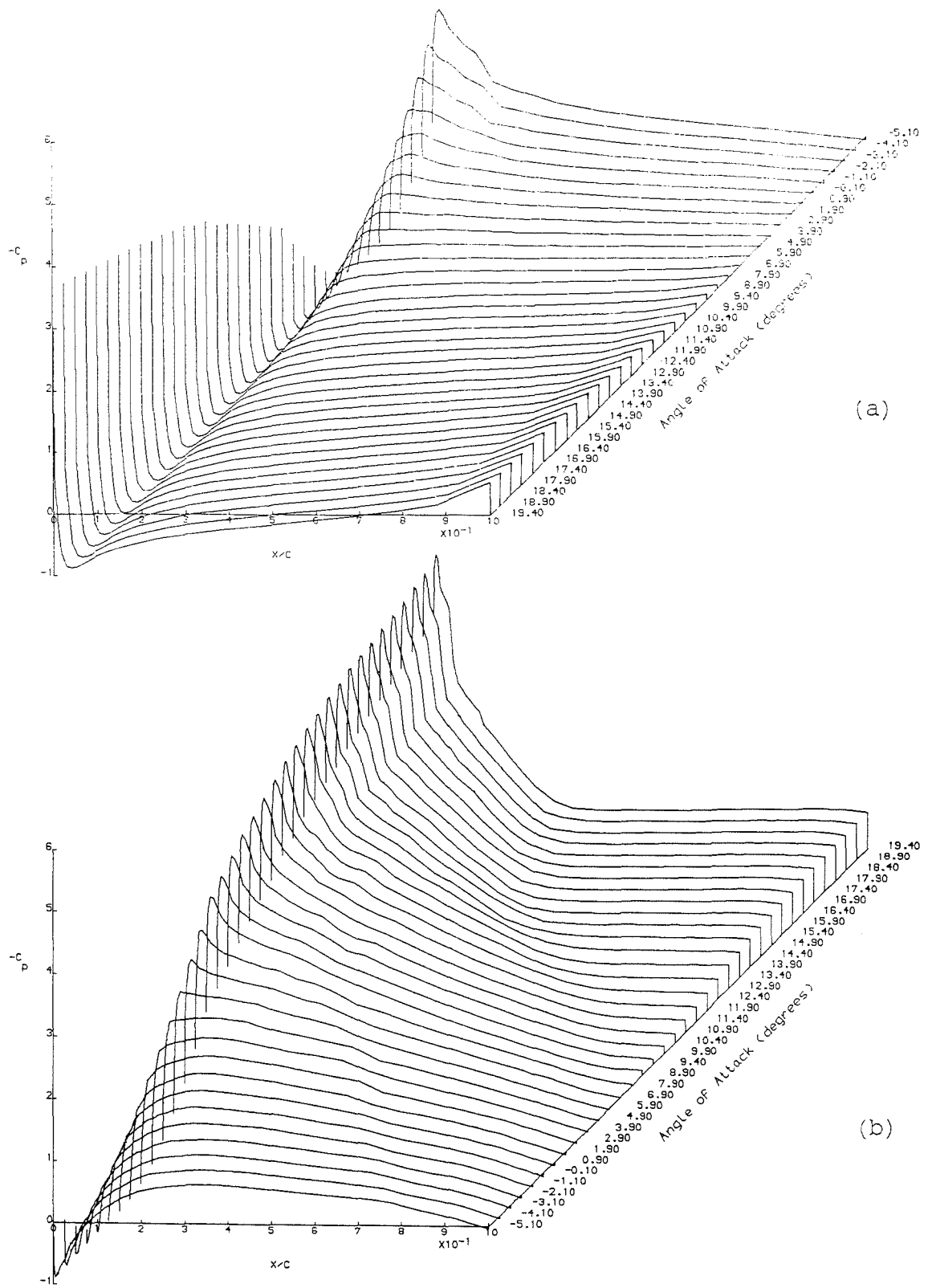


Figure 4.1.14. 3-D Plots of  $C_p$  vs  $x/c$  vs  $\alpha$  for the Lower (a) and Upper (b) Surface of a NACA-4415 Aerofoil Section and  $Re=550,000$ .

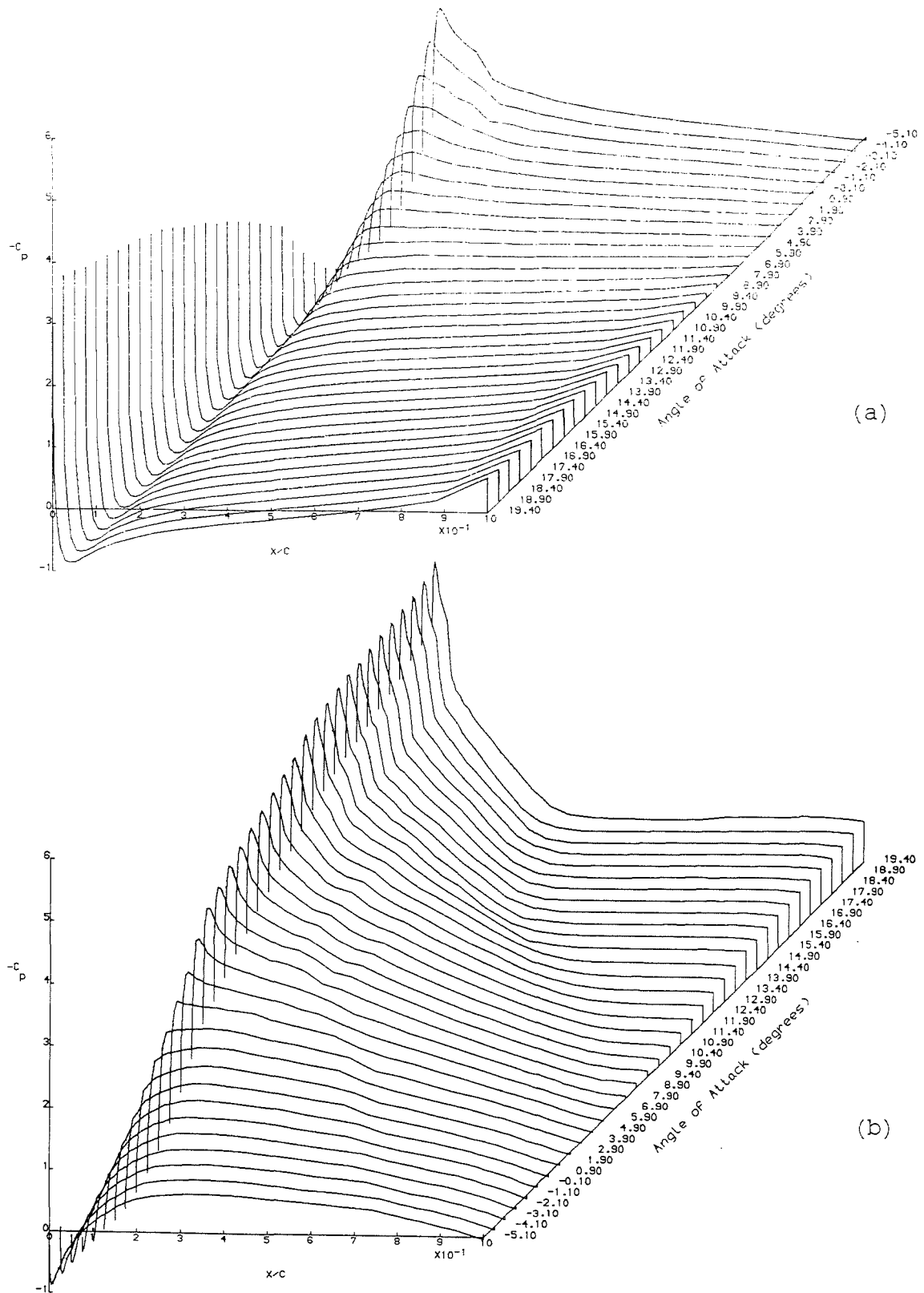


Figure 4.1.15. 3-D Plots of  $C_p$  vs  $x/c$  vs  $\alpha$  for the Lower (a) and Upper (b) Surface of a NACA-4415 Aerofoil Section and  $Re=600,000$ .

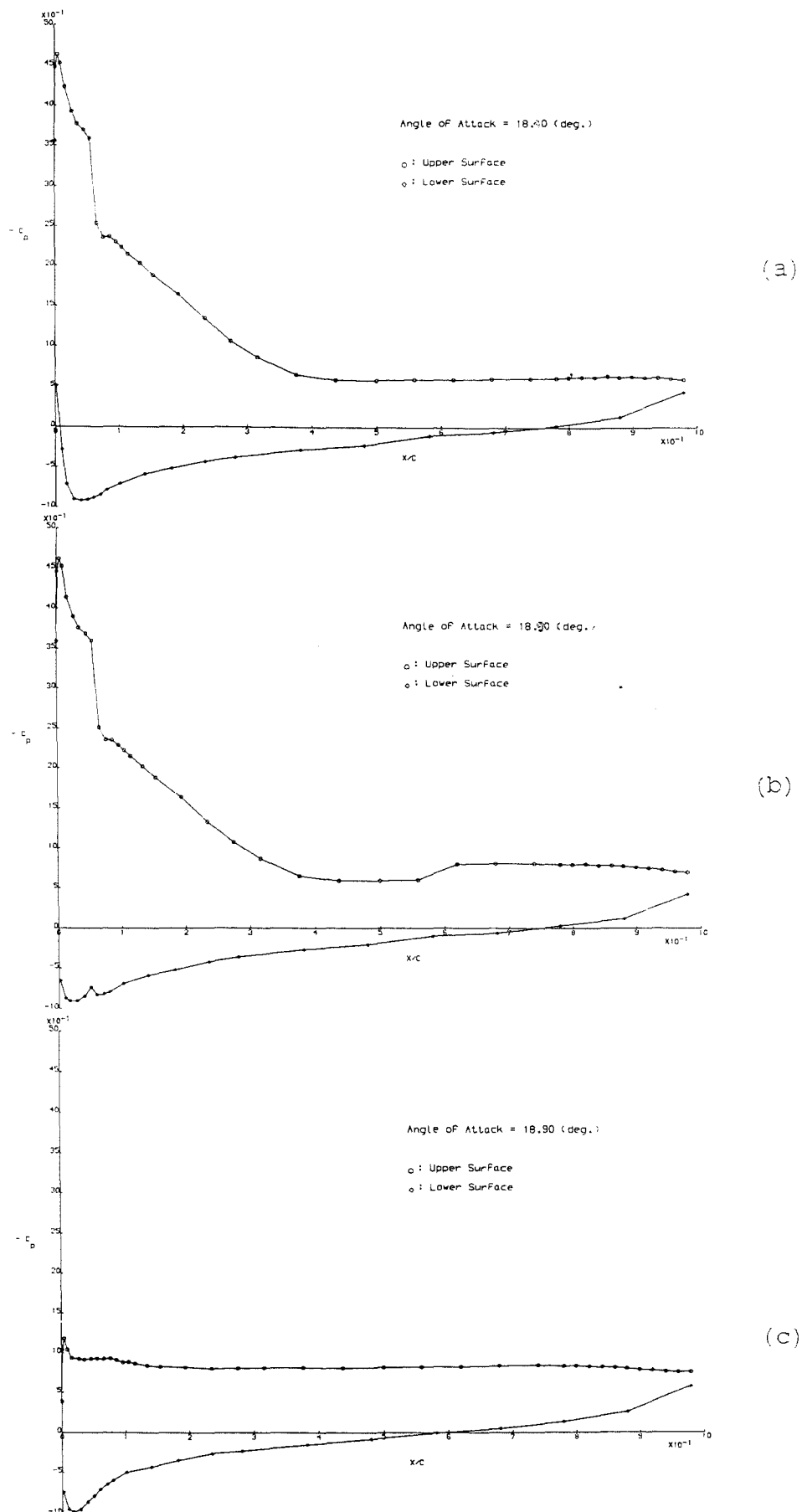


Figure 4.1.16. Pressure Distribution Around the NACA-4415 Aerofoil Section at Incidences Close to Complete Stall ( $Re=300,000$ ).

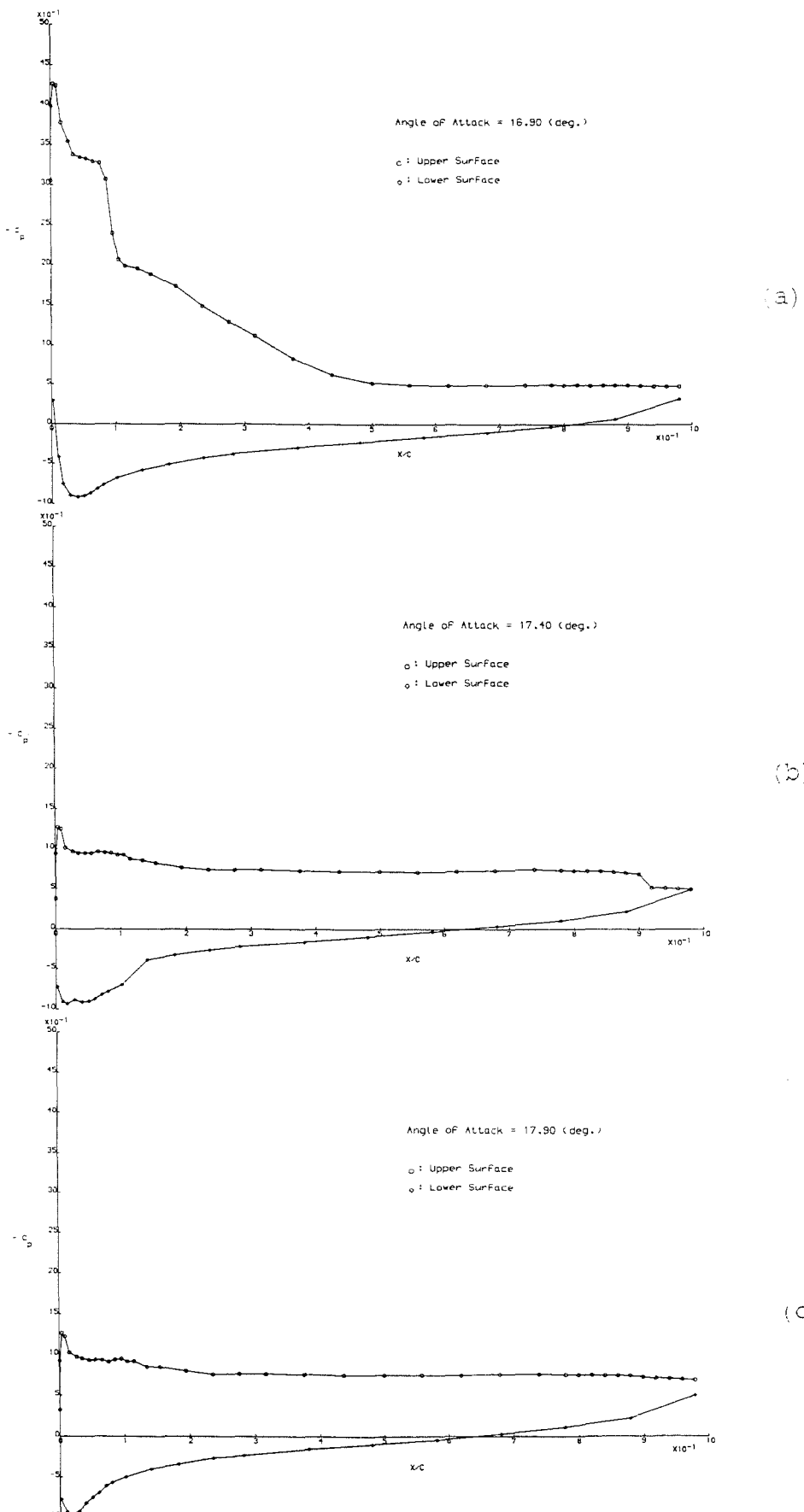


Figure 4.1.17. Pressure Distribution Around the NACA-4415 Aerofoil Section at Incidences Close to Complete Stall ( $Re=175,000$ ).

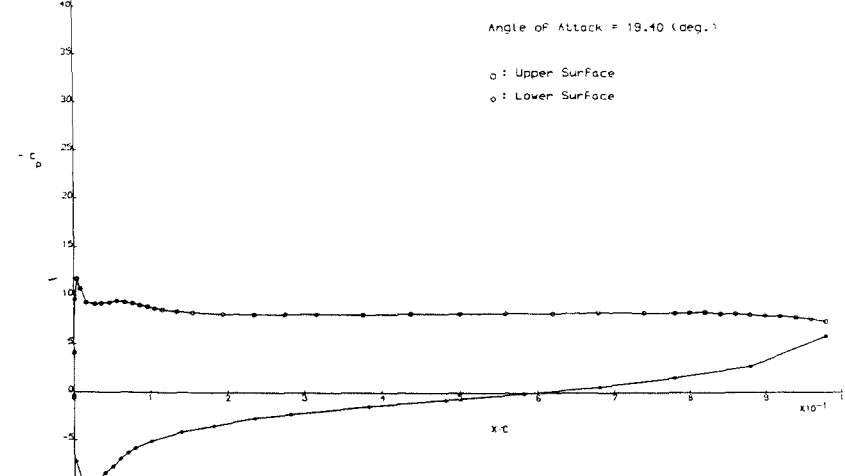
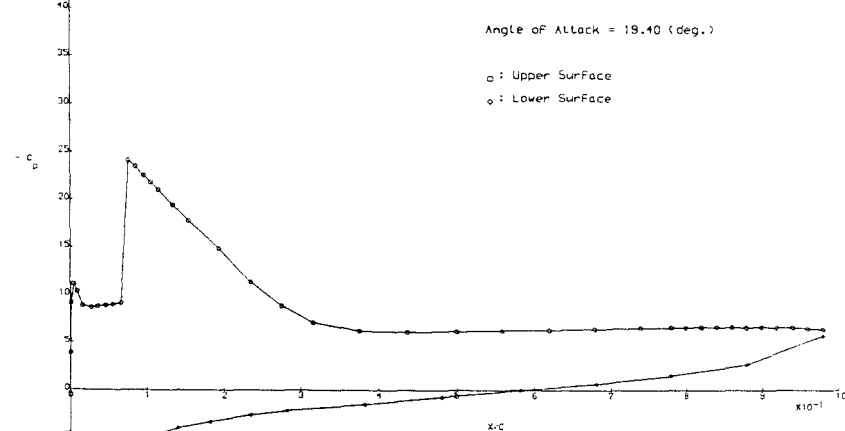
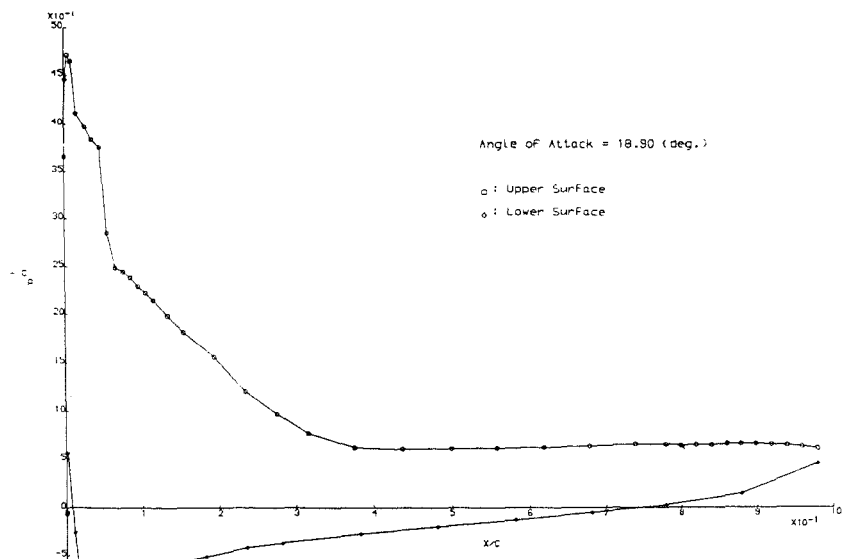


Figure 4.1.18. Pressure Distribution Around the NACA-4415 Aerofoil Section at Incidences Close to Complete Stall ( $Re=400,000$ ).

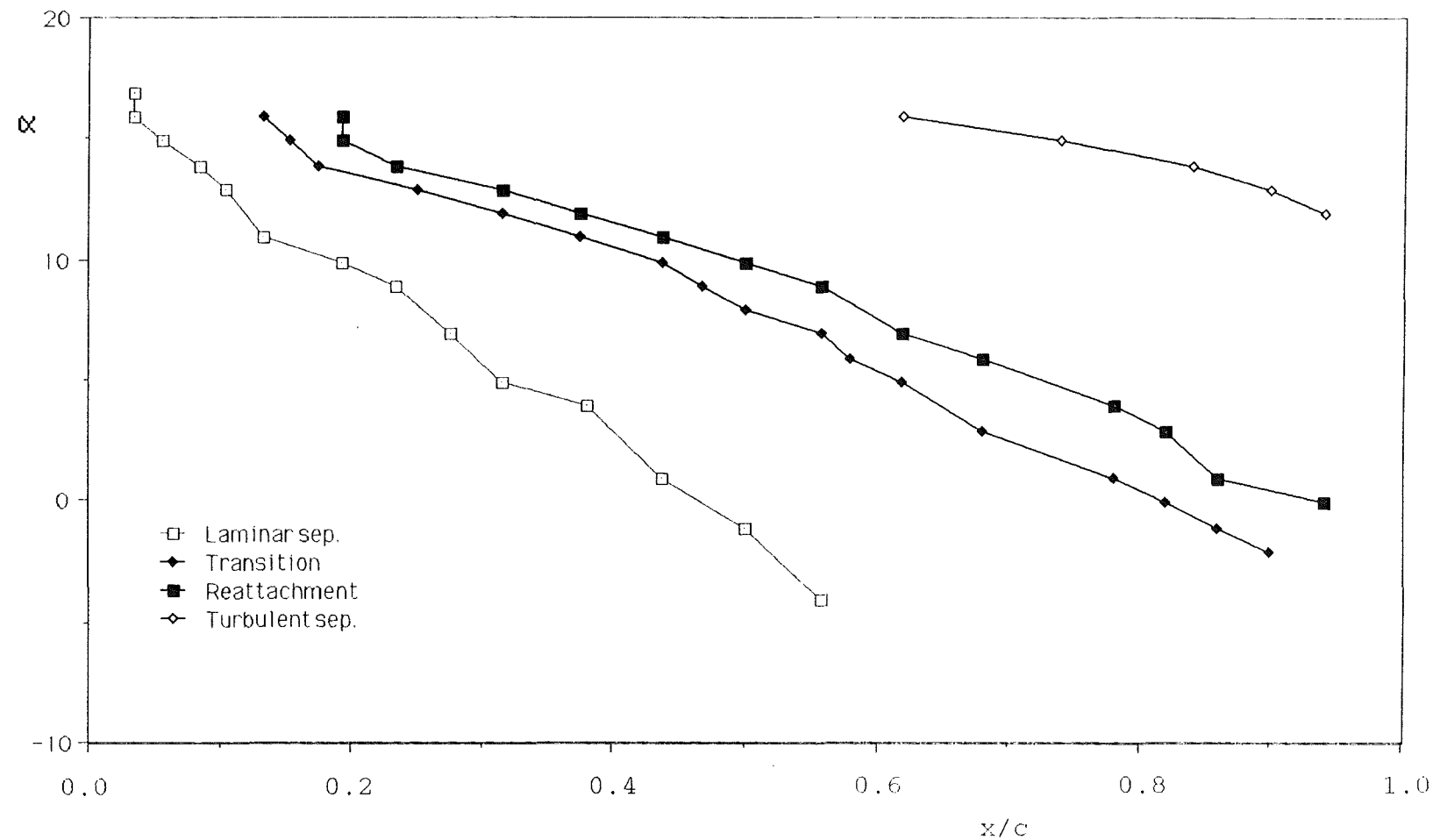


Figure 4.1.19. Locations of the Various Boundary Layer Phenomena on the Upper Surface of the NACA-4415 Aerofoil Section at  $Re=75,000$ .

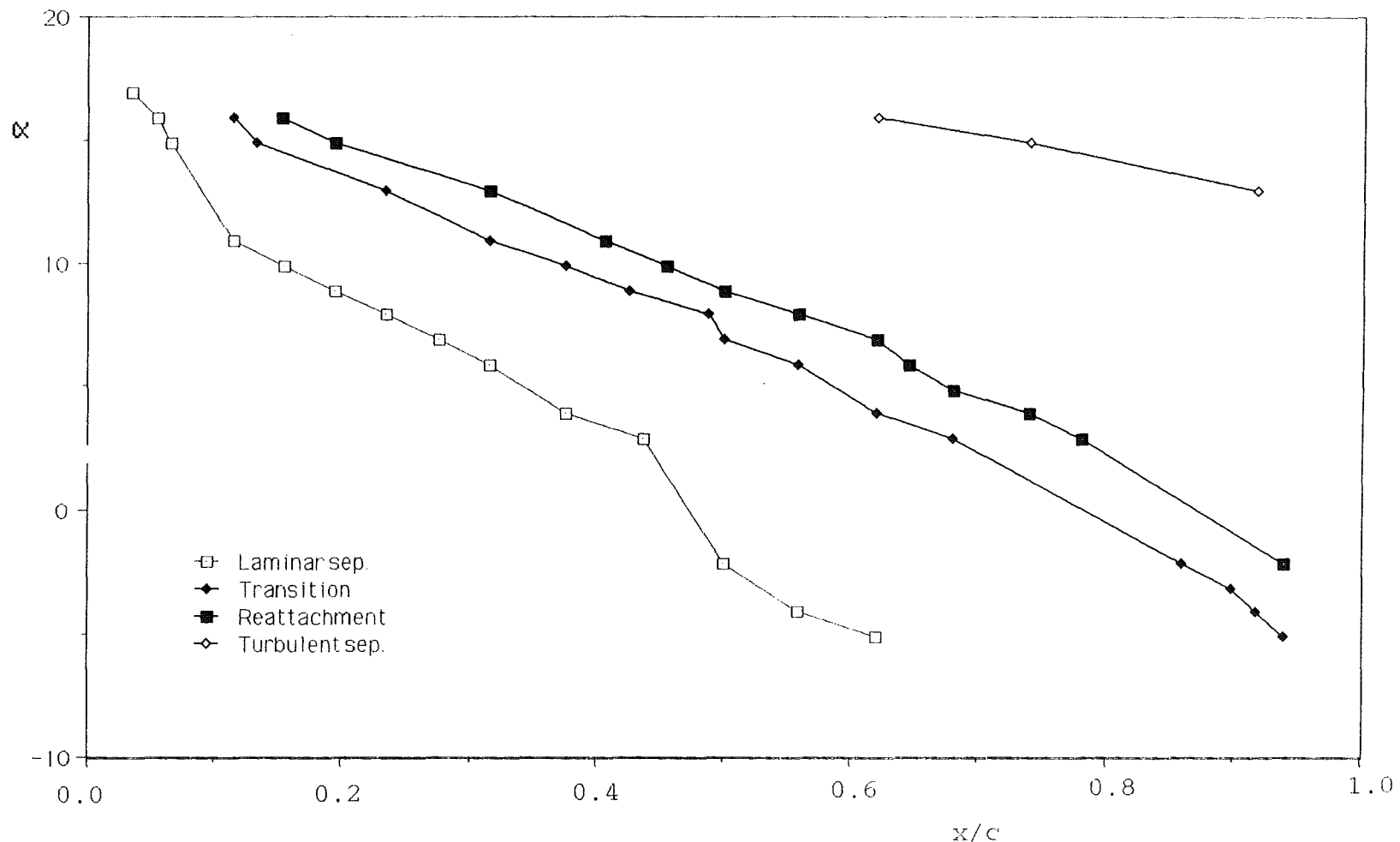


Figure 4.1.20. Locations of the Various Boundary Layer Phenomena on the Upper Surface of the NACA-4415 Aerofoil Section at  $Re=100,000$ .

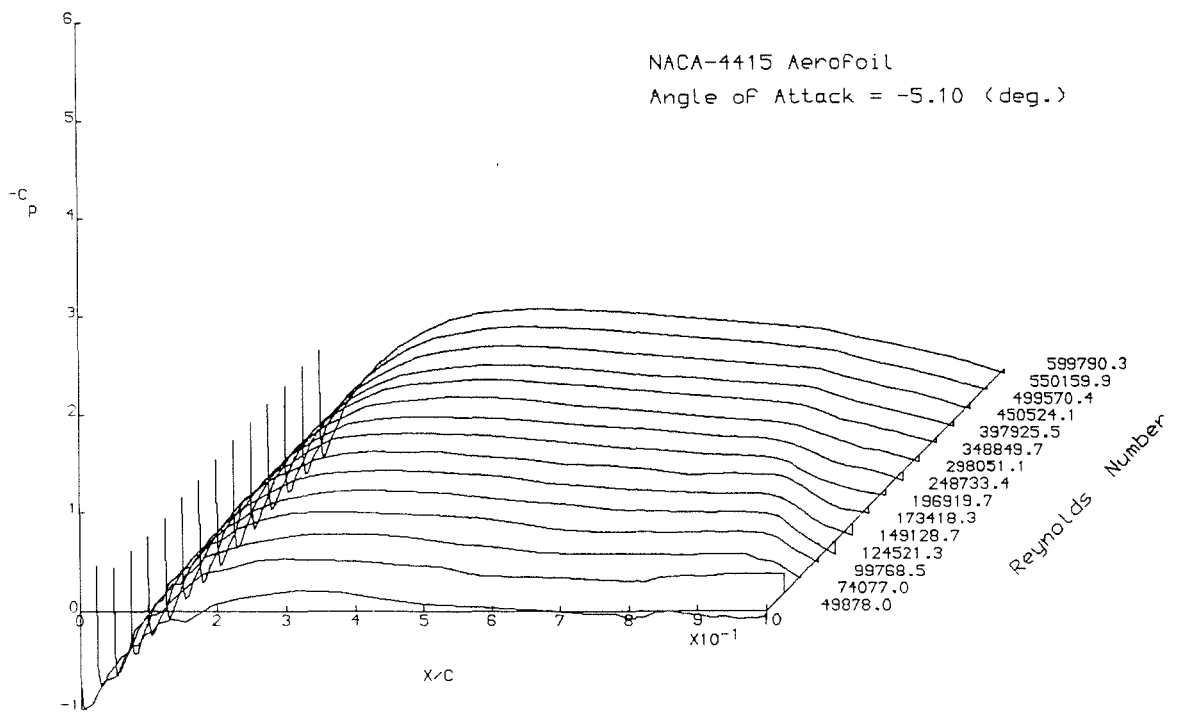


Figure 4.2.1. 3-D Plot of Cp vs x/c vs Re for the Upper Surface of the NACA-4415 Aerofoil Section at  $\alpha = -5.10^\circ$ .

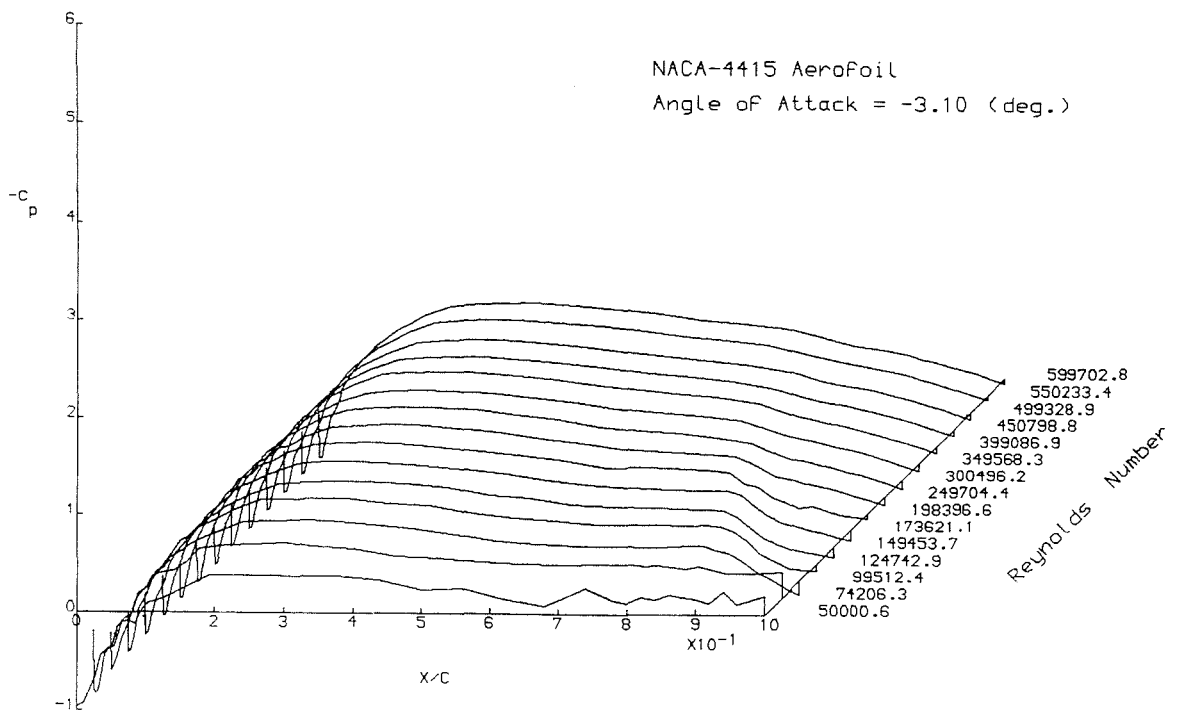


Figure 4.2.2. 3-D Plot of Cp vs x/c vs Re for the Upper Surface of the NACA-4415 Aerofoil Section at  $\alpha = -3.10^\circ$ .

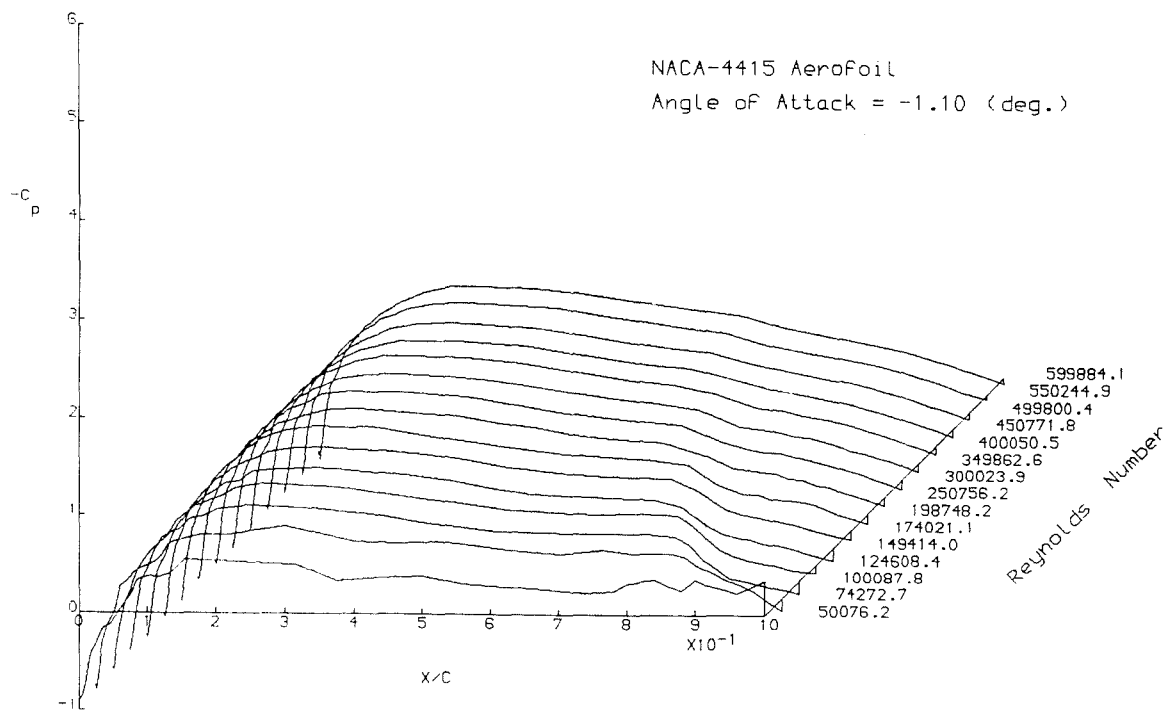


Figure 4.2.3. 3-D Plot of  $C_p$  vs  $x/c$  vs  $Re$  for the Upper Surface of the NACA-4415 Aerofoil Section at  $\alpha = -1.10^\circ$ .

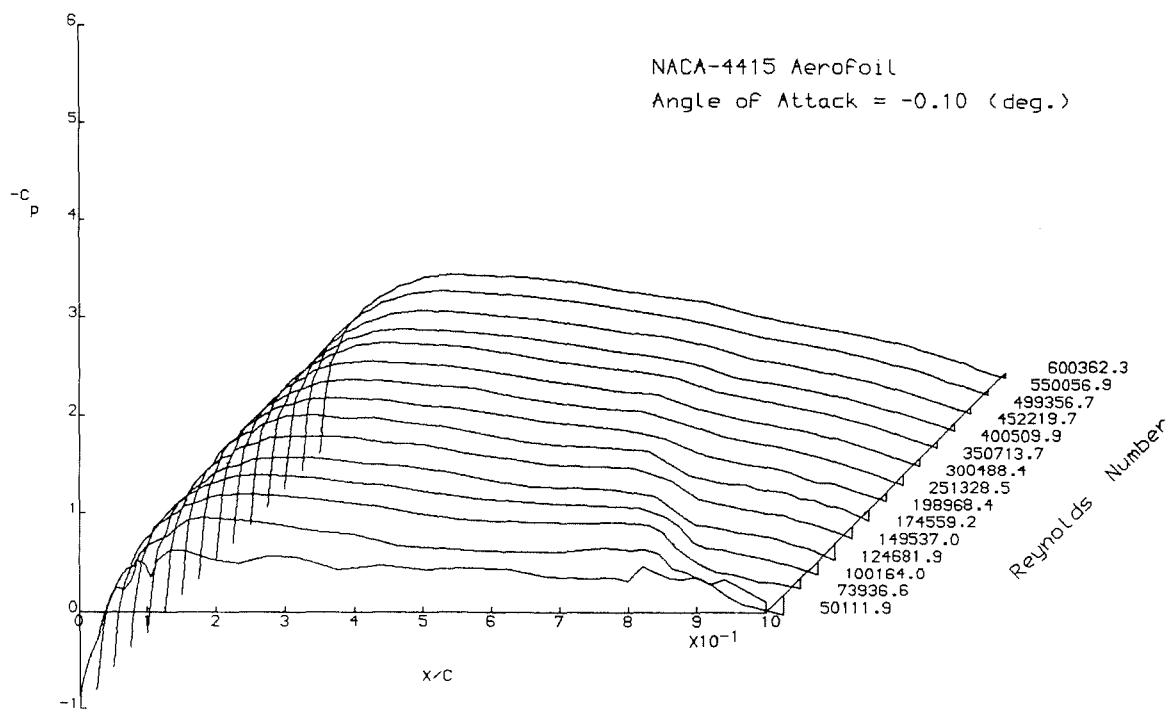


Figure 4.2.4. 3-D Plot of  $C_p$  vs  $x/c$  vs  $Re$  for the Upper Surface of the NACA-4415 Aerofoil Section at  $\alpha = -0.10^\circ$ .

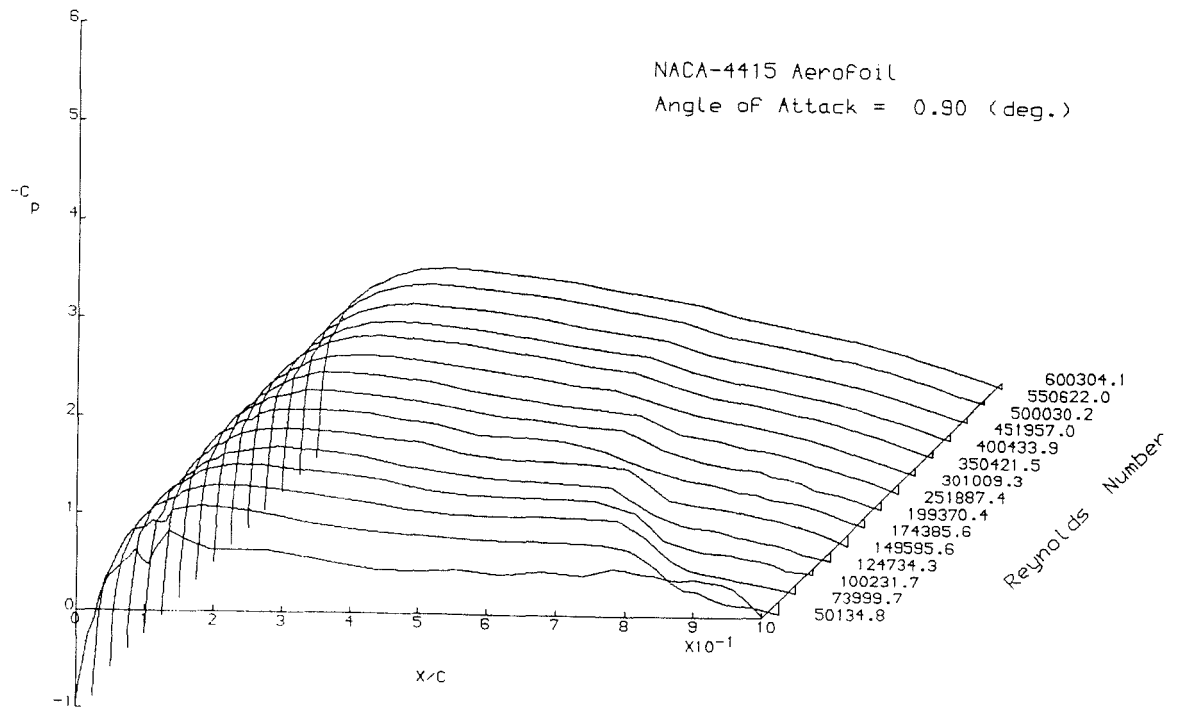


Figure 4.2.5. 3-D Plot of Cp vs x/c vs Re for the Upper Surface of the NACA-4415 Aerofoil Section at  $\alpha = 0.90^\circ$ .

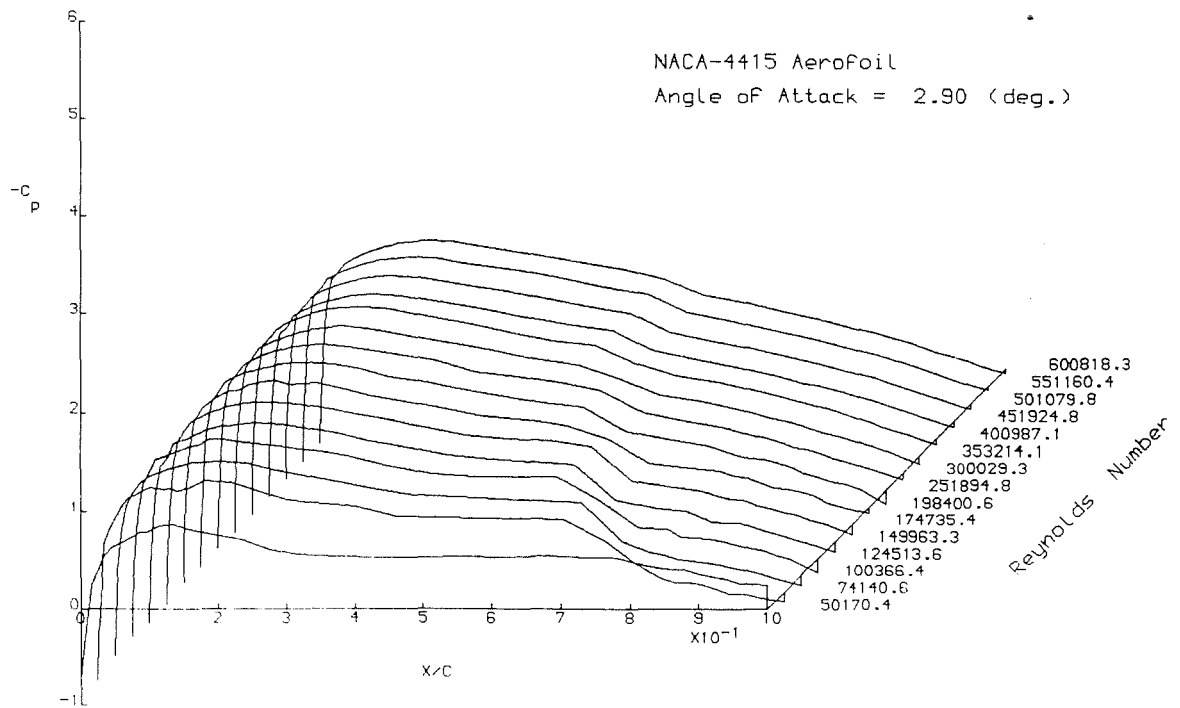


Figure 4.2.6. 3-D Plot of Cp vs x/c vs Re for the Upper Surface of the NACA-4415 Aerofoil Section at  $\alpha = 2.90^\circ$ .

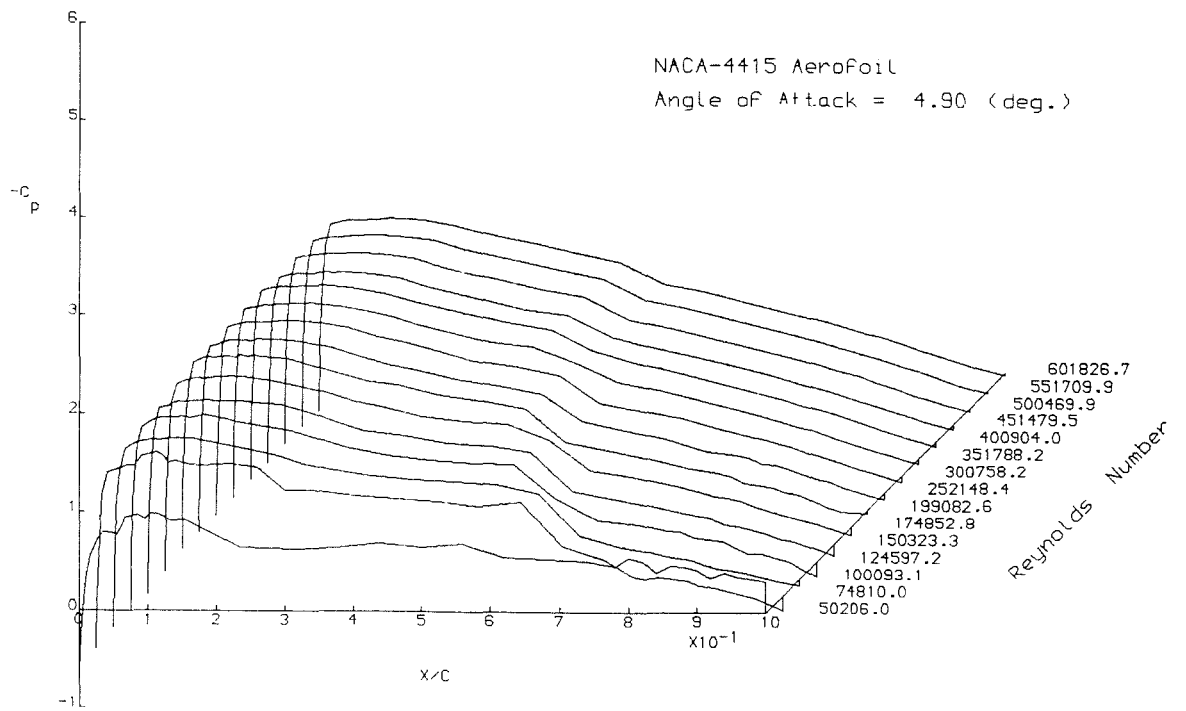


Figure 4.2.7. 3-D Plot of  $C_p$  vs  $x/c$  vs  $Re$  for the Upper Surface of the NACA-4415 Aerofoil Section at  $\alpha = 4.90^\circ$ .

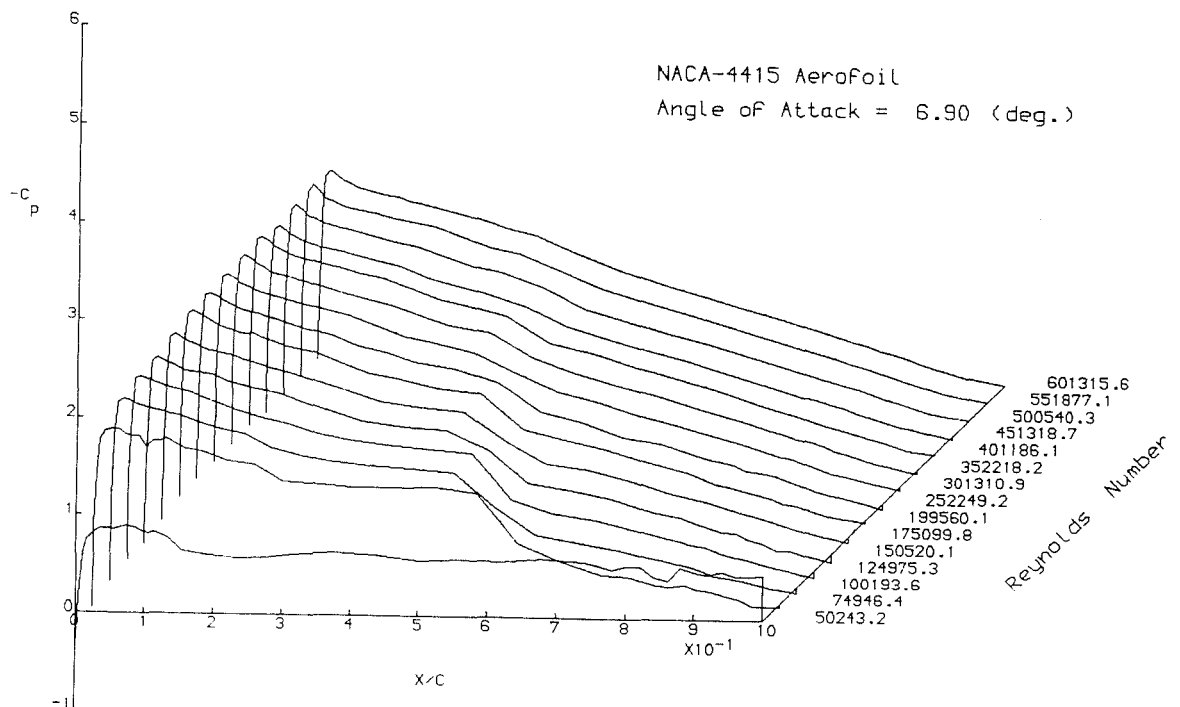


Figure 4.2.8. 3-D Plot of  $C_p$  vs  $x/c$  vs  $Re$  for the Upper Surface of the NACA-4415 Aerofoil Section at  $\alpha = 6.90^\circ$ .

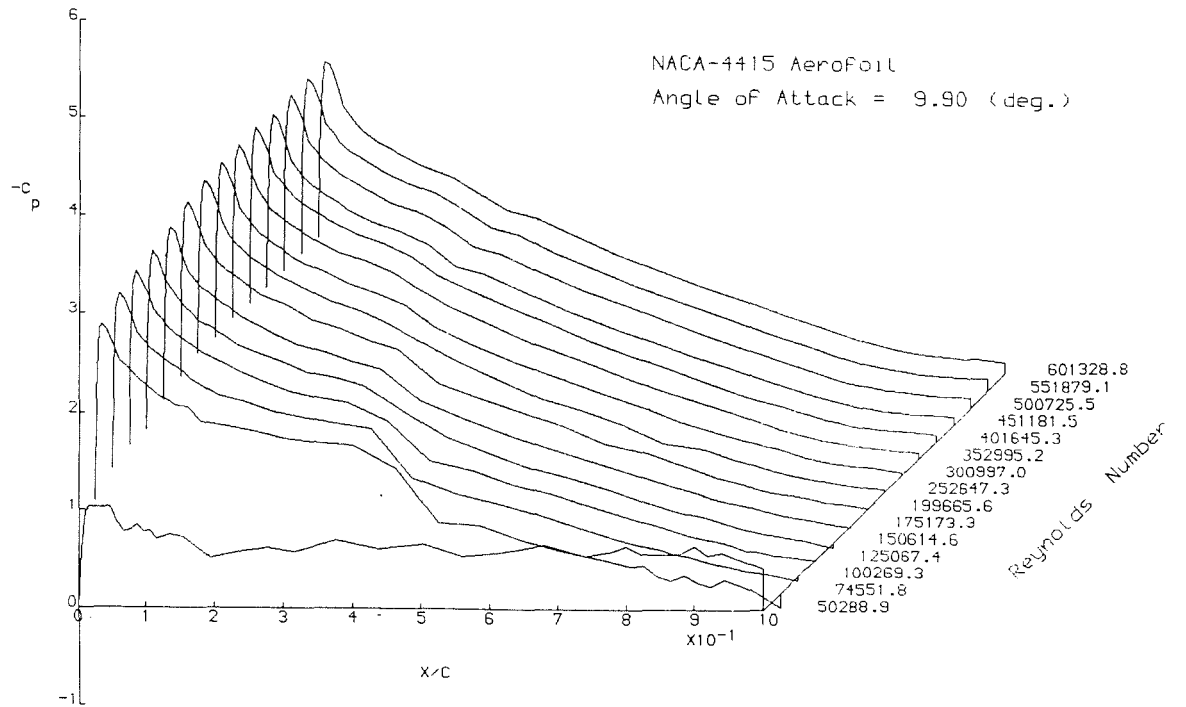


Figure 4.2.9. 3-D Plot of Cp vs x/c vs Re for the Upper Surface of the NACA-4415 Aerofoil Section at  $\alpha = 9.90^\circ$ .

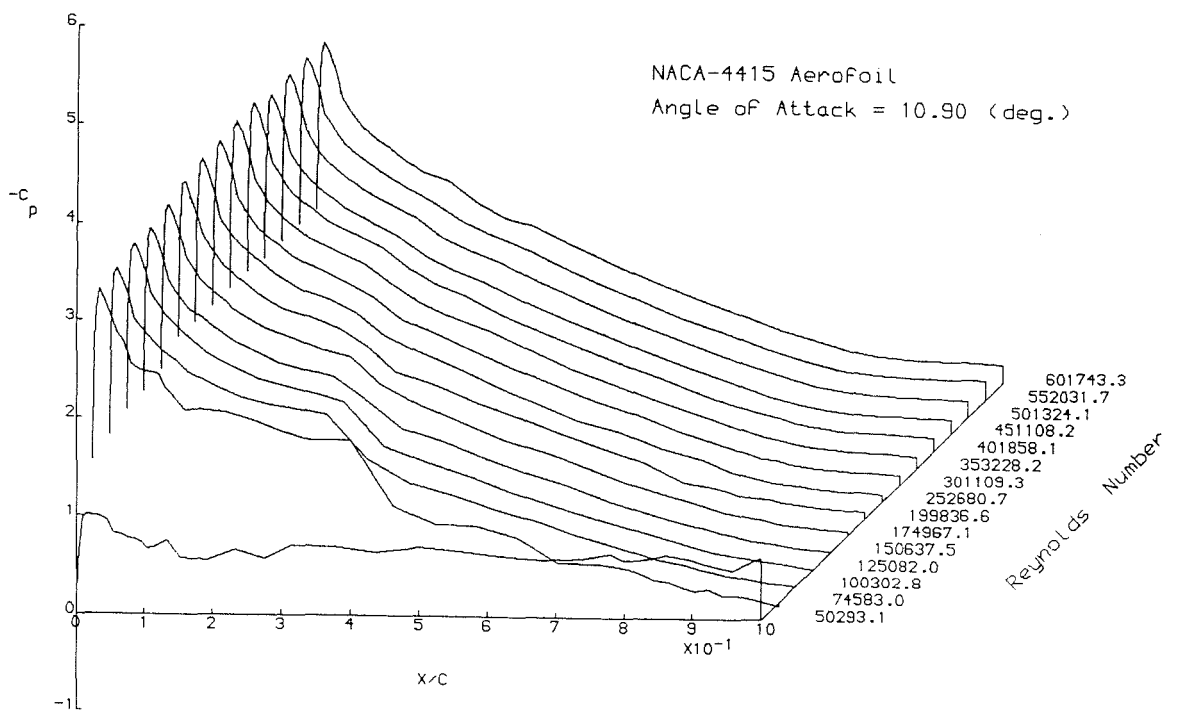


Figure 4.2.10. 3-D Plot of Cp vs x/c vs Re for the Upper Surface of the NACA-4415 Aerofoil Section at  $\alpha=10.90^\circ$ .

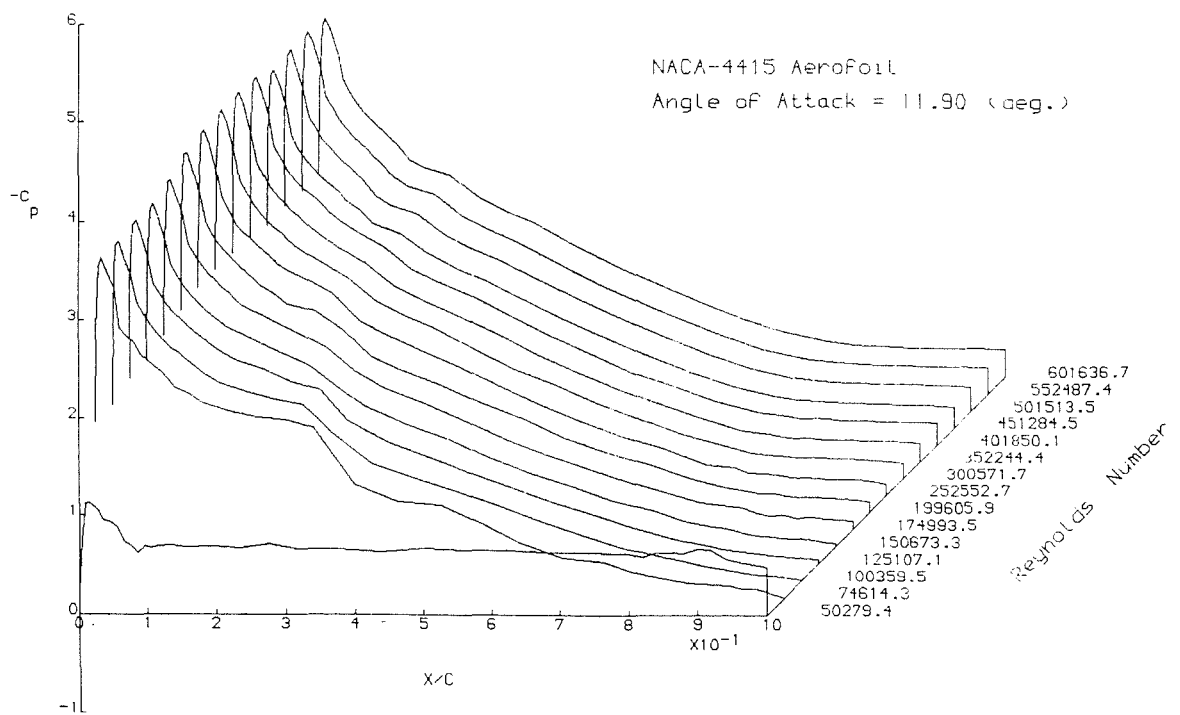


Figure 4.2.11. 3-D Plot of  $C_p$  vs  $x/c$  vs  $Re$  for the Upper Surface of the NACA-4415 Aerofoil Section at  $\alpha=11.90^\circ$ .

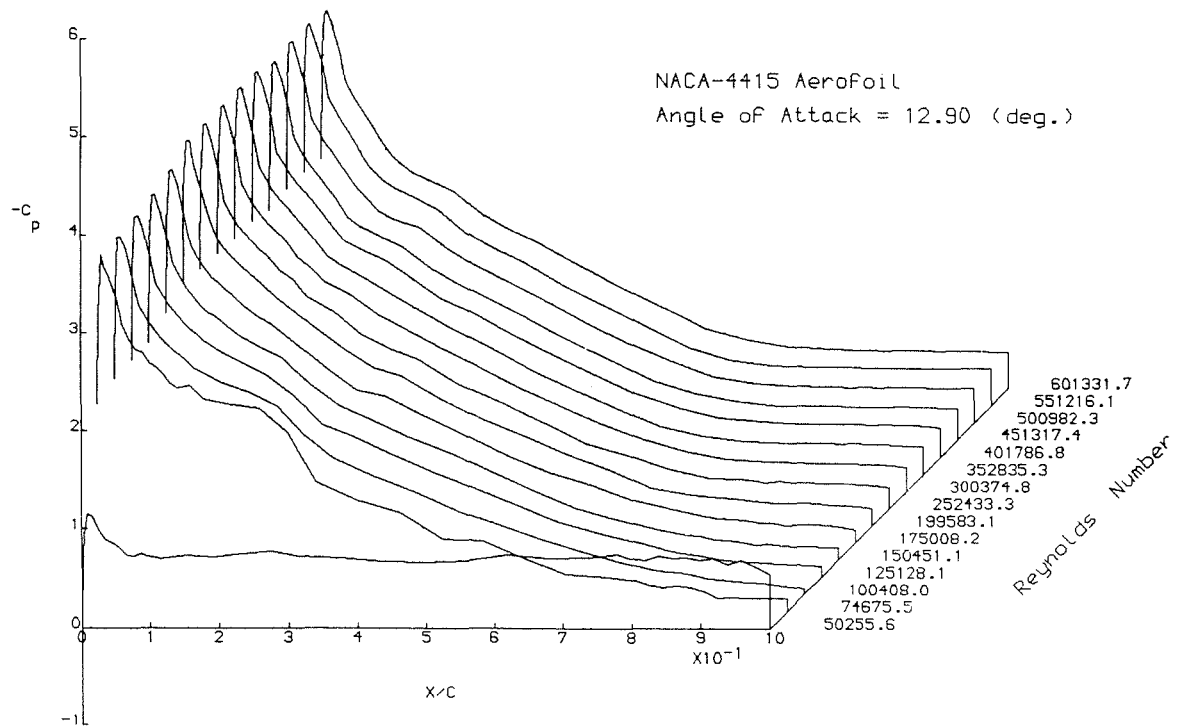


Figure 4.2.12. 3-D Plot of  $C_p$  vs  $x/c$  vs  $Re$  for the Upper Surface of the NACA-4415 Aerofoil Section at  $\alpha=12.90^\circ$ .

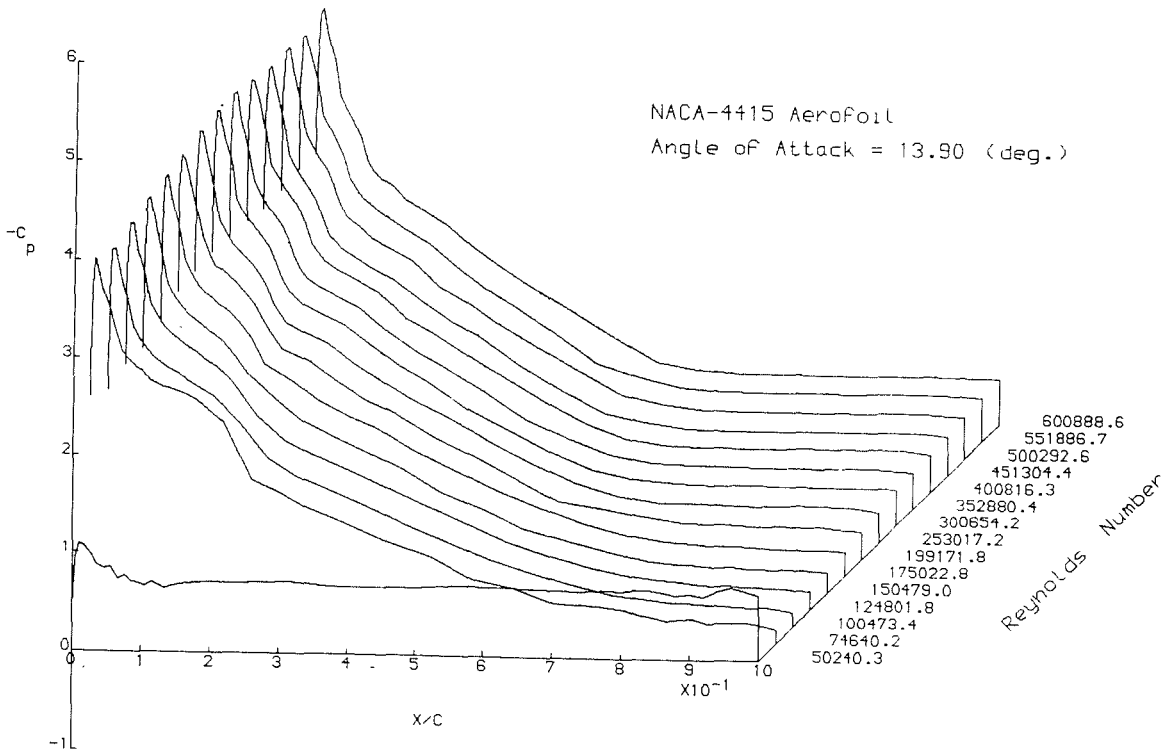


Figure 4.2.13. 3-D Plot of Cp vs x/c vs Re for the Upper Surface of the NACA-4415 Aerofoil Section at  $\alpha=13.90^\circ$ .

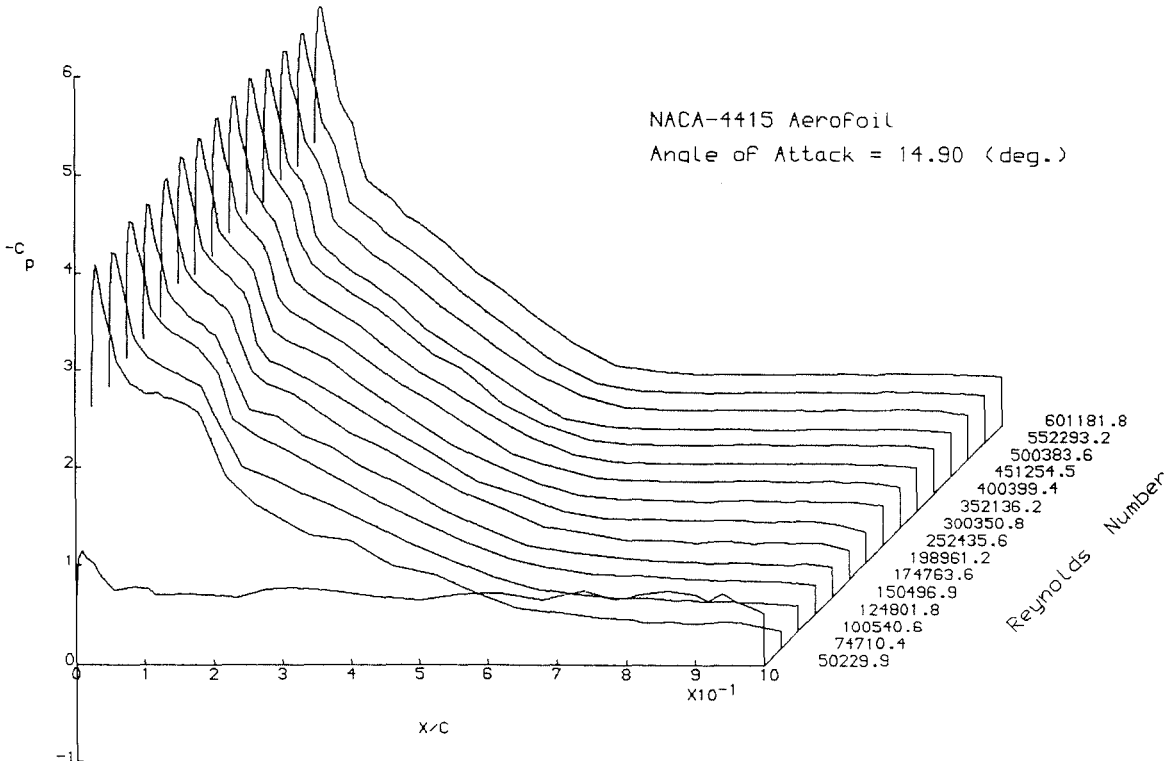


Figure 4.2.14. 3-D Plot of Cp vs x/c vs Re for the Upper Surface of the NACA-4415 Aerofoil Section at  $\alpha=14.90^\circ$ .

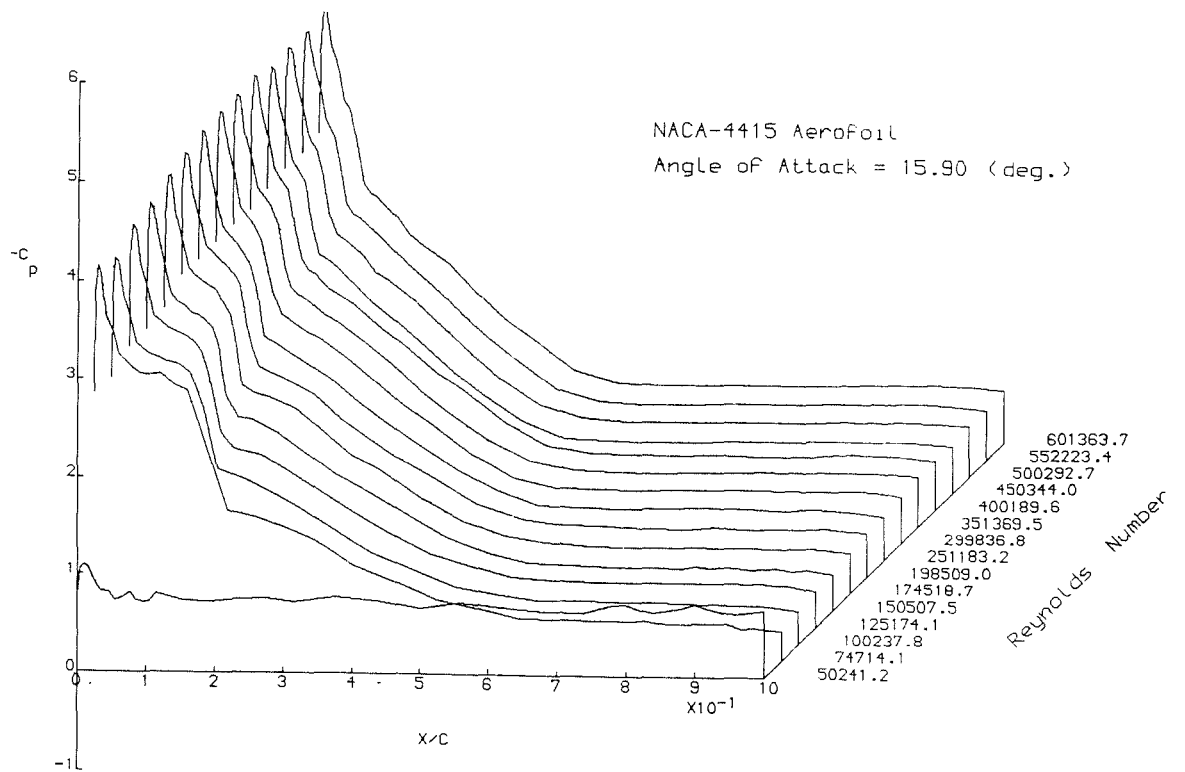


Figure 4.2.15. 3-D Plot of  $C_p$  vs  $x/c$  vs  $Re$  for the Upper Surface of the NACA-4415 Aerofoil Section at  $\alpha=15.90^\circ$ .

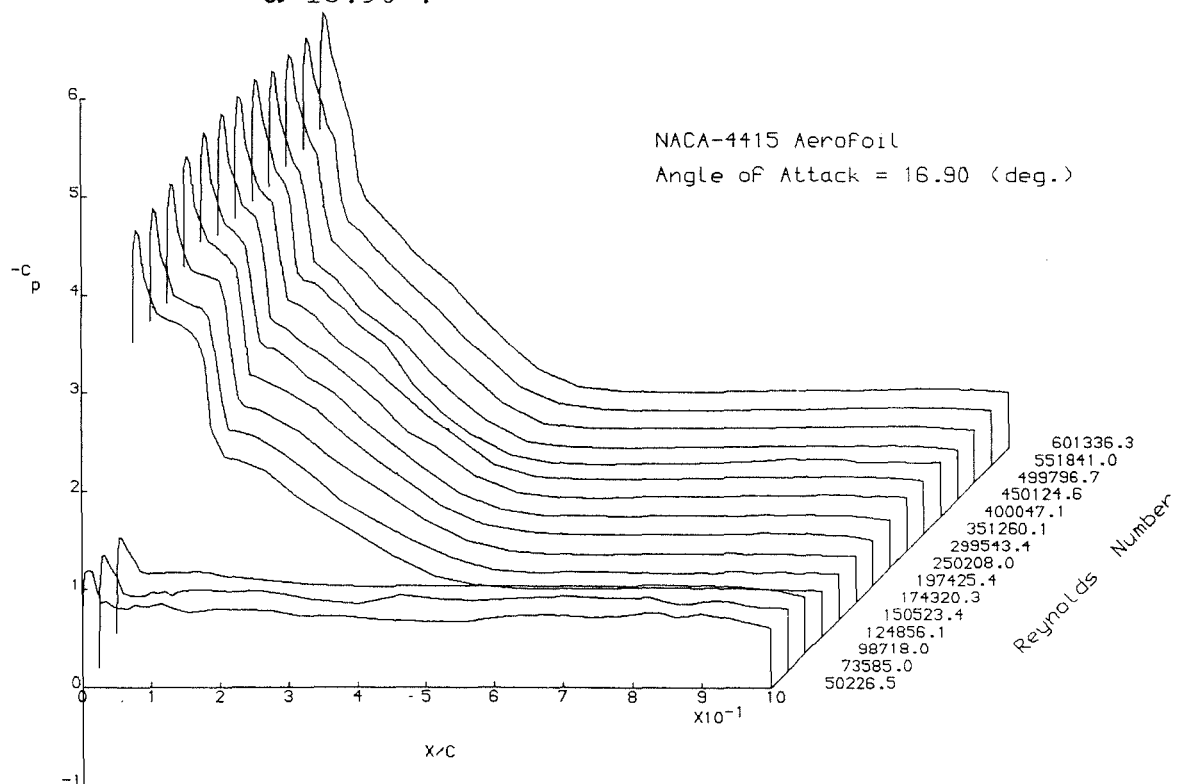


Figure 4.2.16. 3-D Plot of  $C_p$  vs  $x/c$  vs  $Re$  for the Upper Surface of the NACA-4415 Aerofoil Section at  $\alpha=16.90^\circ$ .

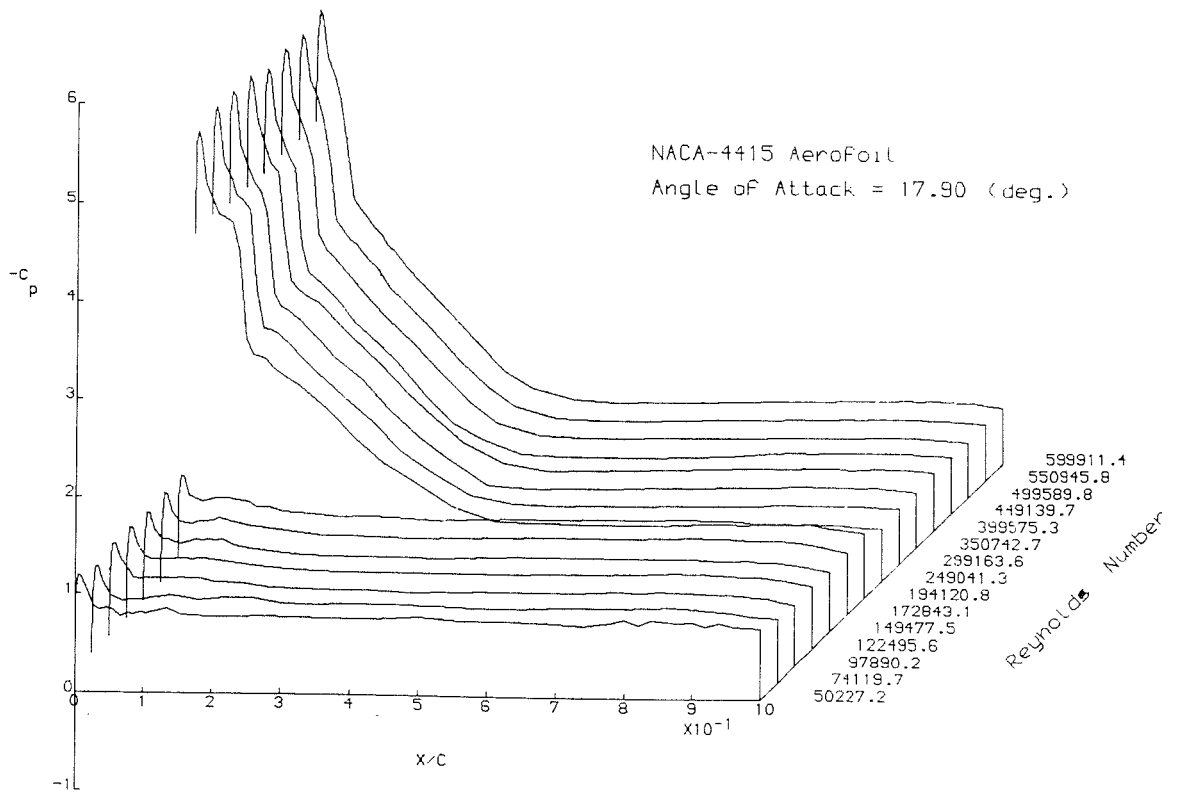


Figure 4.2.17. 3-D Plot of  $C_p$  vs  $x/c$  vs  $Re$  for the Upper Surface of the NACA-4415 Aerofoil Section at  $\alpha=17.90^\circ$ .

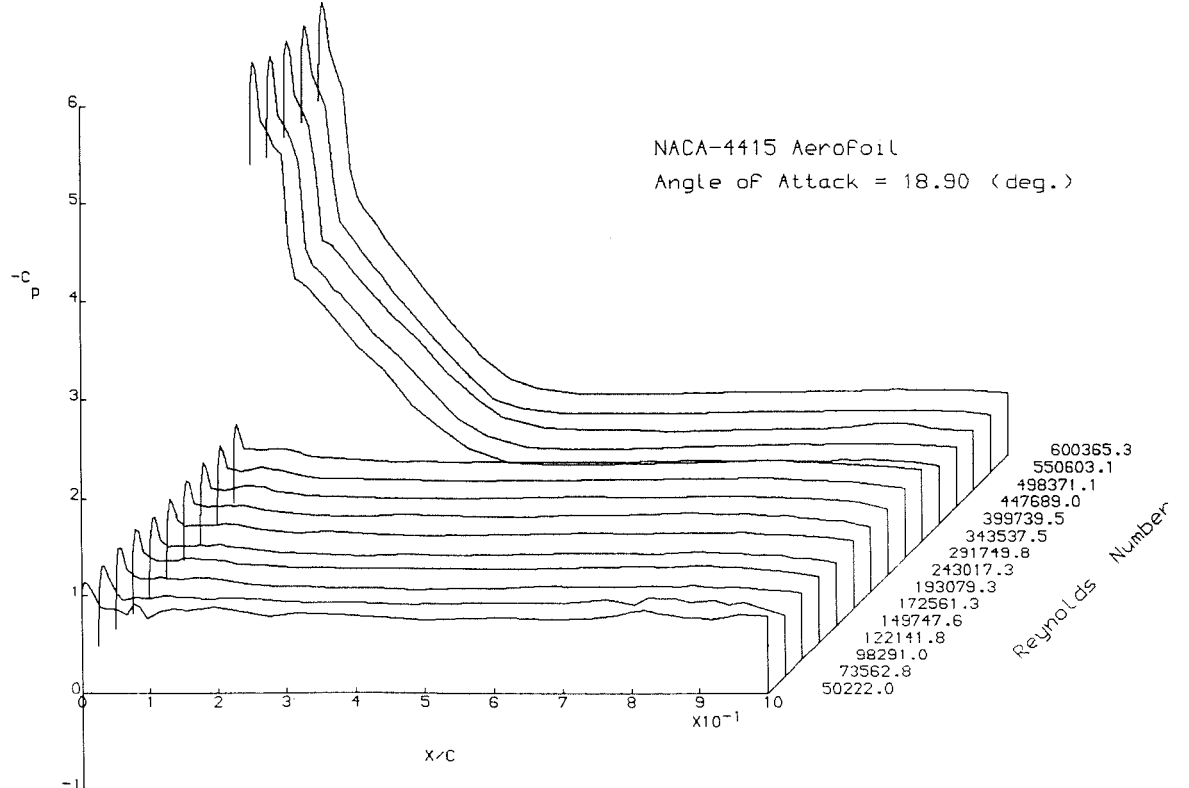


Figure 4.2.18. 3-D Plot of  $C_p$  vs  $x/c$  vs  $Re$  for the Upper Surface of the NACA-4415 Aerofoil Section at  $\alpha=18.90^\circ$ .

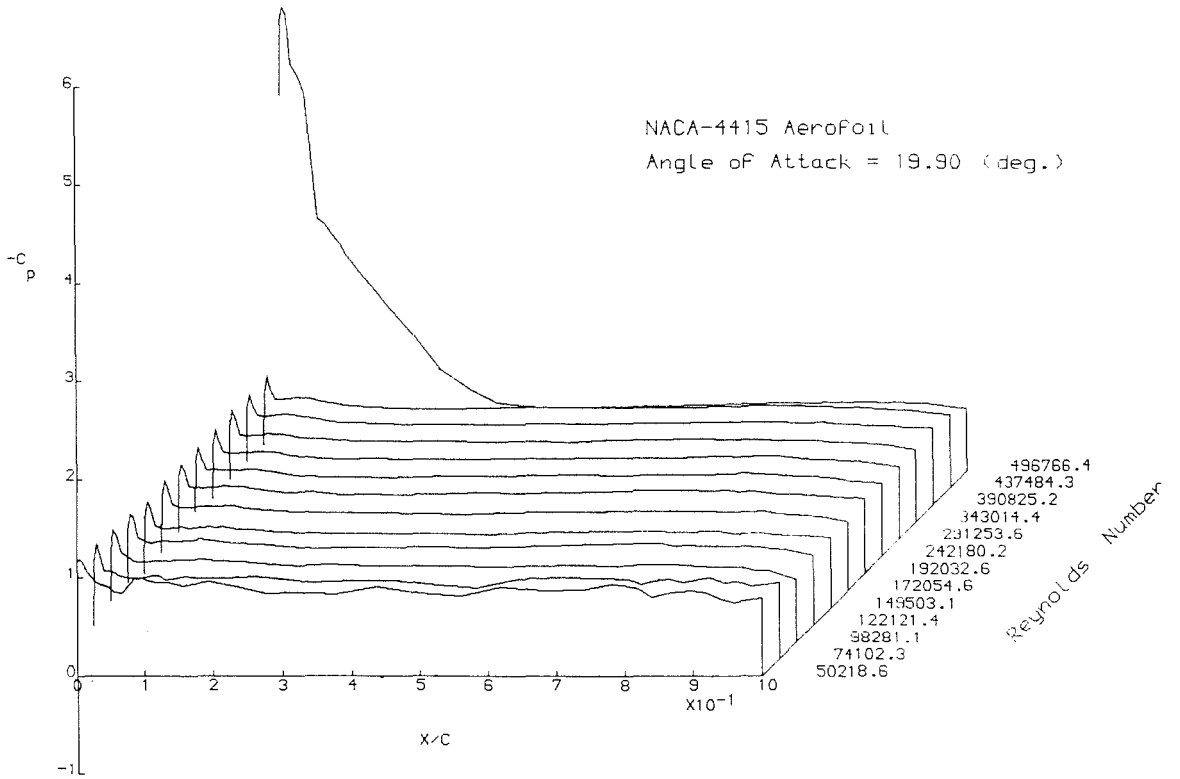


Figure 4.2.19. 3-D Plot of  $C_p$  vs  $x/c$  vs  $Re$  for the Upper Surface of the NACA-4415 Aerofoil Section at  $\alpha=19.90^\circ$ .

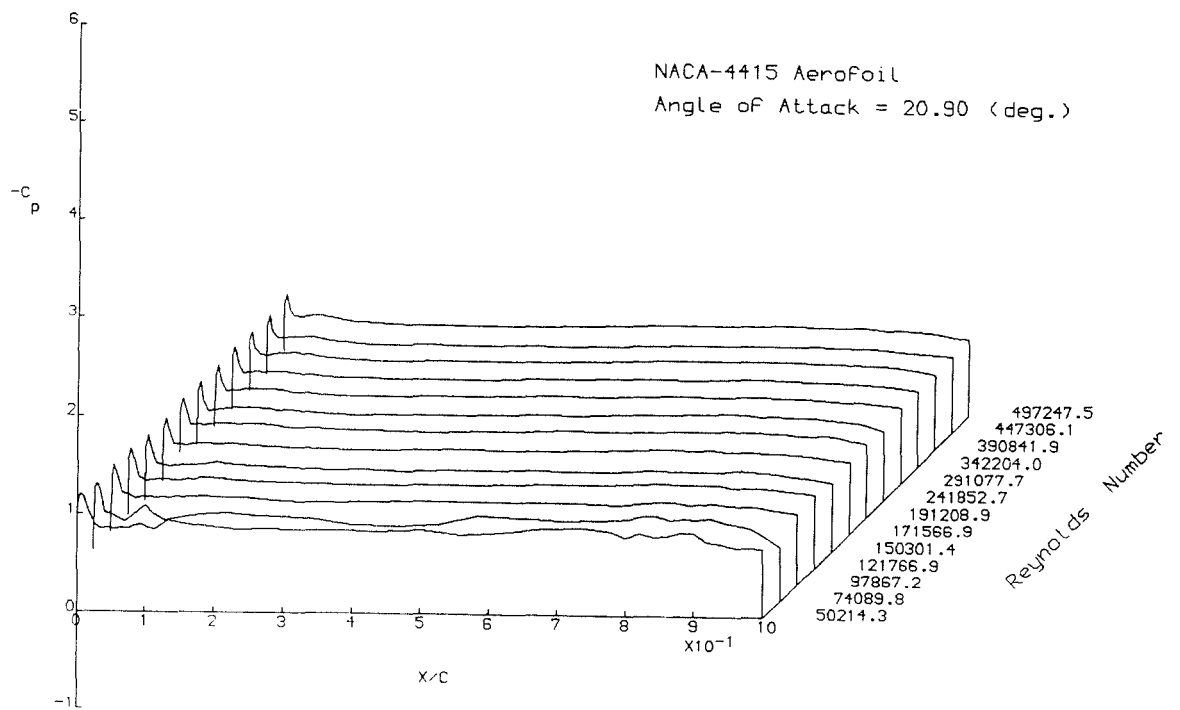


Figure 4.2.20. 3-D Plot of  $C_p$  vs  $x/c$  vs  $Re$  for the Upper Surface of the NACA-4415 Aerofoil Section at  $\alpha=20.90^\circ$ .

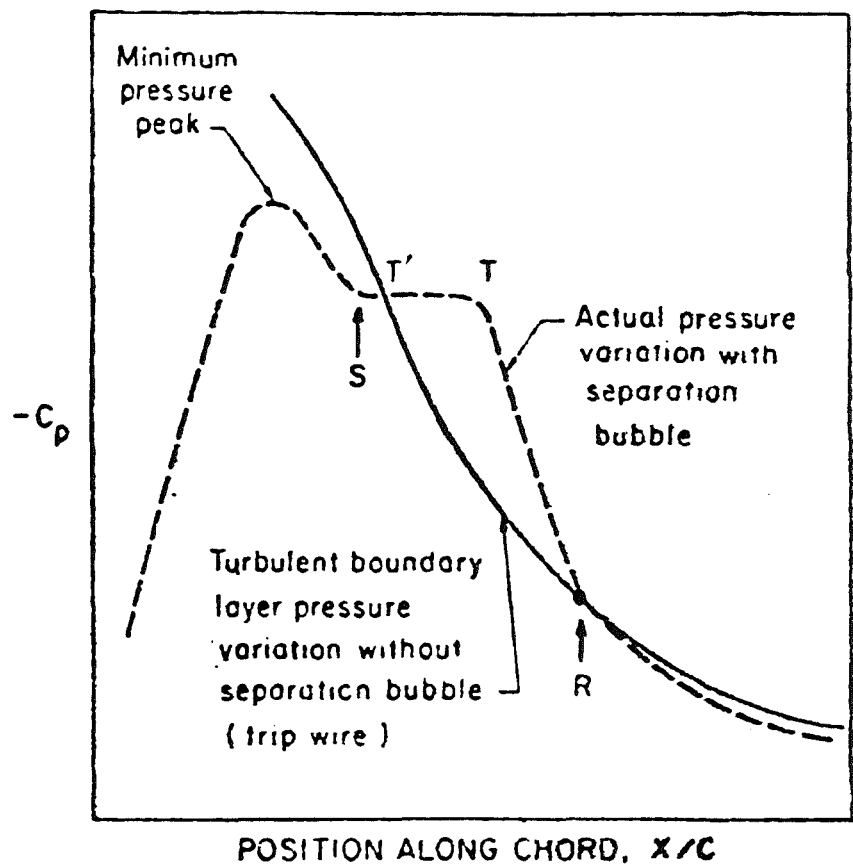


Figure 4.2.21. Typical Surface Pressure Distributions With and Without Separation Bubble.  
 (Adapted from Reference 12)

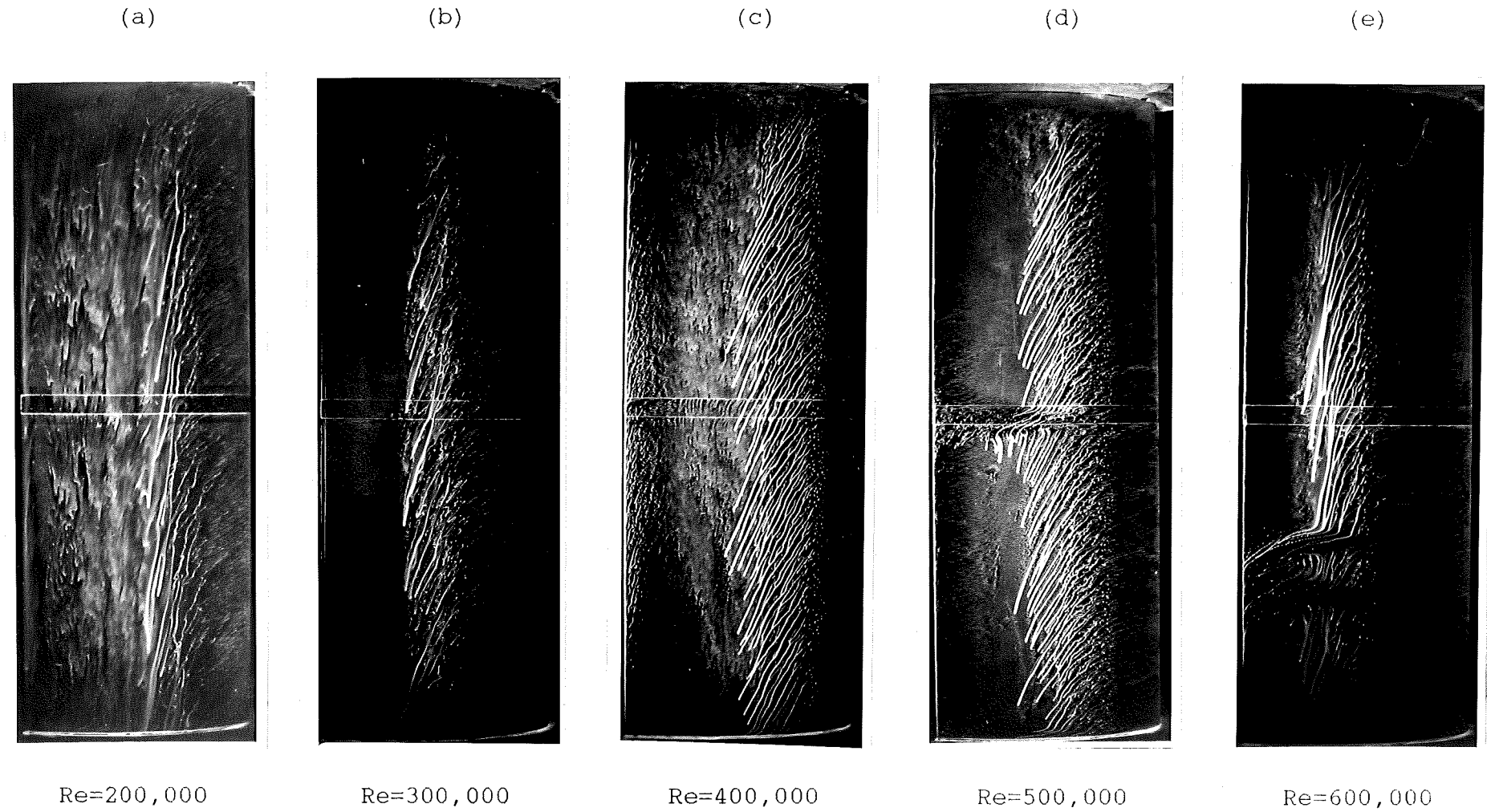


Figure 4.3.1. Flow Visualisation Photographs of the Upper Surface of the NACA-4415 Aerofoil Section at Various Reynolds Numbers and at  $\alpha = -5.10^\circ$ .

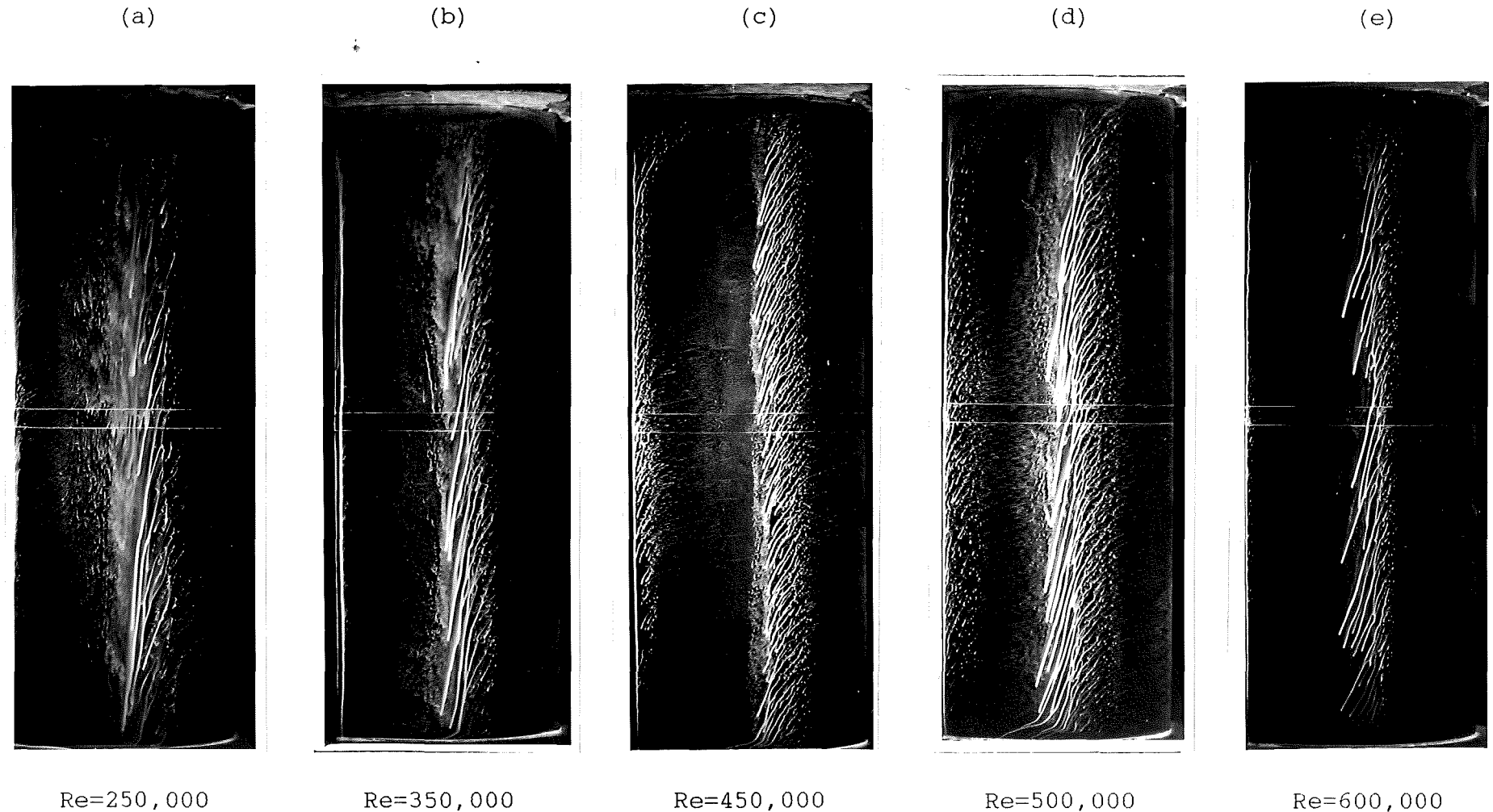


Figure 4.3.2. Flow Visualisation Photographs of the Upper Surface of the NACA-4415 Aerofoil Section at Various Reynolds Numbers and at  $\alpha = -1.10^\circ$ .

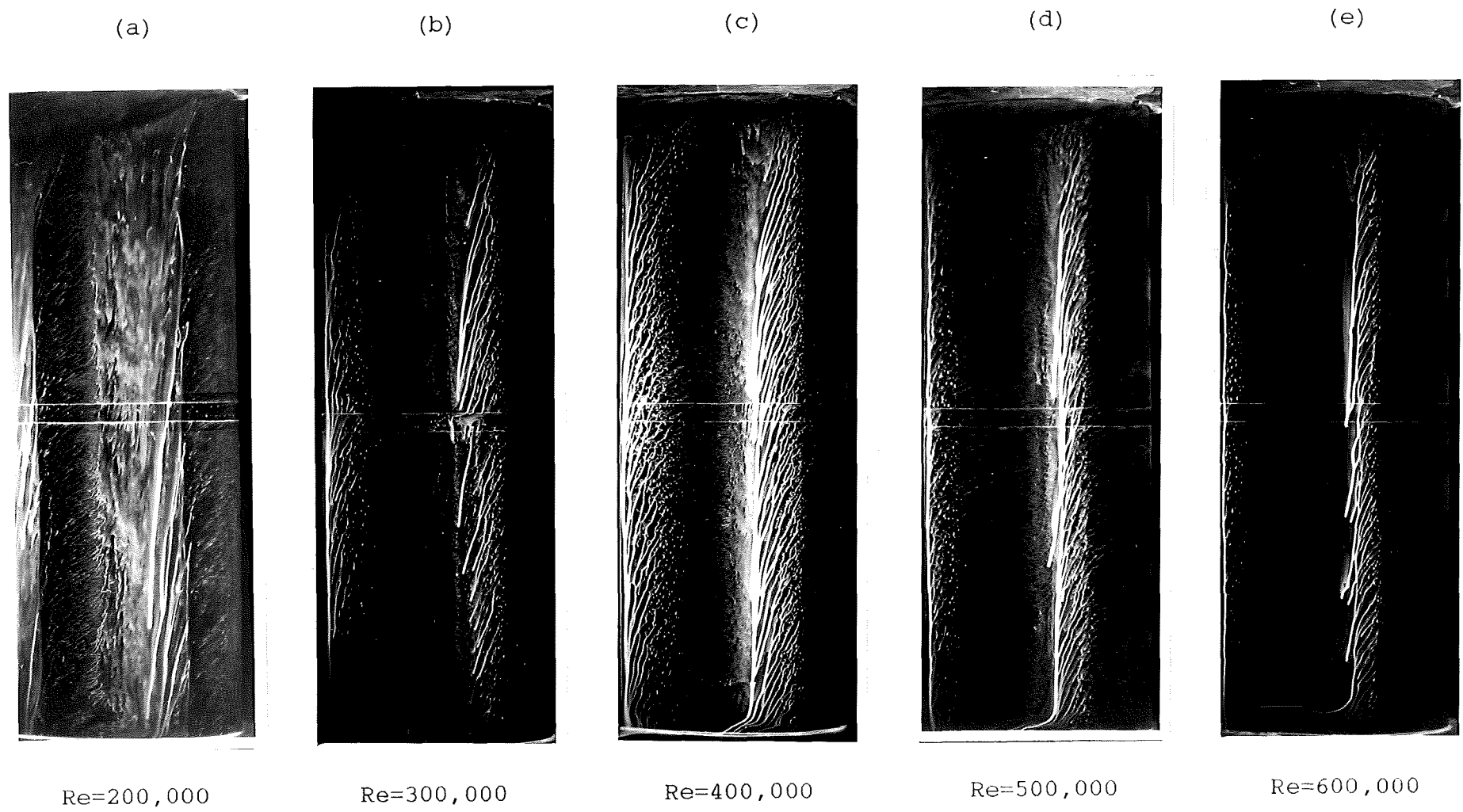


Figure 4.3.3. Flow Visualisation Photographs of the Upper Surface of the NACA-4415 Aerofoil Section at Various Reynolds Numbers and at  $\alpha=2.90^\circ$ .

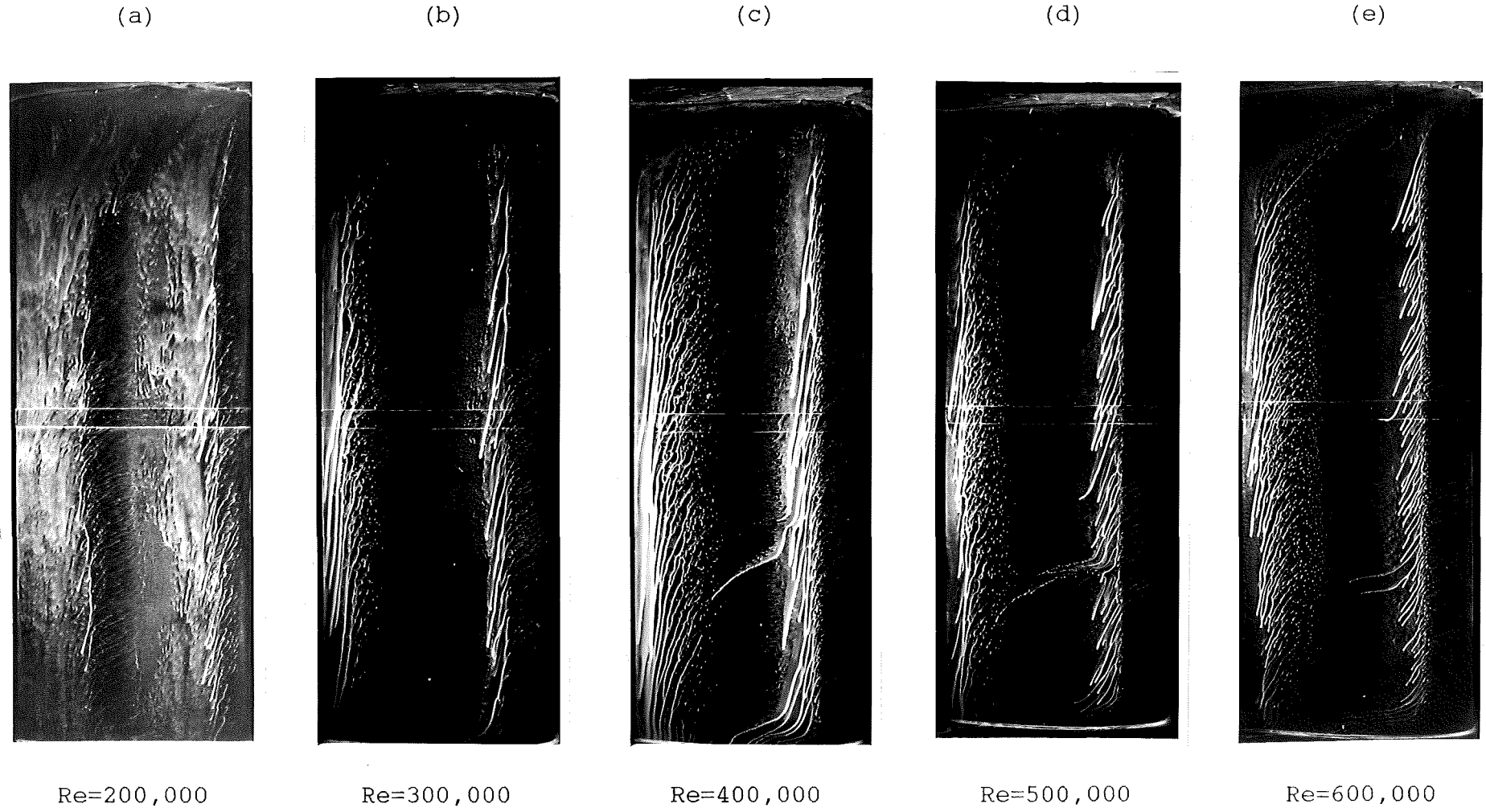


Figure 4.3.4. Flow Visualisation Photographs of the Upper Surface of the NACA-4415 Aerofoil Section at Various Reynolds Numbers and at  $\alpha=6.90^\circ$ .

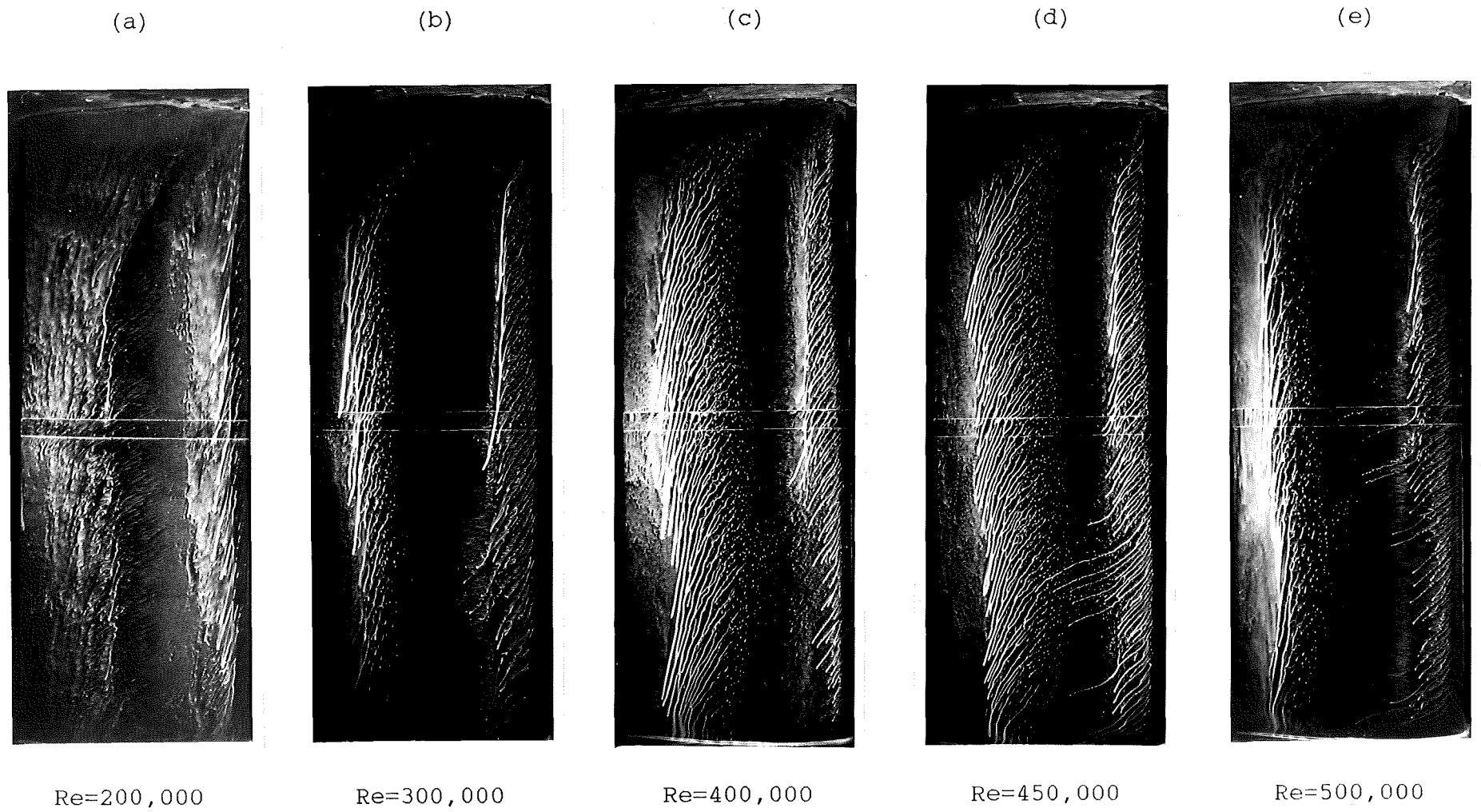


Figure 4.3.5. Flow Visualisation Photographs of the Upper Surface of the NACA-4415 Aerofoil Section at Various Reynolds Numbers and at  $\alpha=9.90^\circ$ .

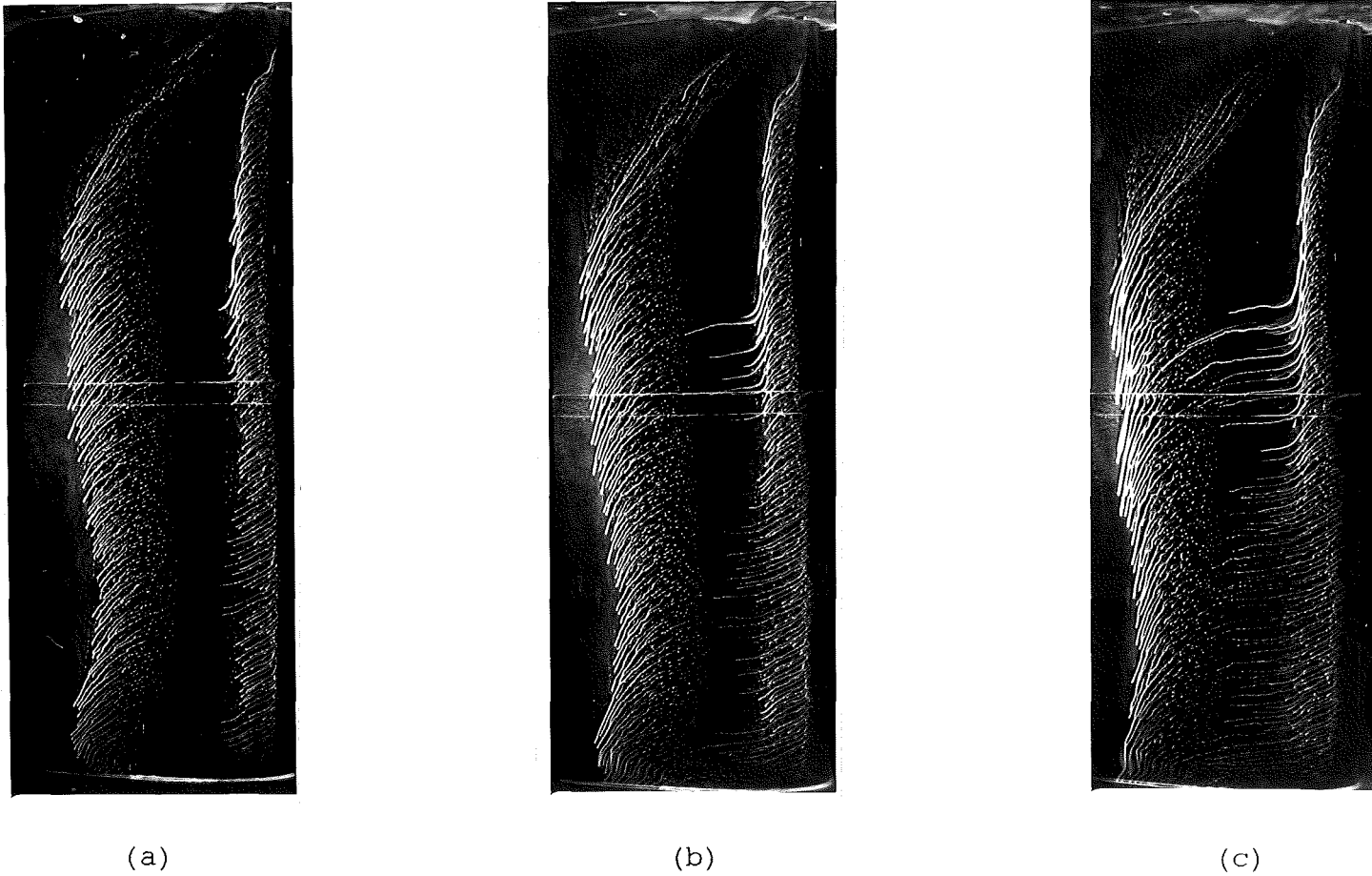


Figure 4.3.6. A Sequence of Flow Visualisation Photographs of the Upper Surface of the NACA-4415 Aerofoil Section at  $Re=600,000$  and at  $\alpha=9.90^\circ$ .

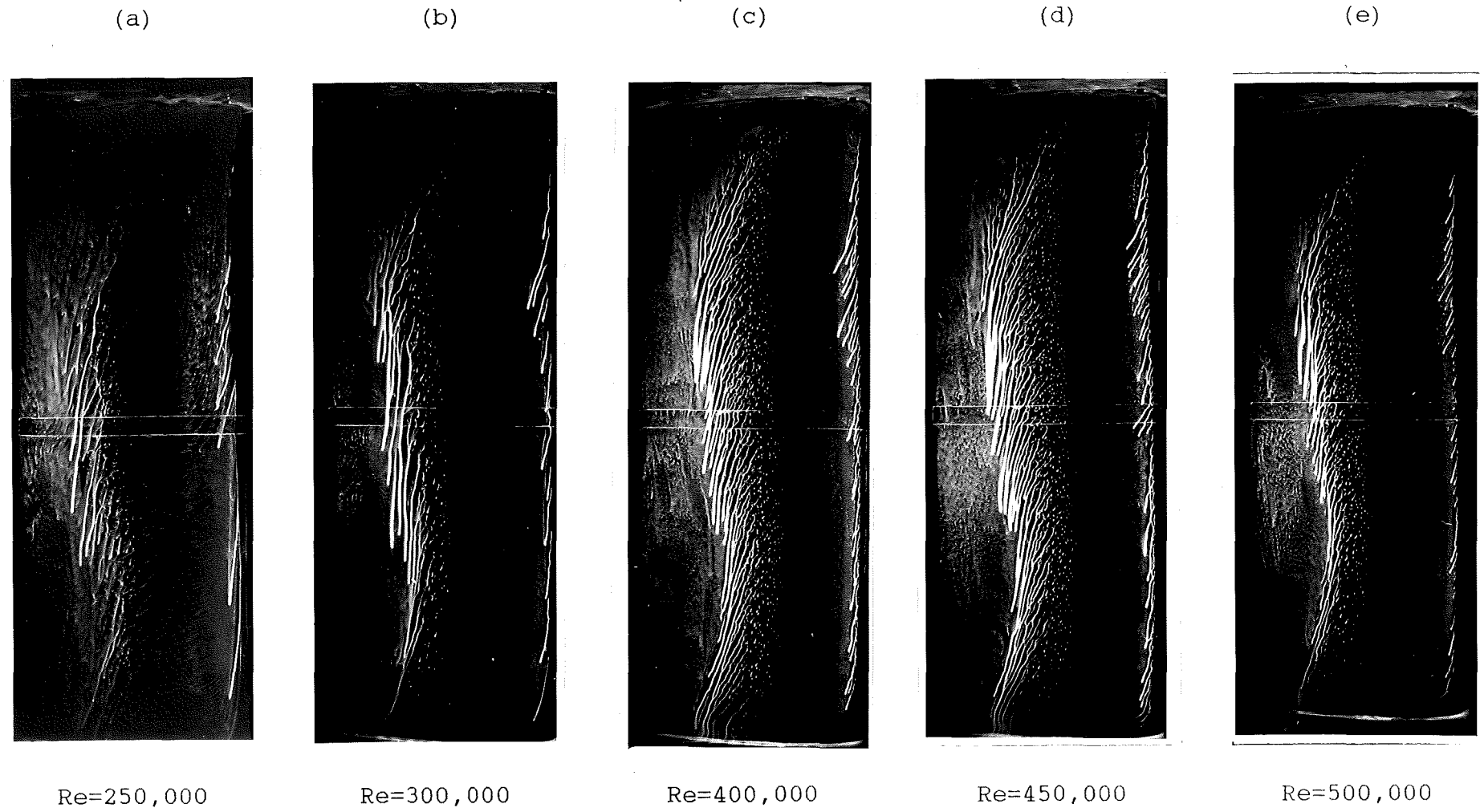


Figure 4.3.7. Flow Visualisation Photographs of the Upper Surface of the NACA-4415 Aerofoil Section at Various Reynolds Numbers and at  $\alpha=11.90^\circ$ .

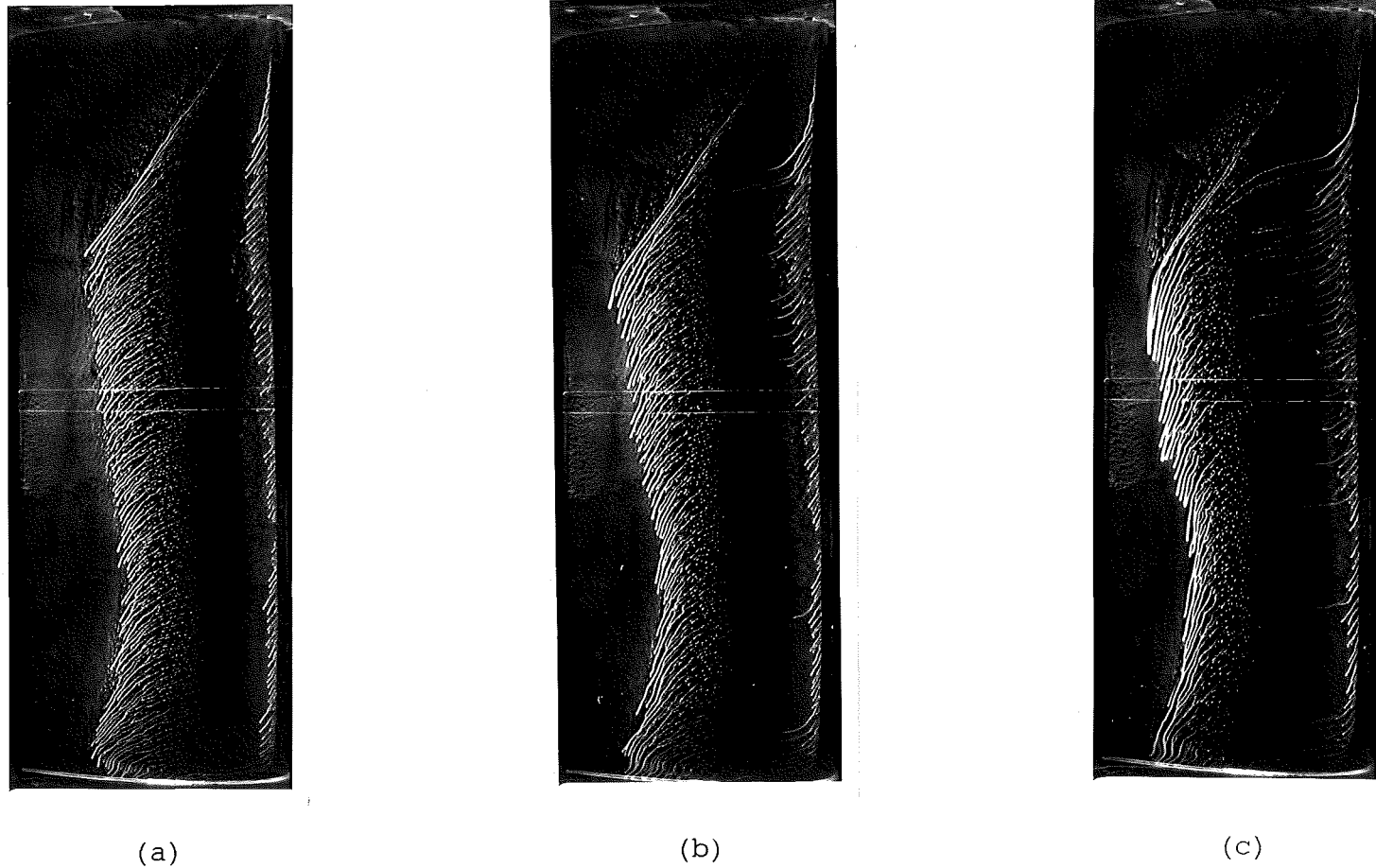


Figure 4.3.8. A Sequence of Flow Visualisation Photographs of the Upper Surface of the NACA-4415 Aerofoil Section at  $Re=600,000$  and at  $\alpha=11.90^\circ$ .

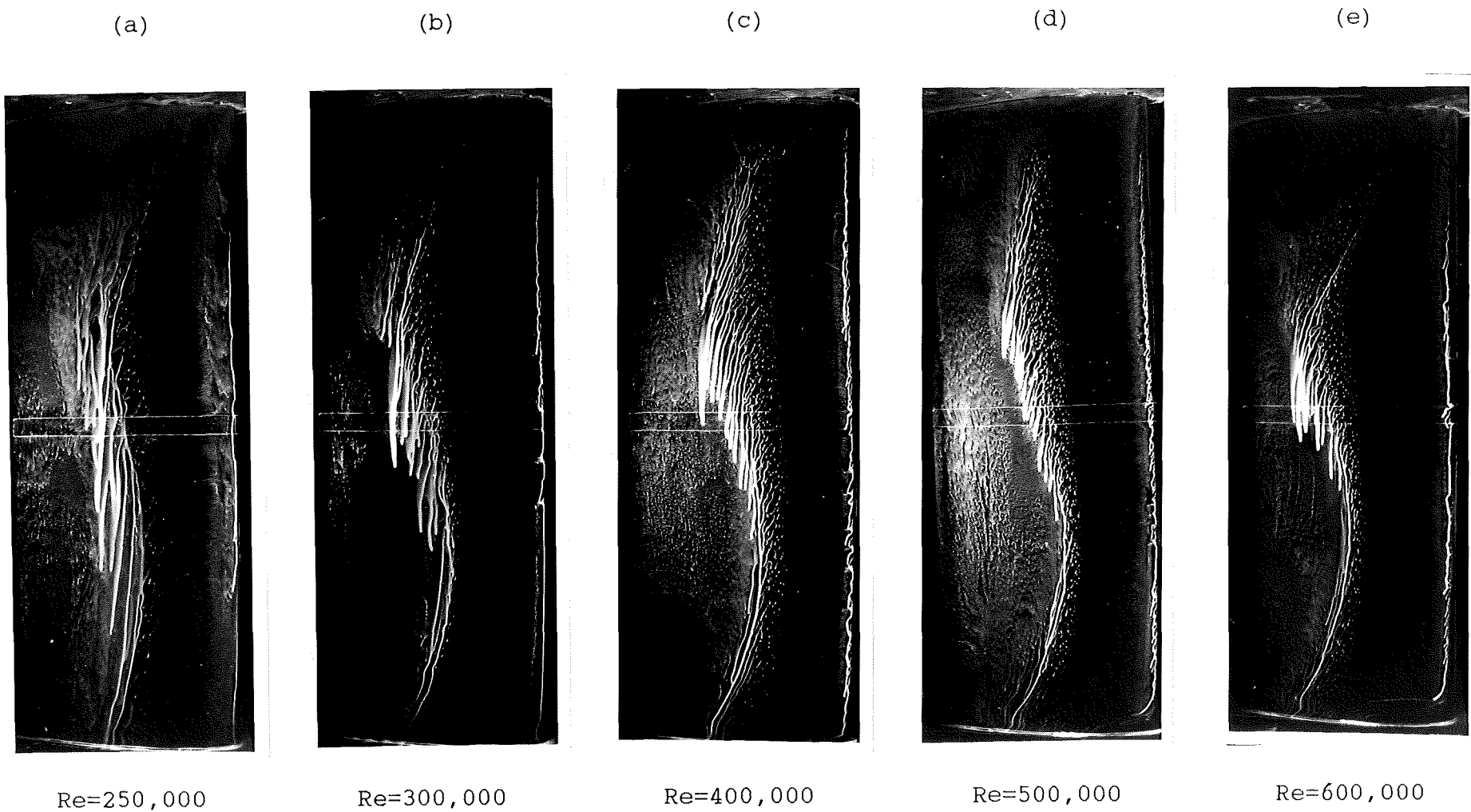


Figure 4.3.9. Flow Visualisation Photographs of the Upper Surface of the NACA-4415 Aerofoil Section at Various Reynolds Numbers and at  $\alpha=13.90^\circ$ .

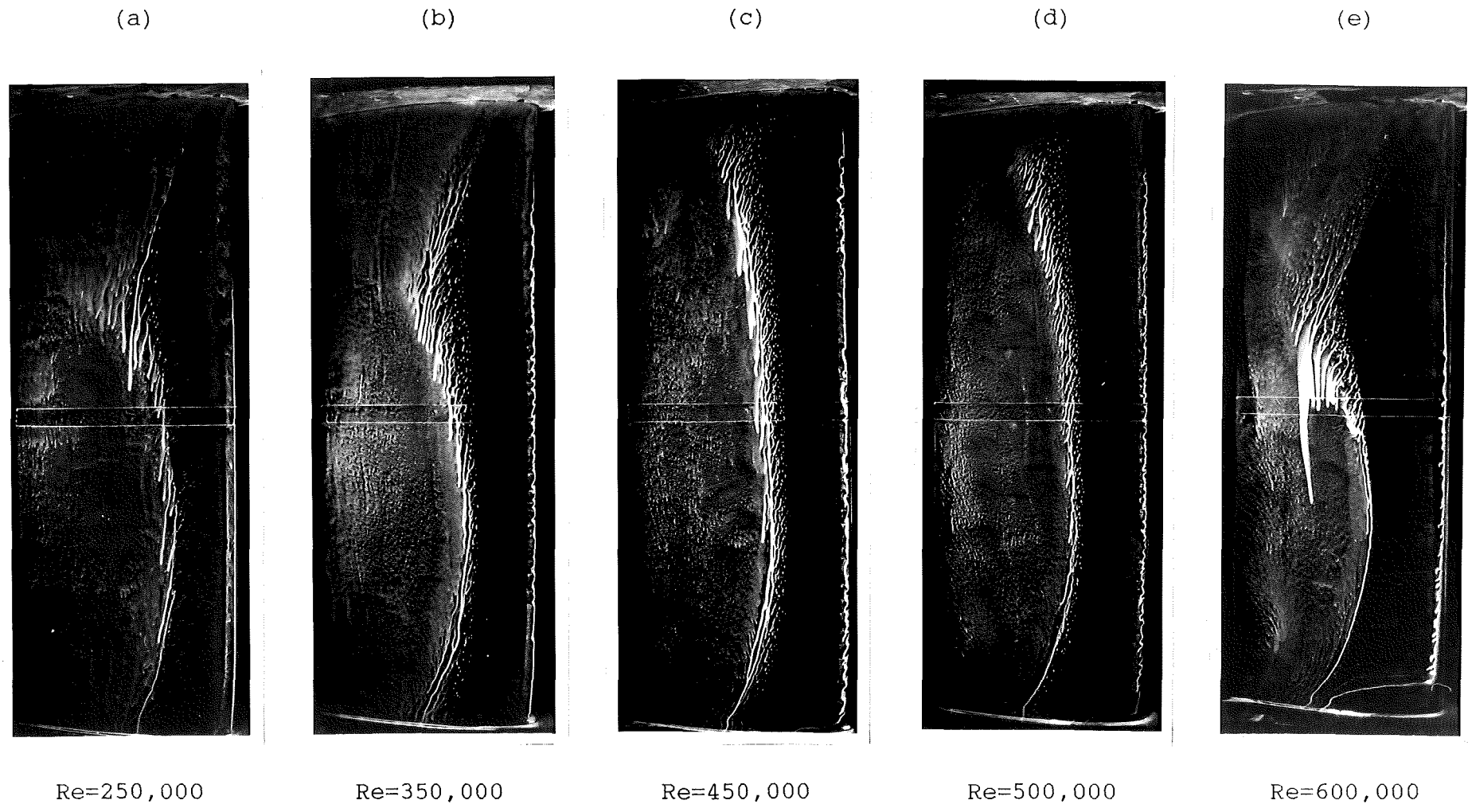


Figure 4.3.10. Flow Visualisation Photographs of the Upper Surface of the NACA-4415 Aerofoil Section at Various Reynolds Numbers and at  $\alpha=15.90^\circ$ .

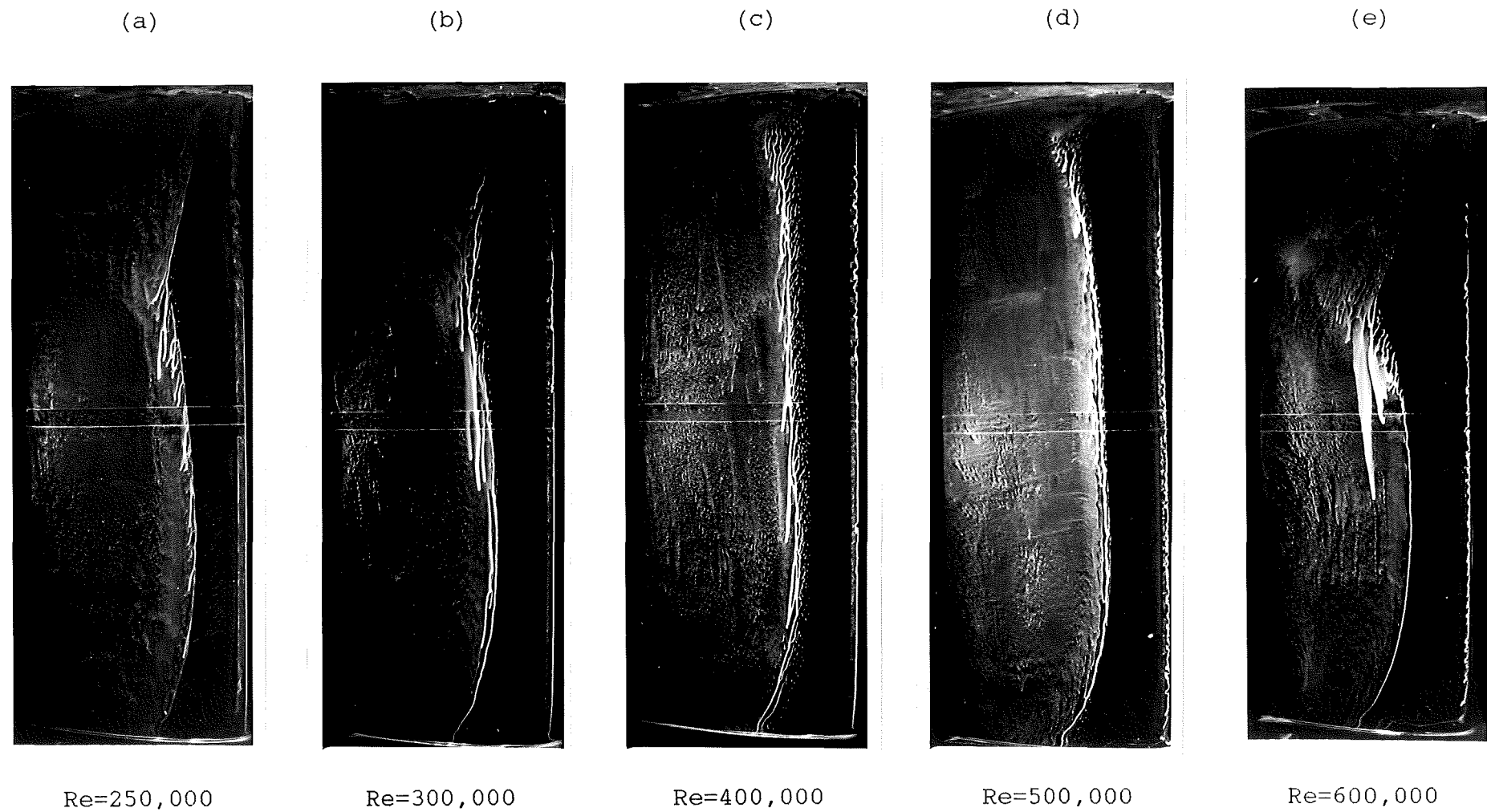


Figure 4.3.11. Flow Visualisation Photographs of the Upper Surface of the NACA-4415 Aerofoil Section at Various Reynolds Numbers and at  $\alpha=17.90^\circ$ .



Figure 4.3.12. Flow Visualisation Photographs of the Upper Surface of the NACA-4415 Aerofoil Section at Various Reynolds Numbers and at  $\alpha=18.90^\circ$ .

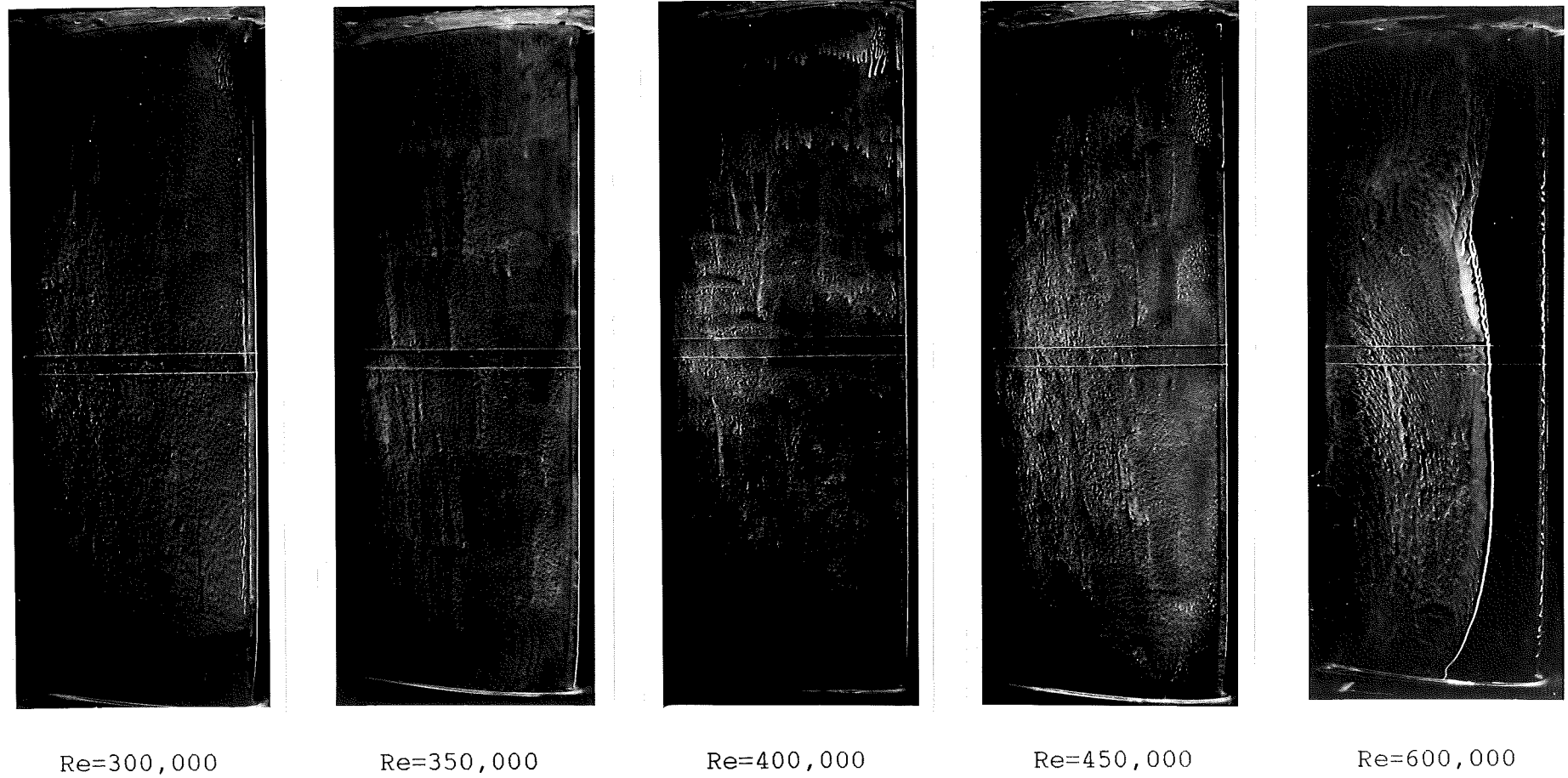
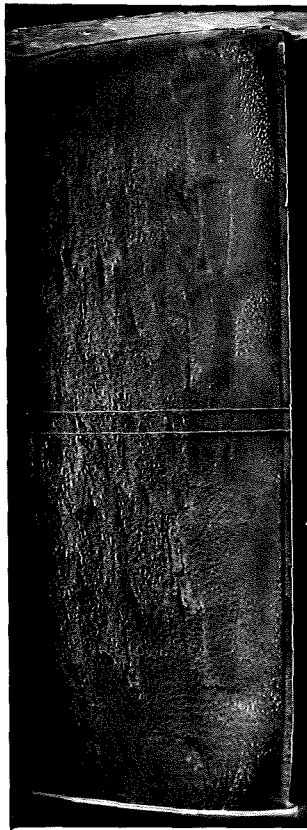
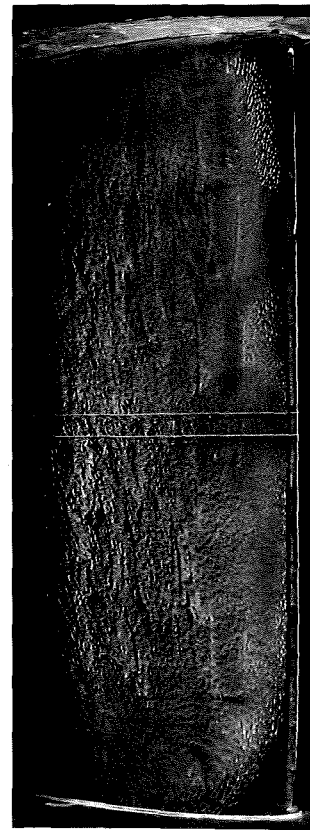


Figure 4.3.13. Flow Visualisation Photographs of the Upper Surface of the NACA-4415 Aerofoil Section at Various Reynolds Numbers and at  $\alpha=19.90^\circ$ .



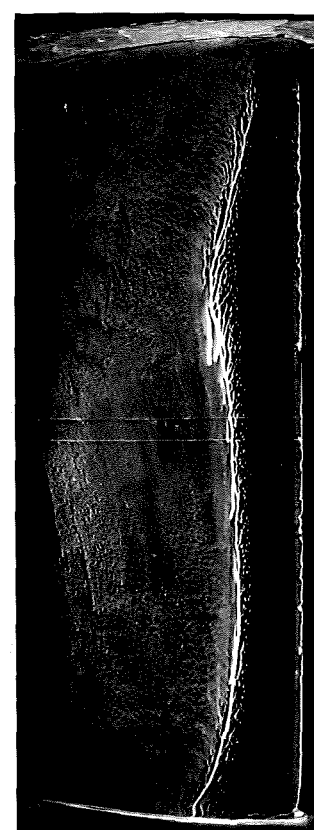
(a)



(b)



(c)



(d)

Figure 4.3.14. A Sequence of Flow Visualisation Photographs of the Upper Surface of the NACA-4415 Aerofoil Section at  $Re=450,000$  and at  $\alpha=19.90^\circ$ .

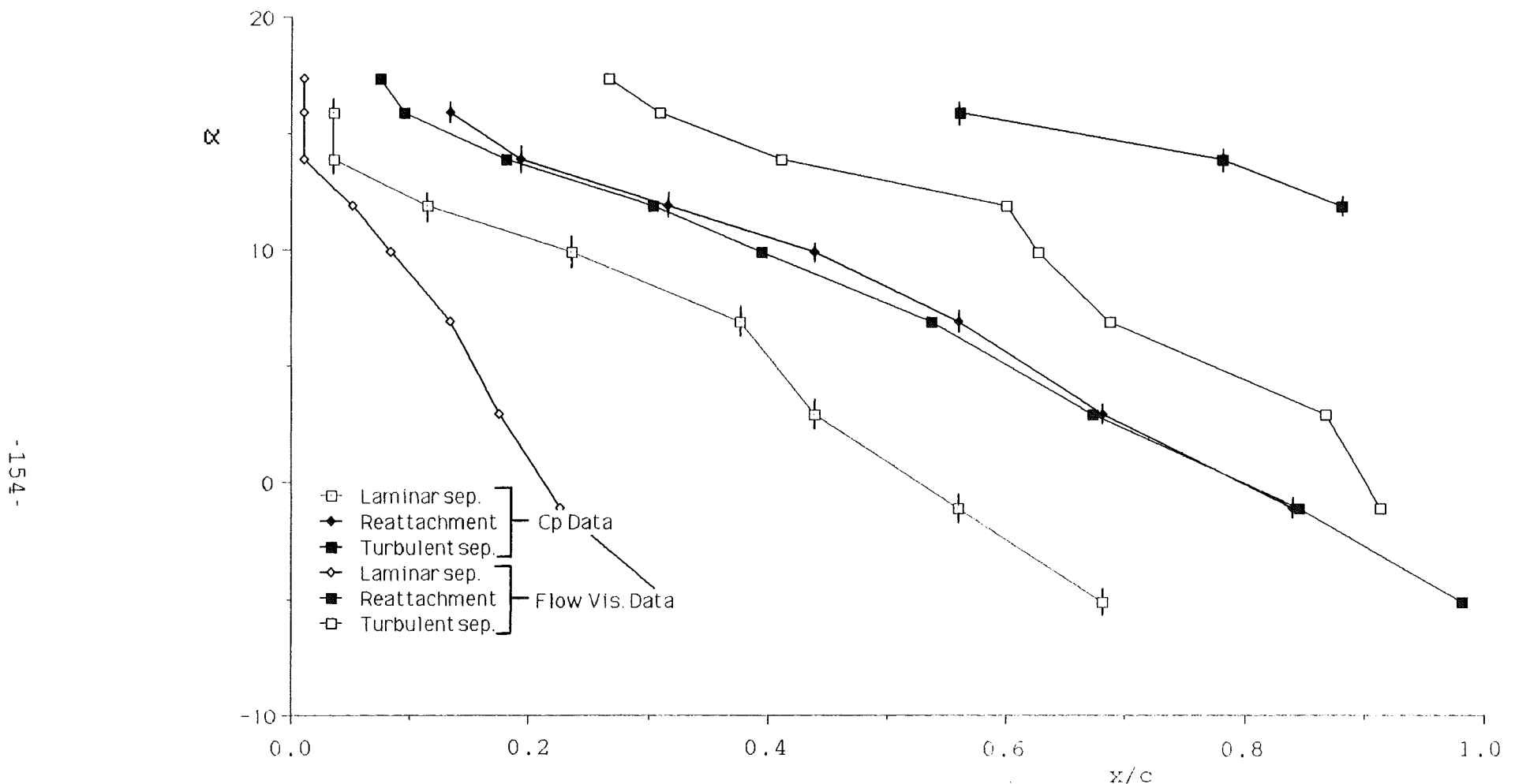


Figure 4.3.15. Comparison Between Cp and Flow Visualisation Data Regarding the Locations of the Various Boundary Layer Phenomena Occurring on the Upper Surface of the NACA-4415 Model at  $Re=150,000$ .

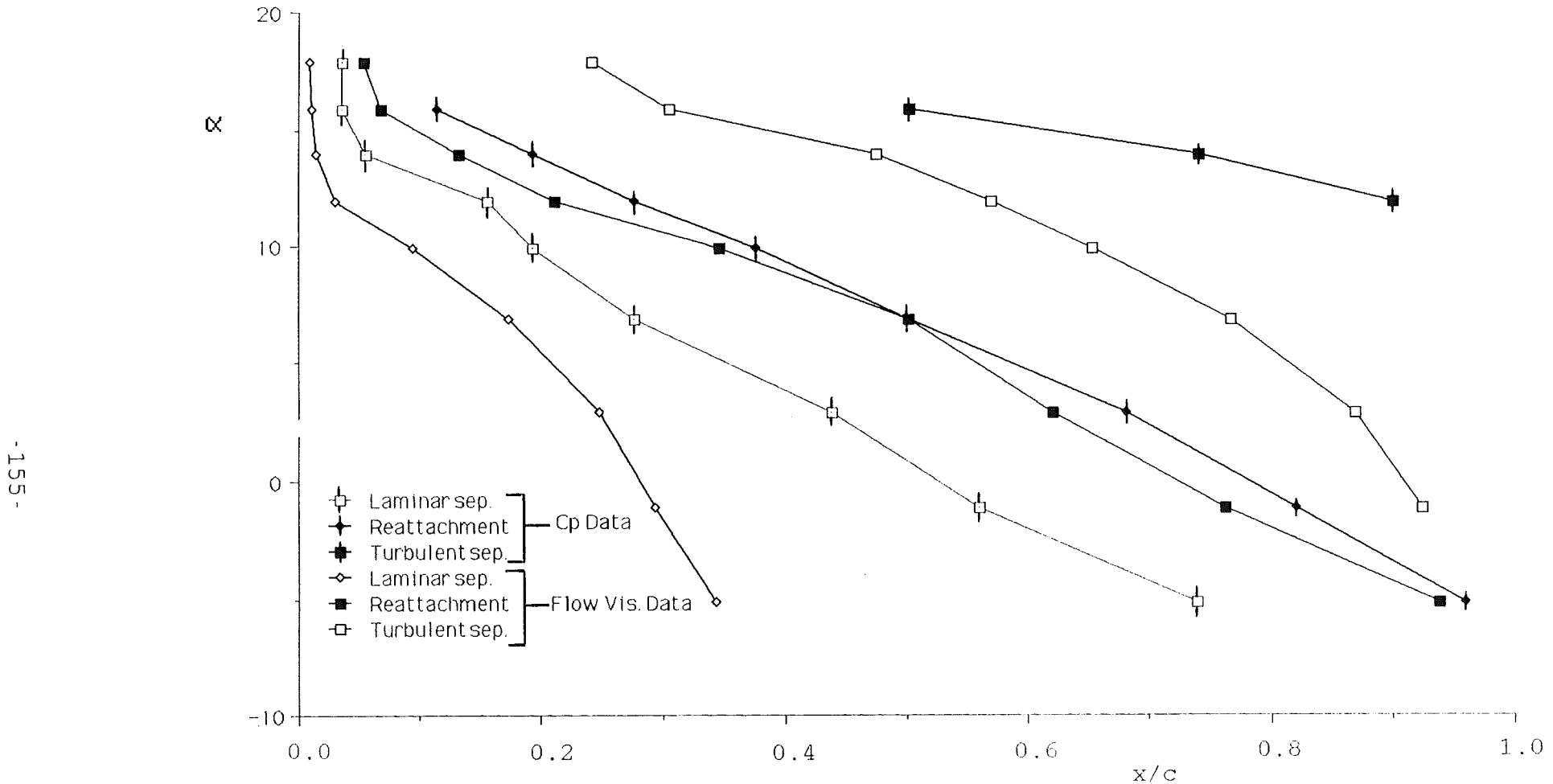


Figure 4.3.16. Comparison Between  $C_p$  and Flow Visualisation Data Regarding the Locations of the Various Boundary Layer Phenomena Occurring on the Upper Surface of the NACA-4415 Model at  $Re=200,000$ .

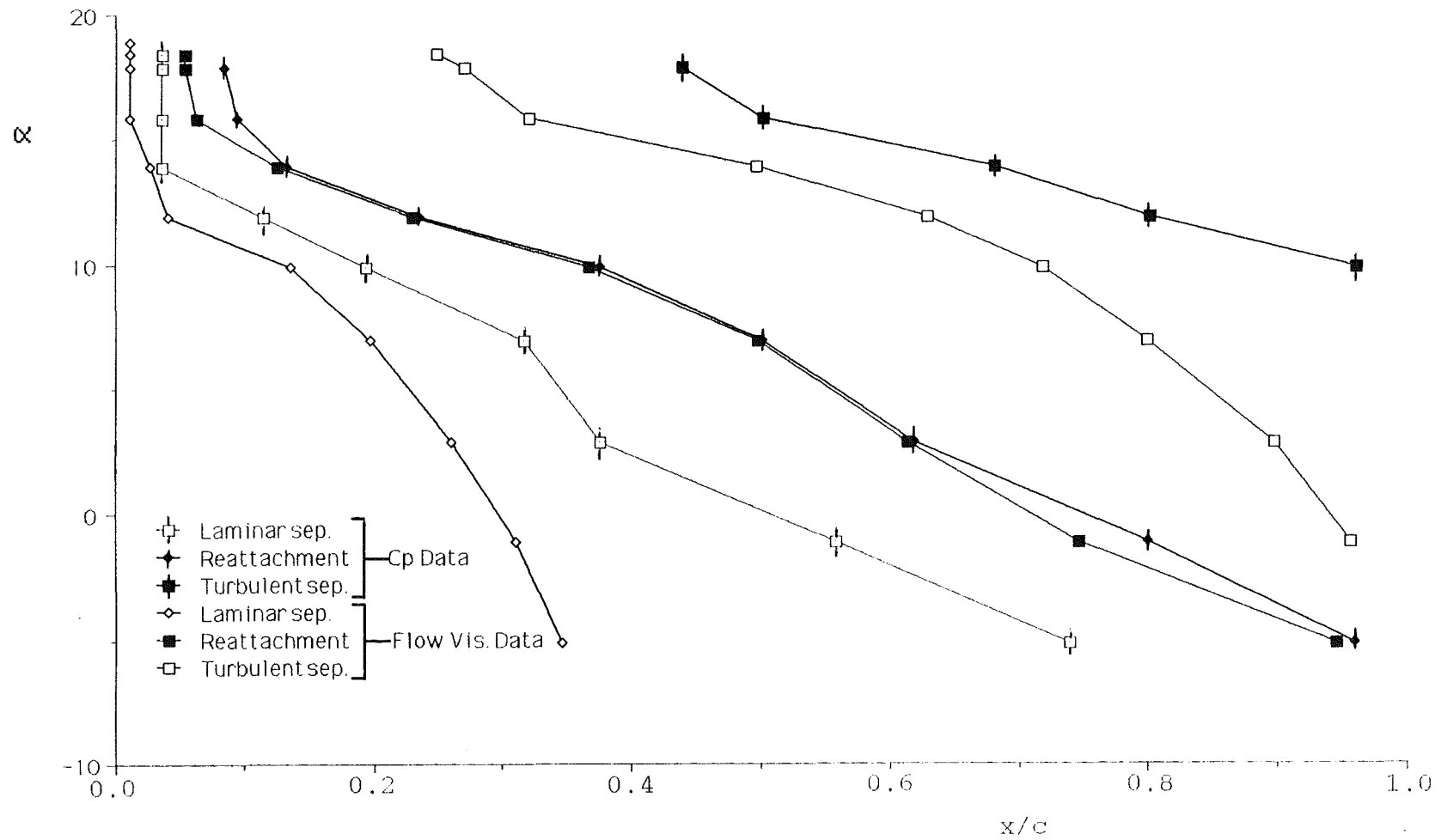


Figure 4.3.17. Comparison Between  $C_p$  and Flow Visualisation Data Regarding the Locations of the Various Boundary Layer Phenomena Occurring on the Upper Surface of the NACA-4415 Model at  $Re=250,000$ .

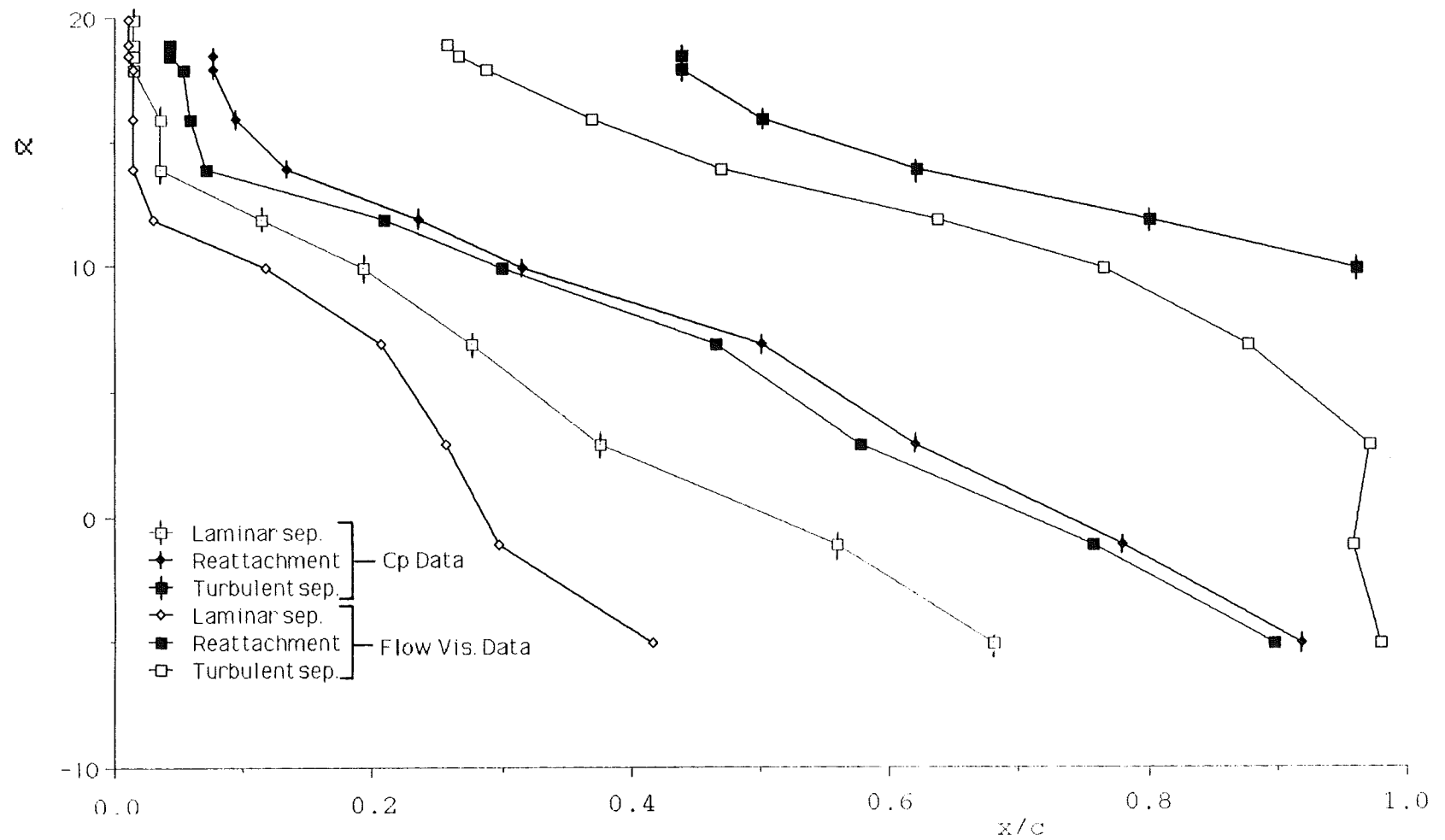


Figure 4.3.18. Comparison Between  $C_p$  and Flow Visualisation Data Regarding the Locations of the Various Boundary Layer Phenomena Occurring on the Upper Surface of the NACA-4415 Model at  $Re=300,000$ .

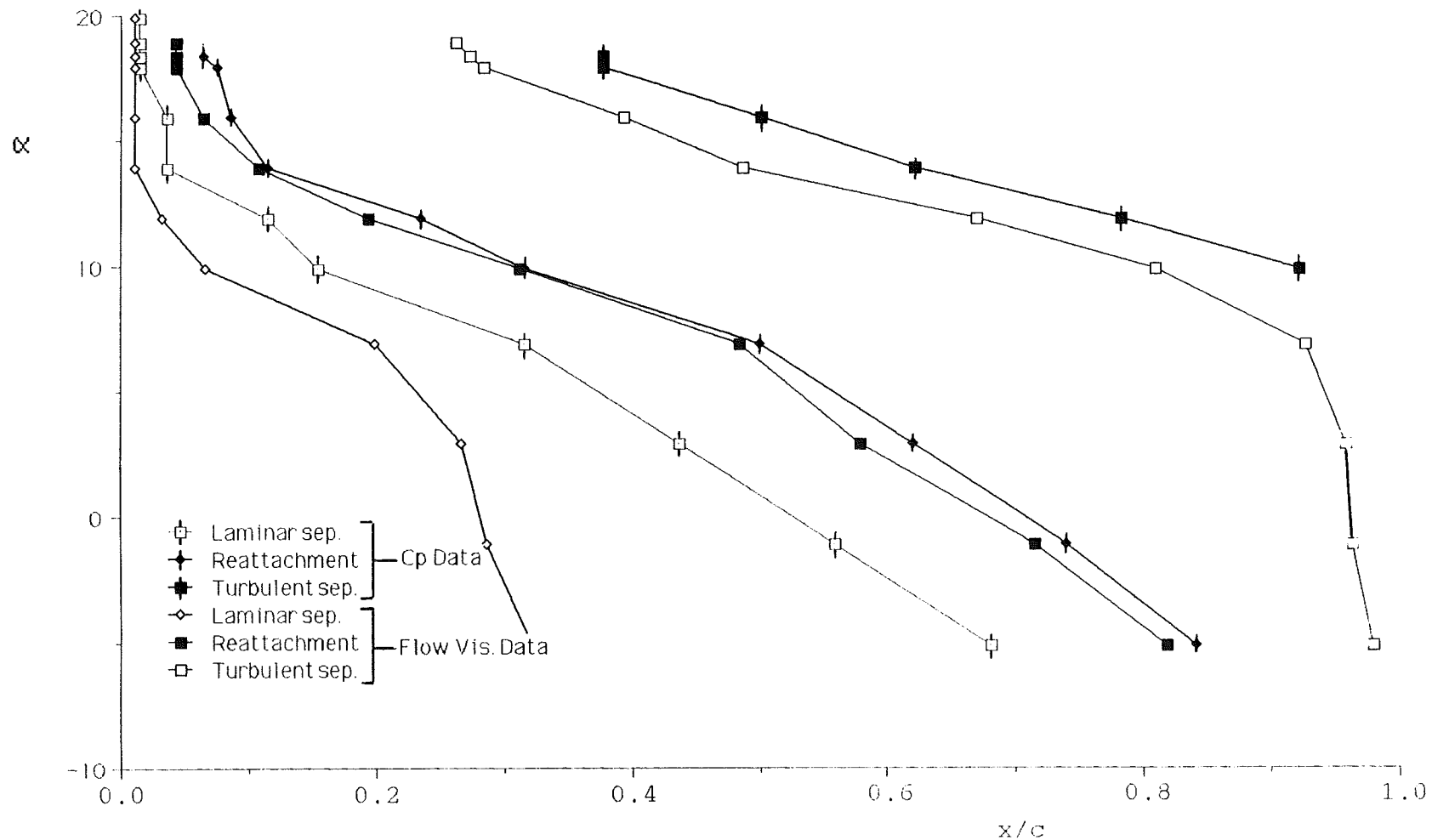


Figure 4.3.19. Comparison Between  $C_p$  and Flow Visualisation Data Regarding the Locations of the Various Boundary Layer Phenomena Occurring on the Upper Surface of the NACA-4415 Model at  $Re=350,000$ .

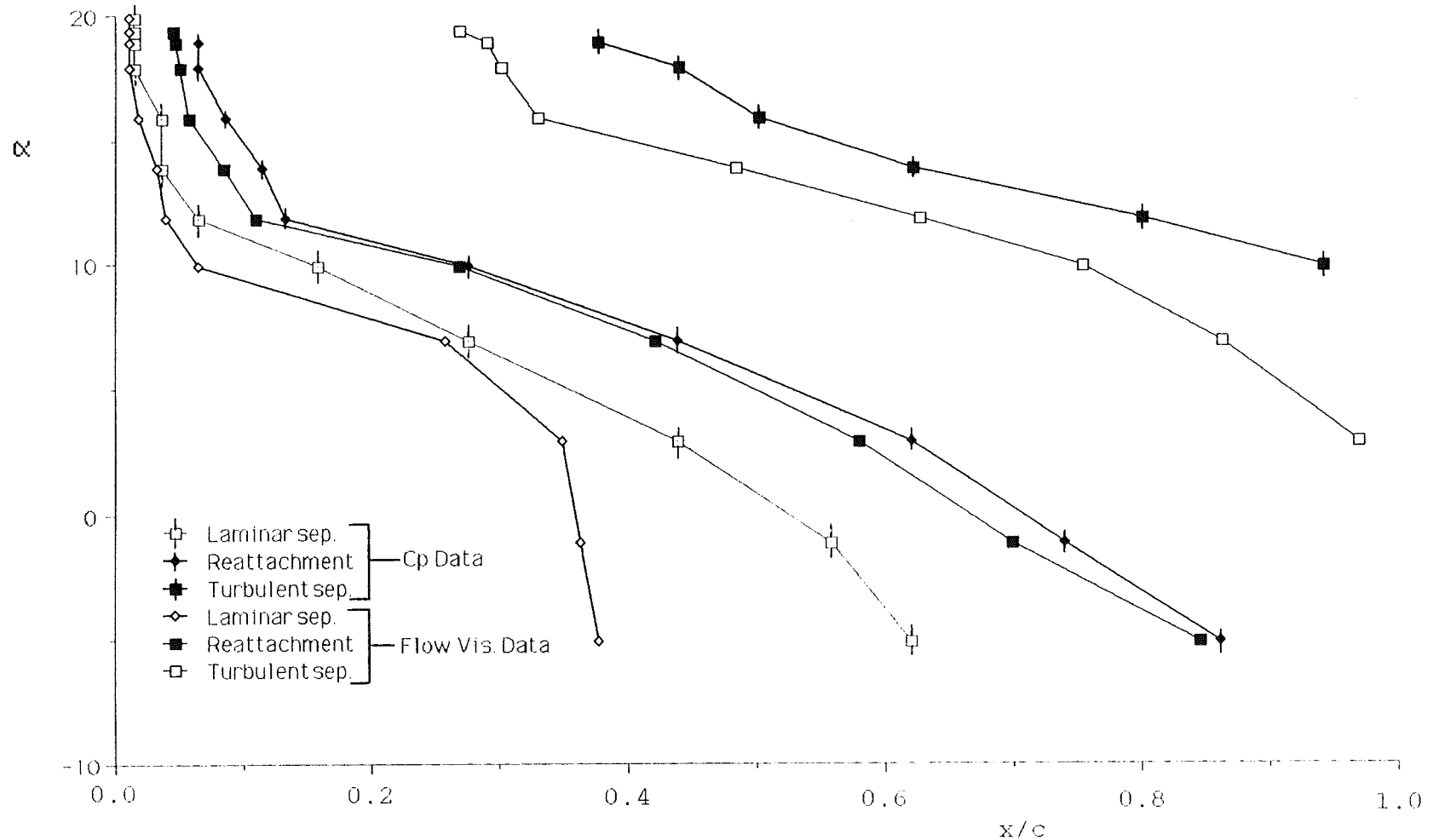


Figure 4.3.20. Comparison Between Cp and Flow Visualisation Data Regarding the Locations of the Various Boundary Layer Phenomena Occurring on the Upper Surface of the NACA-4415 Model at  $Re=400,000$ .

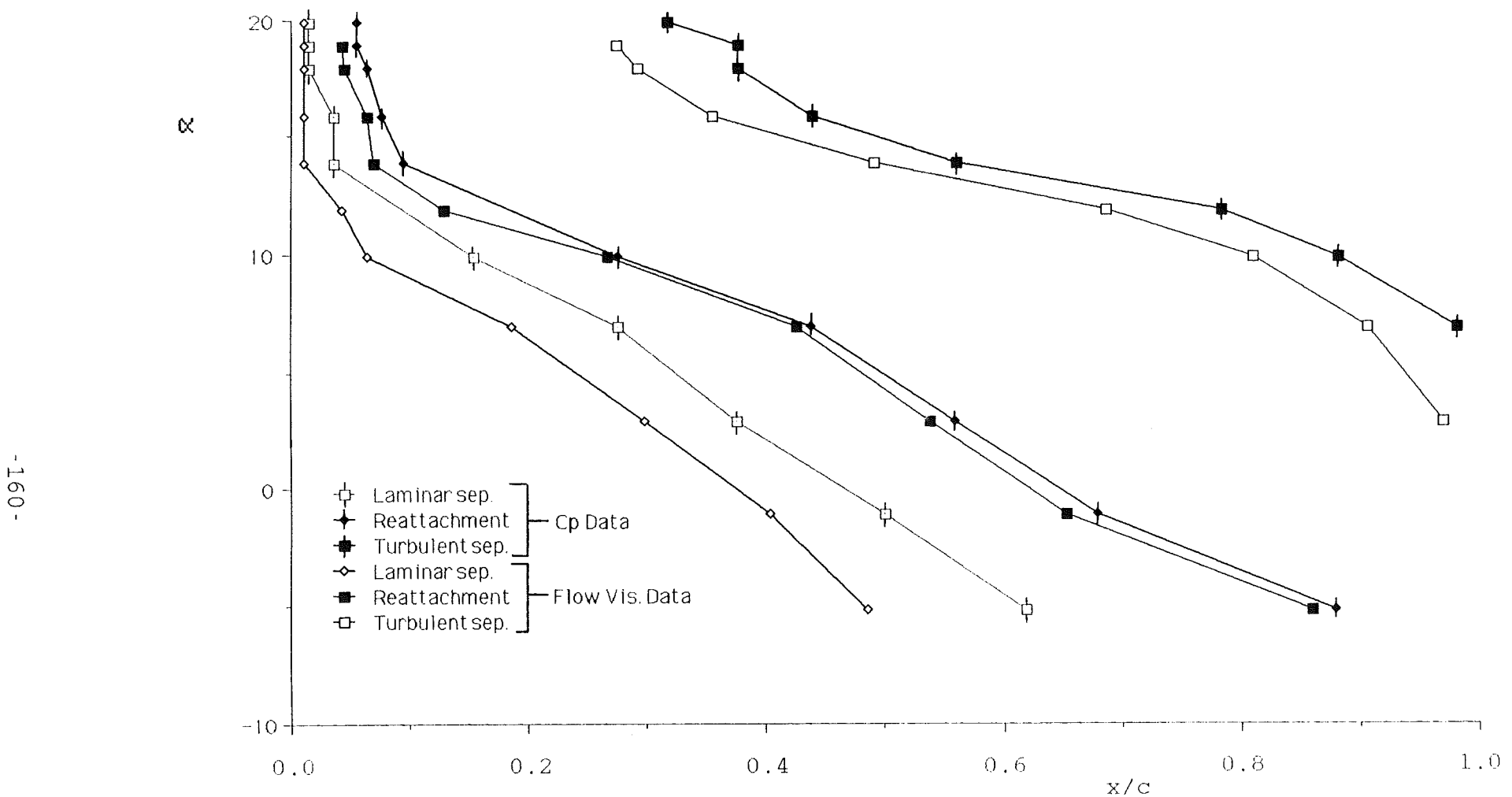


Figure 4.3.21. Comparison Between Cp and Flow Visualisation Data Regarding the Locations of the Various Boundary Layer Phenomena Occurring on the Upper Surface of the NACA-4415 Model at  $Re=500,000$ .

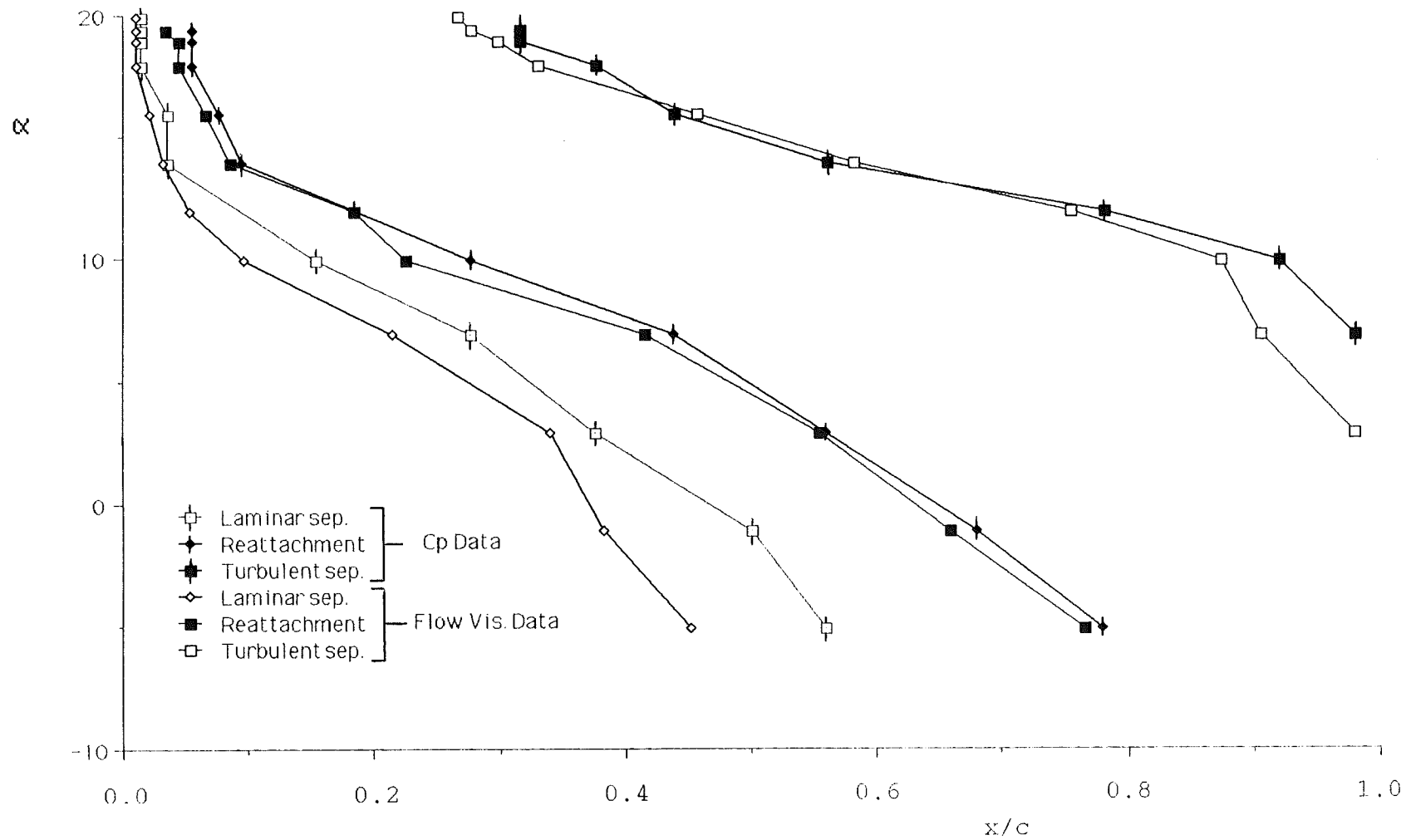


Figure 4.3.22. Comparison Between Cp and Flow Visualisation Data Regarding the Locations of the Various Boundary Layer Phenomena Occurring on the Upper Surface of the NACA-4415 Model at  $Re=600,000$ .

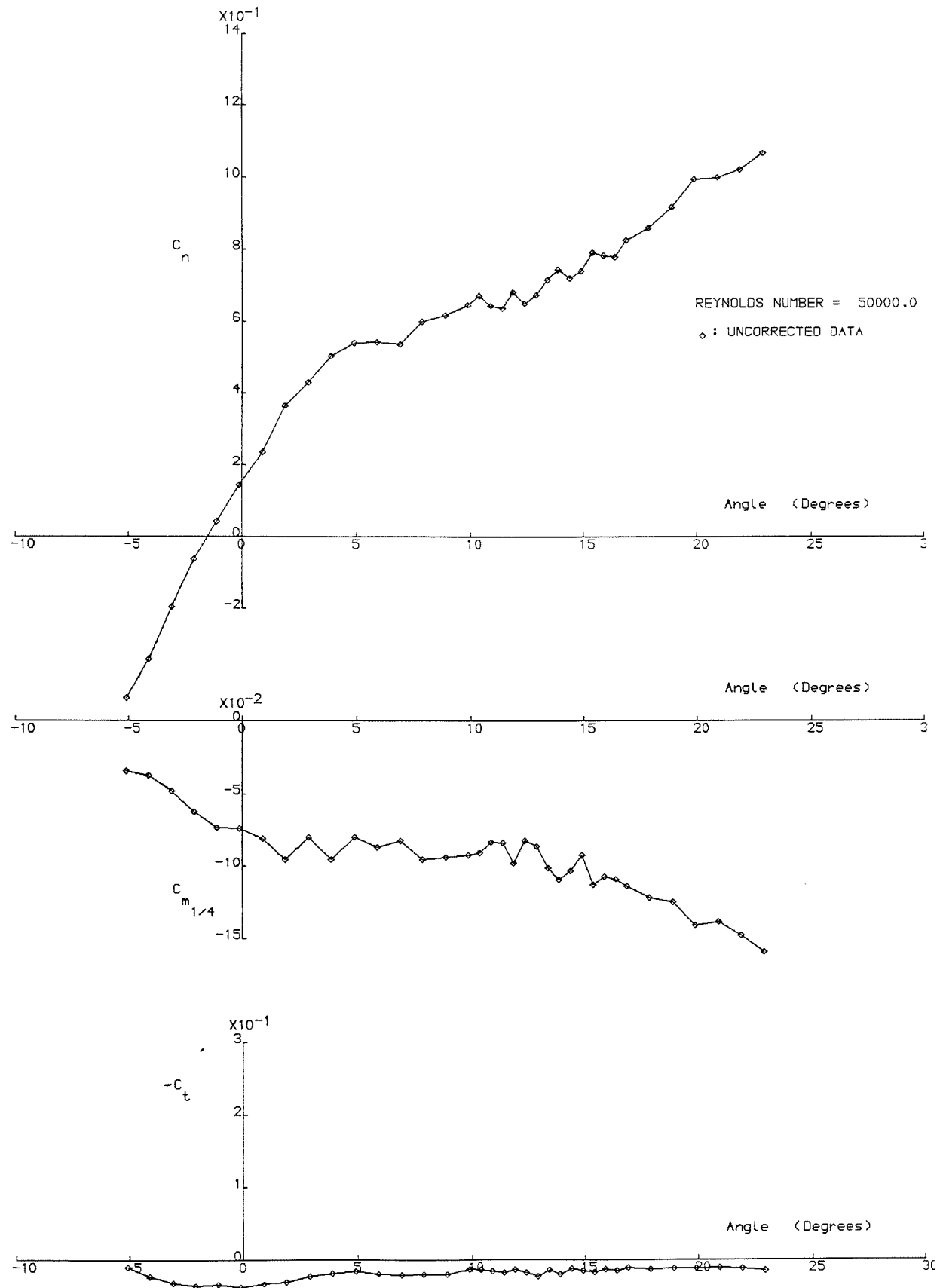


Figure 4.4.1. Normal Force, Quarter Chord Pitching Moment and Tangential Force Coefficient Variation With Angle of Attack at  $Re=50,000$ .

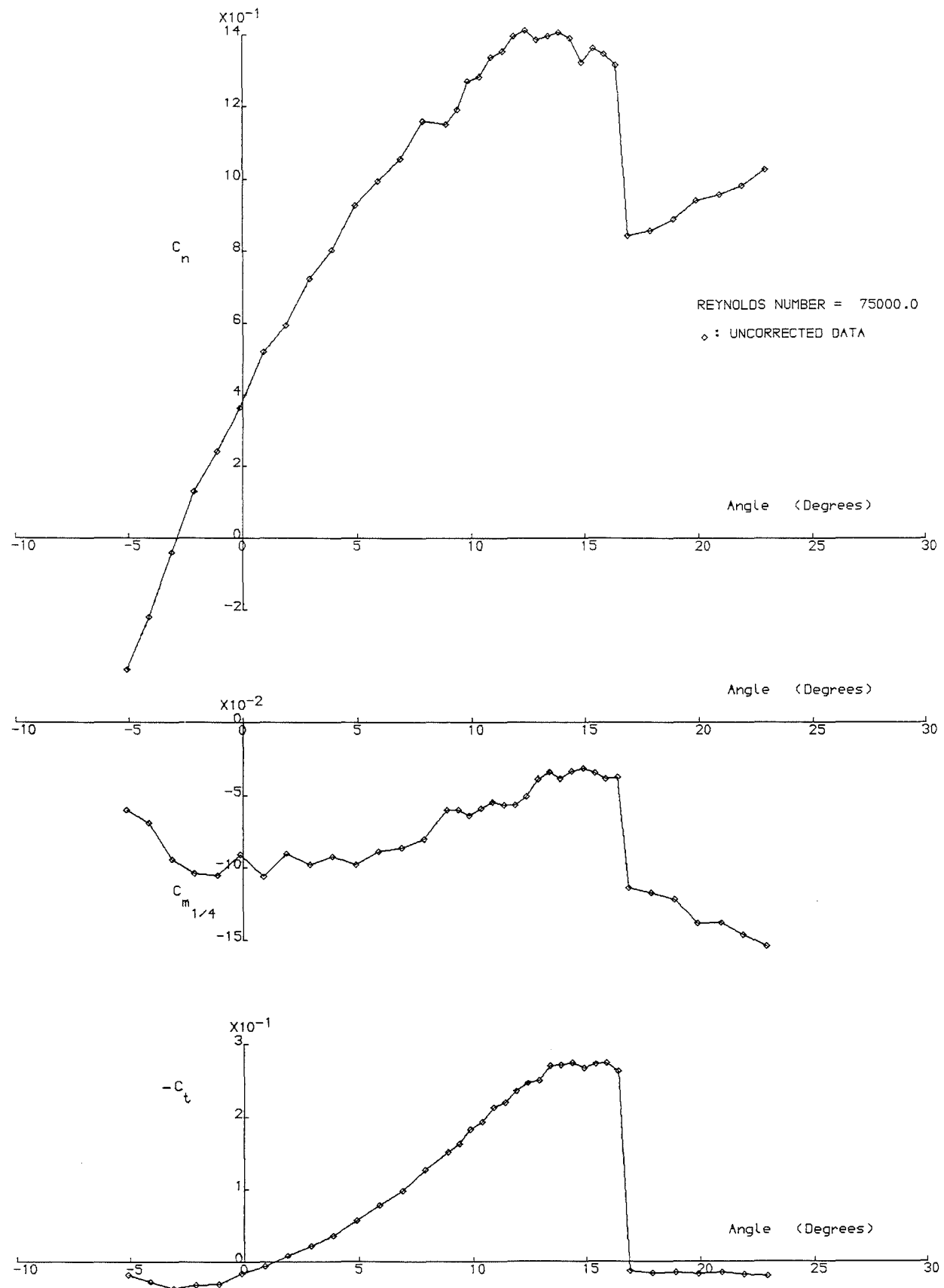


Figure 4.4.2. Normal Force, Quarter Chord Pitching Moment and Tangential Force Coefficient Variation With Angle of Attack at  $Re=75,000$ .

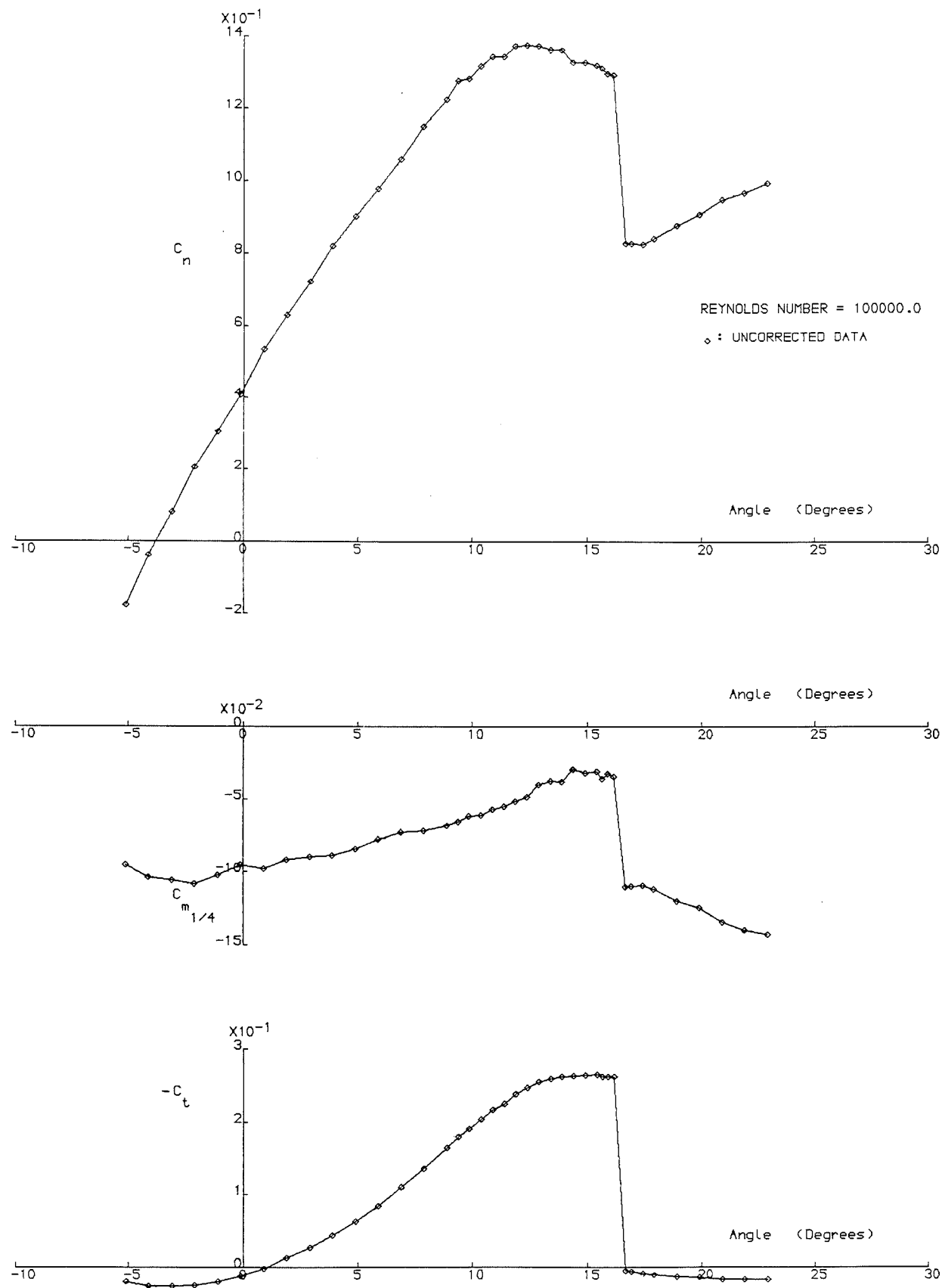


Figure 4.4.3. Normal Force, Quarter Chord Pitching Moment and Tangential Force Coefficient Variation With Angle of Attack at  $Re=100,000$ .

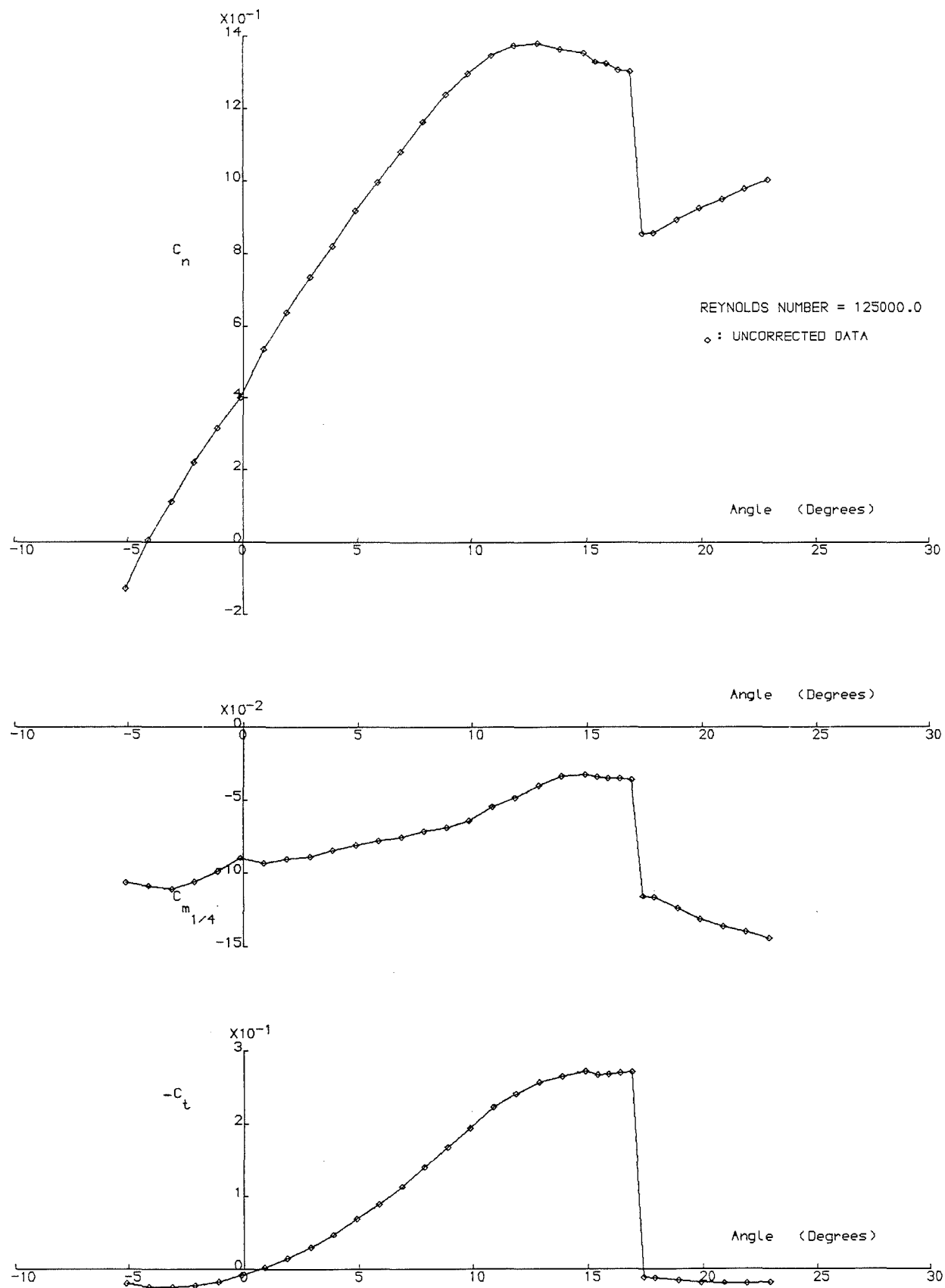


Figure 4.4.4. Normal Force, Quarter Chord Pitching Moment and Tangential Force Coefficient Variation With Angle of Attack at  $Re=125,000$ .

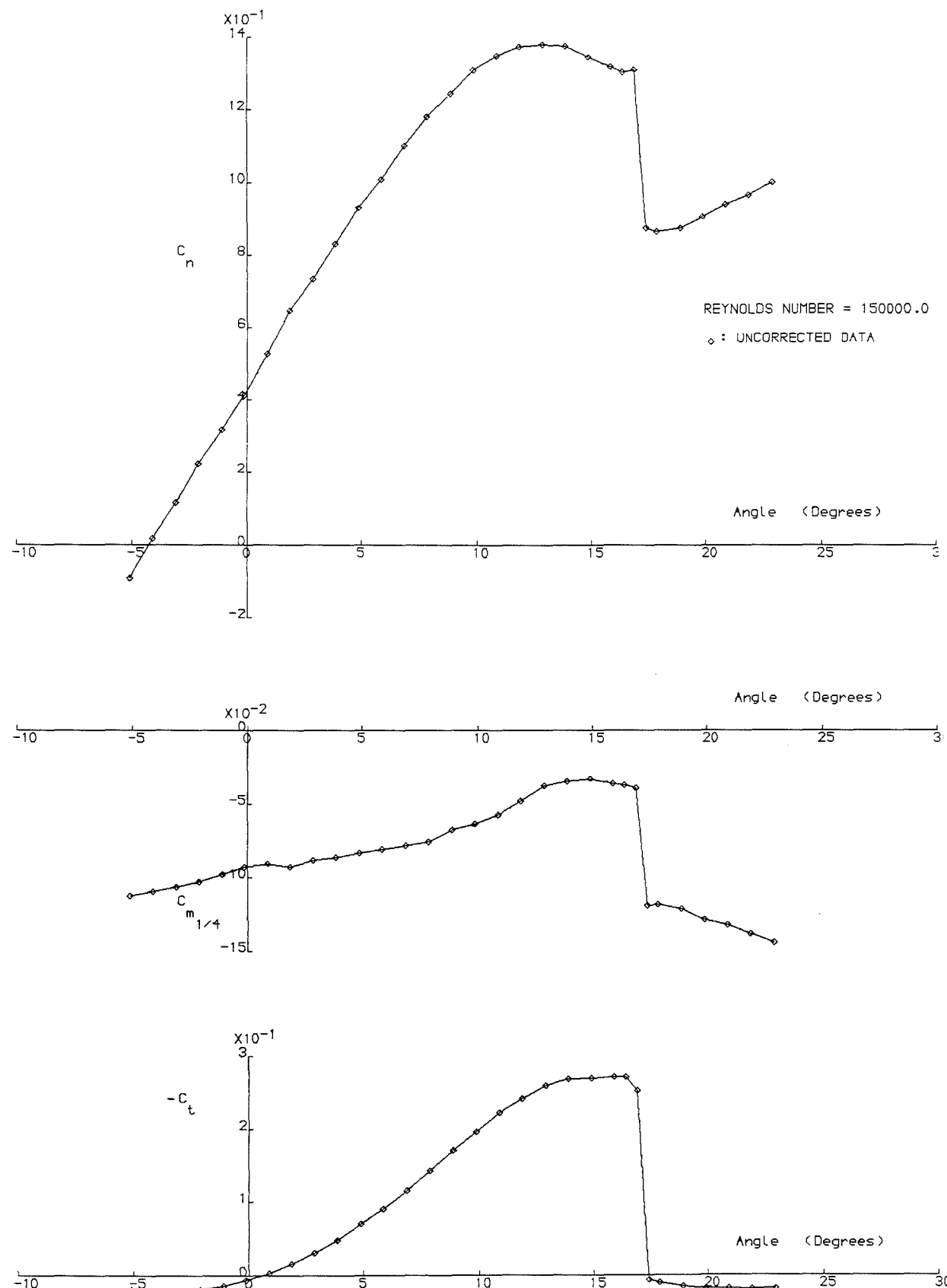


Figure 4.4.5. Normal Force, Quarter Chord Pitching Moment and Tangential Force Coefficient Variation With Angle of Attack at  $Re=150,000$ .

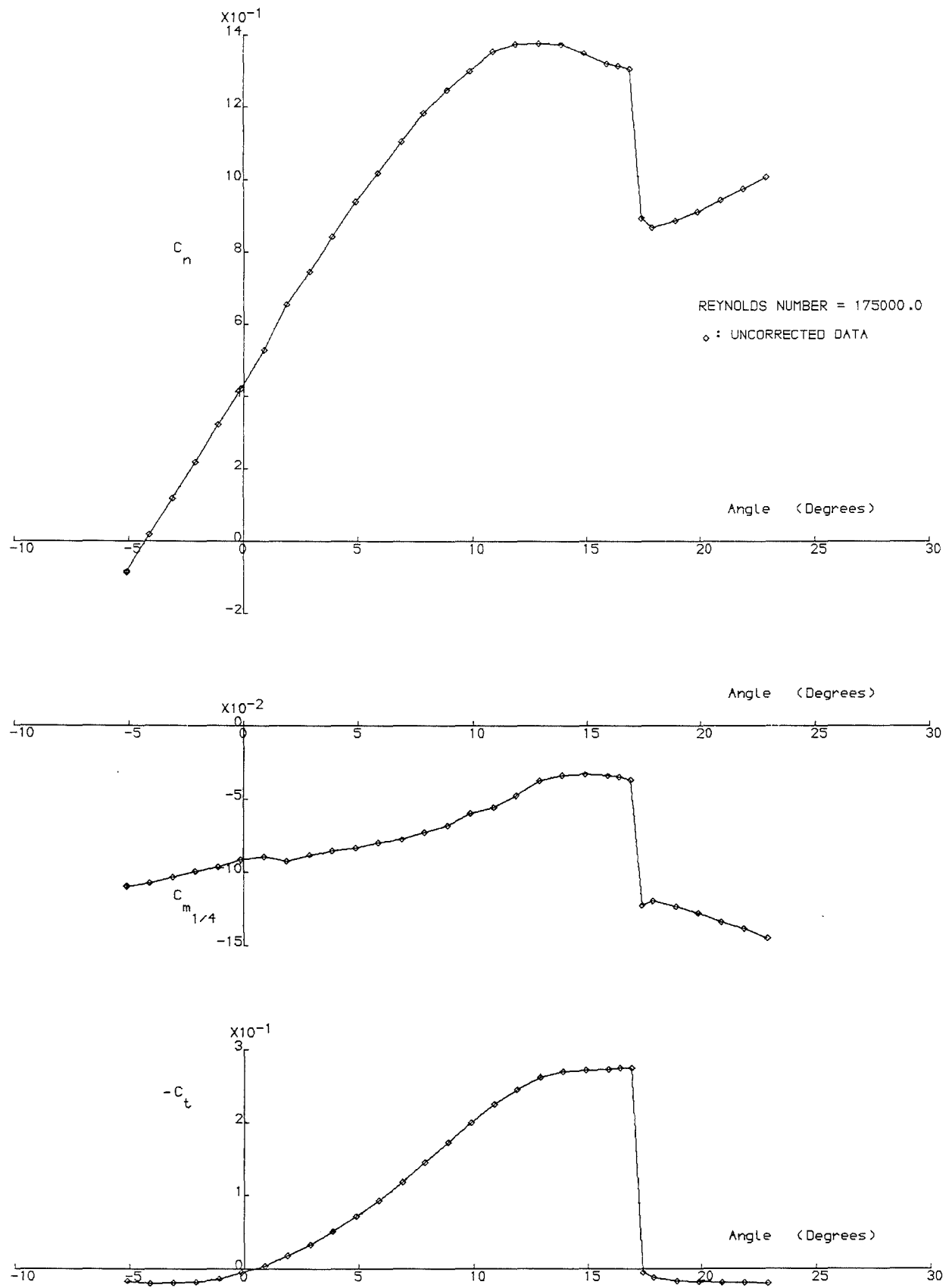


Figure 4.4.6. Normal Force, Quarter Chord Pitching Moment and Tangential Force Coefficient Variation With Angle of Attack at  $Re=175,000$ .

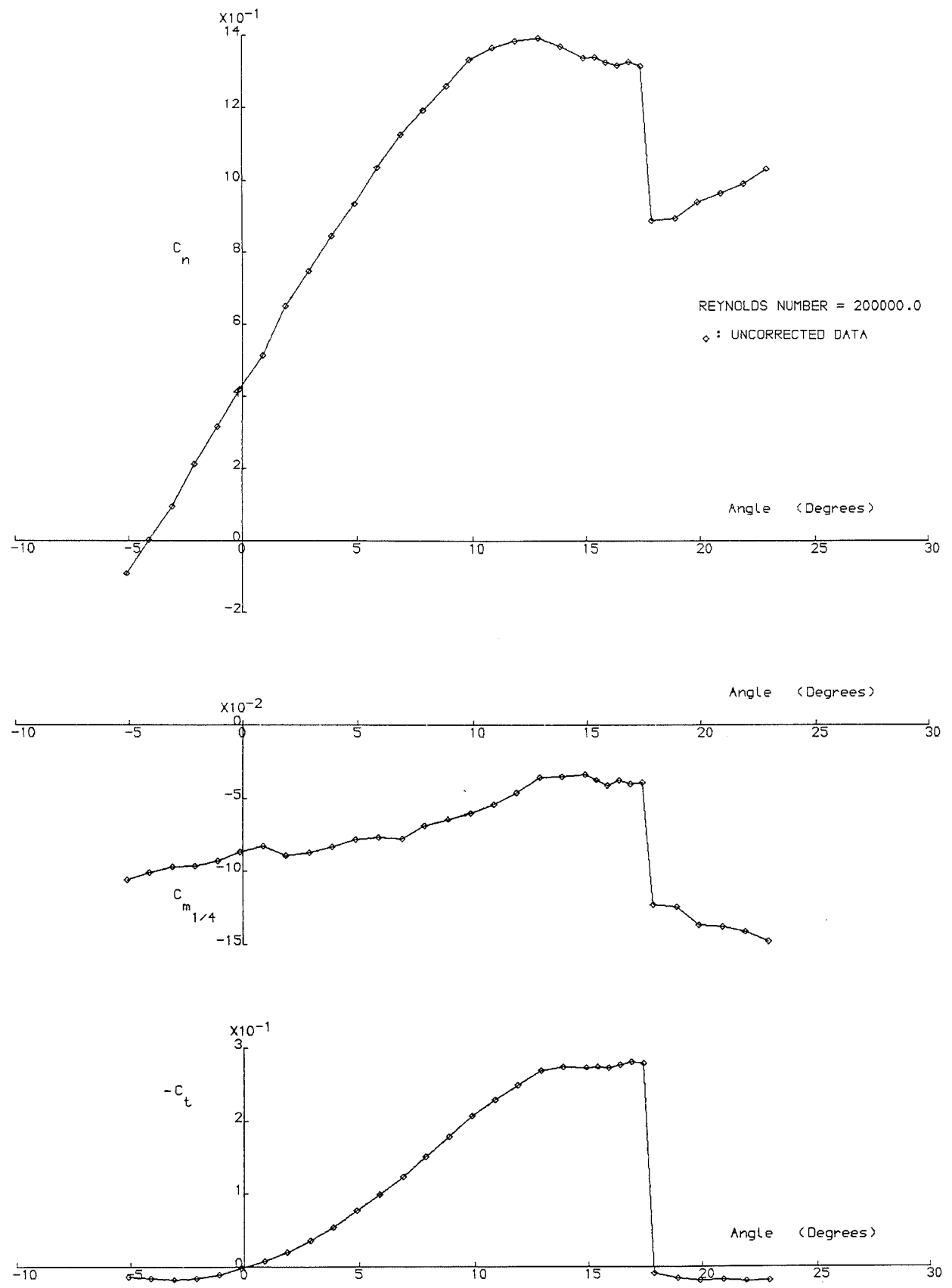


Figure 4.4.7. Normal Force, Quarter Chord Pitching Moment and Tangential Force Coefficient Variation With Angle of Attack at  $Re=200,000$ .

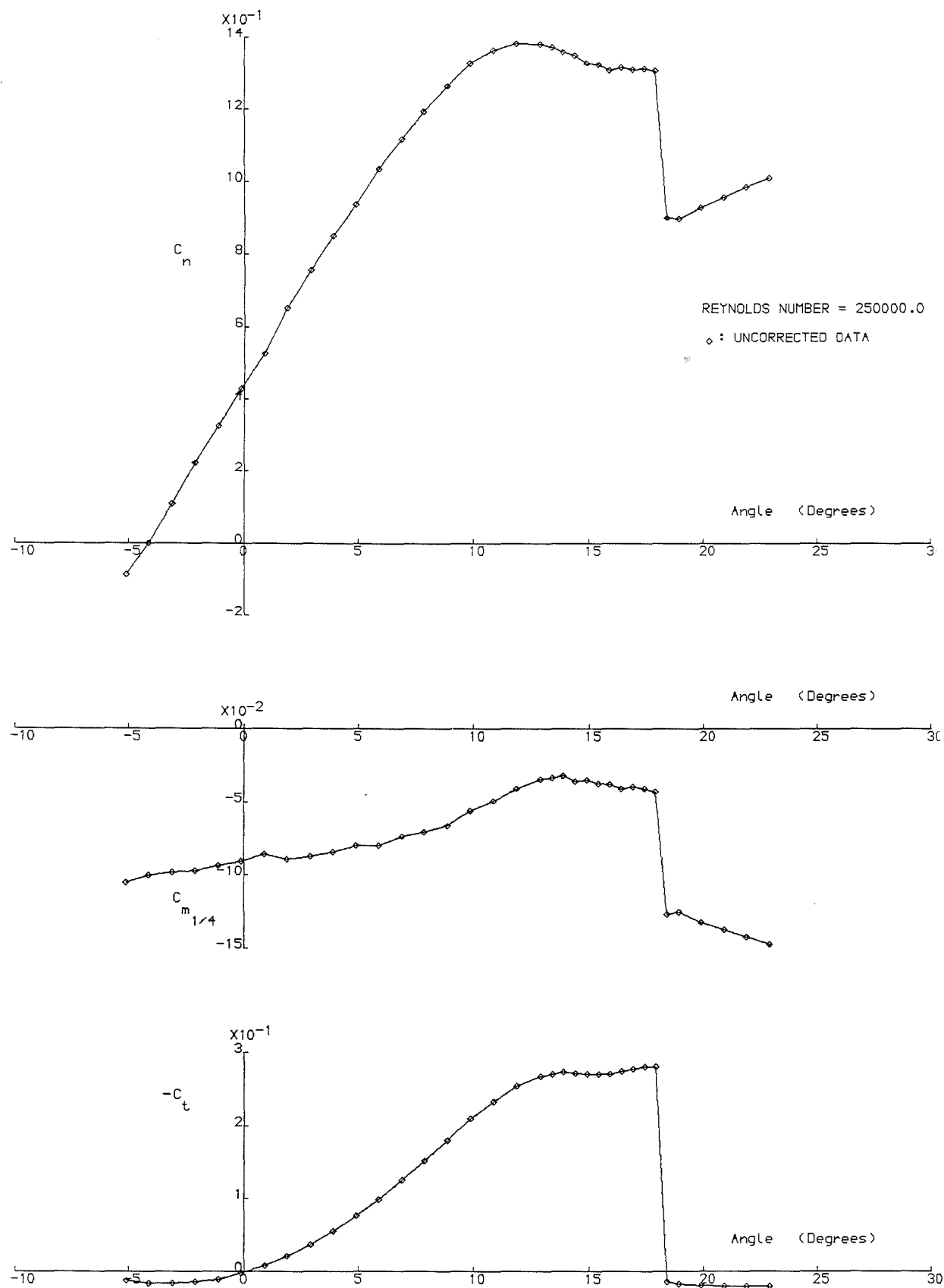


Figure 4.4.8. Normal Force, Quarter Chord Pitching Moment and Tangential Force Coefficient Variation With Angle of Attack at  $Re=250,000$ .

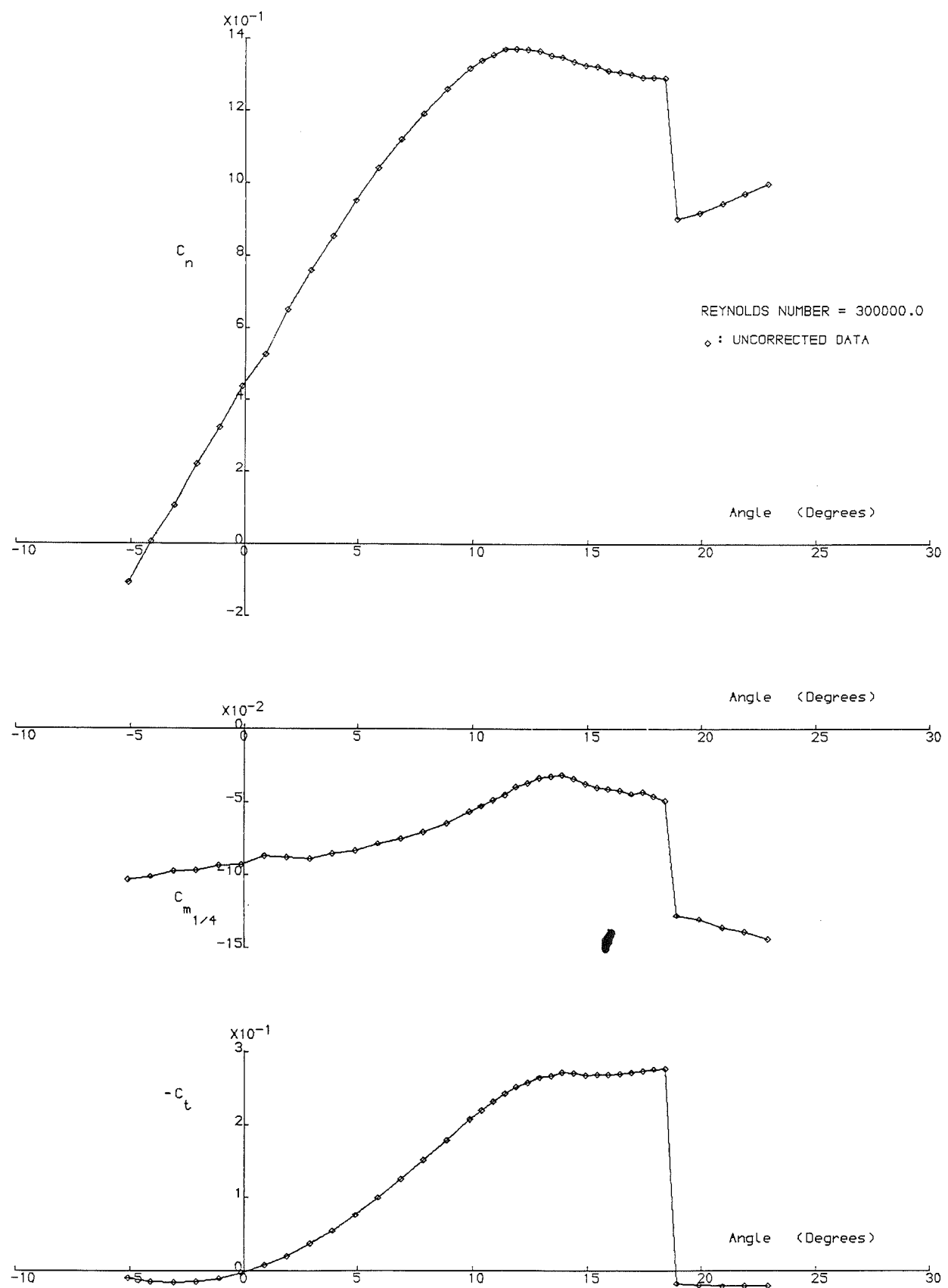


Figure 4.4.9. Normal Force, Quarter Chord Pitching Moment and Tangential Force Coefficient Variation With Angle of Attack at  $Re=300,000$ .

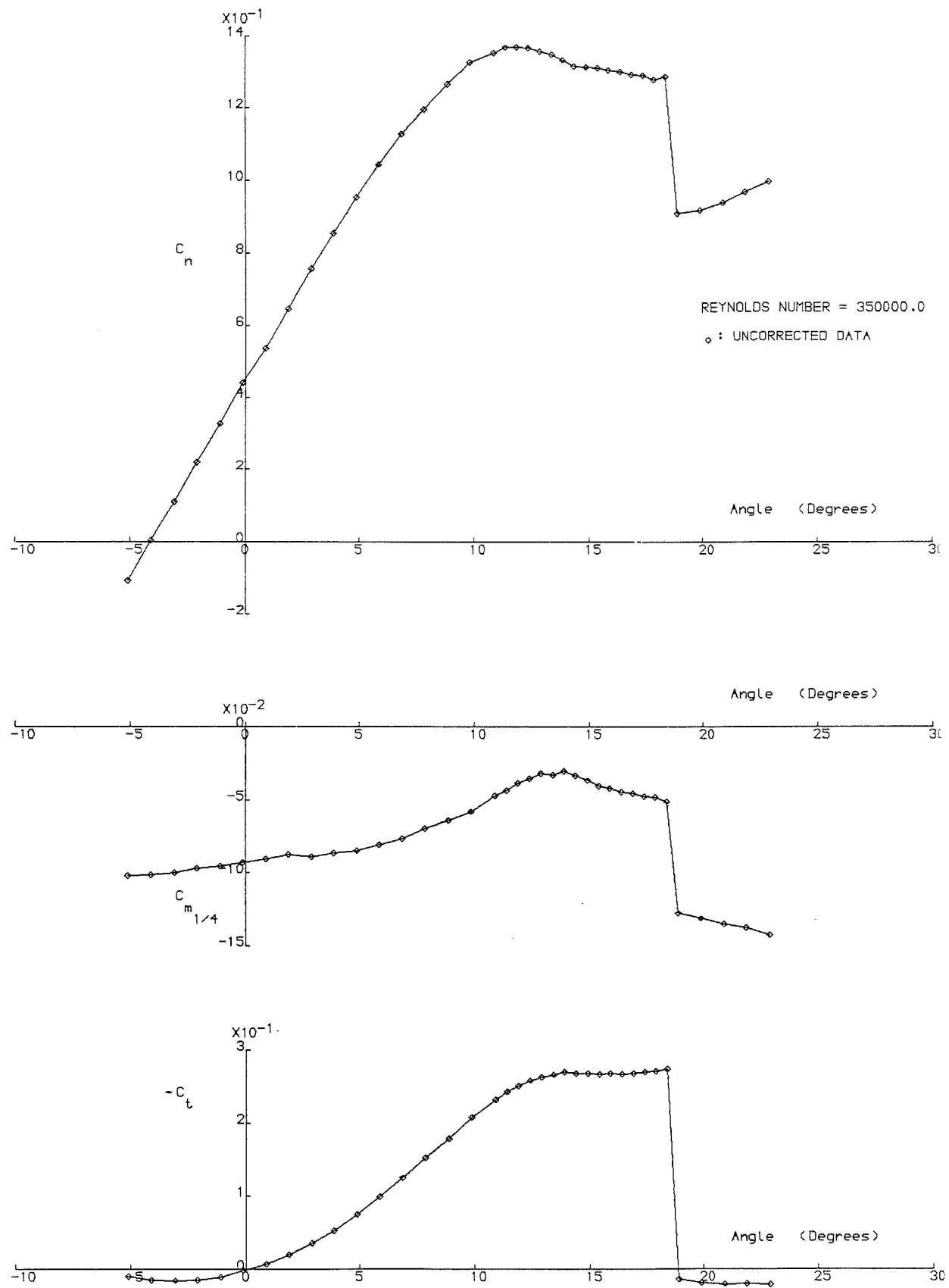


Figure 4.4.10. Normal Force, Quarter Chord Pitching Moment and Tangential Force Coefficient Variation With Angle of Attack at  $Re=350,000$ .

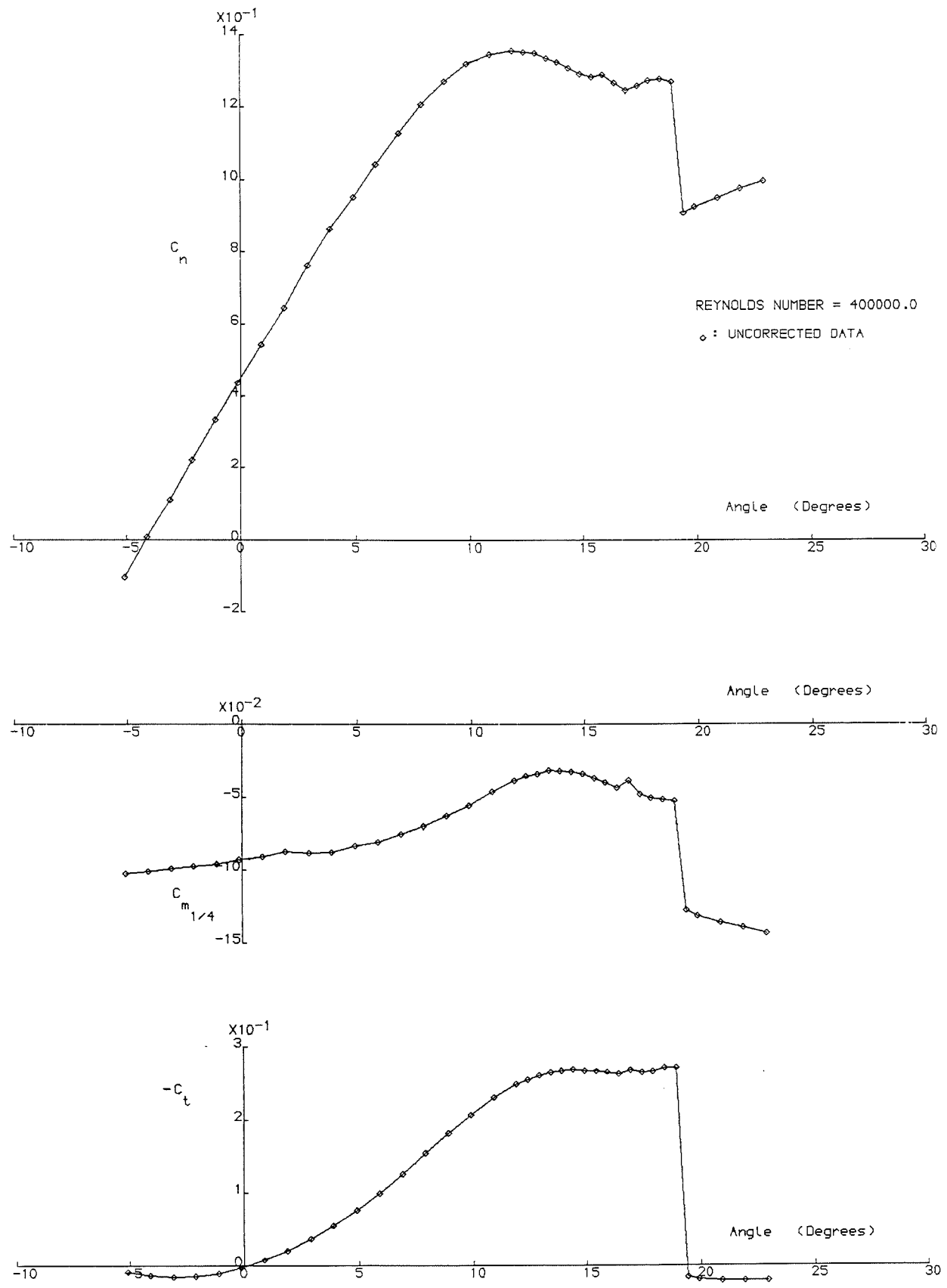


Figure 4.4.11. Normal Force, Quarter Chord Pitching Moment and Tangential Force Coefficient Variation With Angle of Attack at  $Re=400,000$ .

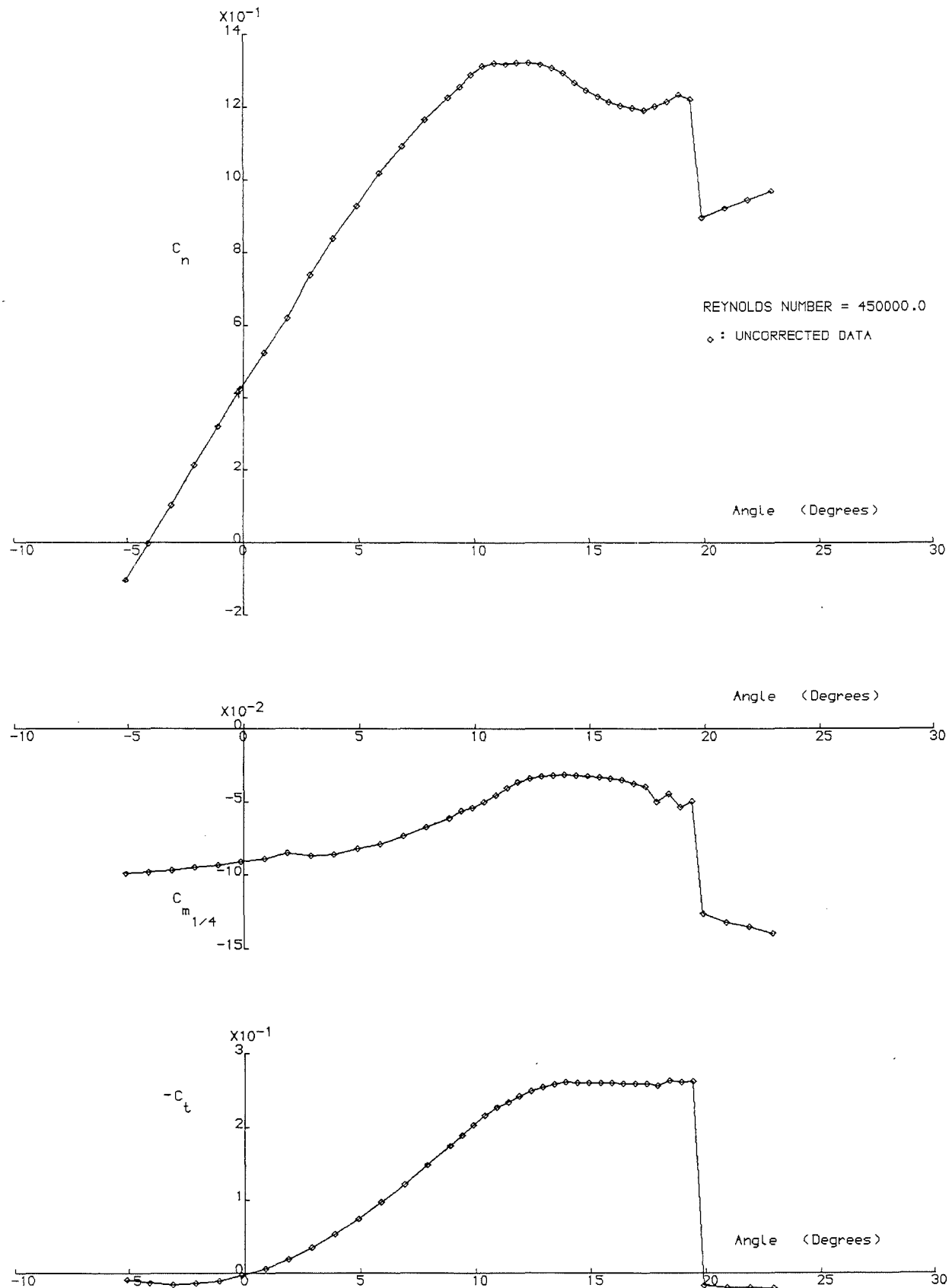


Figure 4.4.12. Normal Force, Quarter Chord Pitching Moment and Tangential Force Coefficient Variation With Angle of Attack at  $Re=450,000$ .

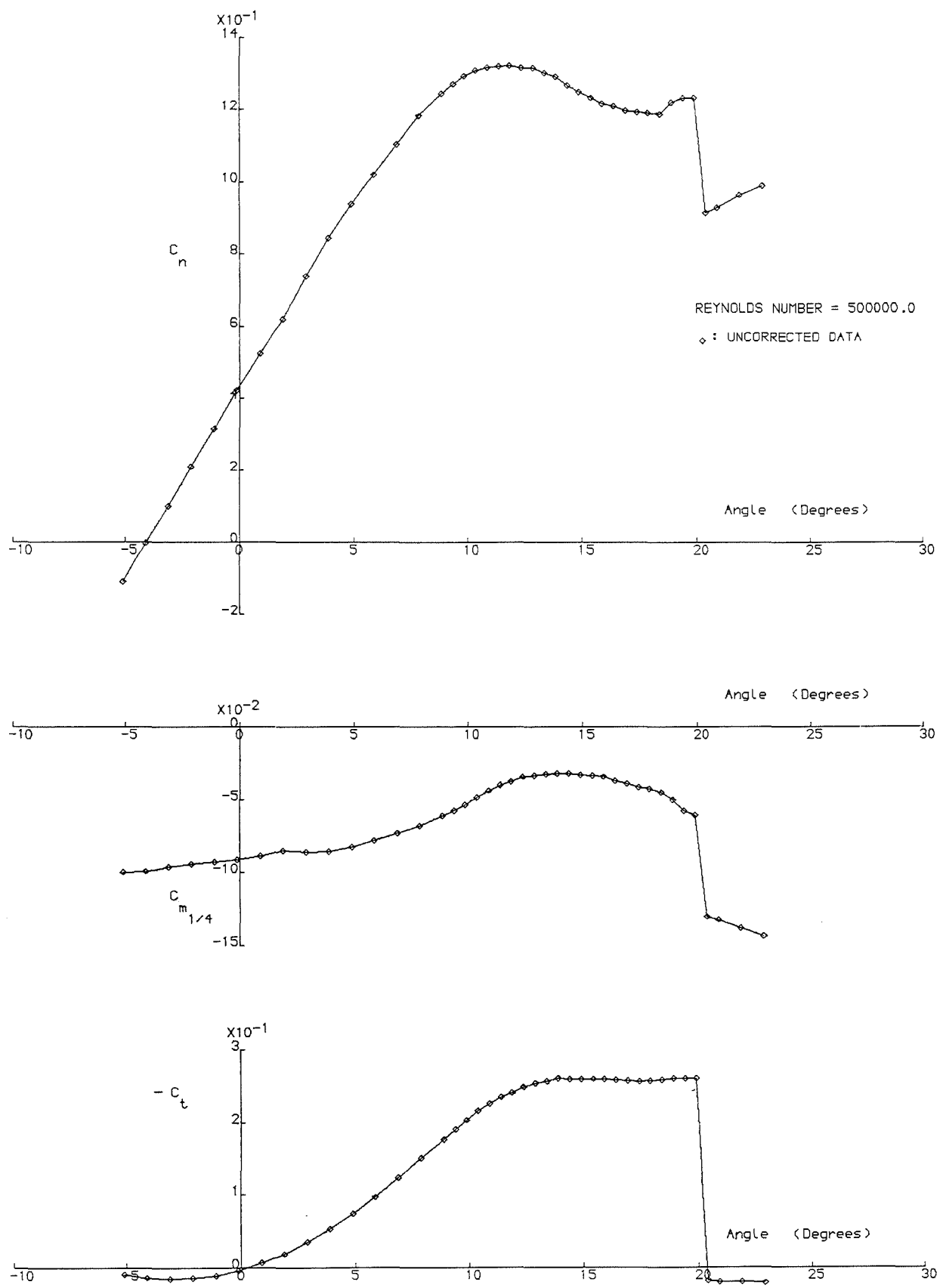


Figure 4.4.13. Normal Force, Quarter Chord Pitching Moment and Tangential Force Coefficient Variation With Angle of Attack at  $Re=500,000$ .

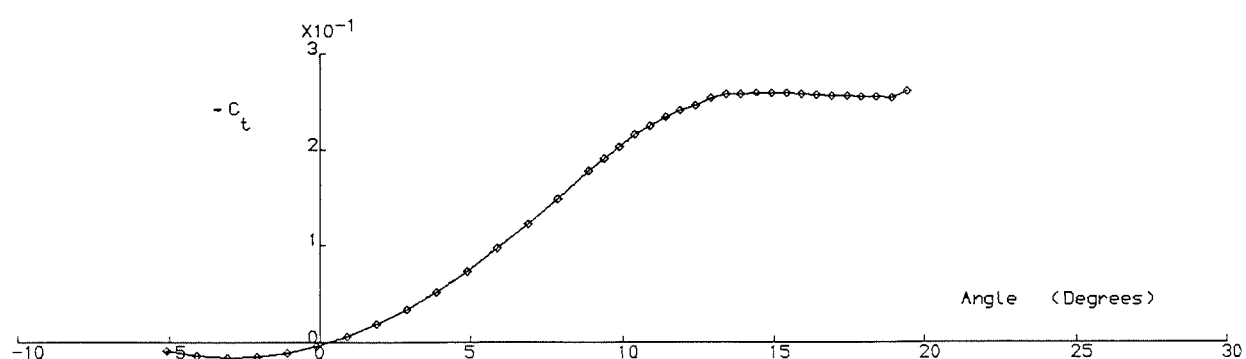
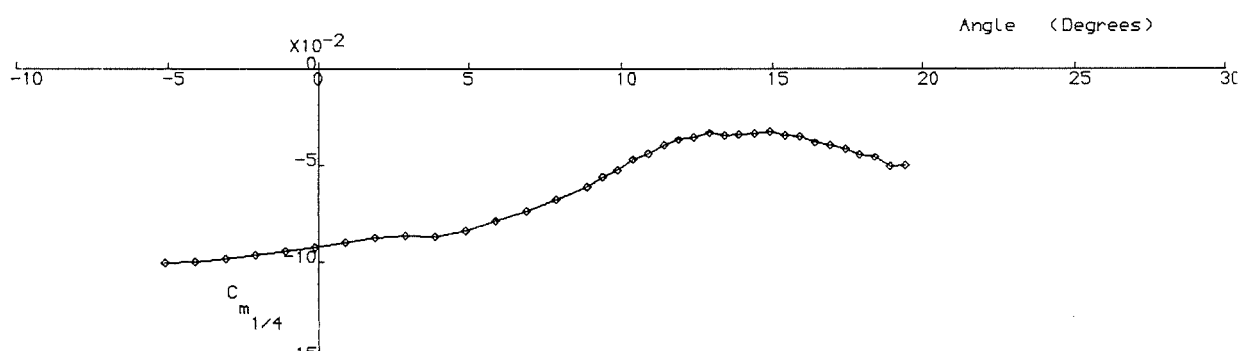
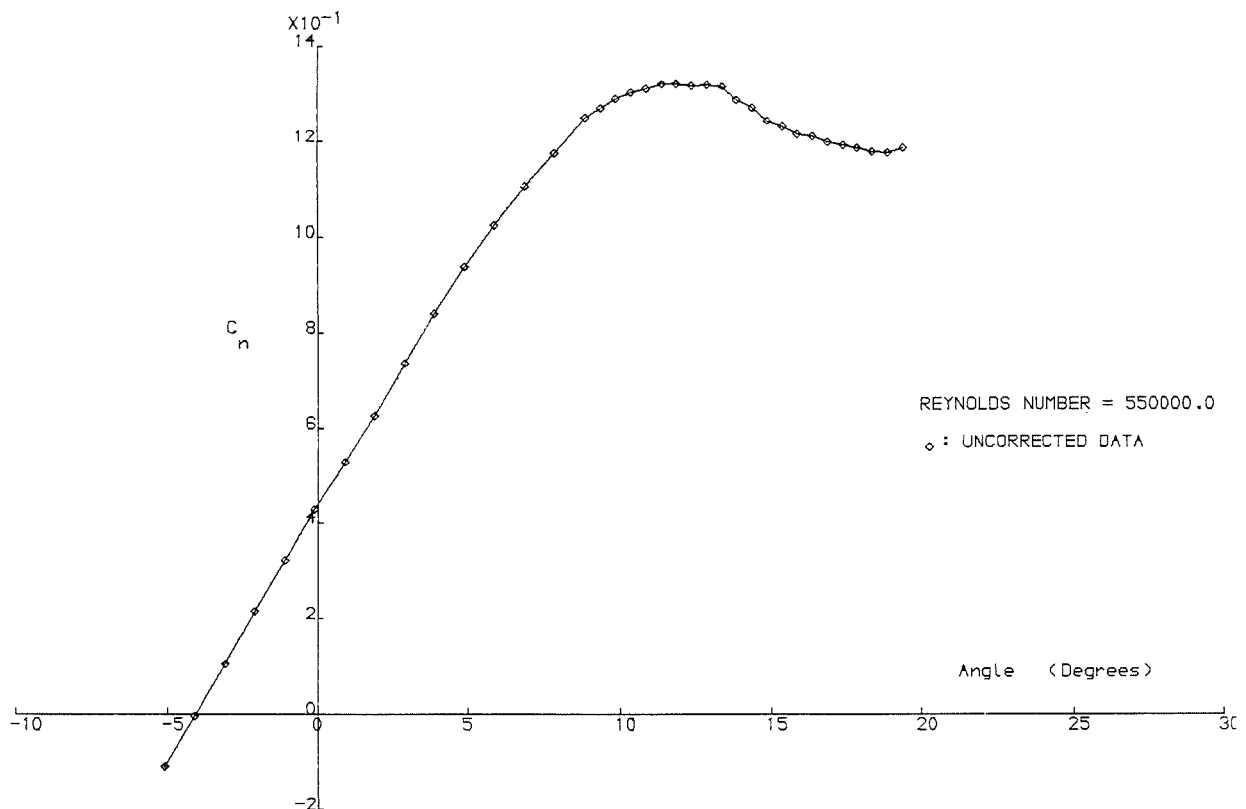


Figure 4.4.14. Normal Force, Quarter Chord Pitching Moment and Tangential Force Coefficient Variation With Angle of Attack at  $Re=550,000$ .

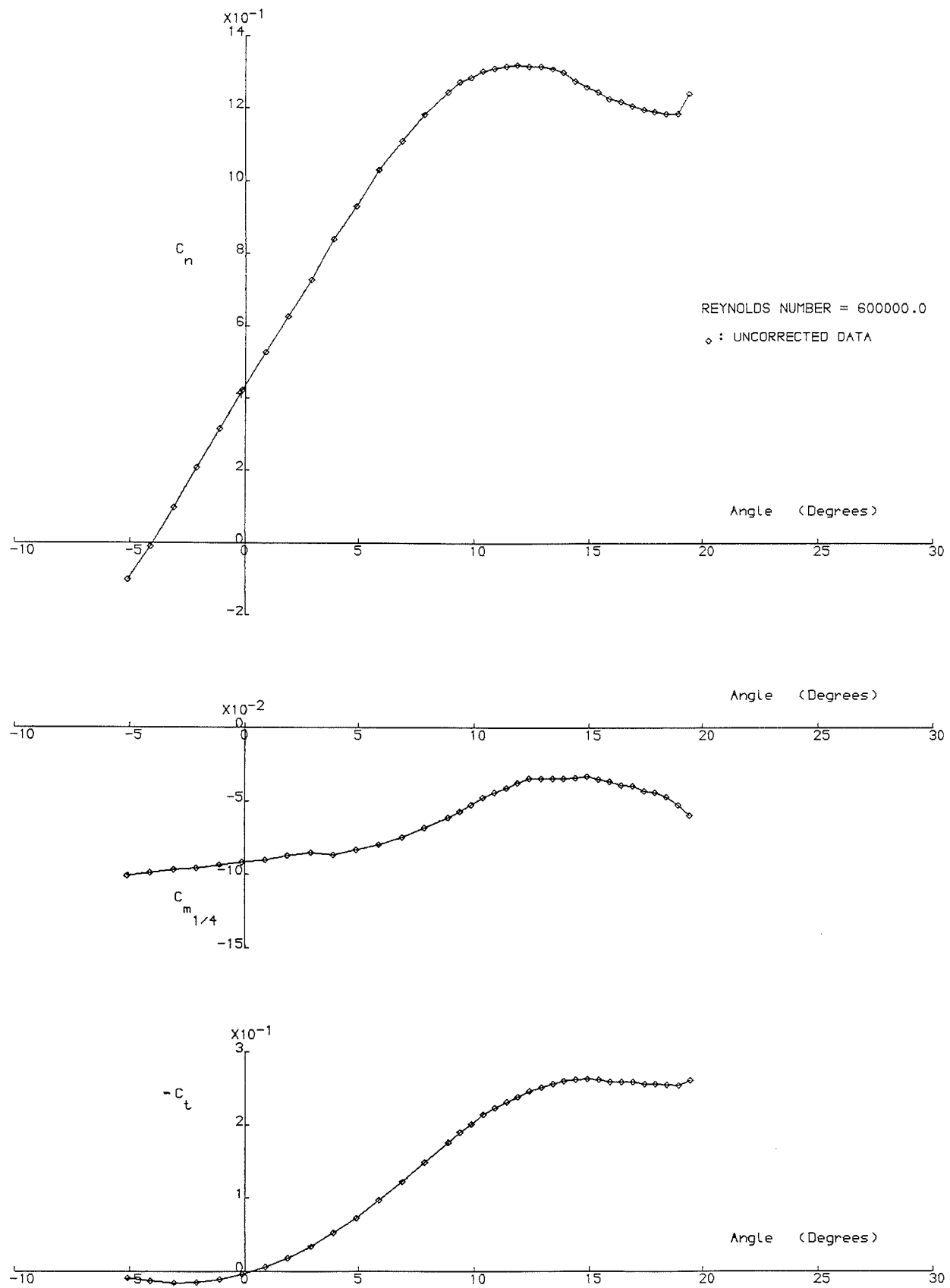


Figure 4.4.15. Normal Force, Quarter Chord Pitching Moment and Tangential Force Coefficient Variation With Angle of Attack at  $Re=600,000$ .

Wortmann  
 FX 63-137  
 Corrected data  
 $R_c = 99,388$   
 $c = 6$  in.  
 Smooth

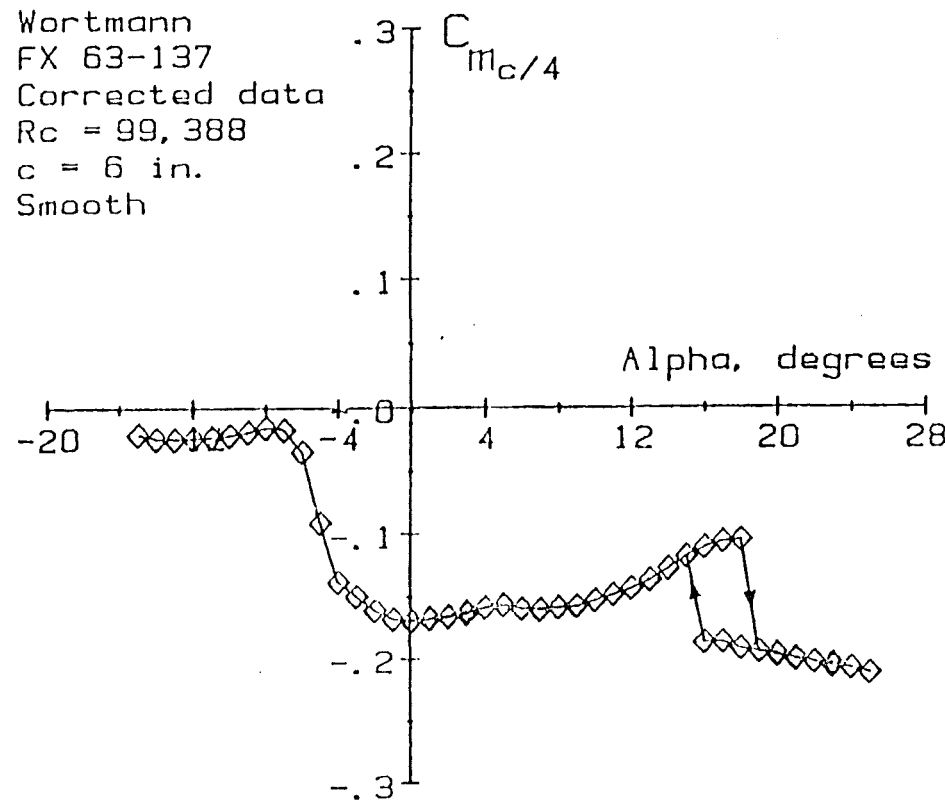


Fig. 4.4.16. Quarter Chord Pitching Moment Coefficient Versus Angle of Attack for the Wortmann FX-63-137 Aerofoil  
 $(R_c=100,000)$

(Adapted from Reference 26)

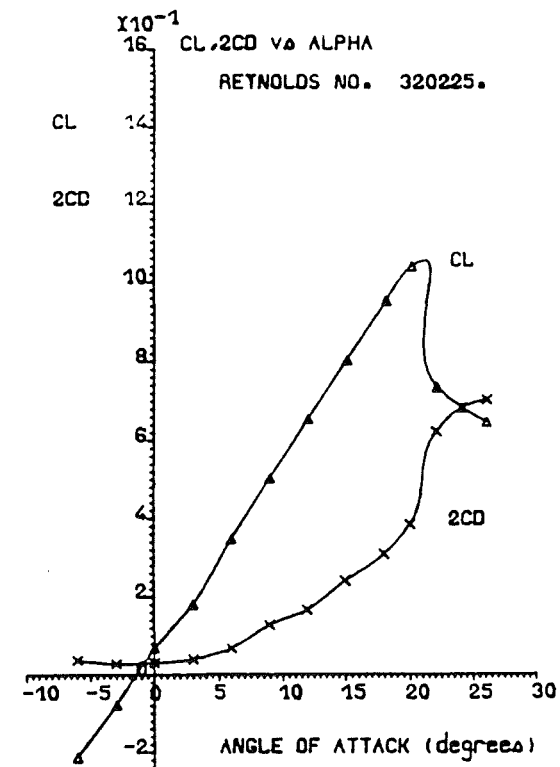


Fig. 4.4.17. NACA-23012 Aerofoil Data for AR=4.0.  
 (Adapted from Reference 36)

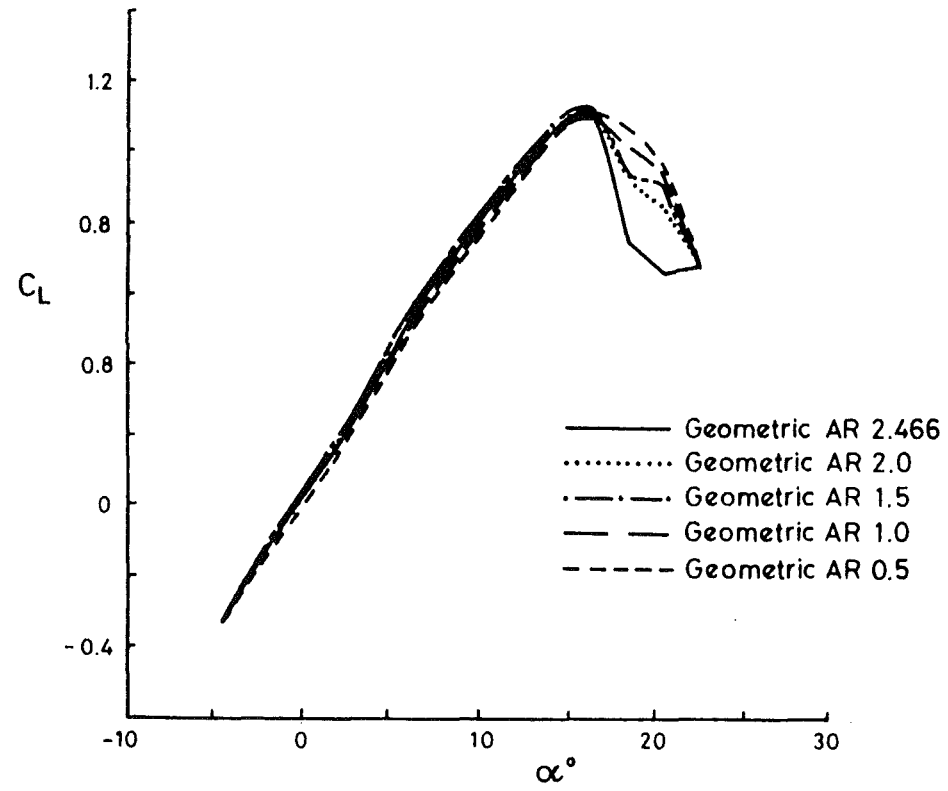


Fig. 4.4.18. Lift Coefficient Versus Uncorrected Incidence of a NACA-23012 Aerofoil at a Reynolds Number of 350,000.

(Adapted from Reference 37)

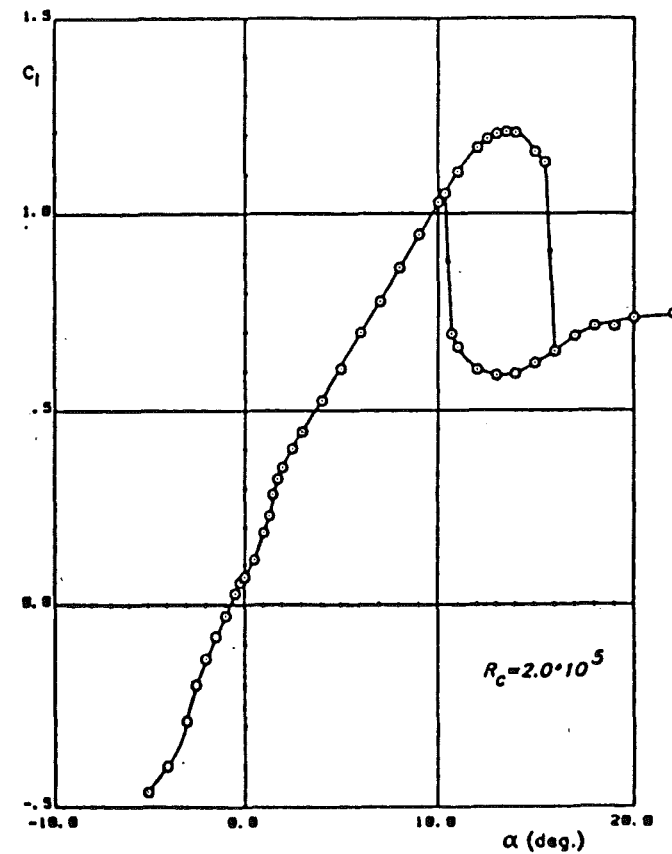


Fig. 4.4.19. Measured Aerodynamic Characteristics of a NACA-23012 Airfoil.

(Adapted from Reference 38)

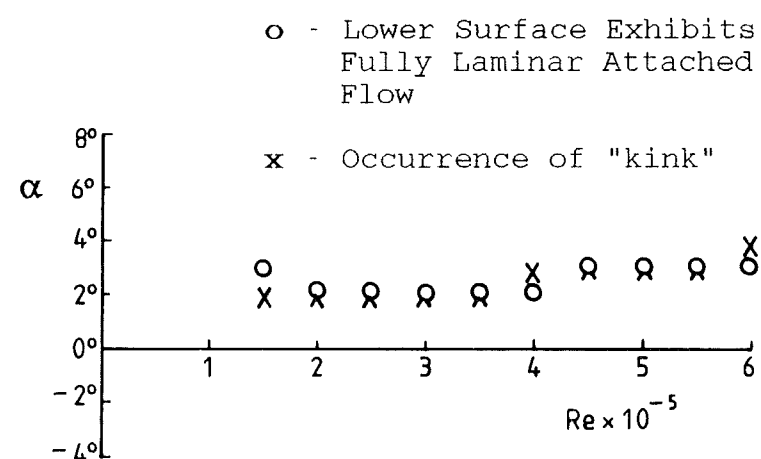


Fig. 4.4.20. Comparison of Results for the Occurrence of the 'kink' on  $C_N$  and  $C_{Mc/4}$  Curves With Those Defining Fully Laminar Flow Using Coton's Method.

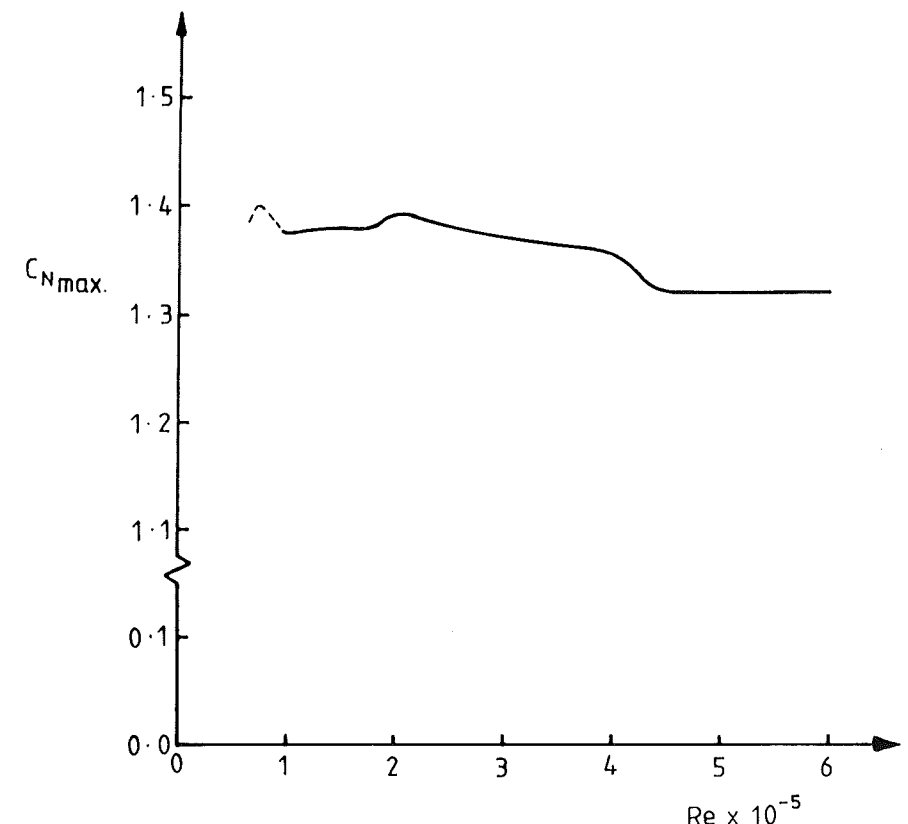


Fig. 4.5.1. Maximum Normal Force Coefficient Variation With Reynolds Number.

Wortmann  
FX 63-137  
 $Re = 77,604$

Uncorrected Data

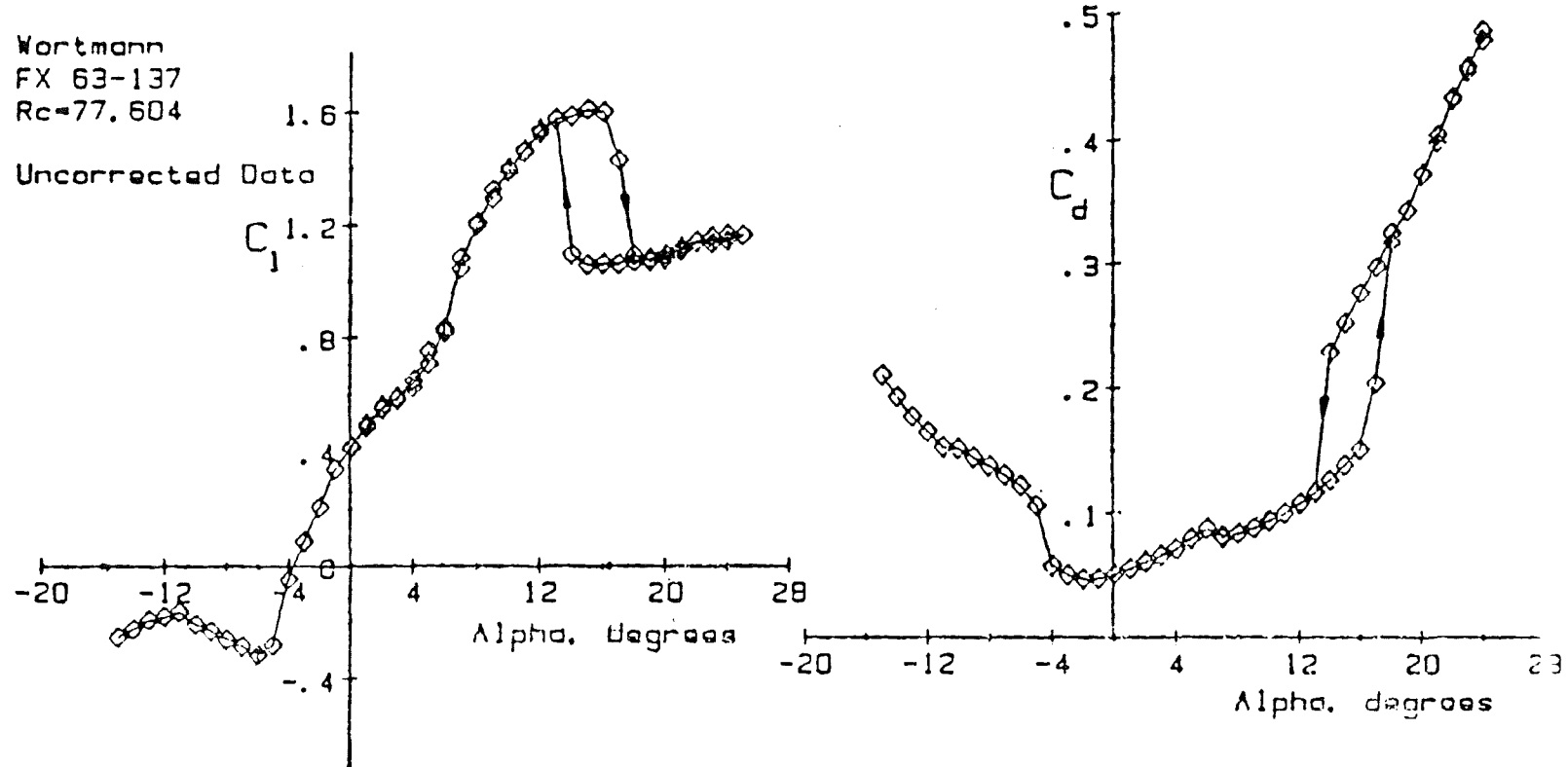


Figure 4.4.21. Two Dimensional Lift and Drag Coefficients versus Angle of Attack,  $Re = 80,000$ .

(Adapted from Reference 33)

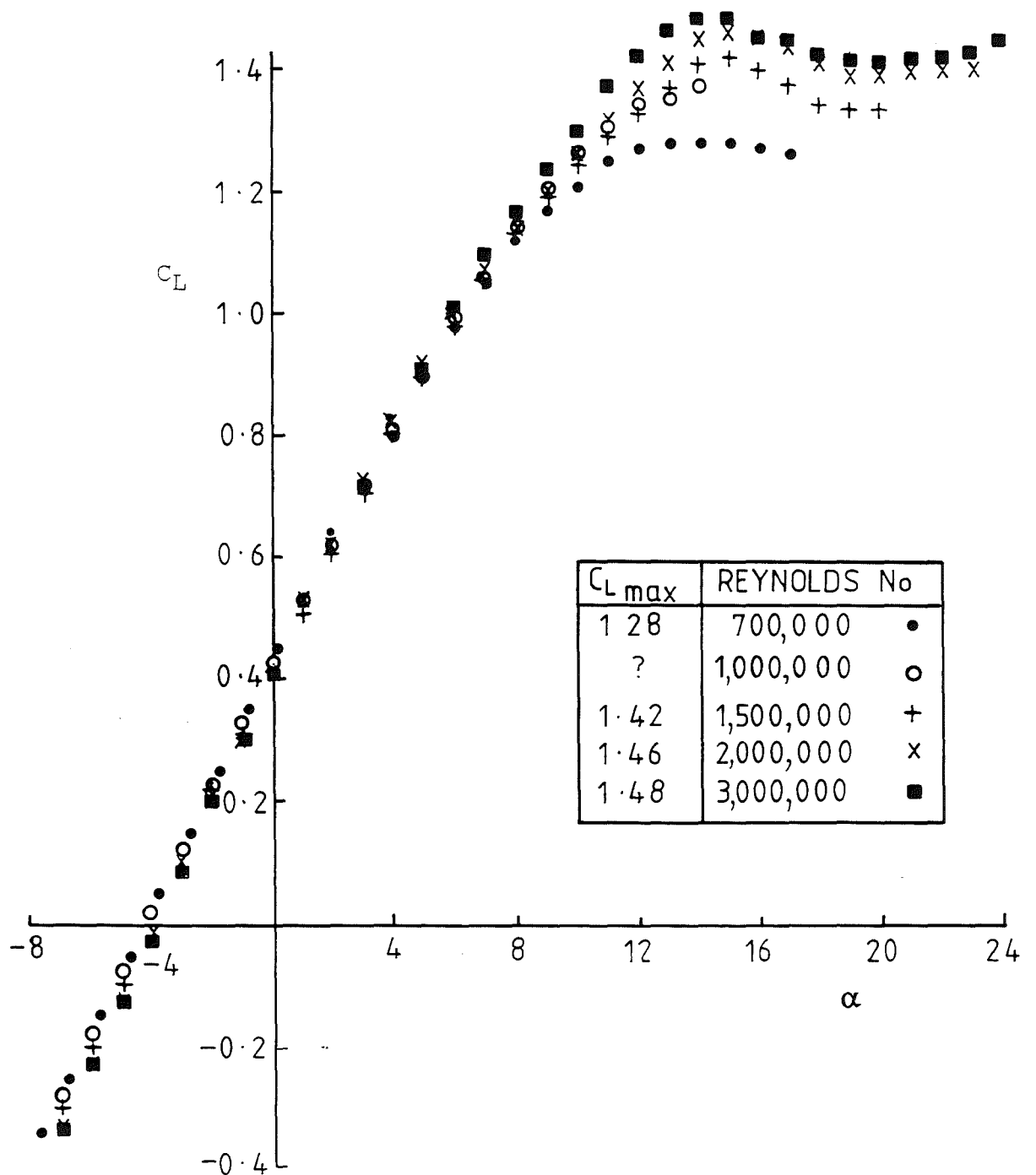


Figure 4.5.2 Lift Coefficient Variation with Incidence and Reynolds Number of a NACA-4415 Aerofoil Tested at Stuttgart (1962-72).

(Adapted from Reference 29)

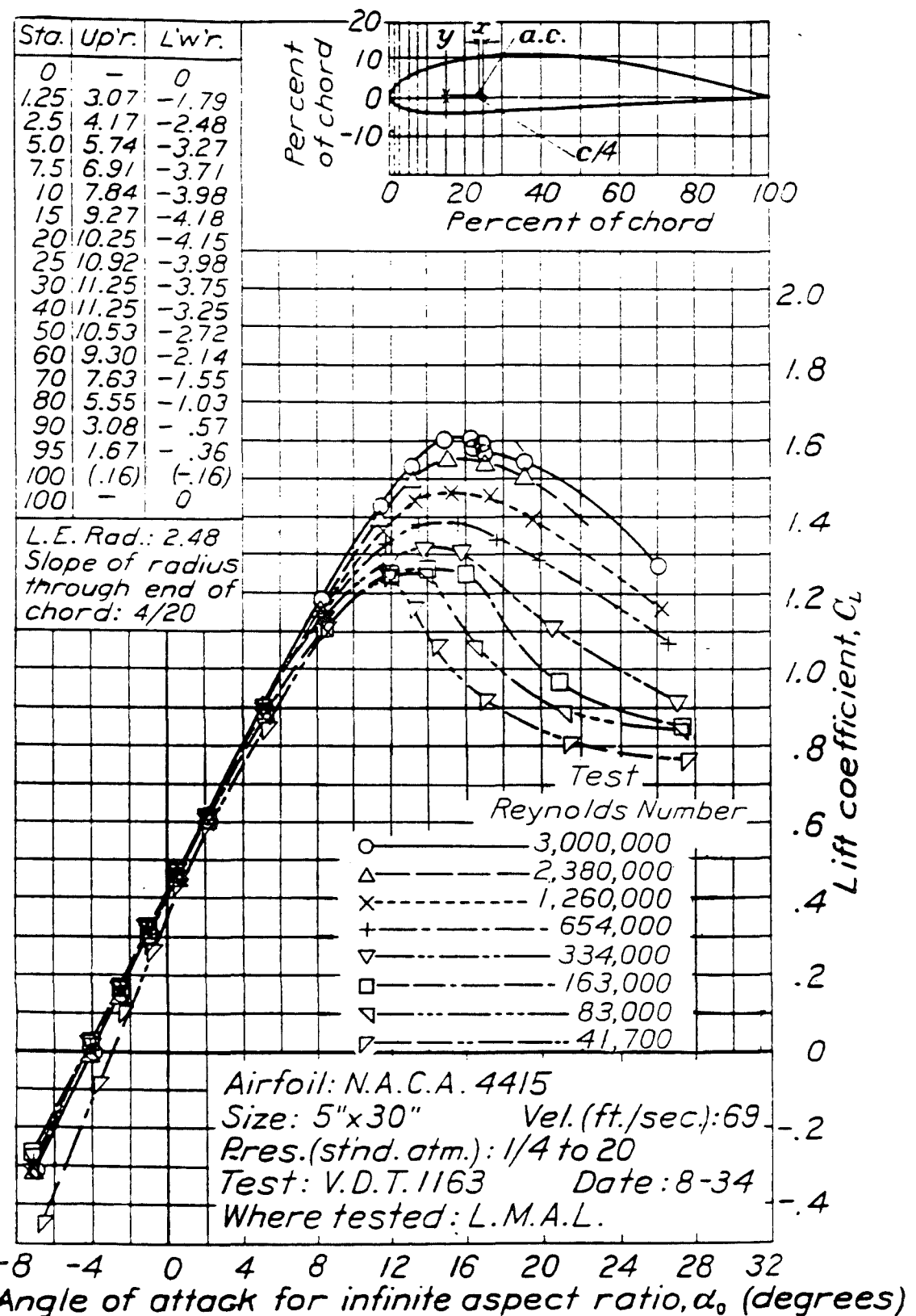


Figure 4.5.3 Lift Coefficient Variation with Incidence and Reynolds Number of a NACA-4415 Aerofoil Tested at NACA VDT (1934).

(Adapted from Reference 34)

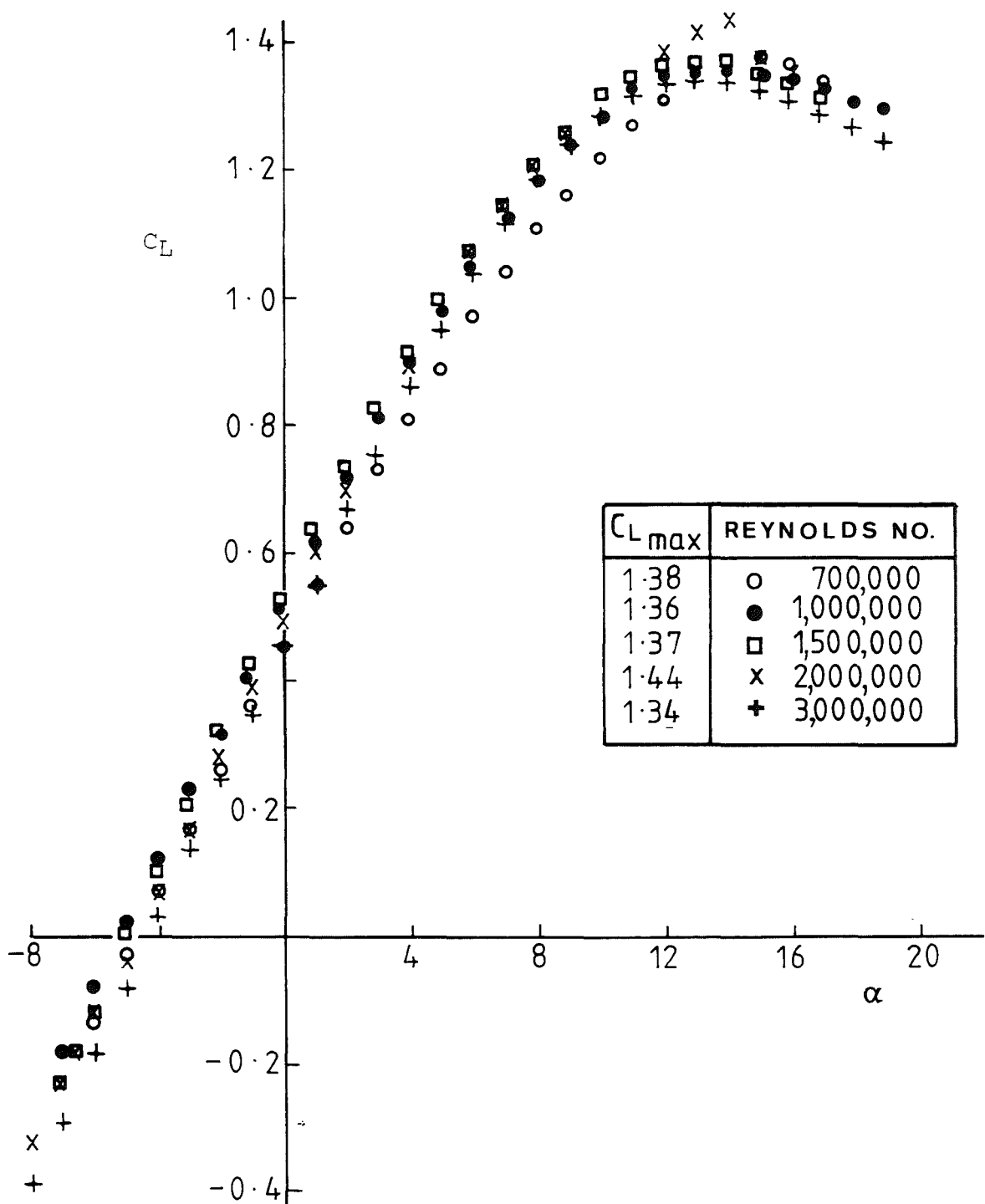


Figure 4.5.4 Lift Coefficient Variation with Incidence and Reynolds Number of a NACA-4415 Aerofoil Tested at NACA LTT (1945).

(Adapted from Reference 28)

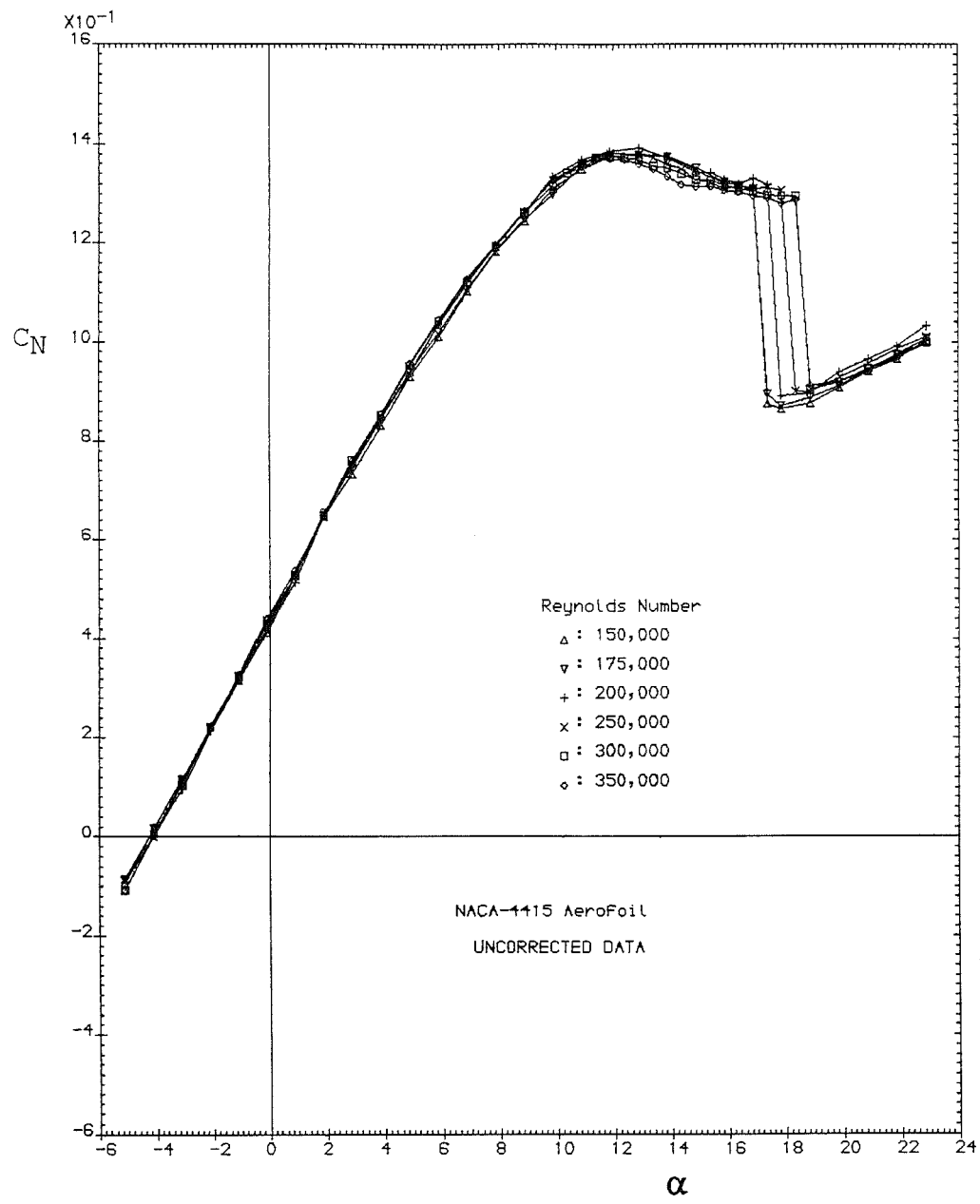


Figure 4.5.5 Normal Force Coefficient Variation with Incidence and Reynolds Number of a NACA-4415 Aerofoil Tested at University of Glasgow (1987).

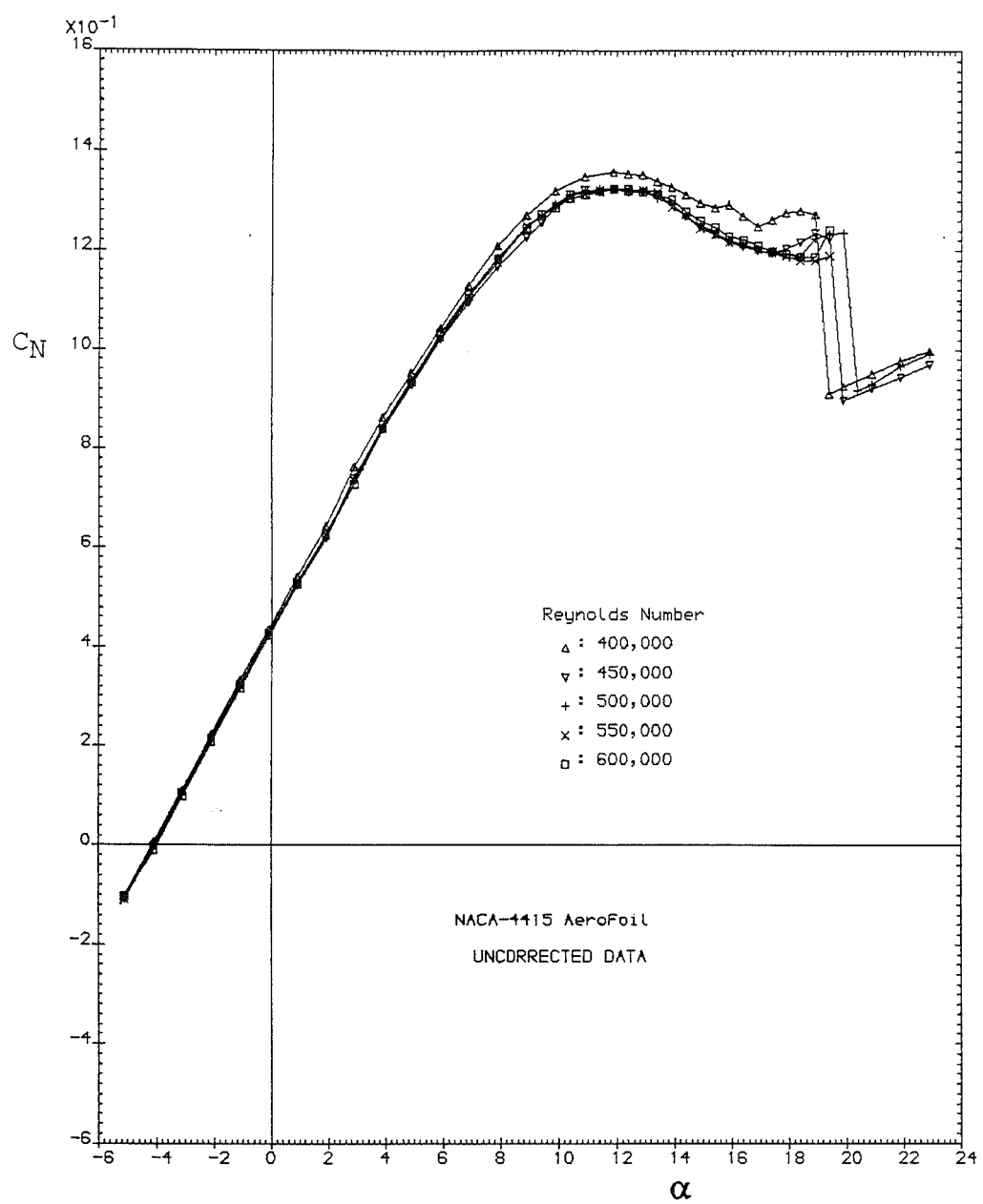


Figure 4.5.5. Concluded

Wortmann  
FX 63-137  
Corrected data  
 $R_c = 199.487$   
 $c = 6$  in.  
Smooth

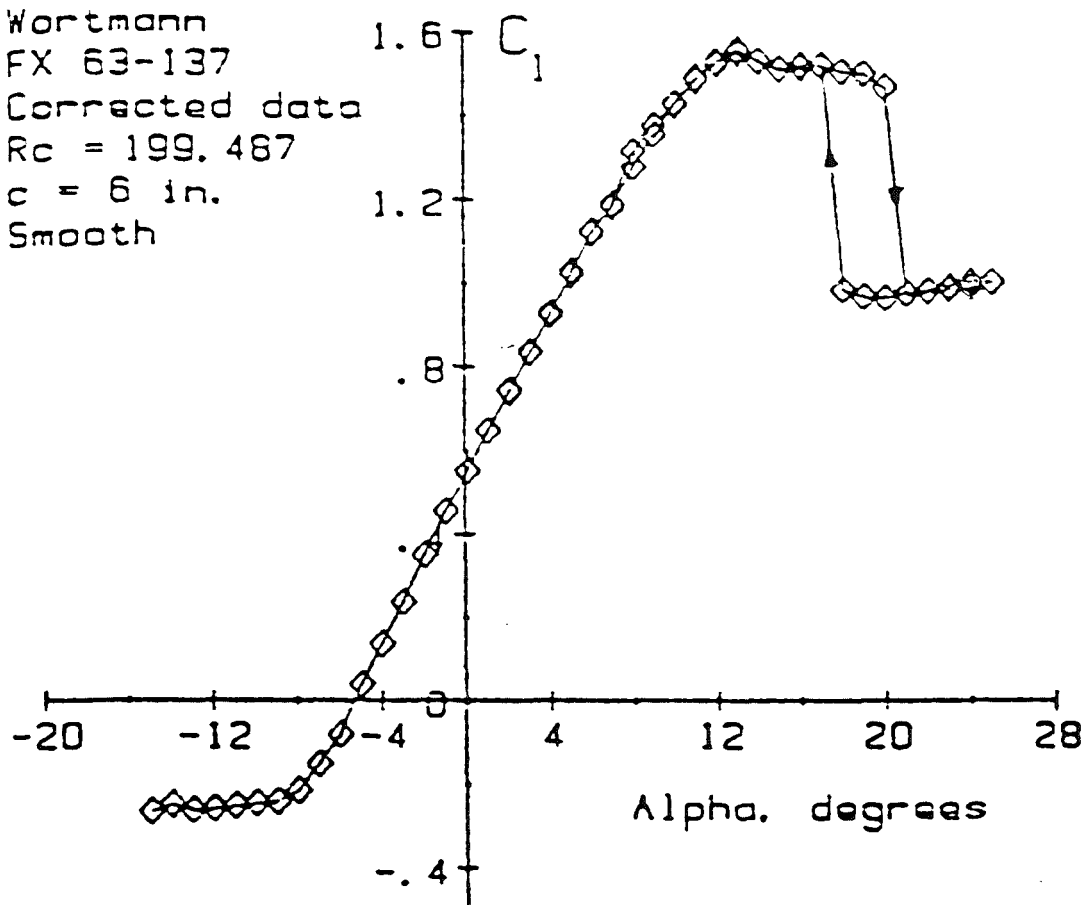


Figure 4.5.6 Lift Coefficient Variation with Incidence of a Wortmann FX-63-137 Aerofoil Tested at a Reynolds Number of 200,000.

(Adapted from Reference 26)

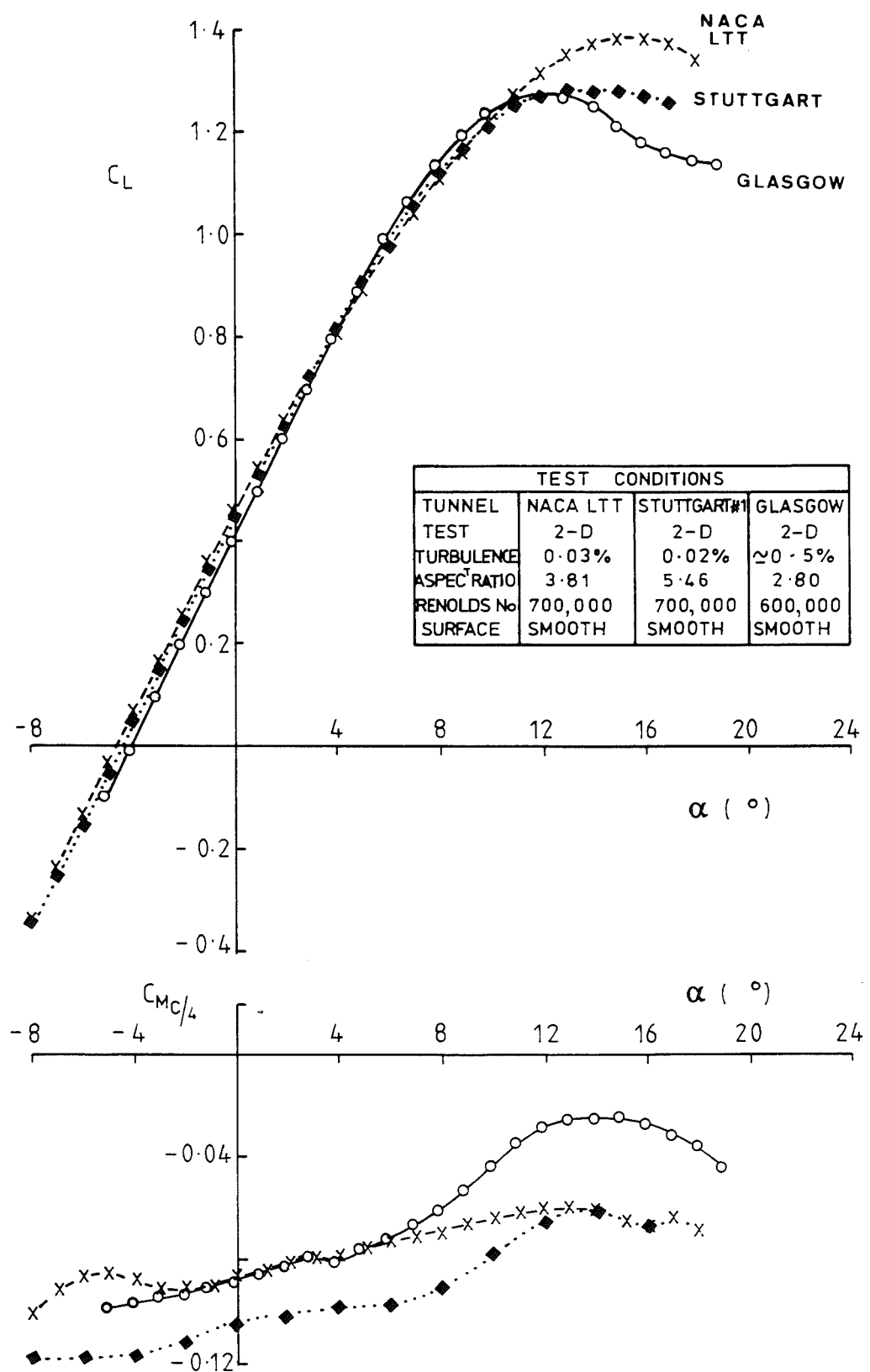


Figure 4.6. Comparison of Lift and Quarter Chord Pitching Moment Coefficients of the NACA-4415 Aerofoil Obtained at Different Test Environments and Wind Tunnels.

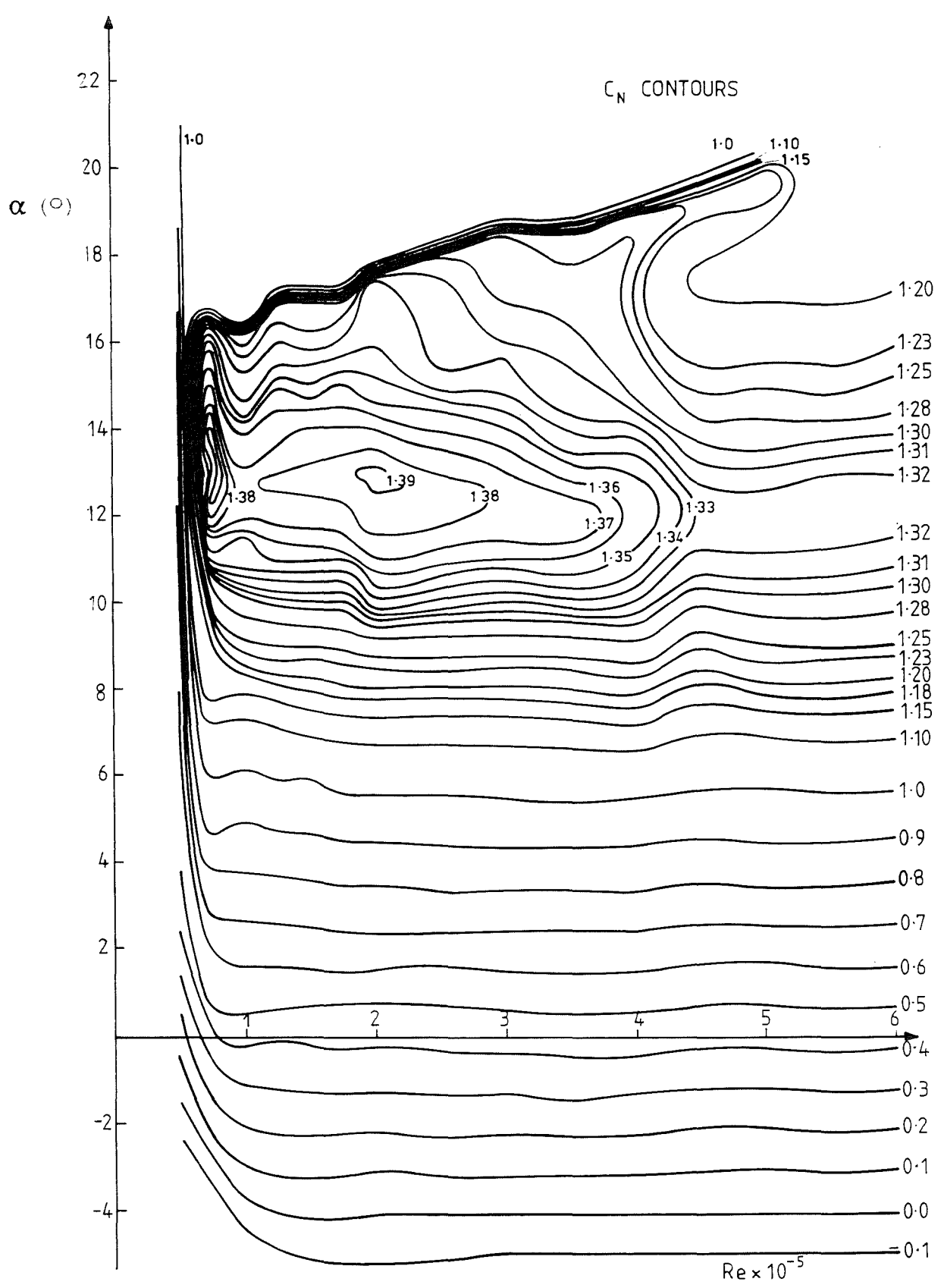


Figure 4.7.1. Normal Force Coefficient Contours for the NACA-4415 Aerofoil with Incidence and Reynolds Number.

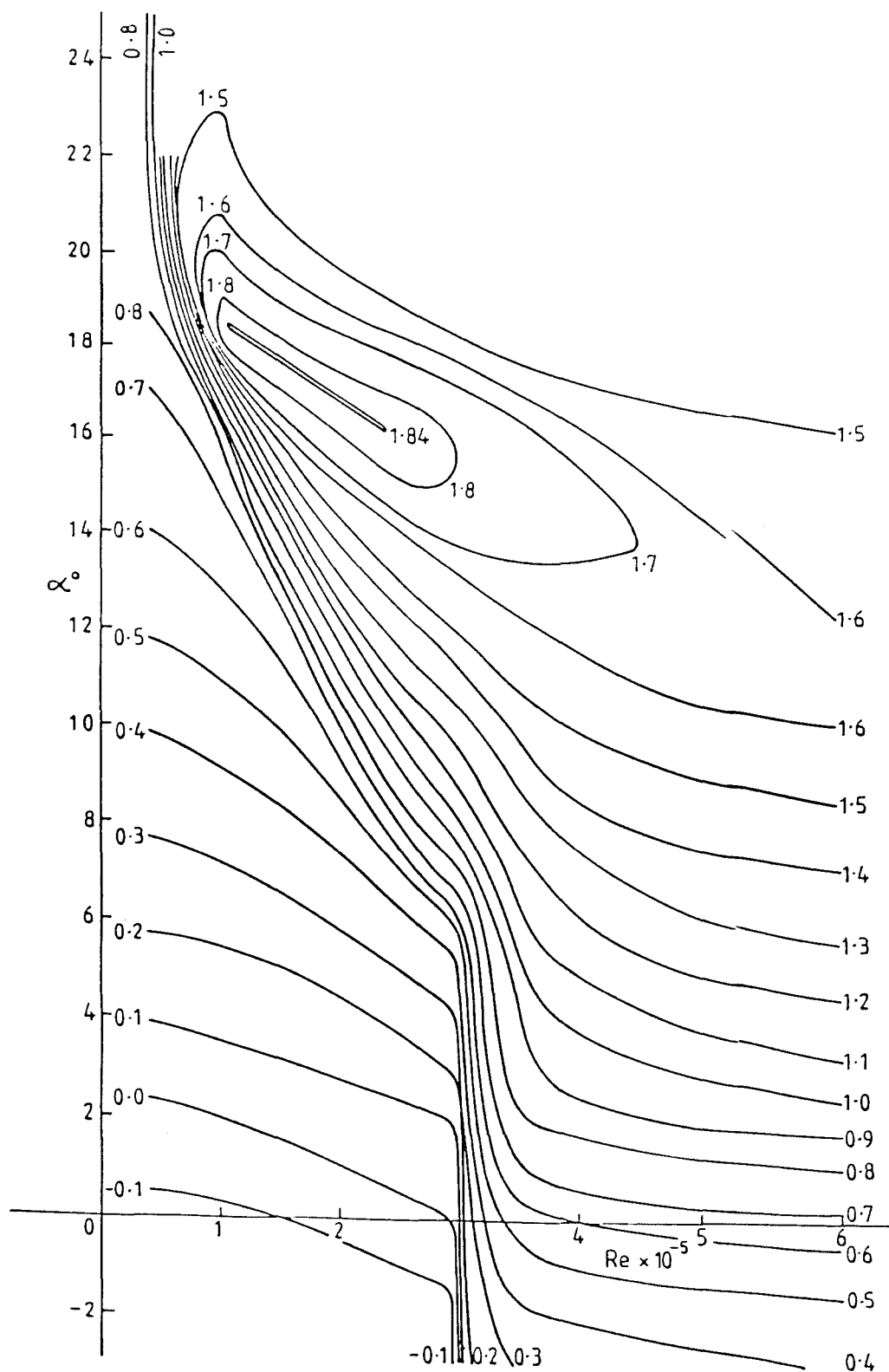


Figure 4.7.2. Normal Force Coefficient Contours for the GU25-5(11)8 Aerofoil with Incidence and Reynolds Number.

(Adapted from Reference 35)

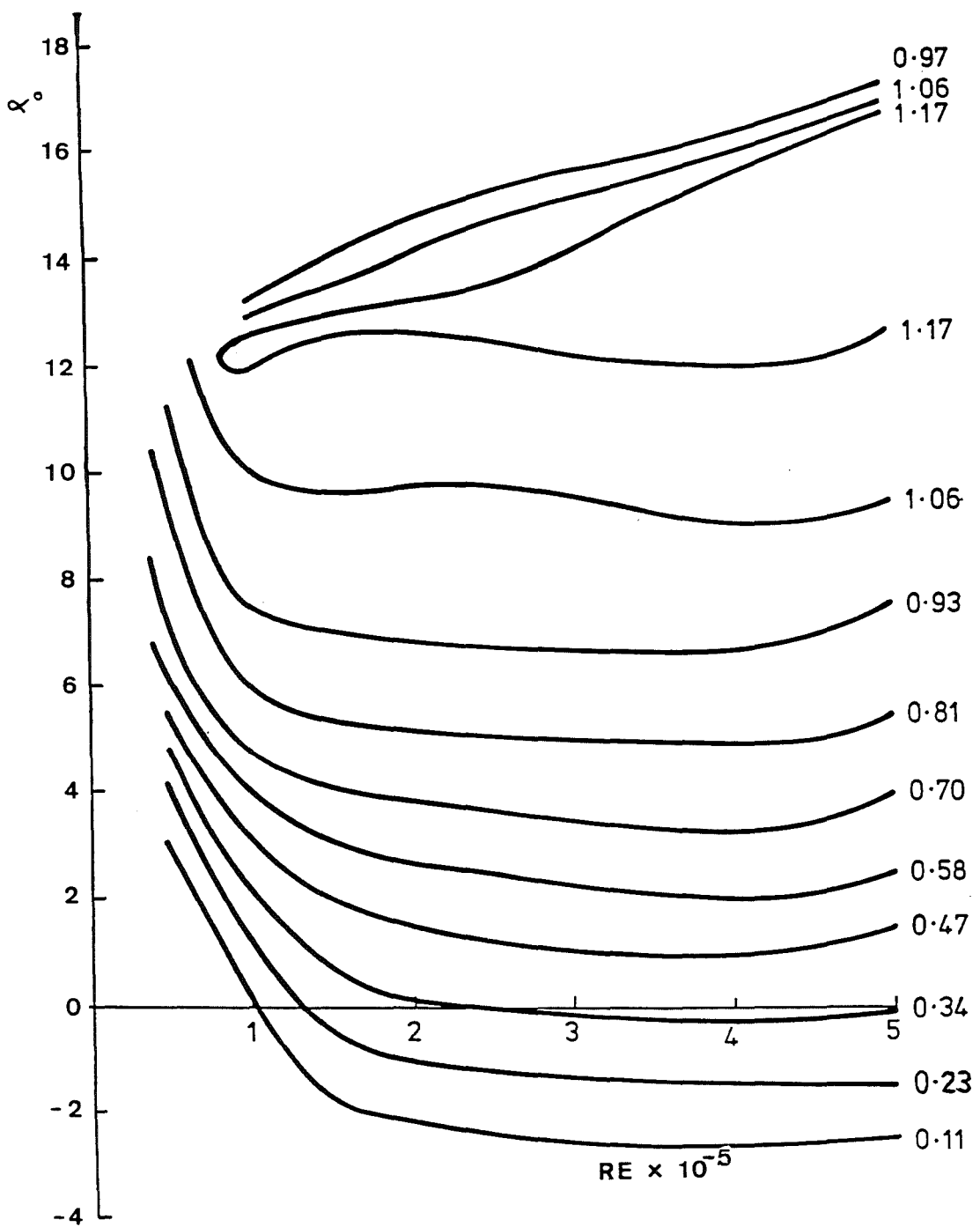


Figure 4.7.3. Normal Force Coefficient Contours for the NASA GA(W)-1 Aerofoil with Incidence and Reynolds Number.

(Adapted from Reference 18)

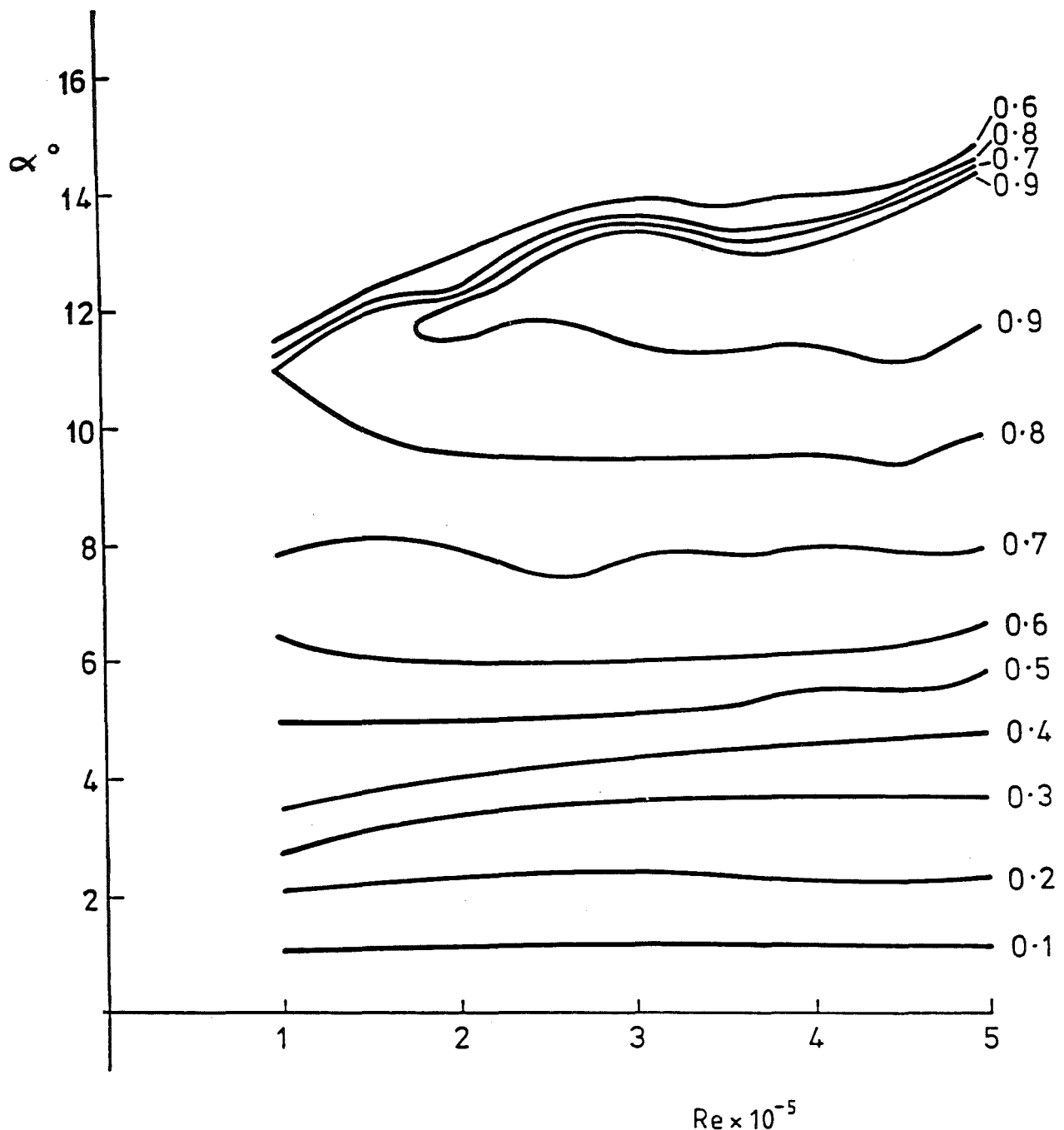


Figure 4.7.4. Normal Force Coefficient Contours for the NACA-0015 Aerofoil with Incidence and Reynolds Number.

(Adapted from Reference 18)

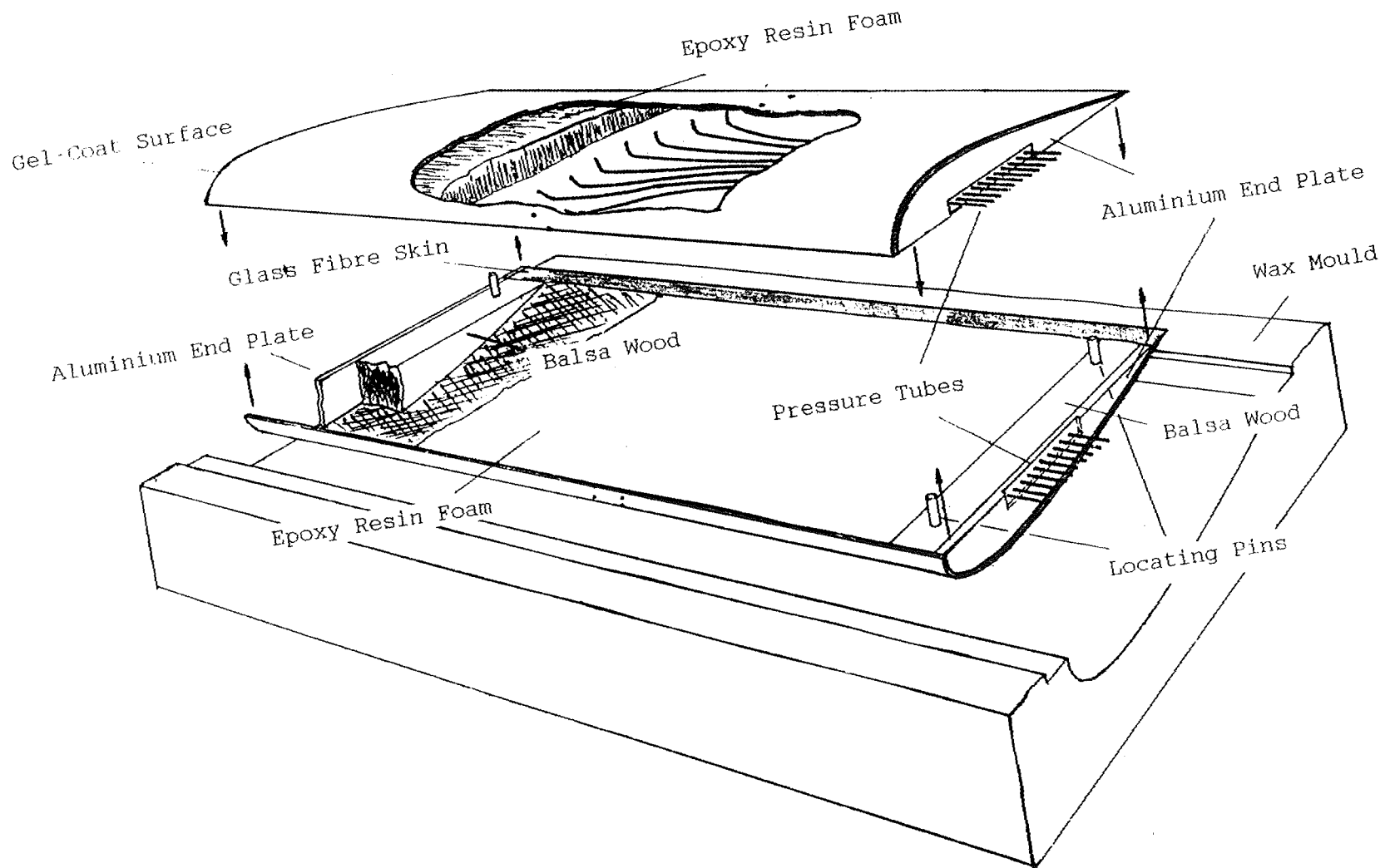


Figure A1. Construction of the NACA-4415 Model